TUM School of Engineering and Design

Robust Methods for the Computation of Compressible Flows with High-Resolution Schemes

Nico Fleischmann

Vollständiger Abdruck der von der TUM School of Engineering and Design der Technischen Universität München zur Erlangung eines

Doktors der Ingenieurwissenschaften (Dr.-Ing.)

genehmigten Dissertation.

Vorsitzender: Prof. Wolfgang Polifke, Ph.D.

Prüfer der Dissertation:

1. Prof. Dr.-Ing. Nikolaus A. Adams
2. Prof. Dr.-Ing. Marcus Herrmann

Die Dissertation wurde am 27.08.2021 bei der Technischen Universität München eingereicht und durch die TUM School of Engineering and Design am 09.02.2022 angenommen.

nico.fleischmann@tum.de

Typesetting LaTeX

Abstract

The flow of fluids accompanies our daily life, starting from the turbulent mixing of milk in a coffee pot over the ride in an aerodynamically shaped car to thunderstorms formed at large scale in weather fronts. Fluid flow phenomena reveal a fascinating complexity over a large variety of scales. Even some of the seemingly simplest phenomena, such as the foam generation in breaking waves, are far from being completely understood. However, a detailed understanding of the occurring mechanisms does not only satisfy scientific curiosity, but it is also essential for the design of technical and medical applications. Compressible fluid dynamics is often directly connected to supersonic aircrafts and the related astonishing effects such as the sonic boom. However, the intriguing behavior of shock waves also allows for a non-invasive treatment of kidney stones and novel drug-delivery techniques.

The numerical flow simulation is a powerful and hazard-free tool that accompanies the investigation of these phenomena, in particular since the practicability of real experiments is often limited. Complex flows include fluid interfaces that are strongly deforming due to interactions with both turbulent structures and shock waves. An accurate prediction of such complex flows requires numerical schemes that maintain the immiscible nature of fluid interfaces and the discontinuous change of state variables across shock waves. Hence, the inherent numerical dissipation of these schemes has to be minimized to avoid smearing of discontinuities during the simulation progress. Today, this target is commonly met by the application of so-called low-dissipation high-resolution methods. The most advanced numerical schemes in the context of compressible multi-component flows are based on such schemes, that were originally established for single-phase compressible flow solvers. However, when such solvers are applied for heavily refined computational grids, recently, some major shortcomings became apparent.

The aim of this thesis is to investigate and overcome the documented shortcomings and failures of low-dissipation high-resolution methods that originate from the underlying finite volume methodology. Two major topics are intensively investigated: First, the artificially broken symmetry in high-resolution simulations in combination with latest low-dissipation schemes, and, second, the grid-aligned shock instability that severely limits an accurate simulation of supersonic flows. A comprehensive discussion of these topics is provided and the predominant mechanisms that lead to the loss of accuracy are uncovered for the first time. The detailed understanding of the problem mechanisms is then utilized to design simple but highly effective modifications that stabilize a variety of popular schemes and significantly improve their accuracy. The robustness of the proposed scheme is tested for a comprehensive set of cases with unprecedented grid resolutions, both in two- and three-dimensional setups. The obtained results indicate that the newly developed methods are highly efficient and effective.

This publication-based thesis is structured as follows: Chapter 1 motivates the presented research topics, and gives a detailed introduction to state-of-the-art compressible flow solvers. Special focus lies on the development of high-order and low-dissipation numerical schemes. Moreover, an introduction to numerically induced symmetry breaking and the numerical flaw of grid-aligned shock instabilities is provided. In Chapter 2, a detailed description of the applied finite volume methodology is provided together with a short discussion of the low Mach number inconsistency in the context of compressible schemes. The main findings of my work are summarized in Chapter 3. Each publication is introduced with a short review of the state of the art, followed by a conclusion of the novel results of the publication. In Chapter 4, a list of all four peer-reviewed journal publications is provided. A concluding discussion across all topics of the thesis is given in Chapter 5 together with an outlook for possible future work. All peer-reviewed publications are reprinted with permission in the appendix. Finally, the bibliography provides a comprehensive list of literature references.

Kurzfassung

Viele alltägliche Phänomene beinhalten komplexe strömungsphysikalische Effekte, sei es die turbulente Durchmischung von Milch und Kaffee, die Fahrt im aerodynamisch geformten Fahrzeug oder auch das Gewitter, das sich entlang einer großen Wetterfront bildet. Die Strömungsphysik von Fluiden weist eine erstaunliche Komplexität und Vielfalt in den auftretenden Größenordnungen auf. Wir sind weit davon entfernt, selbst einige augenscheinlich einfache Vorgänge, wie zum Beispiel die Schaumerzeugung in brechenden Wellen, in all ihren Details zu verstehen. Ein genaues Verständnis der auftretenden Mechanismen dient jedoch nicht nur der Befriedung wissenschaftlicher Neugierde, sondern ist grundlegend für die Gestaltung technischer und medizinischer Anwendungen. Kompressible Strömungsdynamik wird oftmals als Erstes mit Überschallflugzeugen, und dem damit verbundenen faszinierenden Phänomen des Überschallknalls, in Verbindung gebracht. Einige weitere unerwartete Eigenschaften von Stoßwellen erlauben jedoch auch die nicht-invasive Behandlung von Nierensteinen, oder eine innovative Form der nadelfreien Injektion.

Die numerische Strömungssimulation stellt eine mächtiges und zugleich sicheres, begleitendes Werkzeug bei der Untersuchung dieser Phänomene dar, insbesondere da reale Experimente in der Praxis oft nicht durchführbar sind. Komplexe Strömungen beinhalten Grenzflächen zwischen den verschiedenen Fluiden, die sich durch die Wechselwirkung mit turbulenten Strukturen und Stoßwellen stark deformieren können. Die präzise Vorhersage solcher Strukturen erfordert numerische Methoden, welche die scharfe Abgrenzung der Fluide und die sprunghafte Änderung der Zustandsgrößen über Stöße hinweg aufrechterhalten. Die numerische Dissipation, die direkt durch die numerischen Methoden verursacht wird, muss folglich minimiert werden, um ein Verschmieren der Unstetigkeiten im Simulationsverlauf zu verhindern. Dieses Ziel wird heute üblicherweise durch den Einsatz von so genannter "high-resolution" Verfahren mit niedriger numerischer Dissipation erreicht. Die am weitest entwickelten numerischen Methoden im Bereich der kompressiblen Mehrkomponentenströmung basieren dabei auf solchen etablierten Verfahren, die ursprünglich für Einphasenströmungen entwickelt wurden. In den letzten Jahren traten jedoch schwerwiegende Mängel solcher Verfahren auf, wenn sie in Kombination mit sehr fein aufgelösten Rechengittern verwendet wurden.

Das Ziel dieser Doktorarbeit ist die detaillierte Untersuchung und Überwindung dokumentierter Mängel, beziehungsweise Fehler der "high-resolution" Verfahren, deren Ursprünge sich im zugrundeliegenden Finite Volumen Verfahren finden. Zwei Hauptthemen werden dabei intensiv untersucht: Erstens der numerisch bedingte Verlust der Symmetrie beim Einsatz von neuesten "low-dissipation" Verfahren. Zweitens, die gitterabhängig auftretende Schockinstabilität, die oftmals eine präzise Vorhersage bestimmter Überschallkonfigurationen verhindert. Die Arbeit beinhaltet eine umfassende Untersuchung und Diskussion dieser Themen. Dabei werden die dominierenden Mechanismen, die zum Genauigkeitsverlust der Berechnungen führen, erstmals aufgezeigt. Das genaue Verständnis der Problemmechanismen wird schließlich verwendet, um einfache, aber hoch effektive Methoden zu entwickeln, die eine Vielzahl der verbreiteten Verfahren stabilisieren und deren Genauigkeit signifikant verbessern. Die Stabilität der vorgeschlagenen Methoden wird mittels einer umfassenden Serie an Testfällen überprüft. Dabei werden bekannte Referenzfälle in bis dato unerreichter Auflösung sowohl in zwei, als auch in drei Dimensionen simuliert. Die erzielten Ergebnisse bestätigen die hohe Effektivität und Effizienz der neu entwickelten Verfahren.

Die publikationsbasierte Doktorarbeit gliedert sich wie folgt: Die Motivation hinter den behandelten Forschungsthemen, sowie der Stand der Technik der numerischen, kompressiblen Strömungslöser wird in Kapitel 1 dargestellt. Dabei liegt ein besonderes Augenmerk auf der Entwicklung der "high-resolution" Verfahren höherer Ordnung. Darüber hinaus wird eine Einführung in die Literatur des numerisch bedingten Symmetrieverlustes und des numerischen Fehlers der gitterabhängigen Schockinstabilität gegeben. Kapitel 2 beinhaltet eine detaillierte Beschreibung des verwendeten Finite Volumen Ansatzes. Zusätzlich wird auf die Inkonsistenzen bei der Anwendung von kompressiblen Lösern für Strömungen mit geringen Machzahlen eingegangen. Die Hauptergebnisse meiner Arbeit werden in Kapitel 3

dargestellt. Jede Veröffentlichung wird durch eine kurze Zusammenfassung des aktuellen Stands der Forschung und einer Kurzfassung der darüber hinausgehenden Ergebnisse erklärt. Kapitel 4 zeigt eine Liste aller vier extern begutachteter und in wissenschaftlichen Fachzeitschriften veröffentlichten Artikel. Alle behandelten Themen der Doktorarbeit werden in Kapitel 5 zusammenfassend diskutiert und es wird ein Ausblick auf mögliche anknüpfende Forschungsthemen gegeben. Alle Veröffentlichungen inklusive der Lizenz zur Wiederverwendung befinden sich im Anhang der Arbeit. Das abschließende Literaturverzeichnis beinhaltet alle verwendeten Quellen und Referenzarbeiten.

Danksagung

Die vorliegende Arbeit ist während meiner Zeit als wissenschaftlicher Mitarbeiter am Lehrstuhl für Aerodynamik und Strömungsmechanik von 2017 bis 2021 entstanden. An dieser Stelle möchte ich all jenen Personen meinen Dank aussprechen, die in besonderer Weise zum Erfolg meiner Arbeit beigetragen haben.

Ich möchte mich zuallererst bei meinem Doktorvater, Herrn Prof. Dr.-Ing. Nikolaus A. Adams, für seine Betreuung und Unterstützung während meiner Zeit am Lehrstuhl bedanken. Das große Vertrauen, dass Sie Ihren Doktoranden entgegen bringen, macht den Lehrstuhl AER zu einem Ort, an dem man gerne arbeitet. Insbesondere möchte ich mich für die vielen Freiheiten bedanken, sei es bei der Wahl der Forschungsthemen oder der Auswahl internationaler Konferenzen. Diese Freiheiten gaben mir die Möglichkeit, mich sowohl fachlich als auch persönlich weiterzuentwickeln.

Des Weiteren möchte ich mich bei Herrn Prof. Dr.-Ing. Marcus Herrmann bedanken. Während meiner Zeit in Arizona konnte ich viele neue Eindrücke und Erfahrungen sammeln. Durch die enge Betreuung ermöglichten Sie mir eine schnelle und reibungslose Einarbeitung in die Thematik, die mich später noch durch meine gesamte Promotion begleiten sollte. Es freut mich daher sehr, dass Sie die Zweitprüfung für meine Arbeit übernommen haben. Auch hierfür vielen Dank.

Mein besonderer Dank gilt Herrn Dr.-Ing. Stefan Adami, meinem Betreuer und Gruppenleiter der Nanoshock Gruppe am AER. Ohne dein freundliches Angebot Teil der Nanoshock Gruppe zu werden, hätte ich aller Wahrscheinlichkeit nach nicht zu promovieren begonnen. Vielen Dank für die zahlreichen fachlichen und persönlichen Gespräche. Ich möchte mich auch herzlich für die Organisation der Gruppenevents, der jährlichen Workshops und des Wanderausflugs bedanken. Diese Veranstaltungen haben immer zu einer guten Atmosphäre über den Büroalltag hinaus beigetragen. Danke auch für die aufmerksame Durchsicht der Arbeit.

Darüber hinaus möchte ich mich bei allen Mitarbeitern am Lehrstuhl bedanken, insbesondere bei den Kollegen der Nanoshock Gruppe. In den Kaffeerunden oder bei Spaziergängen am Nachmittag ergaben sich viele spannende Diskussionen und fachlichen Anregungen. Mein Dank gilt Nils für die durchweg kompetente und äußerst geduldige Unterstützung bei diversen Fragen zu Details der Implementierung und zum Cluster. Ohne deine steten Anmerkungen und die zahlreichen Diskussionen würde mein Programmierstil heute wohl anders aussehen. Jakob, vielen Dank auch an dich für den guten Cappuccino und die interessanten Gespräche über Forschungsthemen, unsere Universität und darüber hinaus. Weiterhin bedanke ich mich bei Angela Grygier und Hua Liu für die wichtige Arbeit, die sie am Lehrstuhl leisten.

Weiterer Dank gilt meinen Freunden und den Kameraden der Feuerwehr. Euer beständiges Nachhaken zum Fortschritt meiner Arbeit waren mir stets motivierender Ansporn.

Mein größter Dank gilt meiner Familie - meinen Eltern und meinem Bruder - für die große Unterstützung während meines gesamten Studiums. Vielen Dank für eure Geduld und euer Verständnis für meine gelegentlich schlechte Laune. Ich möchte mich natürlich auch bei dir bedanken, Stella. Ohne deine subtilen Versuche meine Laune zu retten, sei es durch Kaffee oder Süßigkeiten, wäre die Zeit im Home-Office deutlich anstrengender geworden. Danke auch für deinen steten Anschub mich zum Schreiben zu bewegen.

Contents

Chapter 1

Introduction

1.1 Motivation

This thesis provides a comprehensive overview of my research in the field of numerical method development for compressible flow solvers. The focus lies on the improvement of the classical finite-volume methodology with respect to two major topics: understanding and avoiding of floating-point induced effects on highly resolved simulations with low-dissipation methods, and enhancement of numerical robustness against the grid-aligned shock instability problem (commonly denoted as carbuncle phenomenon).

My research is based on the European Union's Horizon 2020 research and innovation programme project *Manufacturing Shock Interactions for Innovative Nanoscale Processes (grant agreement No. 667483)*. The objective of this project is to discover the intriguing behavior of shock waves with the help of latest state-of-the-art computational methods. Such methods comprise the application of low-dissipation and high-order finite volume schemes combined with a multiresolution grid approach implemented within a massively parallel simulation framework, which allows for the prediction of complex interactions across scales such as shock interactions with turbulent structures and multiphase interfaces. Potential applications range from targeted drug delivery over kidney-stone lithotripsy to advanced aircraft design.

Computational Fluid Dynamics (CFD) plays an important role in today's understanding of complex fluid mechanics. Often, experiments are either complicated to set up, expensive or even dangerous, e.g. when extreme temperatures or pressures are present. Then, simulations provide a powerful and secure alternative to study complex physical behavior. Moreover, accompanying simulations to real experiments are particularly helpful to deepen the understanding of physical phenomena since the availability of state quantities is not limited to measurement points or certain time intervals. Hence, the propagation and interaction of shock waves can be closely followed in the minutest detail, while the dominating flow structures can be easily validated against experimental observations.

The development of low-dissipation and high-order numerical schemes allows for a computation of shock wave phenomena with hitherto unprecedented precision. The massive reduction of inherent numerical dissipation by the schemes thus allows for a precise prediction of shock wave propagation also for long time intervals. Additionally, the constant rise in computational power combined with multiresolution schemes enables extremely fine computational grids. These developments come along with new challenges. The precision limit of floating-point calculations is well known in the scientific-computing community, but this topic has been of little interest to the CFD community so far. Indeed, effects of floating-point inaccuracies may heavily influence numerical results when low-dissipation methods are applied. Even though multiple research groups noticed some unexpected behavior in their results, these effects have not been studied in literature so far [25, 41, 42, 117, 139, 146, 168].

Despite the tremendous improvements in numerical methods over the last decades, the simulation of multi-component compressible flows is still a difficult task. Even though there are various different approaches to include multiple different fluids, all procedures rely on a proper treatment of the wave propagation within each phase. It is therefore of crucial importance to apply robust and accurate single-phase methods in the first place. In his review of developments in CFD since the 1960s, Bram Van Leer [91] denoted the so-called carbuncle phenomenon as the "greatest unresolved problem of classical finite-volume schemes". Surprisingly, even three decades after its detection, this instability that plagues high Mach number simulations with low-dissipation schemes has still not been fully understood.

These topics are of high scientific and industrial interest since they touch the core of the finite volume methodology that most of the state-of-the-art compressible flow solvers are based on. Although the findings presented in this thesis are mainly presented for inviscid Euler equations, the developed methods directly translate to more complex solvers, e.g. multi-component Navier-Stokes solvers. The following sections provide a detailed introduction to the state of the art of high-order schemes and the resultant research questions that are covered by this thesis.

1.2 High-Order and Low-Dissipation Godunov-Type Schemes

The success of Godunov's approach [48] in finite-volume methods during the last two decades is caused both by its rigorous conservation property at the discrete level and by the straightforward application of high-order methods in combination with efficient approximate Riemann solvers. Traditional schemes, such as the Monotonic Upstream-centered Scheme for Conservation Laws (MUSCL) [157] or flux limiting procedures [93, 150], are usually limited to third order [92]. While this is accurate enough in many cases, the prediction of shock interactions with turbulent structures and multiphase interfaces requires very low inherent dissipation of the numerical schemes since such phenomena occur at vanishing physical viscosity. The class of weighted essentially non-oscillatory (WENO) schemes proved appropriate for this task due to their straightforward design principles, which allow the construction of schemes with arbitrary order.

WENO schemes were developed from ENO schemes that were originally proposed by Harten et al. [64]. The basic idea of WENO schemes is to achieve a designed order $2r-1$ in smooth regions by an ideal combination of sub-stencils of order r. The local order will be automatically reduced if a smoothness measure exceeds a predefined threshold. Then, only smooth sub-stencils are taken into account. A weighting procedure was first described by Liu et al. [102], and later optimized by Jiang and Shu in their seminal work [76] resulting in the WENO5-JS. This fifth-order scheme is certainly the most widespread WENO type up to date, and has been applied to various different fields of computational physics [140]. It consists of three third-order sub-stencils combined with smoothness measures that limit the influence of the sub-stencil dependent on a gradient-like evaluation of the stencil points.

Despite the enormous success of this scheme, the stencil has still limited capability to resolve turbulent structures. In fact, it is observed that the order of the scheme often reduces already in smooth areas. This happens in particular in the vicinity of smooth extrema, such as the maximum and minimum regions of sine functions. The WENO-M scheme of Henrick et al. [68] improved the quality near smooth extrema, however, the mapping procedure causes additional computational cost. On the other hand, also the resolution at discontinuities has been further improved. A major progress consists in the introduction of a global smoothness measure that takes the smoothness of the whole stencil region into account. The resulting WENO5-Z scheme of Borges et al. [12] shows a significantly sharper resolution of discontinuities. An alternative approach to further reduce the inherent numerical dissipation is to increase the order. Balsara and Shu [9] were the first to propose WENO schemes up to 13^{th} order. Later, Gerolymos et al. [46] extended the reconstruction stencil even up to 17^{th} order. However, practical relevance of schemes beyond fifth order is limited to this day. WENO schemes with extreme order often lack robustness and have to be combined with monotonicity preserving [9, 46]. Besides the additional cost of stabilization methods, extreme-order stencils also require huge stencil ranges that renders common implementation procedures, e.g. distributed-memory parallelization, increasingly inefficient. Hence, the focus lies on improving existing procedures without further increasing stencil sizes.

Hu et al. [74] developed a six-point stencil that blends between central and upwind schemes smoothly with new types of smoothness indicators. The WENO-CU6 has been further improved by the introduction of a physically-motivated scale-separation formulation [72]. In their work, the authors show that the scale-separation WENO-CU6-M2 scheme leads to a physically consistent implicit subgrid-scale model for incompressible and compressible turbulence, which makes the scheme also applicable for underresolved simulations. This type of scheme has been successfully applied for the direct numerical simulation (DNS) of Richtmyer-Meshkov instabilities [153, 154]. More recently, an alternative group of methods has been proposed by Fu et al. [41, 42]. An ENO-like stencil selection, that considers sub-stencils either with their ideal weight or not at all, allows for a drastic reduction of numerical dissipation. The targeted ENO (TENO) schemes have been successfully applied to simulate compressible multi-component flows [59], chemical reacting flows [30], and turbulence in high-speed compressible flows [60].

Besides the described main developments of WENO-type methods, there is a vast number of contributions with minor improvements of specific schemes. The incremental-stencil WENO reconstruction (WENO-IS) [161] is enhanced for the simulation of multiphase flows. It includes an additional 2-point candidate stencil, which leads to an increased robustness of simulations using the 5-equation model of Allaire [3]. However, the increase in robustness comes along with a higher amount of inherent dissipation [177]. Balsara et al. [8] proposed a class of WENO schemes with adaptive order that builds upon computationally efficient Legendre polynomials. Acker et al. [2] further improved the WENO5-Z by adding an additional term in the smoothness formulations resulting in significant accuracy benefits in smooth parts of the solution. Other incremental modifications have been proposed by multiple different groups [7, 43, 44, 169, 175, 176]. Today, the number of new publications on WENO adaptations makes it increasingly hard to follow each development in detail. The provided list of publications is certainly incomplete and limited to a selection of most interesting developments in the context of our project. The high scientific activity demonstrates the large interest to construct stable and accurate low-dissipation schemes.

While Godunov [48] originally applied an iterative Riemann solver to exactly solve the Riemann problem on each interface, this expensive approach has later been replaced by explicit, approximate Riemann solver. The application of computationally cheaper approximate solver is possible with nearly no impact on the accuracy of the result since only a limited amount of information of the whole Riemann solution is actually required for the flux evaluations [94]. The most important groups of approximate Riemann solver are the Osher approximation [34, 106, 107], the Roe approximation [126] and HLL-type solver [66, 152]. The Osher approximation is commonly applied in the field of steady aerodynamics [150], but can be rarely found in modern CFD solvers. As mentioned by different authors [4, 120], the Osher approximation is one of few schemes that can accurately handle slowly moving shock waves without producing post-shock oscillations.

The Roe approximation represents the group of linearized solvers. Even though this method reveals a number of shortcomings, it is one of the most widespread approximate Riemann solvers today. The approximation relies upon a linearized system matrix built with the help of Roe-averaged quantities. The averaging process has to be derived for each system of equations of interest. This might turn out to be a complicated task, though it has been done for Euler equations with a general equation of state [47, 127] and magnetohydrodynamics [13]. One of the drawbacks of linearized methods is that these schemes cannot properly handle transsonic rarefactions without entropy fix. Non-physical rarefaction shocks are usually avoided by the introduction of additional dissipation [65, 150]. Another well-known difficulty of the Roe approximation is its weak positivity preserving property [114]. In low-density regions of the flow, the solver may produce negative pressure or density states that cause an immediate failure of the simulation. This flaw is amplified when using high-order WENO methods, and it renders a straightforward application on complex flow simulations with latest reconstruction methods problematic.

The HLLC flux is typically more robust, though slightly more dissipative as compared to Roe's approximation. This flux was originally developed by Toro et al. [152] via the introduction of an accurate contact wave treatment into the HLL solver, which builds upon the seminal work by Harten, Lax and Van Leer [62]. Actually, the authors [62] already proposed the possibility of designing two types of fluxes. Note, these two options are denoted as "HLL" and "HLLC" in literature. However, they did not provide suitable signal speed estimates, which are necessary to use these fluxes in flow solvers. Thus, it took several years till Einfeldt [32] and Davis [24] independently from each other proposed signal speed estimates for the HLL solver. Later, Batten et al. [10] completed the set of signal speed estimates that are commonly in use today with an accurate estimate for the contact wave. The HLL-type solvers have been shown to preserve positivity [32] and results are not flawed by nonphysical rarefaction shocks [150]. The HLLC flux is often applied for the simulation of multi-component flows with the four-, five- and six-equation models [77, 132, 134], and has been extended to handle capillary forces to simulate surface tension effects at liquid/gas interfaces [45]. Moreover, its design principles allow for straightforward extensions to other types of hyperbolic equations, e.g. for magnetohydrodynamics [6, 58, 95], by the introduction of additional wave types. The HLLC solver has also been extended for general equation of states [73].

The Roe approximation with entropy fix and the HLLC flux are denoted as complete Riemann solver in context of Euler equations since they accurately capture all occurring wave types. In contrast, incomplete Riemann solvers, e.g. the HLL solver, only model a subset of the existing wave types. This may lead to excessive smearing, especially of contact waves. The same smearing is observed for flux vector splitting schemes, such as the Steger–Warming splitting [145] or the van Leer splitting [158]. While the latter are easy to implement and often used for steady state simulations in aerodynamic applications, their accuracy is often insufficient when applied to Euler equations [159].

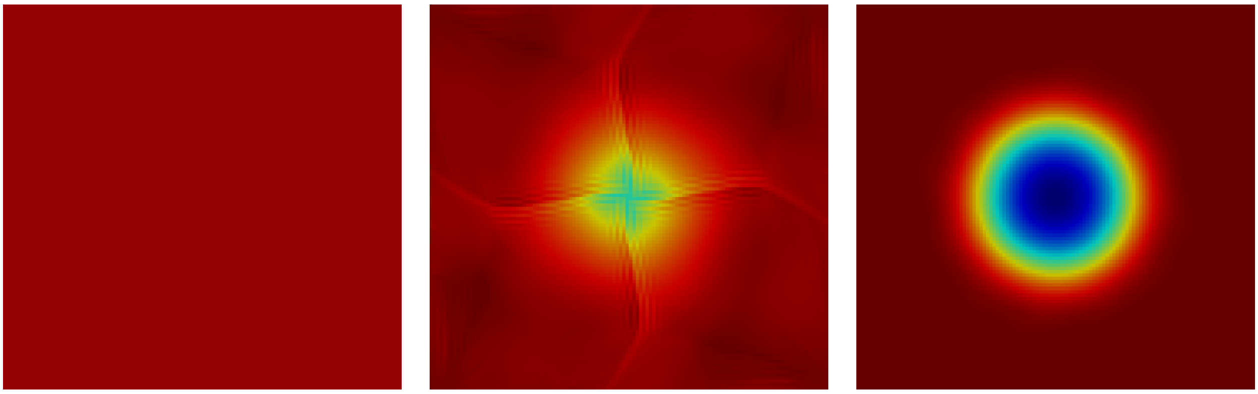

(a) HLL - First Order (b) HLL - WENO3-JS (c) HLL - WENO5-JS

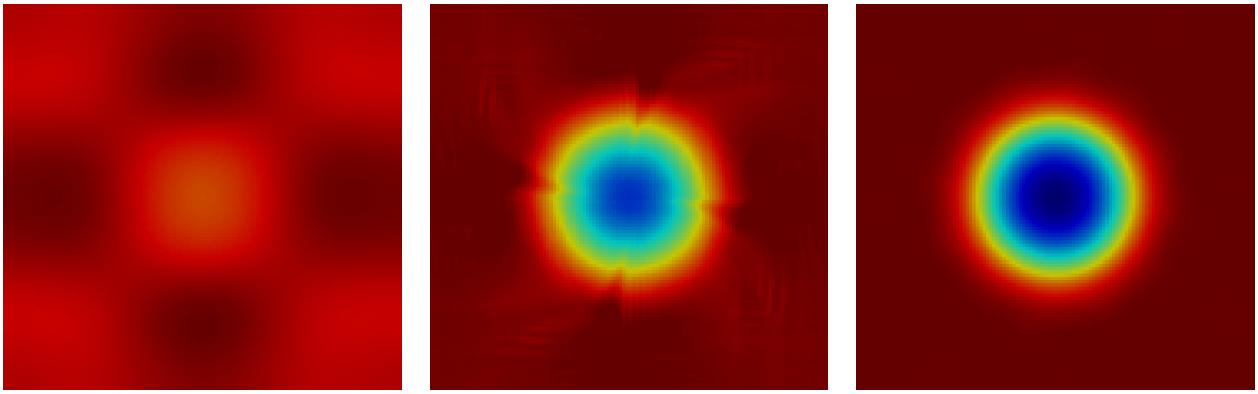

(d) HLLC - First Order (e) HLLC - WENO3-JS (f) HLLC - WENO5-JS

Figure 1.1: Gresho vertex problem - simulated pressure distribution after one advection cycle

While the development of new types of Riemann solver seems finished by the end of the last century, the number of publications for WENO schemes is steadily increasing to this day. A small, illustrative example shall demonstrate the impact of the Riemann solver and reconstruction scheme choice. In Figure 1.1, the advection of a rotating vortex is simulated according to the work of Gresho and Chan [51] with a low-dissipation complete HLLC flux and an incomplete HLL flux combined with spatial reconstruction schemes with increasing order. The pressure distribution after one full advection cycle through the domain is correctly predicted and almost indistinguishable from the initial condition for both Riemann solvers when combined with WENO5-JS. However, the application of a third-order scheme reveals significant effects of numerical dissipation of the HLL flux. Interestingly, the application of a first-order scheme in combination with HLL leads to a pressure field with unit value up to floating-point precision. This simple example demonstrates the large influence of high-order schemes for the accurate prediction of complex flows. When different types of Riemann solver are combined with high-order reconstruction methods, the differences among them often almost vanish. The reduction of numerical dissipation during the last two decades was mainly achieved via the improvement of spatial reconstruction stencils. The developments on Riemann solvers are mainly focused on the improvement of robustness against numerical instabilities, see Section 1.4. Nevertheless, as shown in [37, 39], the numerical dissipation can also be further reduced by adaptations of the Riemann solver itself. Unfortunately, a reduced amount of numerical dissipation decreases the robustness of the simulation. As a remedy, additional positivity-preserving techniques [70, 90, 173] gain further interest to stabilize simulations with latest reconstruction schemes.

1.3 Floating-Point Induced Symmetry Breaking

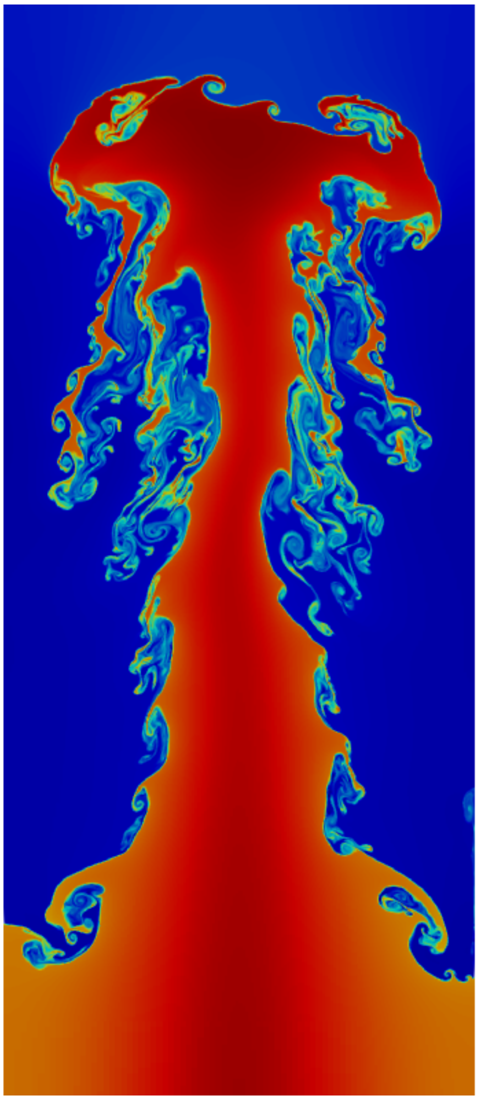

Figure 1.2: Rayleigh-Taylor instability

The developments described in Section 1.2 lead to a significant decrease of inherent numerical dissipation in shock capturing methods. Additionally, modern computer hardware facilitates the use of these schemes with very fine mesh resolution. Thus, simulations with billions of computational cells simulated over thousands of time steps became feasible with widespread mainstream numerical frameworks [69, 116, 128, 163]. Eventually, diminishing numerical dissipation fails to suppress numerically triggered instabilities of well-established verification cases for the inviscid Euler equations. In Figure 1.2, a Rayleigh-Taylor instability is shown when simulated with a high-order TENO scheme. Similar results can be found in literature [25, 41, 42, 117, 139, 146, 168]. Even though one might argue that results look somehow physical, since flow fields from experimental images also never look perfectly symmetric, this result cannot be expected for a perfect initial setting of a symmetric problem. Hence, it is highly unsatisfactory to obtain simulation results that include undesired behavior whose origin and properties can only be speculated on.

Remacle et al. [117] were the first to suspect floating-point inaccuracies due to round-off errors to be the reason for numerical symmetry breaking in the context of discontinuous Galerkin methods. It is well known that floating-point calculations suffer from loss of associativity due to round-off errors dependent on the chosen precision [49]. Usually, this flaw does not affect CFD simulations since its effect is suppressed by the inherent dissipation of the numerical scheme. If at all, symmetry breaking typically can only be observed for small-scale structures near the resolution limit. However, when simulations are performed on supercomputers, trillions of floating-point errors may accumulate. Then, with vanishing numerical viscosity using latest methods, the small-scale symmetry breaking exhibits inverse-cascade phenomena and affects the macroscopic flow evolution leading to a drastically changed flow topology.

To this day, there where only few attempts to actively control the influence of round-off errors. Sutherland [147] introduced a cut-off approach to control the floating-point truncation error for simulations in astrophysics. Recently, Don et al. [29] suggested to locally reduce the order of smoothness indicators in WENO schemes to delay the onset and reduce the magnitude of symmetry errors. It is evident that a detailed understanding of the underlying mechanism behind numerical symmetry breaking is desirable. This understanding may also be helpful to gain control over the process in terms of inserting physically meaningful disturbances. This is particularly relevant in view of further increasing computational power and the increasing complexity of numerical methods.

1.4 The Grid-Aligned Shock Instability

In 1988, Peery and Imlay were the first to describe "an unusual numerical phenomenon" [112] in literature. They encountered a severe disturbance of the flow field in the region of the stagnation point similar to the one shown in Figure 1.3. Here, a bow shock around a blunt body was simulated using Roe's approximation revealing the disruptive instability. It was the starting point of three decades of intense investigations and dozens of scientific publications concerned with this complicated issue. Due to its excrescence-like shape, the phenomenon was soon commonly denoted as the "carbuncle phenomenon", though the instability may occur in various different manners, not always being as destructive as in the bow-shock case. In fact, the instability often occurs when strong shock waves move aligned with the computational grid. Other examples are the kinked Mach stem and the odd-even decoupling phenomenon [114]. A representative example of the latter is shown in Fig. 1.4 for the simulation of a shock wave interaction with a helium bubble in air with the HLLC solver. The fact that the instability occurs predominantly in combination with the most successful group of complete Riemann solvers renders the issue particularly harmful.

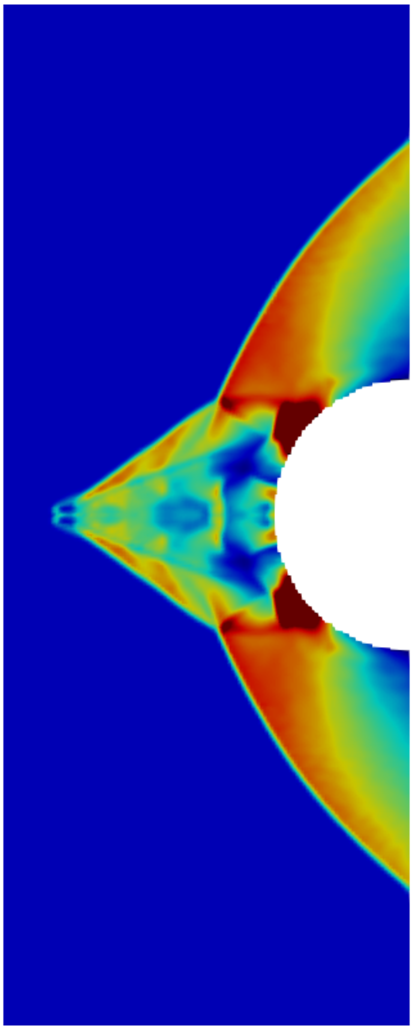

Figure 1.3: Carbuncle phenomenon in bow shock simulation

Quirk [114] performed a systematic investigation of the problem, and noticed that schemes with good shock-capturing properties are more likely to be affected by the instability than more dissipative flux formulations, such as the HLL Riemann solver or flux-vector splitting schemes. He concluded that insufficient dissipation at the contact line might be the reason for the instability, which paved the way for possible treatments of the problem. Afterwards, almost all proposed cures add additional dissipation the one way or the other. Quirk [114] already noticed that the ad-hoc application of Harten's entropy fix to increase numerical dissipation at the contact and shear waves cures the problem, albeit lacking physical justification.

In the following, most investigations of the problem directly focused on specific types of Riemann approximations to cure the problem. For a comprehensive overview of developments for Roe schemes the reader is referred to Section 3.2. Additional findings for HLL-type schemes are summarized in detail in Section 3.3.

In contrast to previous approaches, Rodionov [122] did not try to modify the discretization of the convective term, but he suggested to add additional viscosity via a new source term. He argues that this approach is more consistent with the underlying physical principles, as the Euler equations are complemented to Navier-Stokes-type equations. The proposed scheme delivers stable results and can be easily combined with any desired Riemann solver. The methodology was successfully extended to three-dimensional simulations [123] and to higher-order methods [124]. In fact, Rodionov [123] performed one of few investigations of the carbuncle phenomenon in three-dimensional simulations. Recently, a simplified procedure for the calculation of the artificial viscosity has been proposed [125]. However, Rodionov's method increases dissipation not only in the shock vicinity, but it may contaminate the computational domain even far away of shocks.

Another general approach has been developed by Chen et al. [18–20]. In [20], a simple interface-normal velocity reconstruction procedure is proposed that can be easily applied in combination with existing Riemann solver. The authors argue that a linear reconstruction of the interface-normal velocity between associated neighbor cells takes the high-order properties in the transverse direction of the cell interface into consideration, which has been always neglected in conventional finite volume methods. Although this procedure stabilizes all tested schemes, the physical mechanism behind the modification remains unclear. Further studies on the underlying mechanism were performed in [18] using a newly developed instability analysis model named ”cell–shock–cell system". Their study revealed that the numerical shock instability essentially starts from the grid face perpendicular to the shock rather than the grid parallel to it. They concluded that the shock instability is essentially a multidimensional phenomenon. The negative pressure dissipation of the density flux at the vertical transverse face of a shock was found to trigger the instability. This term has been reformulated subsequently by a transverse pressure dissipation modification in [19]. Again, the proposed general cure can be applied to any desired Riemann solver.

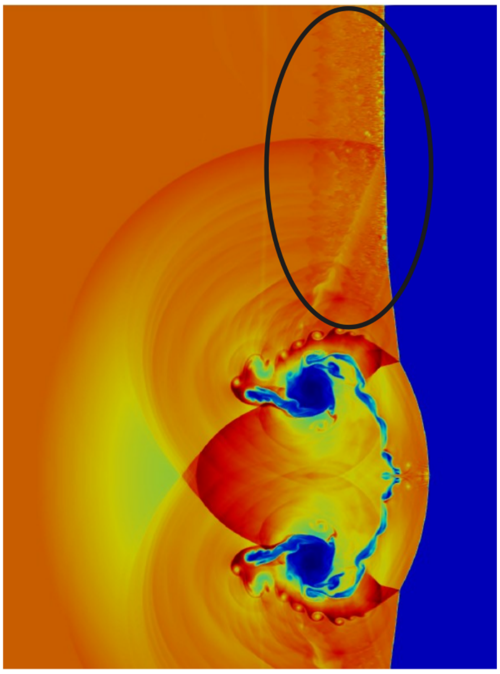

Figure 1.4: Odd-even decoupling in multi-component flow simulation

Note, that all of the techniques reported in literature add additional dissipation to the scheme in one way or another. Additional discussions on grid-aligned shock instabilities with minor modifications of the presented schemes can be found in literature [15, 67, 80, 82, 103, 110, 121, 167]. The grid-aligned shock instability has also been studied in connection with the AUSM family of schemes [16, 85, 88] and for shallow water equations [5, 81, 83].

Along with the efforts to eliminate the occurrence of the instability in numerical simulations, there has also been an intense discussion about possible physical origins of the problem [33, 104, 115, 121]. Robinet et al. [121] studied the stability of two-dimensional plane shock waves. Their theoretical analysis uncovered a previously undetected genuine instability of Euler equations. This instability was conjectured as possible intrinsic origin of both the carbuncle phenomenon and Quirk's odd-even decoupling. The authors supported their assumption by comparison of theoretical predictions with numerical results that showed convincing correlations. As a consequence, they suggested to design numerical methods in the framework of Navier-Stokes equations rather than for Euler equations. However, the theoretical analysis presented in [121] has been heavily criticized in [23], where the authors argue against the existence of a so-far unknown instability of Euler equations. Beyond, the physical background of the carbuncle phenomenon seems to be supported by some experimental observations [79, 84]. In [79], the interaction of vortices and bow shocks is studied. The authors observed flow features that strongly resemble the carbuncle structure. Kikuchi et al. [84] designed experiments based on preliminary numerical simulations that suffered from the bow shock instability. For gases with low ratio of specific heats γ, the shock instability can also be observed in their experiments. As pointed out by [122], experimental observations often include special set-ups that might trigger an instability, whereas the instability in simulations forms by itself. Elling [33] argues that carbuncles may be some special kind of entropy solutions, which can be physically correct in some circumstances. He describes a simple setting using filaments to trigger an instability that resembles the carbuncle phenomenon while being a correct vanishing-viscosity solution. Beside some few cases that can be physically motivated, the strong grid-dependency of many simulation results connected with the instability clearly points to a numerical origin. Nevertheless, the controversial discussion reveals that the problem is still not fully understood.

1.5 The Aim of This Thesis

This thesis aims to summarize my work of the last four years. The presented findings contribute to the advancement of high-resolution schemes for compressible flow solvers in terms of improvement of consistency and numerical robustness allowing for an accurate prediction of complex flow configurations. The previous sections highlighted the large scientific interest to gain additional understanding of both the numerically triggered symmetry breaking and the occurrence of the grid-aligned shock instability. This thesis includes the following four contributions, each of which is published in the peer-reviewed Journal of Computational Physics or Journal of Computer & Fluids respectively:

1. A detailed investigation of floating-point induced symmetry breakdown, which results in a novel generalized consistency-ensuring summation rule to avoid numerical symmetry breakdown, see Section 3.1.

2. A novel explanation of the carbuncle phenomenon, which enables the construction of a shock-stable Roe-type scheme with reduced numerical dissipation, see Section 3.2.

3. A detailed investigation of the grid-aligned shock instability in connection with the HLLC solver, which results in a novel centralized formulation and a novel shock-stable HLLC-LM scheme with reduced numerical dissipation

4. The identification of a mathematical inconsistency of a popular type of signal-speed estimate for HLL-type schemes

Additionally, the findings have been presented at four international conferences, namely, at the GAMM Annual Meeting 2018 in Munich, at the 30th International Conference on Parallel Computational Fluid Dynamics 2018 in Indianapolis (USA), at the 32nd International Symposium on Shock Waves 2019 in Singapore and at the 14th WCCM & ECCOMAS Congress 2020 in Paris.

The remainder of this work is structured as follows: In Chapter 2, the governing equations and the fundamental numerical approach of the finite-volume framework are introduced including spatial and temporal discretization techniques. A detailed description of high-order spatial reconstruction procedures along with the applied Riemann solvers is provided. The proposed new schemes of this work are directly based on these methods. Chapter 2 completes with a short introduction to the shortcomings of Godunov-type schemes in the context of low Mach number flows. In Chapter 3, an overview of the novelties of the four publications is presented. Each of these publications is motivated with a short review on the state of the art, indicating the particular issues that have been overcome in the corresponding publication. A list of all publications is provided in the subsequent Chapter 4. Chapter 5 concludes the findings of the thesis and provides an outlook for possible future topics.

Chapter 2

Mathematical Model and Numerical Approach

2.1 Governing Equations

The physical behavior of the inviscid, compressible flow considered in this work is mathematically modeled by the Euler system of partial differential equations [93, 150]. The three-dimensional formulation in conservative form gives

$$\mathcal{U}_t + \mathcal{F}(\mathcal{U})_x + \mathcal{G}(\mathcal{U})_y + \mathcal{H}(\mathcal{U})_z = 0, \tag{2.1}$$

where $\mathcal{U}$ is the density of the conserved quantities mass ρ, momentum $\rho\mathbf{v} \equiv (\rho u, \rho v, \rho w)$ and total energy $E = \rho e + \frac{1}{2}\rho\mathbf{v}\cdot\mathbf{v}$, with e being the internal energy per unit mass.

The fluxes $\mathcal{F}$, $\mathcal{G}$ and $\mathcal{H}$ are defined as

$$\mathcal{F} = \begin{pmatrix} \rho u \\ \rho u^2 + p \\ \rho uv \\ \rho uw \\ u(E+p) \end{pmatrix}, \quad \mathcal{G} = \begin{pmatrix} \rho v \\ \rho uv \\ \rho v^2 + p \\ \rho vw \\ v(E+p) \end{pmatrix}, \quad \mathcal{H} = \begin{pmatrix} \rho w \\ \rho uw \\ \rho vw \\ \rho w^2 + p \\ w(E+p) \end{pmatrix}. \tag{2.2}$$

The compressible system is closed using the stiffened-gas equation of state, which was first proposed by Harlow and Amsden [61]. The pressure p is given by

$$p = (\gamma - 1)\rho e - \gamma p^{\infty} \tag{2.3}$$

with the ratio of specific heats γ and the background pressure p^{∞}. Note, that this formulation recovers the ideal gas law for vanishing background pressures $p^{\infty} = 0$. The ratio of specific heats for monatomic gases is $\gamma = 1.67$, and $\gamma = 1.4$ for diatomic gases, such as nitrogen and oxygen, which are the main components of air. Water is usually modeled with γ-values between 4 and 7. The background pressure p^{∞} is introduced to mimic the incompressible nature of liquids. It usually takes values as high as $p^{\infty} = 3.0 \cdot 10^8$ for water [71, 77, 131, 133]. Note that γ and p^{∞} are empirically fitted for water to ensure the correct speed of sound.

The speed of sound c for the stiffened-gas equation of state is

$$c = \sqrt{\frac{\gamma \cdot (p + p^{\infty})}{\rho}}. \tag{2.4}$$

The full set of Navier-Stokes equations can be considered by adding viscous force terms and heat conduction terms. Additional source terms, such as gravitation or axisymmetric contributions, can also be easily incorporated. The described system can be extended to describe multi-component flows either by a level-set formulation [71] or by an additional advection equation for material properties [77].

The developed methodological improvements described in Chapter 3 can be easily applied to the full set of Navier-Stokes equations for multi-component flows revealing the same beneficial behavior as presented for the Euler system of equations. However, for the mechanism studies shown in this thesis, it is beneficial to limit investigations to the inviscid Euler system of equations at first as the physical viscosity of Navier-Stokes equations may impede the observability of numerical shortcomings inherent to the modeling of the inviscid system.

2.2 Finite-Volume / Method-of-Lines Approach

Following the finite-volume approach, the continuous domain of interest is discretized by non-overlapping cells to solve the Euler system of equations provided in Section 2.1 numerically. In the following, a Cartesian framework with cell sizes Δx, Δy, Δz is applied. A physical domain with total extent $L_x \times L_y \times L_z$ is then divided into $\left(N_x = \frac{L_x}{\Delta x}\right) \times \left(N_y = \frac{L_y}{\Delta y}\right) \times \left(N_z = \frac{L_z}{\Delta z}\right)$ computational cells. See Figure 2.1 for a two-dimensional schematic representation of the computational grid. The third dimension behaves accordingly. The indices i,j,k denote the i-th cell in x-direction, j-th cell in y-direction and k-th cell in z-direction. Each cell covers $\mathcal{I}_{i,j,k} = [x_{i-1/2}, x_{i+1/2}] \times [y_{j-1/2}, y_{j+1/2}] \times [z_{k-1/2}, z_{k+1/2}]$ with cell center point at $x_i = (i - 0.5) \cdot \Delta x$, $y_j = (j - 0.5) \cdot \Delta y$, $z_k = (k - 0.5) \cdot \Delta z$ and $i = 1 ... N_x$, $j = 1 ... N_y$, $k = 1 ... N_z$. The physical domain $\mathcal{D}$ is given by $\mathcal{D} = \bigcup\limits_{i,j,k} \mathcal{I}_{i,j,k}$.

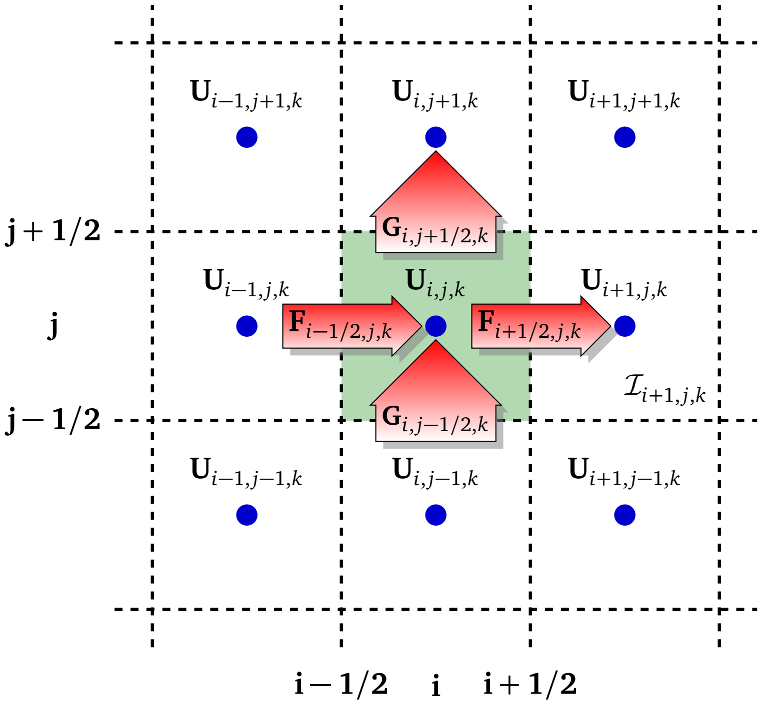

Figure 2.1: Schematic representation of the computational grid in two dimensions with cell center points (blue) and relevant fluxes (red) for the cell of interest (green). The direction of fluxes is shown for positive flux values.

The cell-averaged conservative quantity vector $\mathbf{U}_{i,j,k}$ for a cell with volume $\mathcal{V}_{i,j,k} = \Delta x \cdot \Delta y \cdot \Delta z$ is evaluated from

$$\mathbf{U}_{i,j,k}(t) = \frac{1}{\mathcal{V}_{i,j,k}} \int_{\mathcal{V}_{i,j,k}} \boldsymbol{\mathcal{U}}(x,y,z,t) dx dy dz, \tag{2.5}$$

and stored for each of the computational cells. The definition of $\mathbf{U}_{i,j,k}$ discretizes the continuous distribution with second order [94].

The integration of Eq. (2.1) over the cell volume together with Eq. (2.5) gives the semi-discrete time evolution equation

$$\frac{d}{dt}\mathbf{U}_i = \frac{1}{\Delta x}(\mathbf{F}_{i-\frac{1}{2},j,k} - \mathbf{F}_{i+\frac{1}{2},j,k}) + \frac{1}{\Delta y}(\mathbf{G}_{i,j-\frac{1}{2},k} - \mathbf{G}_{i,j+\frac{1}{2},k}) + \frac{1}{\Delta z}(\mathbf{H}_{i,j,k-\frac{1}{2}} - \mathbf{H}_{i,j,k+\frac{1}{2}}), \tag{2.6}$$

where $\mathbf{F}$, $\mathbf{G}$ and $\mathbf{H}$ approximate the fluxes at the cell faces. The connection to continuous fluxes is shown exemplarily in x-direction

$$\begin{aligned}\int_{x,y,z} \mathcal{F}(x,y,z,t)_x dxdydz = \int_{y,z} \left[\mathcal{F}(x_{i+1/2},y,z,t)dydz - \mathcal{F}(x_{i-1/2},y,z,t)\right] dydz \approx \\ \approx \left(\mathbf{F}_{i+1/2,j,k}(t) - \mathbf{F}_{i-1/2,j,k}(t)\right) \cdot \Delta y \cdot \Delta z.\end{aligned} \tag{2.7}$$

Eq. (2.6) recovers the fundamental property of conservation laws that the magnitude of conserved quantities can only be changed in time through fluxes across cell boundaries. Figure 2.1 shows the situation exemplarily in two dimensions. The total amount of conserved quantities is necessarily maintained since quantities leaving one cell are directly entering the respective neighboring cell. This conservation property, also called "telescoping" property, is a necessary condition for correct wave speed predictions, and therefore, it is fundamental for accurately solving compressible flow dynamics [94, 150].

Various different numerical algorithms have been developed to approximate the numerical fluxes $\mathbf{F}$, $\mathbf{G}$ and $\mathbf{H}$ [66, 107, 126]. Today, most common approaches built on a method that was first described by Godunov [48]. In his seminal work, Godunov suggests to solve Riemann problems at each cell face. The comparatively easy extension to high spatial orders renders Godunov's scheme particularly favorable. Details of the flux computation will be discussed in Section 2.2.2 and Section 2.3.

2.2.1 Temporal Discretization

The semi-discrete ordinary differential equation (ODE) (2.6) is integrated in time using high-order strong stability-preserving (SSP) Runge-Kutta schemes [50, 141]. Note, that an application of the explicit Euler forward time integration directly results in Godunov's method [94]. However, this method is unstable when the fluxes are discretized with high order [162].

The righthand side of Eq. (2.6) can be abbreviated using the operator $\mathcal{L}$ resulting in

$$\frac{d}{dt}\mathbf{U} = \mathcal{L}(\mathbf{U}) \tag{2.8}$$

An optimal strong stability-preserving second-order Runge-Kutta scheme as proposed by Gottlieb et al. [50] is given by

$$\begin{aligned}\mathbf{U}^{*} &= \mathbf{U}^{n} + \Delta t \cdot \mathcal{L}(\mathbf{U}^{n}),\\ \mathbf{U}^{n+1} &= \frac{1}{2}(\mathbf{U}^{n} + \mathbf{U}^{*}) + \frac{1}{2} \cdot \Delta t \cdot \mathcal{L}(\mathbf{U}^{*}).\end{aligned} \tag{2.9}$$

The corresponding optimal strong stability-preserving third-order Runge-Kutta scheme [50] is given by

$$\begin{aligned}\mathbf{U}^{*} &= \mathbf{U}^{n} + \Delta t \cdot \mathcal{L}(\mathbf{U}^{n}),\\ \mathbf{U}^{**} &= \frac{3}{4} \cdot \mathbf{U}^{n} + \frac{1}{4} \cdot \mathbf{U}^{*} + \frac{1}{4} \cdot \Delta t \cdot \mathcal{L}(\mathbf{U}^{*}),\\ \mathbf{U}^{n+1} &= \frac{1}{3} \cdot \mathbf{U}^{n} + \frac{2}{3} \cdot \mathbf{U}^{**} + \frac{2}{3} \cdot \Delta t \cdot \mathcal{L}(\mathbf{U}^{**}).\end{aligned} \tag{2.10}$$

The authors in [162] show that all optimal first- and second-order strong-stability-preserving Runge-Kutta methods are linearly unstable when coupled with WENO5. However, for all calculations within the scope of this thesis no major differences could be observed between second- and third-order time integration.

The time step has to be restricted using an appropriate CFL condition. The maximum time step is determined by

$$\Delta t = C_{CFL} \cdot \left[\max_{i,j,k} \left(\frac{|u_{i,j,k}| + c_{i,j,k}}{\Delta x} + \frac{|v_{i,j,k}| + c_{i,j,k}}{\Delta y} + \frac{|w_{i,j,k}| + c_{i,j,k}}{\Delta z} \right) \right]^{-1} . \tag{2.11}$$

The applied CFL number C_{CFL} ranges between 0.3 and 0.8. This choice for the maximum time step calculation is commonly applied [111, 150], and leads to stable calculations in most cases. However, it should be noticed that these simple signal speed predictions do not bound the true wave speeds in general. Signal speeds emerging from the interaction of the data at each cell interface may have higher magnitudes than predicted by Eq. (2.11) [149]. Algorithms to determine theoretical bounds for the signal speeds are available [53], but computationally costly as they may lead to unnecessarily small time steps. When additional physics are considered, such as viscosity, surface tension or gravity, their inherent maximum signal speeds also have to be considered for the maximum admissible time step evaluation.

A suitable set of initial values has to be provided for the initial time step to solve the initial-value problem (2.6). No further starting procedure is required as only single-stage time integration schemes are applied here.

2.2.2 Spatial Discretization - Flux Evaluation

The applied spatial discretization techniques are focused on an accurate and consistent approximation of the cell-face fluxes required from Eq. (2.6). These fluxes are determined solving a Riemann problem at each cell face [48]. While originally, the Riemann problem has been solved exactly with the help of iterative methods [150], the majority of state-of-the-art methods nowadays relies on approximate Riemann solvers. This practice is motivated by the high cost of iterative methods required for exact Riemann solutions together with the fact that only a limited number of information of the solution is used for the flux computation. Approximate solvers proved to be efficient with negligible accuracy drawbacks. Two major groups of approximate Riemann solver are applied in this thesis, the Roe-type Riemann solver [126] and the HLL-type Riemann solver [66, 152]. Due to their central relevance for this thesis, these solvers are discussed in detail in Section 2.3.

Only first order in space can be achieved when the Riemann solvers directly take the cell-averaged states of cells directly connected to the face as left and right state of the Riemann problem. Thus, the second major task consists in the application of high-order methods. This target is usually met by the introduction of high-order weighted essentially-non-oscillatory (WENO) reconstructions [63, 76, 141]. The reconstruction is applied dimension-by-dimension either on the states or on characteristic fluxes depending on the applied Riemann solver.

WENO5-JS

Today, the fifth-order WENO reconstruction proposed by Jiang and Shu [76] called WENO5-JS [140] is the most popular one of the ENO-type schemes. Since a full 5-point stencil may generate spurious oscillations due to Gibbs' phenomenon or may diverge near discontinuities, e.g. shocks, the reconstruction is performed using a nonlinearly weighted combination of sub-stencils instead. WENO5-JS consists of three second-order sub-stencils S^1, S^2, S^3. Figure 2.2 shows the sub-stencils exemplarily for left and right interface state reconstructions in x-direction. Additionally, nonlinear smoothness measures are computed for each of the sub-stencils. When discontinuities are present within the 5-point stencil, the smoothness measures are used to only involve information from smooth sub-stencils for the reconstruction. In case of smooth input data, the designed fifth order of the reconstruction is theoretically recovered

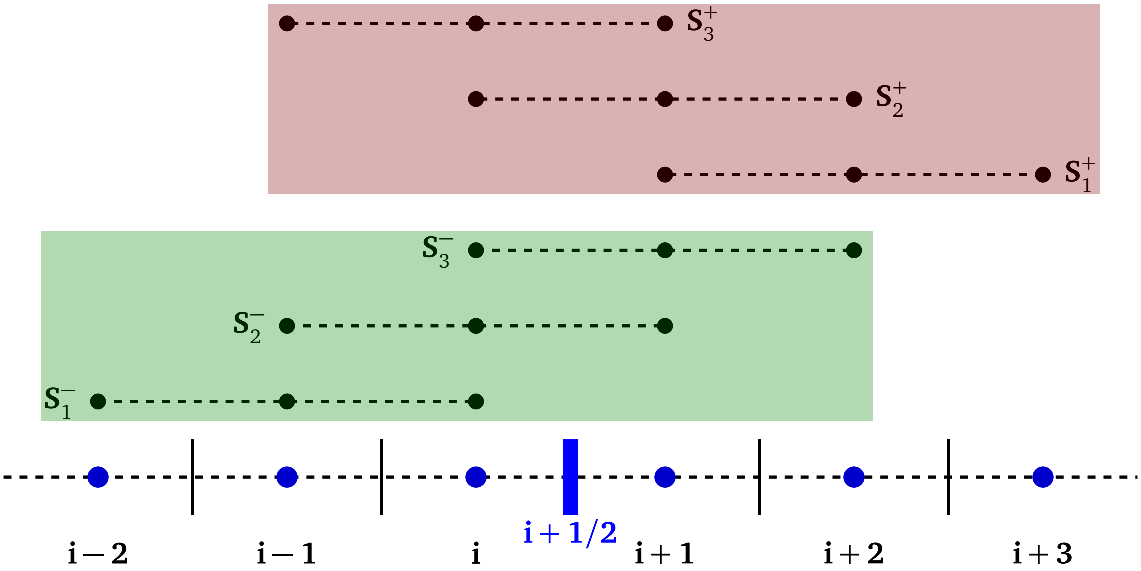

Figure 2.2: Schematic representation of sub-stencils for classical fifth-order WENO reconstructions at cell interface i+1/2. The sub-stencils $\mathbf{S}$ required for the left interface flux $\mathbf{F}^{-}_{i+1/2}$ are highlighted in green, and sub-stencils $\mathbf{S}$ required for the right interface flux $\mathbf{F}^{+}_{i+1/2}$ are highlighted in red. Solid circles represent nodes where cell-averaged values are available.

by an optimal combination of sub-stencils. The input stencil is shifted by one cell depending on whether the reconstruction is performed from the left or from the right side. Since both procedures are symmetric, only the left reconstruction (green) will be presented in detail. The reconstruction of the right interface value is obtained accordingly. The final reconstructed value u^{RECON} is determined by a combination of the reconstructed values of each sub-stencil u^{S_k} and nonlinear smoothness measures ω_k via

$$u^{RECON} = \sum_{k=0}^{3} \omega_k \cdot u^{S_k}. \tag{2.12}$$

The reconstructed values u^{S_k} for each sub-stencil S_k are calculated from

$$u^{S_1} = \frac{1}{3}u_{i-2} - \frac{7}{6}u_{i-1} + \frac{11}{6}u_i, \quad u^{S_2} = -\frac{1}{6}u_{i-1} + \frac{5}{6}u_i + \frac{1}{3}u_{i+1}, \quad u^{S_3} = \frac{1}{3}u_i + \frac{5}{6}u_{i+1} - \frac{1}{6}u_{i+2}. \tag{2.13}$$

The nonlinear normalized weights ω_k are defined by

$$\omega_k = \frac{\alpha_k}{\sum_{k=0}^{3} \alpha_k} \quad \text{with} \quad \alpha_k = \frac{d_k}{(\epsilon + \beta_k)^2} \tag{2.14}$$

and nonlinear smoothness indicators β_k

$$\begin{aligned}
\beta_1 &= \frac{13}{12}\left(u_{i-2} - 2u_{i-1} + u_i\right)^2 + \frac{1}{4}\left(u_{i-2} - 4u_{i-1} + 3u_i\right)^2, \\
\beta_2 &= \frac{13}{12}\left(u_{i-1} - 2u_i + u_{i+1}\right)^2 + \frac{1}{4}\left(u_{i-1} - u_{i+1}\right)^2, \\
\beta_3 &= \frac{13}{12}\left(u_i - 2u_{i+1} + u_{i+2}\right)^2 + \frac{1}{4}\left(3u_i - 4u_{i+1} + u_{i+2}\right)^2.
\end{aligned} \tag{2.15}$$

The ideal weights, which recover the full order of the scheme, are $d_1 = 0.1$, $d_2 = 0.6$ and $d_3 = 0.3$. The ϵ value was originally set to 10^{-6} in order to avoid a division by 0 [76]. However, Borges et al. [12] argued that the epsilon may have significant impact on the order reduction near smooth extrema. They suggested a value of 10^{-40} to avoid any unintended order reduction. The simulations presented in this thesis are performed using ϵ equal to machine precision to avoid any influence of ϵ besides the division-by-zero control.

TENO5

The targeted essentially non-oscillatory (TENO) scheme developed by Fu et al. [41] significantly reduces the numerical dissipation introduced by the spatial reconstruction. This reduction allows for a more accurate simulation of turbulent flow behavior [40]. While classical WENO schemes apply a weighted combination of all sub-stencil contributions, TENO schemes either apply a candidate stencil with its original linear weight, or they remove its contribution completely when discontinuities are detected by the smoothness indicators. This procedure leads to an efficient separation of discontinuities and small-scale fluctuations.

The reconstructed sub-stencil u^{S_k} values are identical to the ones given in Eq. (2.13), and the smoothness indicators β_k are identical to Eq. (2.15). However, the simple weights α_k are calculated using the global smoothness measure of Borges et al. [12]

$$\alpha_k = 1 + \frac{\tau_5}{\beta_k + \epsilon} \quad \text{with} \quad \tau_5 = |\beta_3 - \beta_1| \, . \tag{2.16}$$

The weight α_k then leads to a decision parameter b_k that decides whether the stencil is included in the final reconstruction or completely ignored. Thus, the finial weights ω_k are computed from

$$\omega_k = b_k \cdot d_k \quad \text{with} \quad b_k = \begin{cases} 0 & \text{if } \left(\frac{\alpha_k}{\sum_k \alpha_k}\right)^6 \leq C_T, \\ 1 & \text{if } \left(\frac{\alpha_k}{\sum_k \alpha_k}\right)^6 > C_T \end{cases} \tag{2.17}$$

with optimal weights d_k being identical to WENO5-JS. The decision parameter C_T can be utilized to adjust the dispersion and dissipation behavior of the scheme. In this thesis, the value is fixed to $C_T = 10^{-5}$.

This hard cut-off decision rule with an unsteady change in reconstruction results for minor input fluctuations makes the TENO scheme particularly prone to floating-point inconsistencies. Hence, results produced with high-order TENO variants often appear notably crooked as compared to traditional results obtained with WENO methods [40, 42].

Characteristic decomposition

The finite-difference formulation of the Roe Riemann solver requires a transformation into characteristic space to evaluate the characteristic flux contributions [126, 150]. A characteristic decomposition has also been demonstrated to be favorable for finite-volume formulations, where the states are reconstructed first and the Riemann problem is solved for the reconstructed values in a second step. The reconstruction of characteristic states instead of conservative or primitive states may avoid an interaction of characteristic waves of different families [77, 113]. This leads to a significantly reduced level of numerical oscillations in results.

In the following, the characteristic decomposition is presented in x-direction. The formulations in y- and z-directions are analogous. Conservative states are projected onto characteristic space by $\mathbf{W} = \mathbf{L} \cdot \mathbf{U}$ with $\mathbf{L}$ being the left eigenvector matrix. For the Euler equations, the linearized system reads as

$$\mathbf{L} = \begin{pmatrix} \frac{1}{4}\frac{q^2}{\hat{H}-\frac{1}{2}q^2} + \frac{1}{2}\frac{\hat{u}}{\hat{c}} & \frac{1}{2}\frac{\hat{u}}{\hat{H}-\frac{1}{2}q^2} - \frac{1}{2\hat{c}} & -\frac{1}{2}\frac{\hat{v}}{\hat{H}-\frac{1}{2}q^2} & -\frac{1}{2}\frac{\hat{w}}{\hat{H}-\frac{1}{2}q^2} & \frac{1}{2}\frac{1}{\hat{H}-\frac{1}{2}q^2} \\ -q^2 + \hat{H} & \hat{u} & \hat{v} & \hat{w} & -1 \\ \hat{v} & 0 & -1 & 0 & 0 \\ -\hat{w} & 0 & 0 & 1 & 0 \\ \frac{1}{4}\frac{q^2}{\hat{H}-\frac{1}{2}q^2} - \frac{1}{2}\frac{\hat{u}}{\hat{c}} & \frac{1}{2}\frac{\hat{u}}{\hat{H}-\frac{1}{2}q^2} + \frac{1}{2\hat{c}} & -\frac{1}{2}\frac{\hat{v}}{\hat{H}-\frac{1}{2}q^2} & -\frac{1}{2}\frac{\hat{w}}{\hat{H}-\frac{1}{2}q^2} & \frac{1}{2}\frac{1}{\hat{H}-\frac{1}{2}q^2} \end{pmatrix} \tag{2.18}$$

with the enthalpy $H = (E+p)/\rho$, and the Roe-averaged velocity magnitude $q^2 = \hat{u}^2+\hat{v}^2+\hat{w}^2$. Quantities with hat-notation "$\hat{\cdot}$" denote density-based Roe averages of the cell-averaged variables of the cells adjacent to the face [126]. The Roe-averaged speed of sound is evaluated from $\hat{c} = \sqrt{(\gamma-1)\cdot(\hat{H}-0.5\cdot q^2)}$.

The remaining Roe averages for $k = u, v, w, H$ are evaluated from

$$\hat{k} = \frac{\bar{k}_i \cdot \sqrt{\rho_i} + \bar{k}_{i+1} \cdot \sqrt{\rho_{i+1}}}{\sqrt{\rho_i} + \sqrt{\rho_{i+1}}}. \tag{2.19}$$

The back-transformation onto physical space is performed by $\mathbf{U} = \mathbf{R} \cdot \mathbf{W}$, with $\mathbf{R}$ being the right eigenvector matrix of the linearized system given by

$$\boldsymbol{R} = \begin{pmatrix} 1 & \frac{1}{\hat{H}-\frac{1}{2}q^2} & 0 & 0 & 1 \\ \hat{u}-\hat{c} & \frac{\hat{u}}{\hat{H}-\frac{1}{2}q^2} & 0 & 0 & \hat{u}+\hat{c} \\ \hat{v} & \frac{\hat{v}}{\hat{H}-\frac{1}{2}q^2} & -1 & 0 & \hat{v} \\ \hat{w} & \frac{\hat{w}}{\hat{H}-\frac{1}{2}q^2} & 0 & 1 & \hat{w} \\ \hat{H}-\hat{c}\hat{u} & \frac{\hat{H}}{\hat{H}-\frac{1}{2}q^2}-1 & -\hat{v} & \hat{w} & \hat{H}+\hat{c}\hat{u} \end{pmatrix}. \tag{2.20}$$

2.3 Riemann Solvers

For Godunov-type schemes, the initial-value problem

$$\mathbf{U}_t + \mathbf{F}(\mathbf{U})_x = 0 \quad \text{with} \quad \mathbf{U}(x,0) = \begin{cases} \mathbf{U}_L & \text{if } x < 0, \\ \mathbf{U}_R & \text{if } x \geq 0 \end{cases} \tag{2.21}$$

has to be solved for each cell interface to determine the flux over the interface. For this task, the two major groups of approximate Riemann solvers that are commonly in use today are described in this section. Both the Roe-Riemann solver and the HLL-type Riemann solvers are widespread in scientific computational fluid dynamics frameworks. While the main advantage of the Roe-Riemann solver is its low inherent dissipation, the HLL-type solvers are more stable and easier to extend for complex physics, e.g. multiphase formulations or magnetohydrodynamics. A more detailed comparison will be given in Section 2.3.3.

2.3.1 Roe-Type Riemann Solver

The classical Roe formulation [126] gives the following numerical flux function

$$\mathbf{F}^{Roe}_{i+1/2} = \frac{1}{2}\left(\mathbf{F}_{i+1} + \mathbf{F}_i\right) - \frac{1}{2}\mathbf{R}_{i+1/2}\left|\Lambda_{i+1/2}\right|\mathbf{L}_{i+1/2}\left(\mathbf{U}_{i+1} - \mathbf{U}_i\right), \tag{2.22}$$

with $\mathbf{L} = \mathbf{R}^{-1}$ and $\mathbf{R}$ being the left and right eigenvector matrices of the Jacobian $\partial \mathbf{F}/\partial \mathbf{U}$ given by Eq. (2.18) and Eq. (2.20), respectively. The diagonal matrix Λ is formed with the eigenvalues

$$\lambda_1 = \hat{u} - \hat{c}, \qquad \lambda_{2,3,4} = \hat{u}, \qquad \lambda_5 = \hat{u} + \hat{c}. \tag{2.23}$$

Note, that quantities with hat-notation “$\hat{.}$" again denote density-based Roe averages with calculation rules as provided in the end of Section 2.2.2.

The flux-vector splitting form of Eq. (2.22) reads as

$$\mathbf{F}^{+}_{i+1/2} = \mathbf{F}_i + \mathbf{R}_{i+1/2}\left|\Lambda_{i+1/2}\right|\mathbf{R}^{-1}_{i+1/2}\mathbf{U}_i \tag{2.24}$$

and

$$\mathbf{F}^{-}_{i+1/2} = \mathbf{F}_{i+1} - \mathbf{R}_{i+1/2}\left|\Lambda_{i+1/2}\right|\mathbf{R}^{-1}_{i+1/2}\mathbf{U}_{i+1}, \tag{2.25}$$

and allows the application of high-order finite-difference WENO reconstructions in characteristic space. The final high-order flux is obtained by

$$\mathbf{F}^{Roe}_{i+1/2} = \frac{1}{2}\left(\mathbf{F}^{+}_{i+1/2} + \mathbf{F}^{-}_{i+1/2}\right). \tag{2.26}$$

Note, that the inherent linearization of the scheme using discontinuous jumps is incorrect for waves with continuous change in flow variables [150]. Hence, the Roe Riemann solver may produce entropy-violating weak solutions, such as rarefaction shocks. Different strategies have been described to circumvent the occurrence of non-physical weak solutions [62, 65, 94]. In the popular approach of Harten and Hyman [65], additional viscosity is introduced to trigger the physically valid solution. This method is motivated by the vanishing viscosity approach. An alternative method proposed by Leveque [94] splits the single wave that represents the rarefaction fan in two waves connected by an intermediate state. This procedure concentrates on a proper treatment of transsonic rarefaction waves.

Since the additional numerical viscosity introduced by these fixes may impede the observability of numerical shortcomings studied in this thesis, no entropy fix has been applied in any of the presented cases. The experience shows that the Roe solver is less prone to rarefaction shocks when combined with high-order methods. Except of few specific flow conditions that are not considered in this thesis, no entropy-violating solutions were observed. However, it should be pointed out that entropy fixes are highly recommended when the Roe solver is applied to general configurations. Otherwise, results always have to be critically evaluated for the appearance of nonphysical shocks.

Componentwise local Lax-Friedrichs flux

Besides the possible occurrence of non-physical solutions, the Roe solver is prone to positivity violations [114]. As a remedy, the componentwise local Lax-Friedrichs flux was proposed and adds a slightly increased amount of dissipation. The componentwise local Lax-Friedrichs flux differs from the Roe flux in the choice of the eigenvalues Λ. Instead of density-based Roe averages, the eigenvalues in the componentwise local Lax-Friedrichs flux are determined by

$$\begin{aligned} |\lambda_1| &= \max\left(|u_i - c_i|, |u_{i+1} - c_{i+1}|\right), \\ \left|\lambda_{2,3,4}\right| &= \max\left(|u_i|, |u_{i+1}|\right), \\ |\lambda_5| &= \max\left(|u_i + c_i|, |u_{i+1} + c_{i+1}|\right). \end{aligned} \tag{2.27}$$

Note that as compared to the original local Lax-Friedrichs flux, often called Rusanov flux [129], this definition has different eigenvalues for each characteristic field. As a consequence of the minor change in eigenvalues, results are still close to the one obtained with the classical Roe solver, though the robustness of the scheme is significantly increased.

2.3.2 HLL-Type Riemann Solver

HLL-type Riemann solvers do not rely on a linearization of the nonlinear Euler equations, but they are the result of integral considerations connected with consistency conditions [150]. Thus, these schemes reveal some beneficial properties. They do not require entropy fixes, and positivity is guaranteed at least for first-order evaluations. Even though the positivity property does not translate to high-order reconstructions [70], these methods are still considerably more robust than the Roe solver.

HLL Riemann Solver

The HLL (Harten-Lax-Van Leer) flux [66] is a simple type of an incomplete Riemann solver. In Figure 2.3, the elementary solution of the Riemann problem (2.21) for the Euler system is sketched schematically for the interface $x_{i+1/2}$. The HLL formalism models the Riemann problem only including the two nonlinear

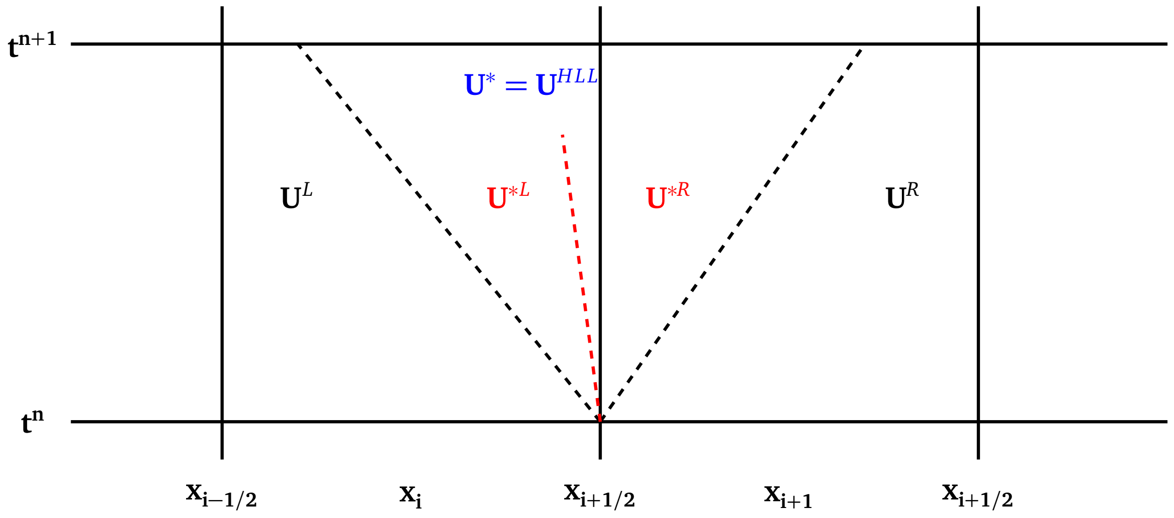

Figure 2.3: Schematic propagation of elementary waves in space-time coordinate system with nonlinear waves (dashed black) and contact wave (dashed red). The HLL flux models an averaged intermediate state $\mathbf{U}^*$ (blue), whereas the HLLC flux models the full system with two intermediate states $\mathbf{U}^{*L}$ and $\mathbf{U}^{*R}$ (red).

waves that separate the left and right initial states from an averaged intermediate state $\mathbf{U}^*$. $\mathbf{U}^*$ is obtained from

$$\mathbf{U}^* = \frac{S_R \mathbf{U}_R - S_L \mathbf{U}_L + \mathbf{F}_L - \mathbf{F}_R}{S_R - S_L} \tag{2.28}$$

with $\mathbf{F}_{L/R} = \mathbf{F}\left(\mathbf{U}_{L/R}\right)$. The left and right signal speeds $S_{L/R}$ denote the nonlinear wave speeds. The final flux is given by

$$\mathbf{F}^{HLL} = \begin{cases} \mathbf{F}_L & \text{if } S_L \geq 0, \\ \mathbf{F}_R & \text{if } S_R \leq 0, \\ \frac{S_R \mathbf{F}_L - S_L \mathbf{F}_R + S_L S_R (\mathbf{U}_R - \mathbf{U}_L)}{S_R - S_L} & \text{else.} \end{cases} \tag{2.29}$$

S_L and S_R can be obtained from different algorithms as described in the end of this section.

HLLC Riemann Solver

The incomplete modeling of the HLL solver may lead to an excessive smearing of contact discontinuity lines. Toro et al. [152] introduced the missing contact wave to overcome this deficiency. The resulting HLLC flux includes all waves present in the Euler system. Hence, the HLLC solver is a complete solver for this system. The additional contact wave separates the intermediate state into a right and left intermediate state $\boldsymbol{U}_{*L/R}$ as shown in red in Figure 2.3.

Two formulations are commonly applied to compute the HLLC flux. The classical approach proposed by Toro [152] gives

$$\mathbf{F}^{HLLC} = \begin{cases} \mathbf{F}_L & \text{if } S_L \geq 0, \\ \mathbf{F}_{*L} = \mathbf{F}_L + S_L \cdot (\mathbf{U}_{*L} - \mathbf{U}_L) & \text{if } S_L < 0 \cap S_* \geq 0, \\ \mathbf{F}_{*R} = \mathbf{F}_R + S_R \cdot (\mathbf{U}_{*R} - \mathbf{U}_R) & \text{if } S_R > 0 \cap S_* \leq 0, \\ \mathbf{F}_R & \text{if } S_R \leq 0. \end{cases} \tag{2.30}$$

Today, the shorter formulation [77]

$$\mathbf{F}^{HLLC} = \frac{1 + sign(S_*)}{2}\left[\mathbf{F}_L + S^- (\mathbf{U}_{*L} - \mathbf{U}_L)\right] + \frac{1 - sign(S_*)}{2}\left[\mathbf{F}_R + S^+ (\mathbf{U}_{*R} - \mathbf{U}_R)\right], \tag{2.31}$$

with

$$S^- = \min(S_L, 0), \qquad S^+ = \max(S_R, 0), \tag{2.32}$$

is more often implemented as it avoids the computationally expensive case evaluations. The signal speed estimates S_L, S_R, S_* are discussed later in this section. The formulations (2.30) and (2.31) give identical results for most cases, however certain signal speed estimates may lead to different behavior [38]. The intermediate states, $\mathbf{U}_{*L}$ and $\mathbf{U}_{*R}$, are determined from

$$\boldsymbol{U}_{*K} = \frac{S_K - u_K}{S_K - S_*} \begin{pmatrix} \rho_K \\ \rho_K S_* \\ \rho_K v_K \\ \rho_K w_K \\ E_K + (S_* - u_K)\left(\rho_K S_* + \frac{p_K}{S_K - u_K}\right) \end{pmatrix} \tag{2.33}$$

with $K = L, R$.

Signal Speed Selection

Both the HLL and the HLLC solver have to be combined with suitable signal speed estimates as proposed by different authors [10, 24, 32, 54, 151]. A group of estimates proposed by Davis [24]

$$S_L^{Davis} = \min(u_L - c_L, u_R - c_R), \qquad S_R^{Davis} = \max(u_L + c_L, u_R + c_R) \tag{2.34}$$

and the estimates of Einfeldt [32]

$$S_L^{Einfeldt} = \hat{u} - \hat{c}, \qquad S_R^{Einfeldt} = \hat{u} + \hat{c} \tag{2.35}$$

using a generalized formulation for the speed of sound

$$\hat{c}^2 = \frac{c_L{}^2 \cdot \sqrt{\rho_L} + c_R^2 \cdot \sqrt{\rho_R}}{\sqrt{\rho_L} + \sqrt{\rho_R}} + \frac{1}{2} \frac{\sqrt{\rho_L}\sqrt{\rho_R}}{\left(\sqrt{\rho_L} + \sqrt{\rho_R}\right)^2} \left(u_R - u_L\right)^2, \tag{2.36}$$

and the Roe-averaged velocity

$$\hat{u} = \frac{u_L \cdot \sqrt{\rho_L} + u_R \cdot \sqrt{\rho_R}}{\sqrt{\rho_L} + \sqrt{\rho_R}} \tag{2.37}$$

are most frequently applied in scientific codes. It is interesting to note that neither the choices of Davis [24] nor the ones of Einfeldt [32] do limit the nonlinear signal speeds in general [151]. Nevertheless, this rarely leads to stability issues. Guermond et al. [54] proposed iterative methods to determine true bounds for the physical wave speeds. Recently, various authors determined $\hat{u}$ and $\hat{c}$ from arithmetic averages $\bar{u} = \frac{1}{2}\left(u^L + u^R\right)$ and $\bar{c} = \frac{1}{2}\left(c^L + c^R\right)$ [21, 45, 164]. This simplified approach yields acceptable results in cases with sufficiently weak shocks, but it may also catastrophically fail in certain flow conditions [38]. In this thesis, a blend of both classical approaches with

$$S_L^{Blend} = \min(u_L - c_L, \hat{u} - \hat{c}), \qquad S_R^{Blend} = \max(u_R + c_R, \hat{u} + \hat{c}) \tag{2.38}$$

is applied [78]. This blend delivers slightly improved estimates in terms of robustness and accuracy.

Following Batten et al. [10], the contact wave speed for the HLLC flux is obtained from

$$S_* = \frac{p_R - p_L + \rho_L u_L (S_L - u_L) - \rho_R u_R (S_R - u_R)}{\rho_L (S_L - u_L) - \rho_R (S_R - u_R)}. \tag{2.39}$$

2.3.3 Discussion on Approximate Riemann Solvers

There is a significant difference among the two groups of Riemann solver that was only briefly mentioned so far. While the Roe flux can be extended to high order using the described flux-vector splitting procedure of Eq. (2.24) and Eq. (2.25), this is generally not possible for HLL-type schemes. The latter are extended to high order via the finite-volume approach, i.e. the left and right input states are first reconstructed with high order. While there is no difference in one-dimensional calculations, the finite-volume approach has significant performance drawbacks in multidimensional simulations. Here, an expensive Gauss integral evaluation over the cell face including multiple reconstructed state values has to be performed to maintain the formal order of the scheme [140]. Explicit procedures are available [148] and have been applied for two-dimensional simulations [22, 78]. However, for three dimensional simulations, this procedure is about nine times more expensive than the flux-splitting approach, which drastically limits its practical relevance. The weighted compact nonlinear schemes (WCNS) have been developed to overcome this issue [26, 27, 105, 172]. With this approach, only state pairs have to be reconstructed, and high order is obtained by the application of the WCNS scheme on the fluxes afterwards. While this procedure heavily reduces the computational cost, there is still an overhead when compared to finite-difference schemes. During my studies, I implemented both the Gauss evaluation and the WCNS procedure and compared results to the application of the midpoint flux evaluation that requires no additional treatment. Besides the large performance differences, no significant accuracy differences could be observed during an extensive evaluation of multiple single- and multi-component cases. These results confirm previous findings of Zhang et al. [171] for configurations including shock waves. Without additional treatments, the finite-volume approach reduces the formal order of a flux evaluation in x-direction to $\mathcal{O}\left(\Delta x^5, \Delta y^2, \Delta z^2\right)$. However, this has little to no effect on our simulation results. This might be explained by the fact, that the theoretical order of the scheme is technically only relevant if all features of the solution are properly resolved. For high-speed or even inviscid simulations with small-scale structures, simulations are certainly under-resolved. Since the thesis focuses on this type of simulations, the midpoint rule is directly applied for finite-volume type schemes without additional procedures resulting in a comparable performance of Roe and HLL-type schemes.

An interesting comparison of the solution structure can be performed when the HLL-type schemes are written in a centralized form [37]

$$\begin{aligned}
\mathbf{F}^{HLL} &= \frac{1}{2}\left(\mathbf{F}_L + \mathbf{F}_R\right) - \frac{1}{2}\left[|S_R|\left(\mathbf{U}_R - \mathbf{U}_*\right) + |S_L|\left(\mathbf{U}_* - \mathbf{U}_L\right)\right], \\
\mathbf{F}^{HLLC} &= \frac{1}{2}\left(\mathbf{F}_L + \mathbf{F}_R\right) - \frac{1}{2}\left[|S_R|\left(\mathbf{U}_R - \mathbf{U}_{*R}\right) + |S_*|\left(\mathbf{U}_{*R} - \mathbf{U}_{*L}\right) + |S_L|\left(\mathbf{U}_{*L} - \mathbf{U}_L\right)\right], \\
\mathbf{F}^{ROE} &= \frac{1}{2}\left(\mathbf{F}_L + \mathbf{F}_R\right) - \frac{1}{2}\mathbf{R}|\Lambda|\mathbf{L}\left(\mathbf{U}_R - \mathbf{U}_L\right).
\end{aligned} \tag{2.40}$$

All schemes reveal a common central term and a solver-specific dissipation term. While there is a specific dependency on the modeling of elementary waves for HLL-type schemes, the elementary waves cannot easily be extracted from the linearized form of the Roe scheme. However, for the Roe scheme it is easier to separate the acoustic and advection contribution to the total dissipation of the scheme since they can easily be connected to the respective eigenvalues. This property will become relevant for the targeted reduction of spurious dissipation contributions that are identified to cause numerical stability problems for high-speed flow.

Note, that for the selection $S_L = S_R = S_* = \lambda_{LF}$ and $\lambda_i = \lambda_{LF}$ for $i = 0...5$, both HLL-type fluxes and the Roe flux degenerate to the Lax-Friedrichs flux in its well-known form

$$\mathbf{F}^{\lambda} = \frac{1}{2}\left(\mathbf{F}_L + \mathbf{F}_R\right) - \frac{1}{2}|\lambda_{LF}|\left(\mathbf{U}_R - \mathbf{U}_L\right). \tag{2.41}$$

2.4 The Low Mach Number Inconsistency of Godunov-Type Schemes

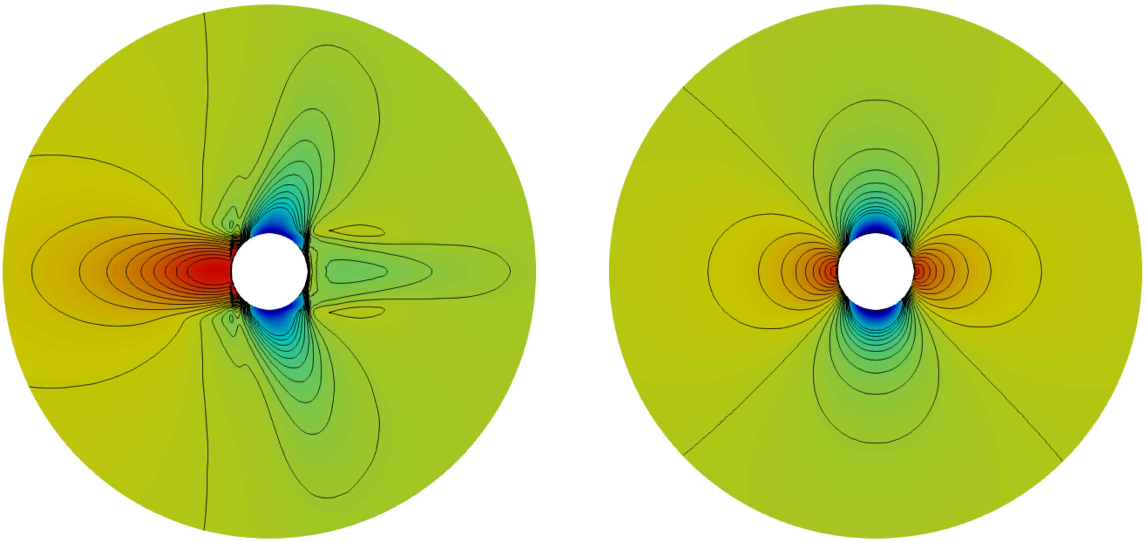

(a) result obtained with a Godunov-type scheme

(b) correct incompressible result

Figure 2.4: Pressure field with isolines for a cylinder flow at $Ma = 0.01$

The problematic behavior of Godunov-type schemes when applied to low Mach number flows is documented by various different groups [55, 56, 89, 96–98, 119, 155]. When the Mach number of a test case is systematically reduced to approach the incompressible limit, simulation results obtained with Godunov-type schemes usually fail to converge to the desired limit solution. Instead, excessive numerical dissipation pollutes the discretized solution. A small, illustrative example shall demonstrate the failure for the simulation of the flow around a cylinder in the incompressible regime. Fig. 2.4 shows inaccurate results that were obtained using a Godunov-type solver along with the incompressible reference solution.

Guillard and Viozat [57] were the first to perform a systematic investigation of the problem with the help of an asymptotic analysis. The authors reveal that pressure oscillations on the order of the Mach number are present in discrete solutions, while the continuous pressure scales with the square of the Mach number. In the following, the asymptotic analysis is described in more detail, as its outcome is of large importance for the thesis. The first step of the asymptotic analysis is to non-dimensionalize the Euler equations. The resultant system only depends on the non-dimensionalized state quantities density, velocity, pressure and Mach number. An asymptotic expansion with the power of the Mach number for each state quantity is inserted in the non-dimensional system and terms are sorted according equal power of Mach number. Now, it is important to notice that the result of the asymptotic analysis depends on the choice of the velocity-scale used to non-dimensionalize time.

Using the advection velocity, the asymptotic analysis reveals that the pressure is constant in space up to second order with the Mach number

$$p = p_0 + \mathcal{O}\left(Ma^2\right). \tag{2.42}$$

Here, p_0 is the ambient pressure imposed by the boundaries. The resulting system is the *incompressible Euler system* with constant density.

If, instead, the speed-of-sound is used during non-dimensionalization of time, the asymptotic analysis reveals that the pressure is constant in space only up to first order with the Mach number

$$p = p_0 + \mathcal{O}(Ma). \tag{2.43}$$

The resulting system is an *acoustic system*. Note, that in addition also the type of the system of equation changes from elliptic to hyperbolic. Thus, the solution of the Euler equations highly depends whether the emphasis is on phenomena occurring at the *time scale connected with the material velocity* or occurring at the *time scale connected with the speed of sound*. Indeed, both limit solutions coexists and superpose each other. The physics of a plane might serve as an example. The integral forces, such as lift and drag, are sufficiently described by the incompressible limit solution, however for a detailed evaluation of the noise generation the acoustic limit is relevant [56].

Thus, it is important to notice that the strong limit solution of the compressible Euler (or Navier-Stokes) equations for vanishing velocities is not necessarily sufficiently described by the corresponding incompressible equations. Guillard and Murrone [55] analyzed the behavior of discretized Godunov-type schemes in such situations. They found the numerical dissipation of the scheme related to the acoustic part of the solution to cause pressure fluctuations in simulation results of low Mach number flows. Hence, the dominant acoustic contribution to numerical dissipation in the the low Mach number limit is responsible for the mismatch of simulation results obtained with a compressible solver and the incompressible limit solution.

Different remedies have been proposed in literature to overcome the accuracy problem. Turkel [155] proposed a preconditioning scheme that became quite popular. Originally, preconditioning methods were introduced to overcome convergence problems for steady-state simulations in the low Mach number limit. The preconditioning procedure gives convergence to the incompressible solution. As shown by [57], this is achieved by enforcing a pressure scaling with the square of the Mach number. An overview of preconditioning methods can be found in [156]. Although preconditioning methods successfully recover the incompressible limit, these methods are computationally expensive and hard to combine with high-order methods. Additionally, implicit time integration is compulsory due to severe stability restrictions. Li et al. [96] developed an all-speed scheme by adapting the non-linear eigenvalues in the numerical dissipation term. The authors demonstrate that pressure fluctuations scale with the square of the Mach number. However, a pressure stabilization term has to be added to the interface fluid velocity to suppress checkerboard decoupling. Rieper [119] proposed an alternative low Mach number fix for the Roe flux. The author found the change in the normal velocity components in the Riemann problem to be responsible for the inaccurate scaling of numerical viscosity. As a remedy, the author suggests to reduce this term by one order of magnitude. An asymptotic analysis is provided that confirms the correct convergence to the incompressible solution of the modified scheme. Numerical examples indicate that the scheme additionally suppresses checkerboard modes. Further developments and a detailed comparison of existing methods can be found in [11, 56, 108].

The so-called low Mach number effect of compressible flow solvers has been thoroughly investigated for globally low Mach number flows. However, the incorrect pressure scaling has never been suspected to compromise the simulation of high-speed compressible flows. Indeed, due to the dimension-by-dimension approach, Riemann problems with vanishing velocity components also occur when the flow is aligned to the computational grid independent of the actual velocity magnitude. As described in detail in Section 3.2 and Section 3.3, the low Mach number effect can be identified as prime reason for the grid-aligned shock instability.

Chapter 3

Accomplishments

3.1 Impact of Floating-Point Induced Round-Off Errors on Large-Scale Simulations with Low-Dissipation Methods

The application of high-order spatial reconstruction schemes as introduced in Section 1.2 may result in severe numerical symmetry breaking, see Section 1.3. This effect is well-documented in literature [6, 25, 40–42, 117, 139, 146, 147, 168, 170, 174], though it is usually not further commented or accepted as introduced by low dissipation [41].

Figure 3.1 shows the potentially large-scale deformation when a low-dissipation scheme is used for the simulation of a standardized implosion test case [101]. There is no obvious reason why the jet should be moving away from the diagonal line since the setup and applied methods are completely symmetric. Remacle et al. [117] were among the first to suspect symmetry breaking to be caused by an insufficient damping of floating-point induces round-off errors. Indeed, symmetry breaking can hardly be observed in simulations with low-order reconstruction schemes and high numerical dissipation. Thus, the problem cannot be found in literature before the rise of high-order schemes.

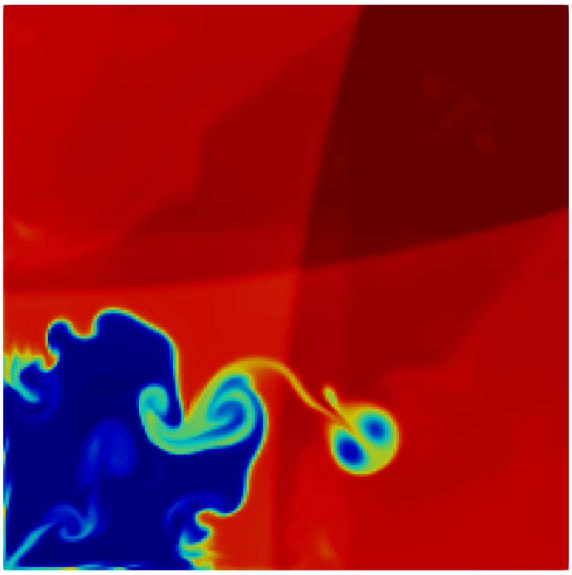

Figure 3.1: Simulation of a two-dimensional implosion with a high-order WENO scheme

Simultaneously to our work, Dong et al. [28, 29] modified the smoothness indicators of WENO-type schemes to improve the symmetry preservation. Results are provided for 7th- and 9th-order schemes. Later, Wang et al. [160] applied a symmetrization algorithm, where state values in symmetrically placed cells are averaged and used in both cells. Even though both approaches improve the symmetry preservation, no rigorous investigation on the roots of the problem has been performed. Additionally, the level of disturbances has only been reduced, but symmetry breaking is not totally avoided with this treatment. It is surprising that beside the provided references, to my best knowledge, there is no further literature dealing with this important topic in the context of highly resolved computational fluid dynamics.

Nico Fleischmann, Stefan Adami, Nikolaus A. Adams: *Numerical symmetry-preserving techniques for low-dissipation shock-capturing schemes.* Computers & Fluids, Volume 189, 94-107, 2019. [36]

In this publication, a thorough investigation of the impact of floating-point induced round-of errors on simulation results of compressible flows with latest low-dissipation methods has been performed. Moreover, for the first time, a procedure is described that ensures exact symmetry preservation for numerical schemes. In the first part of the paper, a HLLC Riemann solver is applied together with the classical WENO5-JS scheme. The presented mechanism study reveals that the lack of associativity

$$(a+b)+c \neq a+(b+c) \tag{3.1}$$

in floating-point operations initiates numerical symmetry breaking. Especially, three-dimensional summations of velocity or flux-vector components are affected, but summations of more than two terms are also present in two-dimensional algorithms. A detailed study of a symmetric implosion test case and a Rayleigh-Taylor instability revealed that minor implementation details can heavily influence the results. For example, a procedure to optimize the evaluation of Roe-averages given by Eq. (2.19) leads to different results, even though the original and the optimized formalism are analytically identical. The characteristic decomposition is identified as one source to trigger numerical symmetry breaking in two-dimensional simulations, since it involves a series of subsequent summations. Additionally, compiler optimizations that ignore the implemented bracketing are triggering symmetry deviations. The influence of initial conditions is also investigated. An imprecise evaluation of the sine function is shown to cause symmetry breaking for high grid resolutions, even when a symmetry-preserving numerical algorithm is applied for the simulation.

In the paper, a generalized solution strategy is provided. Explicit summations techniques are provided for three and four terms, however, can also be extended for more terms. The consistency-ensuring summation of three floating-point values a, b and c is taken according to

$$SUM_{consistent} = \frac{1}{2}\left(\max(s_1, s_2, s_3) + \min(s_1, s_2, s_3)\right) \tag{3.2}$$

with

$$s_1 = (a+b)+c, \quad s_2 = (c+a)+b, \quad s_3 = (b+c)+a \tag{3.3}$$

or

$$s_1 = (a+b)+(c+d), \quad s_2 = (c+a)+(b+d), \quad s_3 = (b+c)+(a+d) \tag{3.4}$$

with four floating-point values a, b, c and d. Finally, the consistency-managed sum has been applied in combination with WENO5, TENO5, WENOCU6 and a 9th-order WENO method to a comprehensive set of benchmark test cases. Simulations of Rayleigh-Taylor instabilities, gas implosions and two-dimensional Riemann problems have been performed with unprecedented resolution. Additionally, a novel three-dimensional version of the implosion test case is proposed. All results maintain perfect symmetry up to floating-point precision. The presented results may also serve as benchmark for upcoming high-performance CFD frameworks. The work proves that symmetry breaking is not a physical result that is uncovered by highly accurate high-resolution schemes, but rather the result of algorithmic artifacts, such as the lack of associativity, which no longer are hidden by numerical dissipation.

My contribution to this work lies in performing the investigation on the roots of symmetry breaking and developing the consistency-ensuring summation. I implemented all described procedures in our inhouse code and performed the presented numerical simulations. Furthermore, I selected the simulation setups presented in the paper, and post-processed the results. Finally, the manuscript for the publication was written predominantly by me.

3.2 Connection between the Low-Mach Effect and the Carbuncle Phenomenon

The occurrence of grid-aligned shock instabilities in the context of low-dissipation numerical schemes limits the accurate prediction of complex flows involving high Mach numbers. A comprehensive introduction to the problem has been provided in Section 1.4. In this section, the most important developments to cure the Roe Riemann solver from the instability are summarized.

In a linear analysis of the problem, Sanders et al. [130] detected insufficient cross-flow dissipation to cause the problem and proposed a multidimensional modification to the Roe approximation. Their cure became later known as the H-correction due to the spatial arrangement of incorporated interfaces to the entropy fix. The H-correction was further improved by Pandolfi and D'Ambrosio [109], who modified it for the application to high-speed flow boundary layers. Moreover, the authors of [109] compared different flux formulations and came to the conclusion that schemes that explicitly capture the contact discontinuity are always, to some extend, prone to the grid-aligned shock instability. This confirms the previous findings of Gressier and Moschetta [52] and Quirk [114].

At the same time, Liou [100] found the dissipative pressure term in the mass flux to be responsible for the instability. He conjectured that schemes with a mass flux that is independent of the pressure term are not affected by the carbuncle phenomenon. However, Liou's conjecture was questioned by several authors [31, 52, 109] afterwards with counterexamples including the AUSM$^+$ scheme [99].

Later, Kim et al. [87] introduced a Mach-number-based function that controls the feeding rate of pressure fluctuation into the numerical mass flux to stabilize the Roe scheme. This adaptation is motivated by a linear perturbation analysis of the odd-even decoupling problem.

The rotated Roe scheme developed by Ren [118] shows robust shock-capturing capability with a complete elimination of the shock instability. The upwind direction is determined by the velocity-difference vector and the Riemann problem is rotated to automatically introduce sufficient numerical dissipation. Although the procedure proved to be robust, there is a significant overhead since the Riemann problem has to be solved twice at each cell face. Dumbser et al. [31] developed a matrix stability procedure to analyze the problem quantitatively for steady shock waves. Their analysis confirmed that all complete Riemann solvers are unconditionally unstable. Additionally, they localized the source of the instability in the upstream region. While the instability has often been connected to pressure fluctuations, recently, Chen et al. [17] suspected an inadequate shear viscosity. They introduced a pressure-based sensing function to detect shock regions and stabilized the Roe scheme by introducing shear viscosity into the momentum flux.

Note, that all of the described modifications locally increase numerical dissipation to cure the instability. The main improvements among the methods is to quantify the amount and location of additional dissipation as precisely as possible. Thus, a procedure with same or less numerical dissipation as the original scheme would be highly favorable since then, no supplementary shock sensing procedures are required.

Nico Fleischmann, Stefan Adami, Xiangyu Y. Hu, Nikolaus A. Adams: *A low dissipation method to cure the grid-aligned shock instability.* Journal of Computational Physics, Volume 401, 109004, 2020. [39]

In this publication, we provide a fundamentally different approach to stabilize the Roe flux. For the first time, the problem is connected with another well-known flaw of Godunov-type schemes in the low Mach number limit. We demonstrate that an excessive acoustic contribution to dissipation in the flux calculation in transverse direction to the shock front propagation is the prime reason for the numerical instability. In contrast to all previous methods described in literature, we cure the instability while the dissipation of the scheme is further reduced. Thus, no detection mechanism of strong shocks is necessary. The provided fix is straightforward to implement since it requires only little modification of the original formulation.

In the first part of the paper, the classical Roe flux is presented using a formulation that allows for an easy distinction between two different contributions to the dissipative flux term. The advection contribution is related to the linear eigenvector $|u|$, while the acoustic dissipation is related to nonlinear eigenvalues $|u \pm c|$. For vanishing Mach numbers, i.e. vanishing velocities, it is obvious that the acoustic contribution to dissipation dominates the advection contribution to dissipation. A connection to the supersonic carbuncle phenomenon can be established for flux evaluations in cells where the shock front propagates aligned to the computational grid. In such cells, the transverse velocity component is vanishing, while the magnitude of total velocity is high. These configurations are essential for the onset of all types of carbuncle-like instabilities. Consequently, we denote them "grid-aligned shock instabilities".

In the second part of the paper, we provide a straightforward systematic procedure to reduce the acoustic contribution to dissipation for low Mach numbers. The cure is limited to a modification of nonlinear eigenvalues of the system. The resultant new eigenvalues read

$$\lambda'_{1,5} = \hat{u} \pm \min(\phi \cdot |\hat{u}|, \hat{c}) \qquad \lambda'_{2,3,4} = \hat{u}. \tag{3.5}$$

A constant ϕ-value of five is chosen to limit the influence of the modification to Mach numbers lower than 0.2. Simultaneously, this choice ensures comparable acoustic and advection contributions to the numerical dissipation in the low Mach number direction of the flow. We also provide a similar formalism for a componentwise local Lax-Friedrichs flux. This flux is closely related to the Roe flux but reveals a higher robustness in terms of positivity preservation. The novel fluxes are denoted Roe-M and cLLF-M.

The effectiveness of the presented fluxes is demonstrated for a comprehensive set of test cases that are relevant in the context of shock instabilities. We provide a detailed evaluation of long-term runs for Quirk's odd-even decoupling case to demonstrate the robustness of Roe-M also quantitatively. The Sedov blast wave test case is utilized to reveal the multidimensional nature of the instability. When we apply the modification only in one spatial direction, only the stability of shocks moving to the other direction is affected. Moreover, Roe-M delivers stable results for the double Mach reflection without producing a kinked Mach stem. The corner flow problem is simulated using cLLF schemes due to the known positivity issue of Roe schemes at the singular corner point. With the application of cLLF, no odd-even decoupling can be observed in the backflow of the moving shock front. The modified schemes also prevent the occurrence of carbuncles in classical hypersonic cylinder flows. This is both demonstrated for a moderate Mach number of three and for a high Mach number of twenty. The Elling test case is particularly interesting to simulate with the modified fluxes, since Elling [33] claimed that the carbuncle in this case is physically motivated and should not be suppressed by numerical schemes. The ability of our schemes to simulate the carbuncle structure without additional disturbances along the shock front confirms the predictions of Elling. Finally, the new fluxes are also successfully applied to challenging multi-component flow simulations, such as the shock-induced collapse of an air bubble in water and the interaction of a shock-wave in air with a helium bubble.

My contribution to this work lies in performing the investigations on the connection of the low Mach problem to different shock instability settings in supersonic flows. I implemented all described procedures in our in-house code and performed the presented numerical simulations. Furthermore, I selected the simulation setups presented in the paper, and post-processed the results. Finally, the manuscript for the publication was written predominantly by me.

3.3 Centralized and Shock-Stable Formulation of the HLLC Riemann Solver

The approximate Roe Riemann solver and HLL-type Riemann solvers are widespread in compressible CFD frameworks today. While the shock instability often leads to catastrophic failure in combination with the Roe flux, the flaw is more subtle for the HLLC flux. Thus, the vast majority of literature is focused on investigations of the shock instability connected with the Roe flux. However, some few procedures have also been developed for the HLLC scheme to improve its shock stability.

The incomplete predecessor scheme of the HLLC flux, the HLL flux, is commonly stated to be stable against the shock instability [114]. Hence, most approaches focus on combining both methods with the target to maintain the robustness of HLL and the contact-resolving property of HLLC. In early approaches, simple switches between the original HLL and the HLLC scheme are applied leaving the solvers themselves unchanged. Already 1997, Quirk [114] suggested to apply the HLL scheme near strong shocks, and a low-dissipation scheme for the rest of the domain with the help of a decision rule. This switching procedure was later improved by Kim et al. [86]. They limited the application of the dissipative HLL solver to fluxes in transverse direction of the shock propagation. Another modification of the switching procedure was proposed by Huang et al. [75]. They limit the application of the HLL flux to certain conservative states only. Moreover, they successfully applied the rotated Riemann solver procedure proposed by Ren [118] to the HLLC flux.

Shen et al. [137] adopted the matrix stability analysis proposed by Dumbser et al. [31] to analyze the linear stability properties of hybrid schemes. They concluded that the numerical shock instability originates from the flux in transverse direction of the shock wave propagation. Later, the authors developed a pure HLLC-type flux with shock-stable properties via the introducing of additional shear viscosity [138]. Stability can be achieved via the smearing of the shear velocities on both sides of the contact line. The resulting scheme was denoted as HLLCM. However, the increased amount of dissipation limits an accurate calculation of boundary layers. Thus, a hybrid HLLC-HLLCM version was suggested for application to complex flows. Additionally, a HLL-type solver with a newly introduced vorticity wave has been found to be unstable [138]. Recently, Shen et al. [136] performed a comparative study of HLL-type schemes with respect to the carbuncle phenomenon. They found that nonlinear acoustic waves rather than linear vorticity and shear waves play an important role to damp out the instability. Moreover, the authors found the application of Einfeldt signal speed estimates to be more prone to the instability than Davis estimates. This result again indicates that insufficient dissipation plays a role in the onset of the instability, since Davis estimates are known to be more dissipative than Einfeldt estimates.

Xie et al. [165] performed a comparative study with multiple numerical schemes obtaining results that point in the same direction as those of Shen et al. [138]. They again found additional numerical dissipation corresponding to shear waves to be effective to stabilize low-dissipation schemes. Moreover, they argued that this helps to maintain the consistency of mass flux across the normal shock by smearing the perturbed momentum behind the shock. More recently, the authors proposed an alternative stabilization with an additional pressure-dissipation term that is activated near shocks and damps spurious pressure perturbations [166].

Simon and Mandal [143] separated the HLLC flux into the inherent HLL part and an antidiffusive part. From this starting point, the authors designed a shock-stable scheme denoted as HLLC-ADC, where the activation of the antidiffusive term is controlled by a pressure-ratio-based multidimensional shock sensor. Later, the authors proposed an alternative stabilization strategy with a selective wave modification that increases the inherent dissipative HLL part in the vicinity of shock waves [144]. The antidiffusive term of the resulting HLLC-SWM flux remains identical to that of the original HLLC.

All previous attempts to recover the shock stability of the HLLC flux are strongly connected to the HLL flux. However, any combination of HLLC and HLL inevitably increases the inherent dissipation of the scheme and limits its usability for turbulent flows. Again, a shock-stable HLLC scheme with similar or reduced numerical dissipation would be highly desirable.

Nico Fleischmann, Stefan Adami, Nikolaus A. Adams: *A shock-stable modification of the HLLC Riemann solver with reduced numerical dissipation.* Journal of Computational Physics, Volume 423, 109762, 2020. [37]

The first aim of this publication is to investigate the occurrence of the grid-aligned shock instability in detail for the HLLC flux. Sometimes, the HLLC flux is recommended as a fix to apply, if results using the Roe flux are deteriorated by the carbuncle phenomenon. Indeed, the effects of the instability are often less harmful, and rarely lead to a failure of the simulation when the HLLC flux is applied. Usually, only the odd-even decoupling in the backflow of strong shocks is observed, but no carbuncle structures grow ahead of the shock front. However, we demonstrate that is only true for moderate resolutions and two-dimensional simulations. In three-dimensional simulations, the HLLC flux produces similar carbuncle structures as the Roe flux does. With increasing computational power, three-dimensional calculations will become mainstream, and it is evident that shock-stable versions of the HLLC are required.

The second aim of this publication is to provide such a shock-stable HLLC flux exploiting the previously discovered connection to an exceeding acoustic dissipation in the low Mach number limit [39]. Unlike for the Roe scheme, the structure of the HLLC scheme renders it more complicated to distinguish advection and acoustic contributions to numerical dissipation. For this purpose, we derived a novel centralized formulation of the HLLC flux. This centralized form avoids performance-unattractive case evaluations, and allows for an easier distinction between different dissipation contributions. The centralized HLLC flux formulation reads

$$\mathbf{F}^{HLLC} = \begin{cases} \mathbf{F}_L & \text{if } S_L \geq 0, \\ \mathbf{F}_R & \text{if } S_R \leq 0, \\ \mathbf{F}_* & \text{else} \end{cases} \tag{3.6}$$

with

$$\mathbf{F}_* = \frac{1}{2}\left(\mathbf{F}_L + \mathbf{F}_R\right) + \frac{1}{2}\left[S_L\left(\mathbf{U}_{*L} - \mathbf{U}_L\right) + |S_*|\left(\mathbf{U}_{*L} - \mathbf{U}_{*R}\right) + S_R\left(\mathbf{U}_{*R} - \mathbf{U}_R\right)\right]. \tag{3.7}$$

Interestingly, this formulation demonstrates a strong connection to the Lax-Friedrichs flux. If all signal speed estimates of the HLLC flux are set to the scalar maximum signal speed of the Lax-Friedrichs flux, then the HLLC flux directly reduces to the Lax-Friedrichs flux. A reduction of the acoustic contribution to dissipation can now be easily achieved via a systematic reduction of nonlinear eigenvalues according to

$$S_L^{HLLC-LM} = \phi \cdot S_L, \qquad S_R^{HLLC-LM} = \phi \cdot S_R, \tag{3.8}$$

where ϕ is a factor that smoothly reduces to zero for vanishing Mach numbers.

Properties of the resulting HLLC-LM scheme have been thoroughly tested for a comprehensive set of cases. The corner flow problem is applied to demonstrate both the consistency of the centralized formulation and the stability of the HLLC-LM flux against the odd-even coupling in the backflow of the shock. A significant reduction of dissipation of HLLC-LM at slip lines is revealed for the Rayleigh-Taylor instability. The shock stability has been quantified utilizing Quirks odd-even decoupling case. A double Mach reflection and a Sedov blast wave have been simulated with large grid resolutions to demonstrate the stability for strongly refined meshes. The later case has also been evaluated in three dimensions. In this case, the original HLLC develops carbuncle-like spikes, whereas results for the HLLC-LM are perfectly smooth. A significantly improved accuracy of the HLLC-LM scheme can also be observed for a global low Mach number flow around a cylinder. Finally, the scheme is tested for complex single- and multi-component flows with extreme grid resolutions, both in two and three dimensions.

My contribution to this work lies in performing simulations to uncover the increasing vulnerability of the HLLC flux for higher resolutions and three-dimensional simulations. Furthermore, I derived the centralized formulation and applied the dissipation reduction procedure. I implemented all described procedures in our in-house code and performed the presented numerical simulations. Moreover, I selected the simulation setups presented in the paper, and post-processed the results. Finally, the manuscript for the publication was written predominantly by me.

3.4 Evaluation of Signal Speed Estimates for HLL-Type Solver

In their seminal work, Harten, Lax, and van Leer [66] described possible design strategies for a novel group of Riemann solvers. However, the authors did not provide the necessary signal speed estimates, which are required for the practical application of these schemes. Yet, they stated that estimates for signal speeds have to bound the physical wave speeds. It took five more years till both Einfeldt [32] and Davis [24] independently proposed accurate estimates to complete the first Riemann solver of this group. Interestingly, both estimates are in widespread use to this day, even though they do not fulfill the design requirements requested by Harten et al. [66]. Both estimates do not bound the physical wave speeds as demonstrated by Toro et al. [151]. Davis estimates are easy to implement and independent of the applied equation of state. Only the sound speed has to be provided. Instead, Einfeldt estimates are designed for ideal gases assuming reasonable γ-values. They are less dissipative when compared to Davis estimates, however, extension to complex equation of states is more complicated. Thus, Davis estimates are still popular for multi-component flow simulations in diffuse-interface schemes, while Einfeldt estimates are traditionally more popular for single-phase gas flows. Batten et al. [10] provided a signal speed estimate for the contact wave, which is commonly applied today. Moreover, Toro et al. [150] suggested a signal speed calculation based on a constant intermediate pressure instead of using direct estimates. However, this approach is rarely applied in CFD codes.

More recently, there have been attempts to design signal speed estimates that constitute true bounds of the physical values [54, 151]. Guermond and Popov [54] designed a fast algorithm for the computation of maximum signal speeds in the Riemann solution for Euler equations with a co-volume equation of state. Their algorithm shows a cubic convergence rate. Even though their procedure is efficient and guarantees true bounds, it rarely leads to significant differences in results. Therefore, it is often not necessary to spend additional computational effort as compared to traditional explicit schemes.

In a series of recent publications [21, 45, 164], traditional signal speed estimates have been replaced by a simple arithmetic-averaging procedure for the speed of sound. The authors justify the simplification by numerical verification upon a series of test cases. However, in contrast to traditional methods a theoretical argumentation for this simple approach is only given for sufficiently weak shocks, as already remarked by Einfeldt [32]. Thus, a general applicability of arithmetic-average estimates is questionable and desires further investigation. Due to the increasing complexity of CFD algorithms backtracking of errors can be a challenging task. There is a particular interest that Riemann solvers, which represent the lowest level of compressible schemes, deliver reliable results.

Nico Fleischmann, Stefan Adami, Nikolaus A. Adams: *On an inconsistency of the arithmetic-average signal speed estimate for HLL-type Riemann solvers.* Journal of Computational Physics: X, Volume 8, 100077, 2020. [38]

In this publication, we perform a detailed investigation on popular signal speed estimates for HLL-type solver. We demonstrate a major deficiency of the arithmetic-average estimate both via theoretical considerations and a numerical test case.

We evaluate the signal speed estimates of Davis, Einfeldt, Toro and the simplified arithmetic-average estimate for a simple moving shock wave, which is described by the Rankine-Hugoniot locus. As depicted in Figure 3.2, the arithmetic-average estimates significantly underestimate the true wave speeds. Moreover, for Mach numbers higher than 3.4, the estimate of the contact signal speed reveals a higher magnitude than the nonlinear signal speed estimate. This is a violation of the fundamental assumption $S_L < S_* < S_R$. Similar results are obtained for a steady shock configuration.

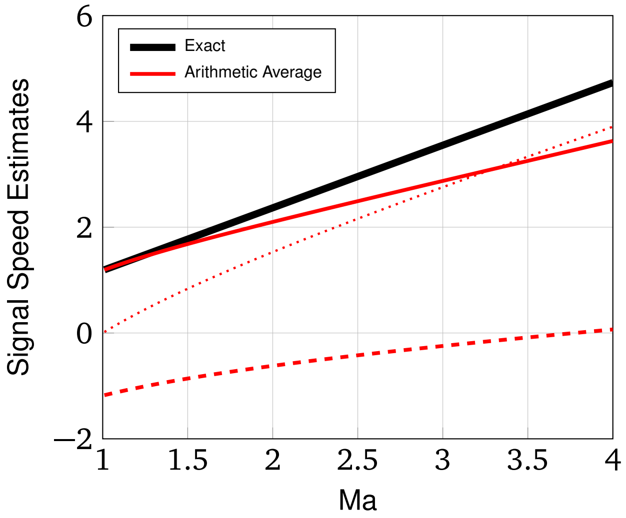

Figure 3.2: Arithmetic-average signal speed estimates for the HLL(C) approximation evaluated for a simple right-traveling shock wave for different Mach numbers (solid: right nonlinear; dotted: contact; dashed: left nonlinear)

In the second part of the paper, the effect of these theoretical considerations is demonstrated for the prediction of a bow shock in a simulation of a hypersonic flow around a cylinder. The application of arithmetic-average estimates leads to non-physical results, whereas all other estimates obtain the physically valid result. Additionally, special attention is required when a popular sign formulation of the HLLC solver is applied. Then, the flaw of the arithmetic-average estimate is almost completely hidden, which makes errors due to inaccurate signal speed estimates particularly difficult to detect and may lead to undefined behavior. Considering the findings in the paper, the arithmetic-average estimate cannot be recommended to apply, especially since cheap and consistent alternative formulations are available.

My contribution to this work lies in uncovering the shortcomings of the arithmetic-average signal speed estimates. Additionally, I performed the theoretical analysis of simplified moving and steady shock configurations to understand the erroneous simulation results for bow shock simulations. I implemented all described procedures in our in-house code and MATLAB, and performed the presented numerical simulations. Moreover, I selected the simulation setups presented in the paper, and post-processed the results. Finally, the manuscript for the publication was written predominantly by me.

Chapter 4

List of Peer-Reviewed Journal Publications

- **Nico Fleischmann, Stefan Adami, Nikolaus A. Adams**: *Numerical symmetry-preserving techniques for low-dissipation shock-capturing schemes.* Computers & Fluids, Volume 189, 94-107, 2019. [36]
- **Nico Fleischmann, Stefan Adami, Xiangyu Y. Hu, Nikolaus A. Adams**: *A low dissipation method to cure the grid-aligned shock instability.* Journal of Computational Physics, Volume 401, 109004, 2020. [39]
- **Nico Fleischmann, Stefan Adami, Nikolaus A. Adams**: *A shock-stable modification of the HLLC Riemann solver with reduced numerical dissipation.* Journal of Computational Physics, Volume 423, 109762, 2020. [37]
- **Nico Fleischmann, Stefan Adami, Nikolaus A. Adams**: *On an inconsistency of the arithmetic-average signal speed estimate for HLL-type Riemann solvers.* Journal of Computational Physics: X, Volume 8, 100077, 2020. [38]

Chapter 5

Concluding Discussion with Respect to the State of the Art

Despite substantial progress in the development of numerical schemes in the last decades, the simulation of compressible flows remains to be a challenge that various different scientific groups investigate worldwide. Nowadays, scientific research for compressible flows is increasingly focused on the precise prediction of the interaction of shock waves with different material interfaces [3, 71, 77, 132]. Especially, material interfaces that reveal a significant change in the physical behavior of the involved materials, such as air-water and air-solid interfaces, challenge state-of-the-art numerical solvers [134]. Interestingly, a limited accuracy or even breakdown of such simulations is not always triggered by the interface treatment itself. Instead, it is often inherited from an inconsistent single-phase treatment [114]. Latest multi-component flow solvers heavily built upon the numerical treatment of single-phase configurations [14, 135, 163]. Early diffuse-interface approaches only extend the set of equations by an additional advection equation [1, 142]. The resulting system of equations is then solved using the exact same numerical approach as for the single phase [78]. Even though sharp-interface methods, such as the level-set method, introduce a more sophisticated treatment of fluid interfaces including surface tension effects, large regions of the flow that are not directly located at an interface completely rely on a precise single-phase treatment [35, 71]. Note that in some cases, an imprecise single-phase treatment may show its adverse effects not until it is applied for the more challenging multi-component flow situations. For example, the artificial asymmetry of simulation results is heavily amplified by the level-set method. This is a well-known fact in the scientific community, however, rarely reported in literature. Hence, a consistent and robust single-phase treatment is crucial for the accurate calculation of complex flow situations. The novel results presented in this thesis serve this purpose in multiple ways.

The effect of symmetry breaking in numerical results when low-dissipation schemes are applied is well-documented in literature [6, 25, 40–42, 117, 139, 146, 147, 168, 170, 174]. Moreover, severe symmetry deviations were sometimes judged as a beneficial property of the scheme to uncover previously hidden underlying physics [41, 42]. However, a detailed explanation of this effect has not been described in literature so far. In this thesis, the reason for numerically induced symmetry breaking has been investigated. Floating-point truncation errors have been identified as the prime reason to trigger instabilities. High-order discretization schemes in combination with highly resolved meshes decrease numerical viscosity to a point where damping of the inherent physical instabilities of the inviscid Euler equations becomes insufficient. It is pointed out that the onset of symmetry breaking with such low-dissipative schemes first is a manifestation of algorithmic imperfections rather than of the low dissipation of the numerical scheme. The argumentation is supported by an easy and cheap procedure to completely avoid numerically induced symmetry breaking, independent of the inherent dissipation of the scheme and the grid resolution. Simulations have been performed with so far unprecedentedly large resolutions for a set of benchmark cases with schemes up to ninth order. This work *improves the consistency* of the numerical simulation and demonstrates the increasing relevance of implementation verification that accompanies the evolution from peta- to exascaling computing power.

Another widespread flaw in numerical simulations of high-speed aerodynamics is the so-called carbuncle phenomenon [114]. This instability occurs when strong shock waves move aligned to the computational grid, and it prevents an accurate computation of high Mach number flows using low-dissipation shock-capturing methods [31]. To this day, the mechanism of this instability is still not fully understood [91]. All available attempts to cure the shock instability introduce additional numerical dissipation [122]. The additional dissipation may help to suppress the instability to a certain extend, but many procedures are less effective when the computational grid is refined. Additionally, they counteract the target of decreasing numerical dissipation. In this thesis, a novel explanation of the instability is provided. It connects the problem to another well documented shortcoming of Godunov-type schemes in the incompressible limit [56, 57]. It is demonstrated that an inaccurate scaling behavior of acoustic and advection contribution to the numerical dissipation triggers the instability. The flux calculation in transverse direction to the shock-front propagation incorporates a vanishing velocity component that resembles a low Mach number situation in the local Riemann problem. A reduction of acoustic dissipation for low local componentwise Mach number is demonstrated to be efficient to stabilize the simulation of hypersonic flows while further reducing the numerical dissipation of the underlying scheme. The *improved accuracy and robustness* of the novel approach has been demonstrated with newly designed Roe and componentwise local Lax-Friedrichs schemes for a comprehensive set of benchmark cases and heavily refined computational grids.

Moreover, the previously described approach to cure the grid-aligned shock instability has also been extended to another important group of complete Riemann solvers. A direct application to the HLLC flux is shown to be ineffective. Thus, a novel centralized formulation of the HLLC flux is derived. This centralized formulation allows for a straightforward reduction of acoustic dissipation in the low Mach number limit. The resultant flux is denoted HLLC-LM. Again, multiple properties of the novel scheme are demonstrated for complex two- and three-dimensional test cases. The HLLC-LM scheme reveals excellent results and demonstrates its capability to simulate complex super- and hypersonic flow physics while *improving accuracy and robustness*.

During the reformulation of the HLLC scheme a consistency problem with a specific signal speed estimate, that recently gained a lot of popularity, became apparent [21, 45, 164]. A detailed investigation of the behavior of the arithmetic-average signal speed estimate for HLL-type schemes revealed an extremely poor prediction of nonlinear signal speeds in some specific cases, such as bow shocks. Moreover, as a consequence of the erroneous nonlinear estimates evaluated with arithmetic-average estimates, principle assumptions of the underlying HLL-type solver, such as $S_L < S_* < S_R$ may be violated. Aiming for *a consistent methodology*, this simplification of the signal-speed estimates should be avoided and classical estimates are required instead.

The findings presented in this thesis improve the quality of classical finite-volume schemes and deepen the understanding of underlying numerical effects. The proposed modifications are easy to apply to many commonly applied methods. Since they improve single-phase finite-volume methodology, which constitutes the basis of latest multi-component solvers, there is a large potential for future applications. The methods can be directly applied in combination with both diffuse- and sharp-interface methods. Tests with these types of multi-component solvers have been performed and no additional difficulties became apparent. An application of the proposed methods to related physics, such as shallow water equations or magnetohydrodynamics, seems also possible.

Even though the symmetry breaking and the grid-aligned shock instability could be classified as pure numerical effects in the first place, both effects are closely connected to inherent instability mechanisms of the underlying Euler system. Indeed, the non-symmetric shapes obtained in many low-dissipation solutions closely resemble experimental results, which never show perfect symmetry. However, instead of imitating this effect via uncontrolled and potentially biased floating-point disturbances, a more sophisticated approach would be to introduce a defined level of disturbances to the simulation. It seems particularly interesting to study the effect of random disturbances on flow phenomena that occur at vanishing physical viscosity. The documented impact of floating-point disturbances clearly reveals the potential of small scale disturbances to affect large scale structures via inverse cascade effects. A physical background is also commonly discussed for the carbuncle phenomenon. In ideal settings, such as for the classical bow shock simulation, the carbuncle phenomenon is clearly a numerical artifact since its occurrence is closely related to the applied computational grid. Nevertheless, with the fact that minor numerical disturbances are sufficient to trigger an instability mechanism, it stands to reason that similar instabilities could also be triggered by minor physical disturbances. Indeed, some experimental observations are documented in literature where similar structures can be detected when bow shocks are artificially disturbed. Such phenomena are rarely investigated and might be an interesting subject for future studies, both numerically and experimentally.

Chapter A

Peer-Reviewed Journal Publications

A.1 Numerical symmetry-preserving techniques for low-dissipation shock-capturing schemes

Home | Help | Live Chat | Sign in | Create Account

Numerical symmetry-preserving techniques for low-dissipation shock-capturing schemes

Author: Nico Fleischmann,Stefan Adami,Nikolaus A. Adams

Publication: Computers & Fluids

Publisher: Elsevier

Date: 15 July 2019

Journal Author Rights

Please note that, as the author of this Elsevier article, you retain the right to include it in a thesis or dissertation, provided it is not published commercially. Permission is not required, but please ensure that you reference the journal as the original source. For more information on this and on your other retained rights, please visit: https://www.elsevier.com/about/our-business/policies/copyright#Author-rights

BACK CLOSE WINDOW

Computers and Fluids 189 (2019) 94–107

Contents lists available at ScienceDirect

Computers and Fluids

journal homepage: www.elsevier.com/locate/compfluid

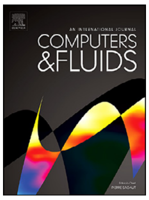

Benchmark solutions

Numerical symmetry-preserving techniques for low-dissipation shock-capturing schemes

Nico Fleischmann*, Stefan Adami, Nikolaus A. Adams

Department of Mechanical Engineering, Chair of Aerodynamics and Fluid Mechanics, Technical University of Munich, Boltzmannstraße 15, Garching 85748, Germany

ARTICLE INFO

Article history:
Received 6 November 2018
Accepted 9 April 2019
Available online 24 May 2019

Keywords:
Symmetry breaking
Floating-point arithmetic
Low-dissipation schemes
High-resolution schemes
WENO
Shock-capturing

ABSTRACT

Modern applications of computational fluid dynamics involve complex interactions across scales such as shock interactions with turbulent structures and multiphase interfaces. Such phenomena, which occur at very small physical viscosity, require high-resolution and low-dissipation compressible flow solvers. Many recent publications have focused on the design of high-order accurate numerical schemes and provide e.g. weighted essentially non-oscillatory (WENO) stencils up to 17th order for this purpose. As shown in detail by different authors, such schemes tremendously decrease adverse effects of numerical dissipation. However, such schemes are prone to numerically induced symmetry breaking which renders validation for the targeted problem range problematic.

In this paper, we show that symmetry-breaking relates to vanishing numerical viscosity and is driven systematically by algorithmic floating-point effects which are no longer hidden by numerical dissipation. We propose a systematic procedure to deal with such errors by numerical and algorithmic formulations which respect floating-point arithmetic. We show that by these procedures inherent symmetries are preserved for a broad range of test cases with high-order shock-capturing schemes in particular in the high-resolution limit for both 2D and 3D.

1. Introduction

Many modern applications of computational fluid dynamics require high-order shock-capturing methods for the accurate prediction of compressible flow features involving shock waves and complex flow structures [1–4]. In order to achieve an efficient and accurate computation, high-order spatial reconstructions are employed together with essentially non-oscillatory (ENO) schemes to avoid spurious oscillations near discontinuities [5–7].

In their pioneering work, Harten et al. [8] introduced the essentially non-oscillatory (ENO) method. In this method the smoothest interpolation stencil out of a set of candidate stencils is selected to adapt the stencil to the actual solution. A further major development is the weighted-essentially non-oscillatory (WENO) method, first introduced by Liu et al. [9]. They proposed to construct a $(2r-1)$th-order accurate reconstruction from a weighted combination of several candidate stencils of order r. Effectively, the order $(2r-1)$ is recovered in smooth regions of the flow, whereas in the vicinity of discontinuities the ENO property is maintained. The work of Jiang and Shu [10] on the efficient implementation of WENO stencils allowed for a straightforward design of higher-order methods and marks a major breakthrough of the WENO methods family. Due to its robust behavior combined with the increased spatial order, their fifth-order variant WENO5-JS gained rapid popularity in numerical solutions of various kinds of applications not only in the field of fluid mechanics [11–14]. A thorough overview of recent applications is given in [15]. Different authors have further improved the method without changing the overall concept. Henrick et al. [16] dealt with the problem that classical WENO schemes are not able to recover the full order of accuracy near critical points by the introduction of a mapping procedure resulting in the WENO-M scheme. Furthermore, Borges et al. [17] suggested to introduce a high-order global smoothness indicator and increase the weights of non-smooth stencils. With the resulting WENO5-Z stencil the dissipation in the vicinity of discontinuities can be further decreased while maintaining the ENO property.

Despite the remarkable success in many applications, classical WENO schemes are still too dissipative to fully resolve the

---

* Corresponding author.
E-mail addresses: nico.fleischmann@tum.de (N. Fleischmann), stefan.adami@aer.mw.tum.de (S. Adami), nikolaus.adams@tum.de (N.A. Adams).

https://doi.org/10.1016/j.compfluid.2019.04.004

small-scale flow features of turbulence in direct numerical simulations. For this purpose, the order of the methods has been systematically increased starting with the work of Balsara and Shu [18], who followed the design rules of [10], and later by Gerolymos et al. [19], who extended and catalogued the reconstruction for stencils up to 17th order. However, these first high-order methods struggle with stability problems and tend to lose the ENO property without further adaptations [19]. Balsara et al. [20] recently introduced a new class of WENO schemes with adaptive order. By adaptively decreasing the order of the method, stability can be maintained while reaching higher-order in smooth areas. Furthermore, the reconstruction utilizes Legendre polynomials, which enables a more efficient calculation of the smoothness factors. Another approach to further reduce the dissipation is provided by the recently proposed class of targeted ENO (TENO) schemes [21,22]. While using the same stencil size as classical WENO schemes, the numerical dissipation is significantly reduced by an ENO-like stencil selection.

Although high-order methods require an increased amount of computational effort, the steady growth in computational power, that recently is mainly driven by the massive application of parallelization strategies, allows for extreme mesh resolutions (see e.g. Ref. [23]). Certainly, there is an increasing trade-off between reconstruction order and higher numerical resolutions in terms of absolute error level [5]. However, the combination of high-order methods with fine meshes leads to a strong decrease in numerical dissipation. Eventually, diminishing numerical dissipation fails to suppress physical instabilities of well-established verification cases for the inviscid Euler equations, which may develop symmetry breaking as numerical artifact, see e.g. the Rayleigh-Taylor instability [5,21,22,24–27] or the two-dimensional Riemann problems [28,29]. This sort of phenomena depends on the chosen scheme, on mesh resolution, but also on algorithm implementation as it is driven by roundoff errors. For moderate mesh resolutions, such symmetry breaking typically can be observed for small-scale structures near the resolution limit. However, for higher-order schemes with lower dissipation, the small-scale symmetry breaking exhibits inverse-cascade phenomena and affects the macroscopic flow evolution leading to a drastically changed flow topology [22,24].

Remacle et al. [24] already suspected floating-point inaccuracies due to roundoff errors to be the relevant mechanism behind numerical symmetry breaking for discontinuous Galerkin methods. Sutherland [29] introduced an approach to control the floating-point truncation error. Changes to physical variables that are smaller than a defined threshold are considered to be non-physical and therefore discarded. In the context of high-order (W/T)ENO-type methods in fluid mechanics, the problem has not been carefully addressed or it is qualified as induced by the low dissipation [21]. Shock or interface-driven (nearly) inviscid flows are the domain of high-resolution shock-capturing schemes. In this paper, we show that it is exactly these schemes which suffer from non-physical artifacts when they are validated for such flows.

We demonstrate the effect of inaccuracies in floating-point arithmetic for the numerical solution of the inviscid Euler equations with low-dissipative (W/T)ENO-type methods. We demonstrate the occurrence of numerical symmetry breaking and develop strategies to control and avoid this artifact. Unlike Sutherland [29], we do not reduce the accuracy range of the calculations. Instead, we show the importance of consistent algorithms that take into account the shortcomings of floating-point arithmetic systematically. Eventually, fully symmetric results can be achieved even for very low-dissipative schemes at large resolutions, thus enabling verification by grid-converged states and cross-code validation.

The remainder of the paper is organized as follows. Sections 2 and 3 briefly review the inviscid Euler equations as governing equations and the finite volume method along with the method-of-lines approach. Furthermore, the relevant relations for the HLLC approximate Riemann solver and the characteristic decomposition strategy that is applied along with the high-order stencils are presented. In Section 4, we identify numerical symmetry-breaking mechanisms and explain straightforward workarounds as well as a generalized solution strategy. In Section 5, we present simulation results for a set of benchmark cases and an extension of the implosion test case to three dimensions applying both high-order methods and high resolutions. Conclusions are drawn in Section 6.

2. Governing equations

An inviscid compressible flow evolves according to the three-dimensional Euler equations

$$\mathbf{U}_t + \mathbf{F}(\mathbf{U})_x + \mathbf{G}(\mathbf{U})_y + \mathbf{H}(\mathbf{U})_z = 0, \tag{1}$$

where $\mathbf{U}$ is the density of the conserved quantities mass ρ, momentum $\rho\mathbf{v} \equiv (\rho u, \rho v, \rho w)$ and total energy $E = \rho e + \frac{1}{2}\rho\mathbf{v}^2$, with e being the internal energy per unit mass.

The fluxes $\mathbf{F}$, $\mathbf{G}$ and $\mathbf{H}$ are defined as

$$\mathbf{F} = \begin{pmatrix} \rho u \\ \rho u^2 + p \\ \rho uv \\ \rho uw \\ u(E+p) \end{pmatrix}, \quad \mathbf{G} = \begin{pmatrix} \rho v \\ \rho uv \\ \rho v^2 + p \\ \rho vw \\ v(E+p) \end{pmatrix}, \quad \mathbf{H} = \begin{pmatrix} \rho w \\ \rho uw \\ \rho vw \\ \rho w^2 + p \\ w(E+p) \end{pmatrix}. \tag{2}$$

The set of equations is closed by the ideal-gas equation of state, where the pressure p is given by $p = (\gamma - 1)\rho e$ with the ratio of specific heats γ.

3. Finite volume approach

In this section, we briefly recall necessary details of the method-of-lines approach for finite volumes, which is widely used to solve systems of hyperbolic equations. We focus on aspects that are particularly important for considering floating-point inaccuracies. More detailed descriptions of the overall scheme can be found e.g. in [30,31].

The time evolution of the vector of cell-averaged conservative states $\bar{\mathbf{U}}$ is given by

$$\begin{aligned} \frac{d}{dt}\bar{\mathbf{U}}_i = \frac{1}{\Delta x}\big(&\mathbf{f}_{i-\frac{1}{2},j,k} - \mathbf{f}_{i+\frac{1}{2},j,k} \\ &+ \mathbf{g}_{i,j-\frac{1}{2},k} - \mathbf{g}_{i,j+\frac{1}{2},k} + \mathbf{h}_{i,j,k-\frac{1}{2}} - \mathbf{h}_{i,j,k+\frac{1}{2}}\big), \end{aligned} \tag{3}$$

where $\Delta x (= \Delta y = \Delta z)$ is the cell size of a uniform Cartesian grid and $\mathbf{f}$, $\mathbf{g}$ and $\mathbf{h}$ approximate the cell-face fluxes in x-, y- and z-direction, respectively. These fluxes are determined dimension-by-dimension from an approximate Riemann solver combined with a high-order WENO [10,18] or TENO [21] spatial reconstruction scheme. Additional volume source terms, such as gravitational acceleration, are omitted here for simplicity. The resulting ODE (3) is integrated in time using a second-order strong stability-preserving (SSP) Runge–Kutta scheme [32]. Note, that a higher-order time integration does neither trigger symmetry breaking nor affect the general results of the simulations presented in this paper and is therefore omitted to save computational cost.

3.1. HLLC approximate Riemann solver

The majority of state-of-the-art methods relies on approximate Riemann solvers since exact Riemann solvers are computationally expensive. Two common types of approximate Riemann solutions are the Roe [33] and the HLL(C) [34] approximation. With the restoration of the contact wave by Toro et al. [35], the HLLC approximation models all wave types of the Euler equations explicitly. Compared to the Roe approximation it is slightly more dissipative. Nevertheless, the better positivity-preservation of the first-order Godunov scheme with the HLLC approximation renders it favorable for problems with low density or pressures [36]. We focus on a HLLC flux formulation, although for the high-order reconstructions as used in this work, it does not fully maintain positivity, see also [37]. We emphasize that all concepts or workarounds essentially apply also to other approximate Riemann solvers.

As “HLLC solver” we define an algorithm that delivers approximate cell-face fluxes of the Riemann problem with reconstructed left and right face states, $\mathbf{U}^L$ and $\mathbf{U}^R$, respectively. Following the compact formulation of Johnsen and Colonius [38], the HLLC flux is defined as

$$\begin{aligned}\mathbf{f}^{HLLC} &= \frac{1+sign(s^*)}{2}\left[\mathbf{f}^L + s^-\left(\mathbf{U}^{*L} - \mathbf{U}^L\right)\right] \\ &\quad + \frac{1-sign(s^*)}{2}\left[\mathbf{f}^R + s^+\left(\mathbf{U}^{*R} - \mathbf{U}^R\right)\right],\end{aligned} \tag{4}$$

where two intermediate states, $\mathbf{U}^{*L}$ and $\mathbf{U}^{*R}$, are separated by the contact wave and are determined from

$$\boldsymbol{U}^{*K} = \frac{s^K - u^K}{s^K - s^*}\begin{pmatrix} \rho^K \\ \rho^K s^* \\ \rho^K v^K \\ \rho^K w^K \\ E^K + \left(s^* - u^K\right)\left(\rho^K s^* + \frac{p^K}{s^K - u^K}\right)\end{pmatrix} \tag{5}$$

with $k = L, R$. The wave speeds s^- and s^+ are estimated according to Batten et al. [36] from

$$s^- = \min(s^L, 0), \qquad s^+ = \max(s^R, 0), \tag{6}$$

with

$$s^L = \min(\bar{u} - \bar{c}, u^L - c^L), \qquad s^R = \max(\bar{u} + \bar{c}, u^R + c^R). \tag{7}$$

$\bar{u}$ and $\bar{c}$ are determined from arithmetic averages $\bar{u} = \frac{1}{2}\left(u^L + u^R\right)$ and $\bar{c} = \frac{1}{2}\left(c^L + c^R\right)$. Alternatively, Roe averaging can be applied to determine $\bar{u}$ and $\bar{c}$, both procedures achieve nearly identical numerical results [39]. Following Einfeldt et al. [40], the contact wave speed is obtained from

$$s^* = \frac{p^R - p^L + \rho^L u^L\left(s^L - u^L\right) - \rho^R u^R\left(s^R - u^R\right)}{\rho^L\left(s^L - u^L\right) - \rho^R\left(s^R - u^R\right)}. \tag{8}$$

3.2. High-order spatial reconstruction with application of local characteristic decomposition

At the beginning of each time step, only cell-averaged conservative variables $\bar{\mathbf{U}}$ are available. For the application of the HLLC procedure as described above, the values at cell faces have to be reconstructed. Different higher-order spatial interpolations, such as WENO and TENO schemes [10,18,21], are available in the literature for this purpose. Note that if the reconstruction is performed directly on conservative variables, spurious oscillations may be introduced in the vicinity of discontinuities due to interactions of different characteristic fields [41]. The issue becomes even more relevant when the order of reconstruction is increased, and essentially non-oscillatory behavior can no longer be guaranteed. As a remedy, all cell-averaged conservative variables within the stencil range are locally projected onto characteristic space and the reconstruction of the cell-face variables is performed with these characteristic variables $\bar{\mathbf{W}}$. Afterwards, the reconstructed characteristic variables at the cell faces are projected back onto physical space and passed to the HLLC solver. This procedure is computationally costly and also challenging in terms of floating-point consistency. Nevertheless, the decomposition is required whenever spurious oscillations cannot be tolerated or positivity of density and pressure is violated.

Here, we present the characteristic decomposition in x-direction in detail. Since the flux is computed dimension-by-dimension, the procedure in y- and z-directions is analogous. All conservative variables within the stencil range are projected onto characteristic space by

$$\bar{\mathbf{W}} = \mathbf{L}\cdot\bar{\mathbf{U}} = \mathbf{L}_1\rho + \mathbf{L}_2\rho u + \mathbf{L}_3\rho v + \mathbf{L}_4\rho w + \mathbf{L}_5 E \tag{9}$$

with $\mathbf{L} = (\mathbf{L}_1, \mathbf{L}_2, \mathbf{L}_3, \mathbf{L}_4, \mathbf{L}_5)$ being the left eigenvector matrix of the linearized system

$$\mathbf{L} = \begin{pmatrix} \frac{1}{4}\frac{q^2}{\hat{H}-\frac{1}{2}q^2} + \frac{1}{2}\frac{\hat{u}}{c} & \frac{1}{2}\frac{\hat{u}}{\hat{H}-\frac{1}{2}q^2} - \frac{1}{2c} & -\frac{1}{2}\frac{\hat{v}}{\hat{H}-\frac{1}{2}q^2} & -\frac{1}{2}\frac{\hat{w}}{\hat{H}-\frac{1}{2}q^2} & \frac{1}{2}\frac{1}{\hat{H}-\frac{1}{2}q^2} \\ -q^2 + \hat{H} & \hat{u} & \hat{v} & \hat{w} & -1 \\ \hat{v} & 0 & -1 & 0 & 0 \\ -\hat{w} & 0 & 0 & 1 & 0 \\ \frac{1}{4}\frac{q^2}{\hat{H}-\frac{1}{2}q^2} - \frac{1}{2}\frac{\hat{u}}{c} & \frac{1}{2}\frac{\hat{u}}{\hat{H}-\frac{1}{2}q^2} + \frac{1}{2c} & -\frac{1}{2}\frac{\hat{v}}{\hat{H}-\frac{1}{2}q^2} & -\frac{1}{2}\frac{\hat{w}}{\hat{H}-\frac{1}{2}q^2} & \frac{1}{2}\frac{1}{\hat{H}-\frac{1}{2}q^2} \end{pmatrix} \tag{10}$$

with $q^2 = \hat{u}^2 + \hat{v}^2 + \hat{w}^2$ and enthalpy H. Note that quantities with hat-notation “$\hat{\cdot}$” denote density-based Roe averages of the cell-averaged variables of the cells adjacent to the face.

After reconstruction, the resulting characteristic cell-face variables $\bar{\mathbf{W}}_{recon}$ are projected back onto physical space by

$$\bar{\mathbf{U}} = \mathbf{R}\cdot\bar{\mathbf{W}}_{recon} = \mathbf{R}_1 w_1 + \mathbf{R}_2 w_2 + \mathbf{R}_3 w_3 + \mathbf{R}_4 w_4 + \mathbf{R}_5 w_5, \tag{11}$$

where $\mathbf{R} = (\mathbf{R}_1, \mathbf{R}_2, \mathbf{R}_3, \mathbf{R}_4, \mathbf{R}_5)$ denotes the right eigenvector matrix of the linearized system and is given by

$$\boldsymbol{R} = \begin{pmatrix} 1 & \frac{1}{\hat{H}-\frac{1}{2}q^2} & 0 & 0 & 1 \\ \hat{u} - \hat{c} & \frac{\hat{u}}{\hat{H}-\frac{1}{2}q^2} & 0 & 0 & \hat{u} + \hat{c} \\ \hat{v} & \frac{\hat{v}}{\hat{H}-\frac{1}{2}q^2} & -1 & 0 & \hat{v} \\ \hat{w} & \frac{\hat{w}}{\hat{H}-\frac{1}{2}q^2} & 0 & 1 & \hat{w} \\ \hat{H} - \hat{c}\hat{u} & \frac{\hat{H}}{\hat{H}-\frac{1}{2}q^2} - 1 & -\hat{v} & \hat{w} & \hat{H} + \hat{c}\hat{u} \end{pmatrix}. \tag{12}$$

4. Mechanisms of numerical symmetry breaking

In the following, we show how nominally symmetric problem configurations may result in asymmetric flow evolution due to floating-point errors in various steps of the numerical algorithm. For simplicity, we first consider two spatial dimensions. Strategies for three-dimensional problems, which reveal additional challenges, are presented afterwards.

We have chosen the Rayleigh-Taylor instability and a gas implosion problem as test cases given their sensitivity to small disturbances.

The Rayleigh-Taylor instability is a common test case for accuracy studies of numerical schemes [5,21,22,24], since it contains both discontinuities and complex flow structures. Two initial gas layers with different densities are exposed to gravity with unity magnitude, where the resulting acceleration is directed towards the lighter fluid. A small disturbance of the contact line triggers the instability. The set-up is chosen according to [5], where the computational domain is $[0,\ 0.25]\times[0,\ 1]$ and the interface is placed at $y = 0.5$. Initial states are given by $(\rho, u, v, p)_{y\le 0.5} = (2, 0, -0.025c\cdot\cos(8\pi x), 2y + 1)$ and $(\rho, u, v, p)_{y>0.5} = (1, 0, -0.025c\cdot\cos(8\pi x), y + 1.5)$, where the speed of sound is $c = \sqrt{\frac{\gamma p}{\rho}}$ with $\gamma = \frac{5}{3}$. Top and bottom boundary states are fixed to (1, 0, 0, 2.5) and (2, 0, 0, 1), respectively. Symmetry boundary conditions are imposed at the left and right boundary.

The second test case describes a two dimensional implosion of a gas in a square box of size $L = 0.6$ as described by Liska and Wendroff [42]. The low-density core region forms another square box, yet its size is smaller and it is centered but rotated

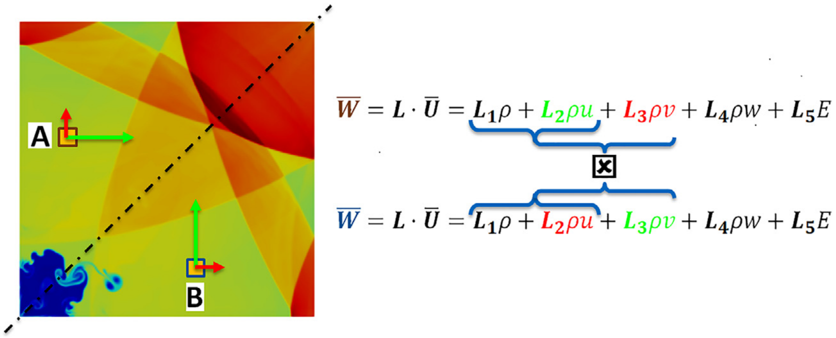

Fig. 1. Illustration of the asymmetric floating-point evaluation of Eq. (9) for two symmetrically placed cells.

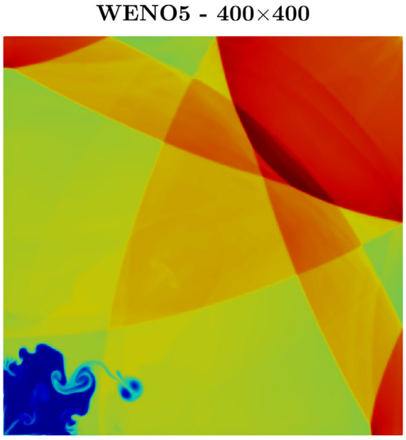
WENO5 - 400×400
WENO5 - 400×400

Fig. 2. Implosion test case $t = 1.0$: density contours from 0.37 (blue) to 1.18 (red); (left) straightforward implementation without sorting during characteristic decomposition; (right) adapted order of evaluations during characteristic decomposition. (For interpretation of the references to colour in this figure legend, the reader is referred to the web version of this article.)

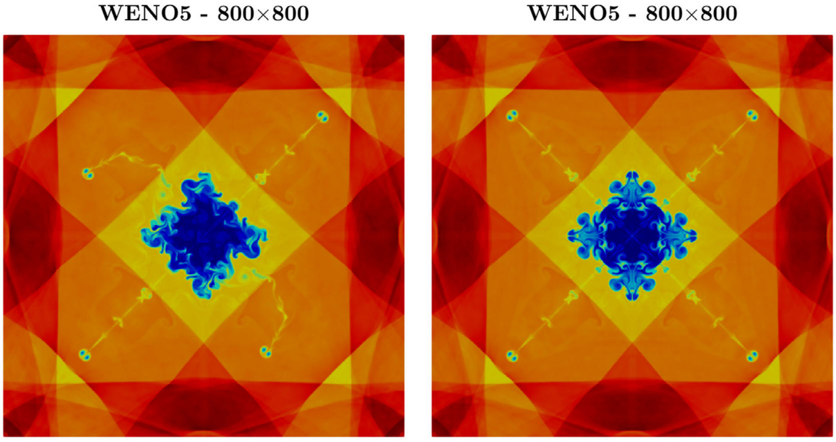
WENO5 - 800×800
WENO5 - 800×800

Fig. 3. Implosion test case $t = 2.5$: density contours from 0.4 (blue) to 1.05 (red); (left) implementation without brackets for contact wave speed calculation; (right) implementation with brackets for contact wave speed calculation. (For interpretation of the references to colour in this figure legend, the reader is referred to the web version of this article.)

by 45º. The corner points of the inner square box are located at $(\pm 0.15, 0)$ and $(0, \pm 0.15)$. Symmetry boundary conditions are applied at all boundaries. Initially, both fluids are at rest with the initial states $(\rho, u, v, p)_{core} = (0.125, 0, 0, 0.14)$ and $(\rho, u, v, p)_{outer} = (1.0, 0, 0, 1.0)$ and $\gamma = 1.4$. For simplicity, this problem is usually studied by employing the two axial symmetries. The reduced problem still reveals an inherent symmetry along the diagonal axis. The evolution of the jet developing along this axis is very sensitive to small disturbances and can be easily deflected, especially for long-time simulations up to $t = 2.5$. Once the symmetry is slightly perturbed, frequent shock-wave interactions lead to a strong increase of asymmetry.

4.1. Lack of associativity

Standard requirements of modern programming languages ensure that summation and multiplication are commutative for two components, i.e. the result given in floating-point notation equals the correctly rounded analytic solution. However, if more than two components are summed up or multiplied, the final floating-point value typically depends on the order of operations, i.e. associativity is lost

$$(a + b) + c \neq a + (b + c). \quad (13)$$

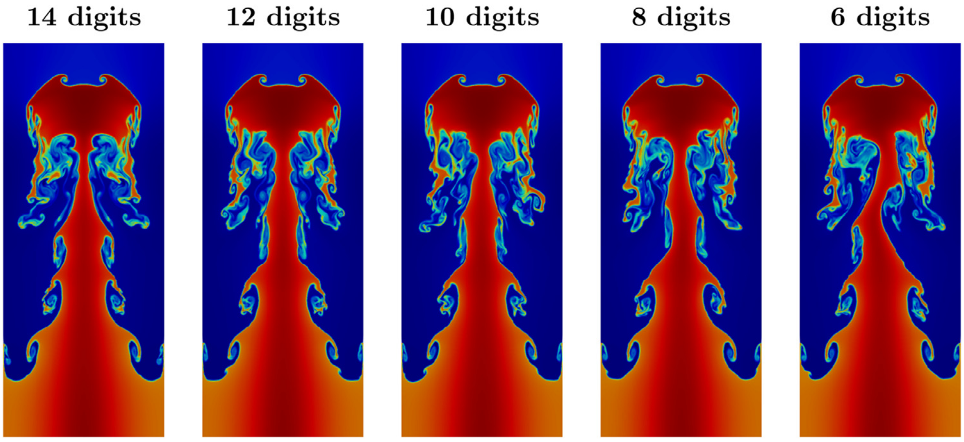

Fig. 4. Rayleigh-Taylor instability $t = 1.95$: density contours from 0.85 (blue) to 2.25 (red); symmetry breaking due to limited representation of π to the given number of digits with a resolution of 256×1024 using a TENO5 stencil. (For interpretation of the references to colour in this figure legend, the reader is referred to the web version of this article.)

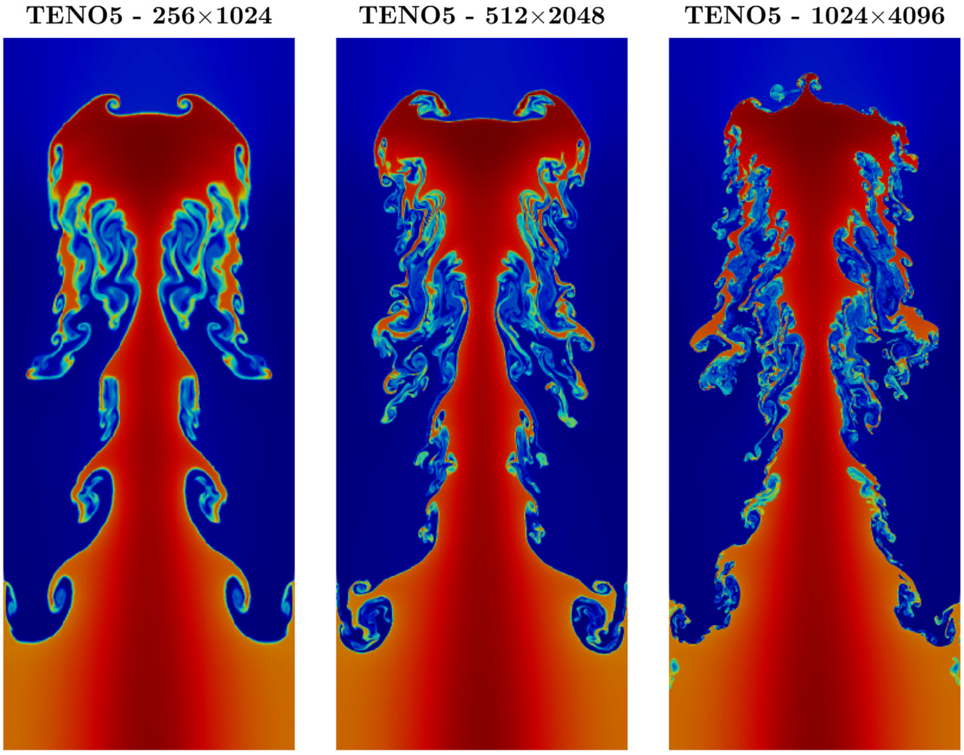

Fig. 5. Rayleigh-Taylor instability $t = 1.95$: density contours from 0.85 (blue) to 2.25 (red); symmetry breaking due to cosine evaluation inaccuracy. (For interpretation of the references to colour in this figure legend, the reader is referred to the web version of this article.)

Numerical algorithms build upon a series of such elementary operations. Accordingly, effects of truncation errors cannot be suppressed completely, however, we found that only few recurring algorithmic patterns trigger asymmetric flow behavior that leads to macroscopic flow deviations. These patterns occur essentially for all employed numerical discretization schemes.

The simulation of the implosion test case using low-dissipative schemes is an illustrative example for symmetry breaking along the diagonal line, see Fig. 1. The effect that triggers this asymmetry can be traced back to operations where directionally dependent quantities are subject to summation or multiplication operations, e.g. for the velocity components. Considering two isolated cells symmetric to the diagonal line, see Fig. 1, and a perfectly symmetric flow at this time instant, the velocity component in x-direction of the cell A equals the velocity component in y-direction of cell B and vice versa. Together with the lack of associativity, Eq. (13), the characteristic projection in Eq. (9) is prone to floating-point round-off errors, and small-scale disturbances are triggered. These disturbances are amplified by physical instability mechanisms of the inviscid flow (e.g. Kelvin-Helmholtz instabilities) and deflect the diagonal jet in the given example. Aiming for preserving symmetry we have to ensure that the algorithmic pattern is dimensionally invariant. Such patterns with explicit directional dependencies together with more than two components occur with the characteristic decomposition in high-resolution schemes.

One straightforward solution to handle the issue is to enforce the order of the evaluation of matrix multiplications by inserting appropriate brackets into the source code. This will force the compiler to handle the operations consistently for any cell. In 2D, Eq. (9) becomes

$$\bar{\mathbf{W}} = \mathbf{L} \cdot \bar{\mathbf{U}} = \mathbf{L}_1 \rho + (\mathbf{L}_2 \rho u + \mathbf{L}_3 \rho v) + \mathbf{L}_4 E. \tag{14}$$

The actual implementation, however, is cumbersome as Eq. (14) is part of a matrix multiplication that involves loops.

Alternatively, we can order the evaluation of Eq. (14) such that the sum of momenta is computed first, and the other terms are added subsequently, i.e.

$$\bar{\mathbf{W}} = \mathbf{L} \cdot \bar{\mathbf{U}} = (\mathbf{L}_2 \rho u + \mathbf{L}_3 \rho v) + \mathbf{L}_1 \rho + \mathbf{L}_4 E. \tag{15}$$

The same procedure is applied to Eq. (11).

When the directional dependence of the characteristic projection is eliminated, the expected perfectly diagonal post-implosion jet is observed, see Fig. 2.

A second example is shown to clarify the symmetry-breaking mechanism for a different part of the solver. The same implosion problem is now calculated on the full domain. The loss of symmetry in the second and fourth quadrant, as shown in the left frame of Fig. 3, is caused by an inconsistent calculation of the wave-speed s^* in the HLLC solver. By enforcing proper summations using additional brackets, Eq. (8) becomes

$$s^* = \frac{\left(p^R - p^L\right) + \left[\rho^L u^L \left(s^L - u^L\right) - \rho^R u^R \left(s^R - u^R\right)\right]}{\rho^L \left(s^L - u^L\right) - \rho^R \left(s^R - u^R\right)}. \tag{16}$$

Remarkably, this marginal modification removes these artifacts, see the right frame of Fig. 3. The only difference between both simulations is the introduction of brackets in one single line of code.

Note, that the driving mechanism behind symmetry breaking in both cases is the lack of associativity. Despite the fact that all results in this paper are demonstrated for one specific type of flow solver (HLLC) for simplicity, we emphasize that the underlying principles and derived best-practice guidelines are not limited to these methods, but apply for high-resolution schemes for flow solvers in general.

4.2. Generalized solution strategy

The simple workarounds that were presented in detail in the previous section demonstrate the fundamental mechanisms, however, they are only applicable to two-dimensional situations. They do not work for more complex problems, especially not for three dimensions. This can be demonstrated exemplarily for the calculation of the velocity magnitude q. Since three components have to be summed, three different floating-point results

$$q^2 = \begin{cases} (v^2 + w^2) + u^2, \\ (w^2 + u^2) + v^2, \\ (u^2 + v^2) + w^2 \end{cases} \tag{17}$$

can be obtained. The same problem arises in several other parts of the algorithm, where subterms related to the three Cartesian directions have to be summed up, e.g. in Eq. (3) the fluxes in x, y, and z-direction. This summation of direction-related terms can be found for a wide range of other algorithms in CFD codes including curvature calculations, multiresolution approaches and level-set methods.

For certain operations, where the preferential direction is known a priori, the simple bracketing strategy is applicable such as

$$q^2 = \begin{cases} (v^2 + w^2) + u^2 & \text{for flux calculation in x-direction,} \\ (w^2 + u^2) + v^2 & \text{for flux calculation in y-direction,} \\ (u^2 + v^2) + w^2 & \text{for flux calculation in z-direction.} \end{cases} \tag{18}$$

However, generalization of this procedure under relaxed conditions is not possible. Instead, we propose to use a consistency-ensuring function for all relevant summations in the code. Consistency means in this context that the result of the summation is identical for all cases of Eq. (17). Thus, the consistency-ensuring summation restores associativity for floating-point numbers. This tailored summation takes the sum of three floating-point values a, b and c according to

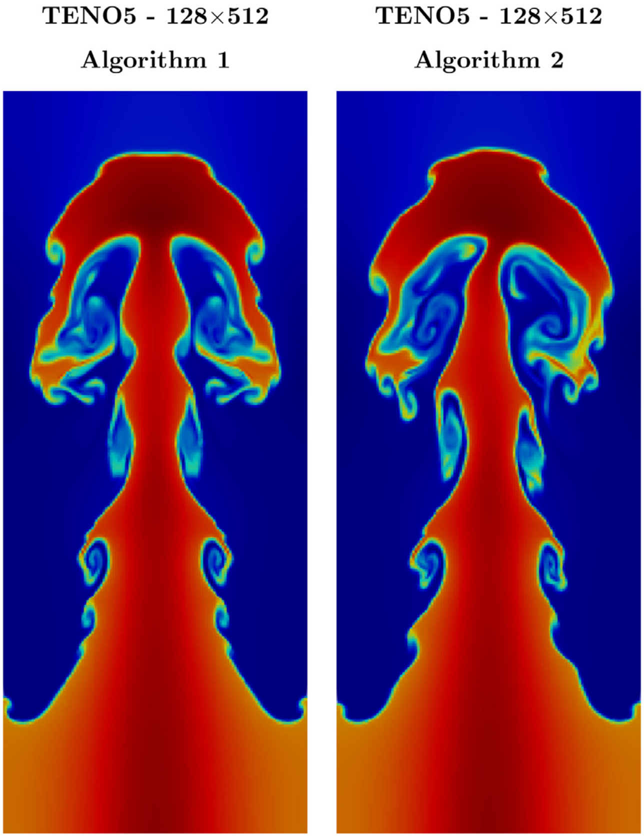

Fig. 6. Rayleigh-Taylor instability $t = 1.95$: density contours from 0.85 (blue) to 2.25 (red); (left) straightforward implementation of Roe-averaging procedure; (right) efficient implementation of Roe-averaging procedure. (For interpretation of the references to colour in this figure legend, the reader is referred to the web version of this article.)

$$SUM_{consistent} = \frac{1}{2}(\max(s_1, s_2, s_3) + \min(s_1, s_2, s_3)) \tag{19}$$

with

$$\begin{aligned} s_1 &= (a + b) + c, \\ s_2 &= (c + a) + b, \\ s_3 &= (b + c) + a, \end{aligned} \tag{20}$$

and four floating-point values a, b, c and d with

$$\begin{aligned} s_1 &= (a + b) + (c + d), \\ s_2 &= (c + a) + (b + d), \\ s_3 &= (b + c) + (a + d). \end{aligned} \tag{21}$$

Note, this procedure does not necessarily provide the floating-point representation of the exact analytical result, but it delivers a consistent result that is independent of the sequence of terms. Hence, the evaluation of the sum becomes directionally independent. Extension to higher numbers of summands is straightforward, yet in our experience not required for common applications. An alternative, well-known approach to avoid errors in the sum of numbers with different order of magnitude is to sort the values before adding them up. In principle, this would also work here, however, we compared the run time of both procedures and found our solution to be around 30 times faster than the application of “std::sort” in C++. The overall performance impact of the

```cpp
//compute density-based Roe averages according to Eq. (24)
double sqrt_rho_i   = std::sqrt(rho_i);
double sqrt_rho_ip1 = std::sqrt(rho_ip1);
double divisor      = 1.0 / ( sqrt_rho_i + sqrt_rho_ip1 );

double u_roe_avg = ((u_i * sqrt_rho_i) + (u_ip1 * sqrt_rho_ip1))
                   * divisor;
double v_roe_avg = ((v_i * sqrt_rho_i) + (v_ip1 * sqrt_rho_ip1))
                   * divisor;
double w_roe_avg = ((w_i * sqrt_rho_i) + (w_ip1 * sqrt_rho_ip1))
                   * divisor;
double H_roe_avg = ((H_i * sqrt_rho_i) + (H_ip1 * sqrt_rho_ip1))
                   * divisor;
```

C++ Code Example 1. A straightforward algorithm of the Roe-averaging procedure.

```cpp
//compute density-based Roe averages according to Eq. (25)
double sqrt_rho     = std::sqrt(rho_ip1 * one_rho_i);
double divisor      = 1.0 / ( sqrt_rho + 1.0 );

double u_roe_avg = (u_i + (u_ip1 * sqrt_rho)) * divisor;
double v_roe_avg = (v_i + (v_ip1 * sqrt_rho)) * divisor;
double w_roe_avg = (w_i + (w_ip1 * sqrt_rho)) * divisor;
double H_roe_avg = (H_i + (H_ip1 * sqrt_rho)) * divisor;
```

C++ Code Example 2. An efficient algorithm of the Roe-averaging procedure.

consistency-managed sums for the simulations shown in this paper is never higher than 10%.

4.3. *Influence of initial disturbance*

Although it seems obvious that perturbations in the initial condition can affect the simulation result, here we want to raise awareness of unintentionally initialized asymmetries.

Consider the classical Rayleigh-Taylor instability where the velocity field is perturbed according to

$$v = -0.025c \cdot \cos(8\pi x). \tag{22}$$

We want to highlight the effect of the accuracy of π when evaluating Eq. (22). In Fig. 4 we show the Rayleigh-Taylor instability at $t = 1.95$ for a resolution of 256×1024 and varying accuracy of the numerical representation of π. Only from 12 digits, the error becomes negligible and the Rayleigh-Taylor instability seems symmetric. Another well-known effect is an inaccurate cosine evaluation with C++ routines, shown in Fig. 5. The fact that $cos(\pi - \epsilon) \neq \cos(\pi + \epsilon)$ is known in the computer science community, yet little attention is payed to its consequences in computational fluid dynamics. Again, the symmetry breaking in Fig. 5 is simply induced by the violation of cosine-symmetry and could lead to wrong interpretations with respect to the quality of numerical schemes. As a remedy, we enforced symmetric initial conditions by

$$v = \begin{cases} -0.025c \cdot \cos(8\pi x), & \text{if } x < 0.125, \\ -0.025c \cdot \cos\left[8\pi\,(0.25 - x)\right], & \text{otherwise} \end{cases} \tag{23}$$

and observed perfectly symmetric results even for unprecedentedly large resolutions for the Rayleigh-Taylor instability as compared to literature (see next section).

4.4. *Caveats of performance optimization*

In this last example, we demonstrate the effect of code optimizations with emphasis on runtime minimization. Given a low-dissipative scheme with careful implementation following our previous guideline, round-off errors can still be triggered from code optimization efforts.

We consider a scheme which involves the density-based Roe-averaging procedures as required for the characteristic decomposition, see Eqs. (10) and (12). Following Roe [33], the average is defined as

$$\hat{k} = \frac{\bar{k}_i \cdot \sqrt{\rho_i} + \bar{k}_{i+1} \cdot \sqrt{\rho_{i+1}}}{\sqrt{\rho_i} + \sqrt{\rho_{i+1}}}, \tag{24}$$

where k is replaced by the averaged quantity of interest, e.g. u, v, w or H. A straightforward algorithm is given in Example 1.

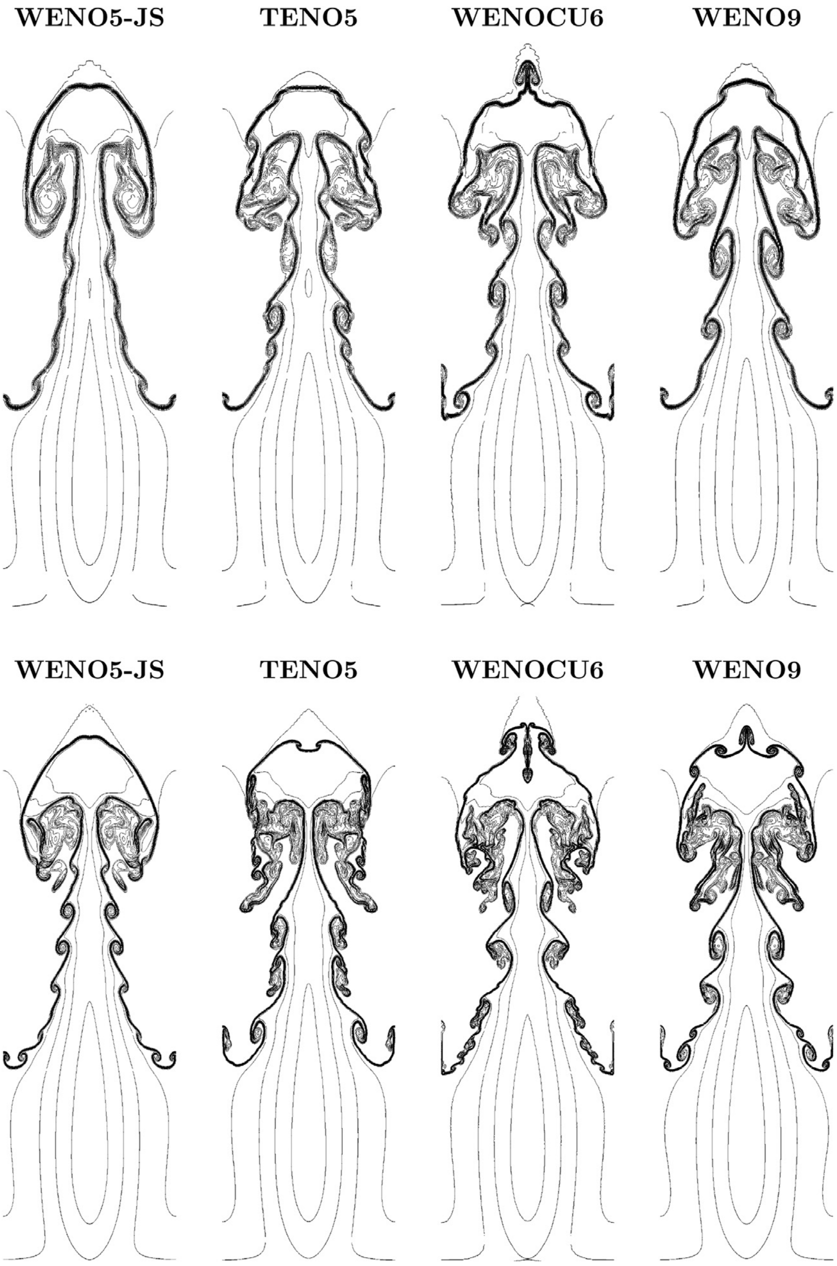

Fig. 7. Rayleigh-Taylor instability: density contours; (top) 128 × 512; (bottom) 256 × 1024.

From a computational efficiency point of view, the operation count of this implementation can be reduced. The evaluation of

$$\hat{k} = \frac{\bar{k}_i + \bar{k}_{i+1} \cdot \sqrt{\frac{\rho_{i+1}}{\rho_i}}}{\sqrt{\frac{\rho_{i+1}}{\rho_i}} + 1} \tag{25}$$

is analytically identical to Eq. (24), yet computationally preferable for the saving of one costly root function evaluation. However, this popular rearrangement causes asymmetry as demonstrated in the following. The optimized C++ code is shown in Example 2.

In Fig. 6, we show two snapshots of the density contours from a Rayleigh-Taylor instability simulation using the implementation of Eq. (24) (left figure) and Eq. (25) (right figure), respectively. Both simulations are performed with TENO5 ($C_T = 10^{-5}$) using 128 × 512 cells and the density is shown at $t = 1.95$. Obviously, the optimized algorithm strongly affects the quality of the results and initiates symmetry breaking. Successive mathematical operations, especially within the costly root function, lead to a fast amplification of floating-point errors that affects the overall flow evolution even for moderate resolutions.

5. High resolution examples and discussion

We have reported several strategies to improve the solver implementations for the Euler equations with symmetry preserving property. In this section, we demonstrate their efficiency for modern low-dissipative numerical schemes together with large spatial resolutions. The Rayleigh-Taylor instability problem, the implosion problem and a classical Riemann problem are computed

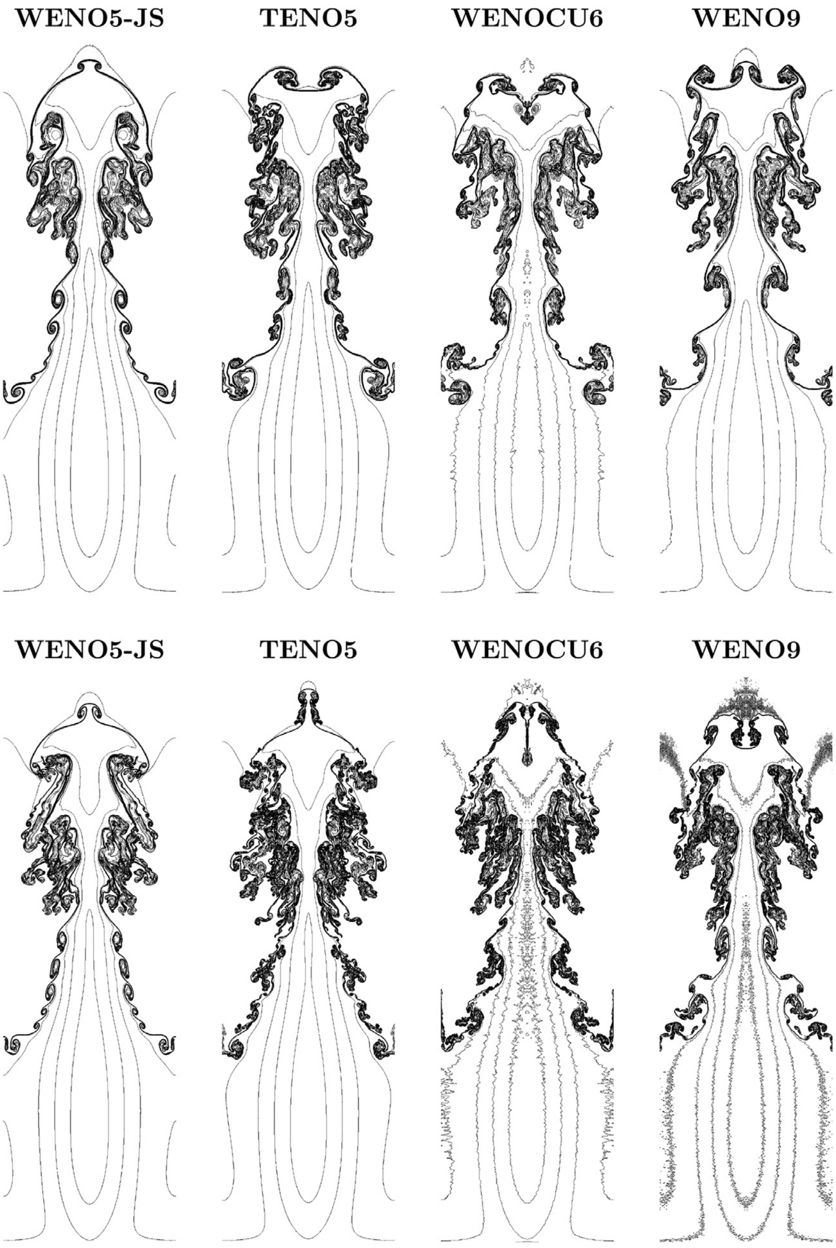

Fig. 8. Rayleigh-Taylor instability $t = 1.95$: density contours; (top) 512 × 2048; (bottom) 1024 × 4096.

in two-dimensions with unprecedented resolution and different high-order stencils. The results are compared to literature data and show very good agreement. Finally, we present a new three-dimensional implosion test case, which is directly obtained by the extension of the two-dimensional case of Liska and Wendroff [42]. The high number of inherent symmetries together with the high number of wave interactions makes this case particularly interesting and challenging to study the directional independence of the framework in three dimensions.

The inviscid Euler equations are formally scale-free due to the infinite Reynolds number, thus numerical schemes with vanishing dissipation predict an infinite cascade evolution of small structures. Numerical dissipation retards small disturbance amplification, thus a delayed evolution of asymmetries is observed. For this reason, often in literature the onset of an asymmetric Rayleigh-Taylor instability evolution is used as an indicator for the amount of artificial numerical dissipation [5,21,22]. In this work, we demonstrate that numerical dissipation does basically determine the growth rate of either initially present or algorithmically induced asymmetric disturbances but does not trigger them itself. In other words, visible symmetry breaking is an indicator of insufficiently damped artificial disturbances rather than the result of some underlying physics that is observable due to higher-order methods.

The CFL number is set to 0.6 for all test cases. Calculations were performed on the SuperMUC Petascale System using CPUs of the type Xeon E5-2697 v3 (Haswell). The C++ source code is compiled using the Intel compiler (ICC) version 16.0.4.

5.1. *Rayleigh-Taylor instability*

We start evaluating the Rayleigh-Taylor instability test case, which is already described in Section 4. This test case is widely

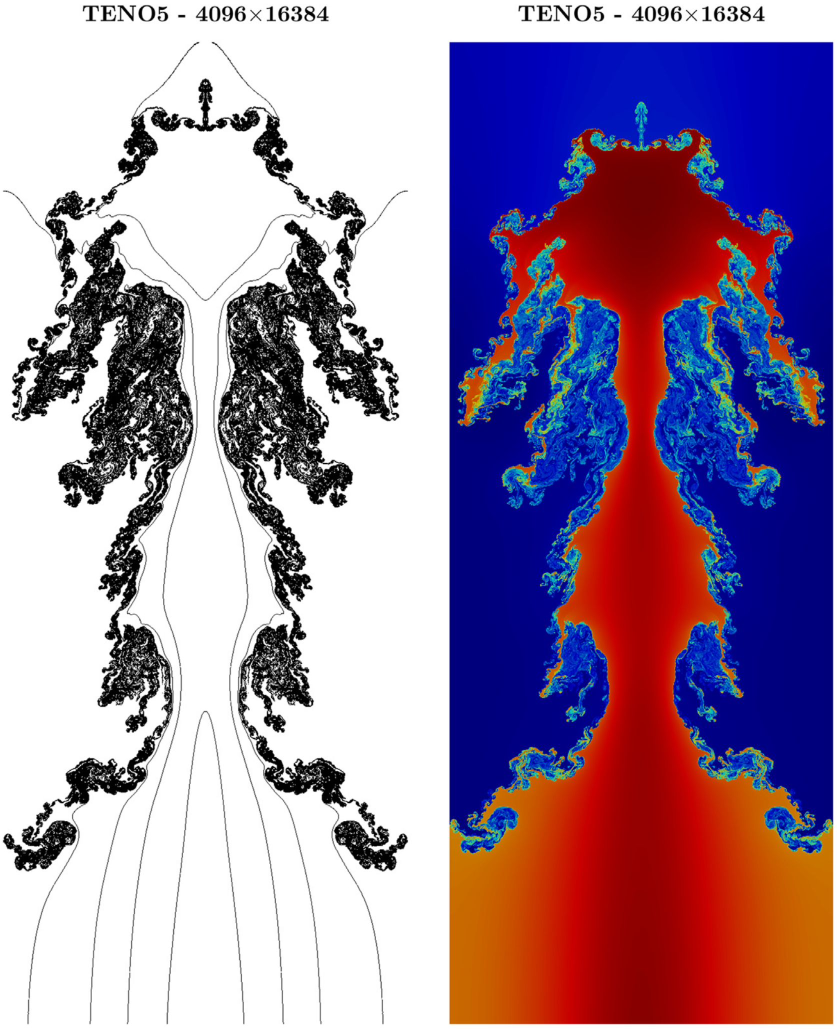

Fig. 9. Rayleigh-Taylor instability $t = 1.95$: (left) density contours; (right) color density map (blue= 0.85 to red= 2.25). (For interpretation of the references to colour in this figure legend, the reader is referred to the web version of this article.)

used for verification of numerical methods. The resolution and richness of vortical structures of this test case can be utilized as a measure of the numerical dissipation introduced by the method. The loss of symmetry in this test case is an effect of reduced numerical dissipation as shown by different authors [5,21,22,24,26]. Remacle et al. [24] supposed that the only cause of the asymmetric behavior of the flow might be due to roundoff errors, however, they did not achieve symmetric results for higher resolutions.

We simulated the Rayleigh-Taylor instability with increasingly high resolution applying four different high-order stencils, namely the WENO5-JS [10], the TENO5 ($C_T = 10^{-5}$) [21], the WENOCU6 [43] and the WENO9 [18] stencil. The resulting density contours are shown in Figs. 7 and 8 for four different resolutions 128 × 512, 256 × 1024, 512 × 2048 and 1024 × 4096. 15 contour lines are equally spaced from $\rho = 0.952269$ to $\rho = 2.14589$ according to [5]. The final simulation time is $t = 1.95$. Unlike in Fig. 2 in [5], Fig. 20 in [21] and Fig. 20 in [22], where asymmetric results are presented for high-order methods, the symmetry is exactly maintained up to floating-point precision. To our best knowledge, there is no result of the Rayleigh-Taylor instability reported in literature for resolutions beyond 512 × 2048.

Fig. 9 shows the Rayleigh-Taylor instability at $t = 1.95$ for an extreme resolution of $4096 \times 16,384$ using the TENO5 scheme. Symmetry is preserved quantitatively up to floating-point precision. Thus, the consistent floating-point arithmetic in our framework enables the usage of high-order methods combined with highly resolved meshes without any numerical symmetry breaking.

5.2. 2D implosion test case

The two-dimensional implosion test case of Liska and Wendroff [42] is a challenging test case due to the presence of non-grid aligned shocks and the appearance of axisymmetric jets, see Section 4 for a more detailed problem description. This test case is often used for code validation in the astrophysics community [29,44]. Sutherland [29] reports the problem of floating-point inaccuracies and handles this by a controlled rounding procedure with a non-physical threshold. Fluctuations smaller than this limit are regarded as floating-point noise and intentionally eliminated. However, following the implementation principles of Section 4, we achieve strong symmetry preservation without the usage of any additional error-cancellation procedure, and furthermore we are able to maintain the full precision range. In [29,42,44] only the first quadrant of the implosion problem is simulated. The symmetry around the diagonal of the first quadrant does not necessarily ensure the symmetry around the diagonals of all other quadrants

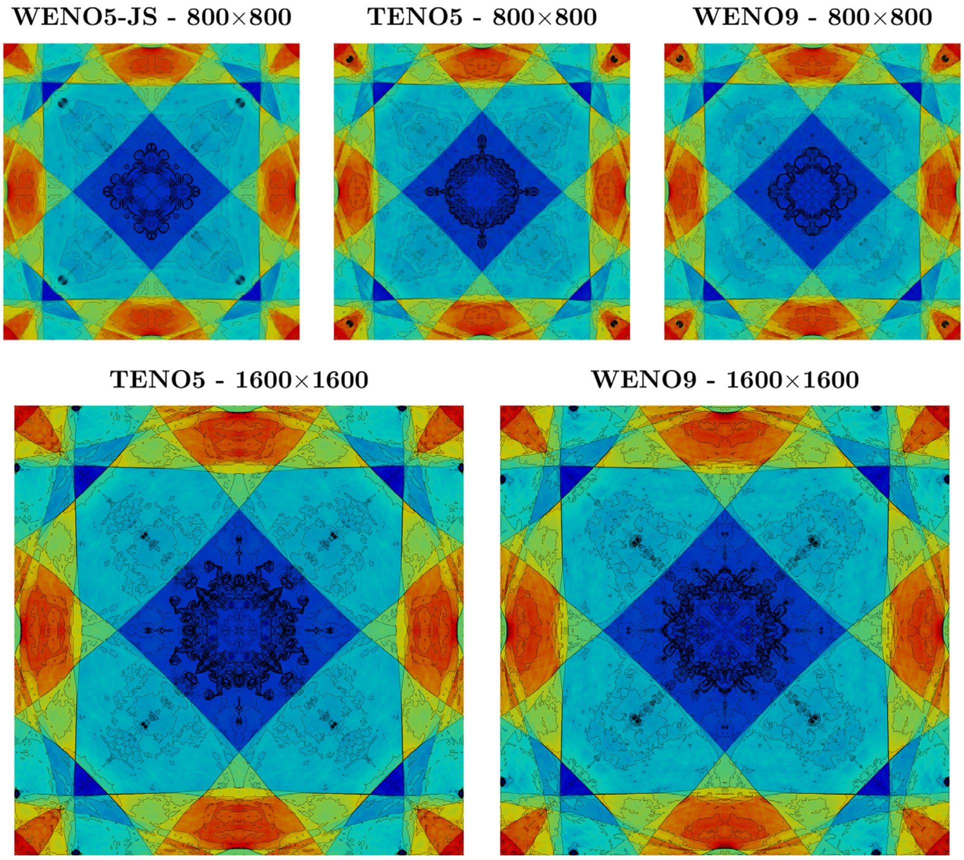

Fig. 10. Implosion $t = 2.5$: color pressure map (blue= 0.7 to red= 1.15) is overlaid by 31 density contours (0.35 to 1.1). (For interpretation of the references to colour in this figure legend, the reader is referred to the web version of this article.)

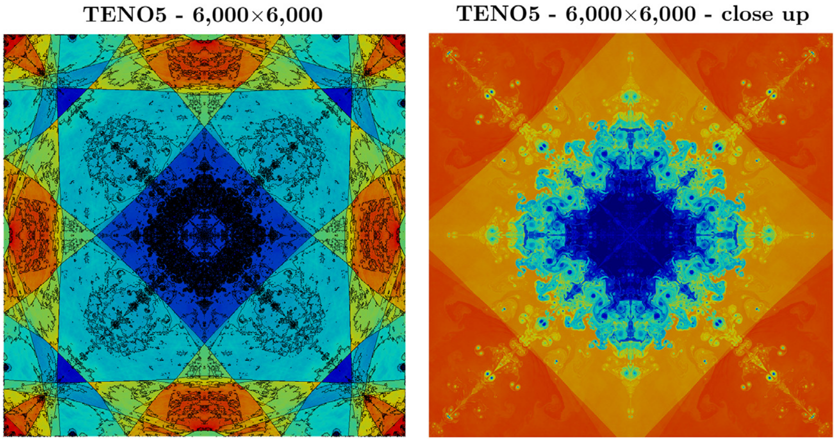

Fig. 11. Implosion $t = 2.5$: (left) color pressure map (blue= 0.7 to red= 1.15) is overlaid by 31 density contours (0.35 to 1.1); (right) color density map of the inner region $[0.15, 0.45] \times [0.15, 0.45]$ (blue= 0.4 to red= 1.0) . (For interpretation of the references to colour in this figure legend, the reader is referred to the web version of this article.)

as shown in Fig. 3. Thus, here we simulated the full problem domain.

Results for the final pressure and density distribution are given in Fig. 10. The lowest presented resolution is chosen according to [42] and delivers comparable results for the WENO5-JS stencil. For higher resolutions, the jet moves further in diagonal direction and reaches the end of the domain, where it is then split into two parts. Thus, the progress of the jet can be used as a measure of the magnitude of numerical dissipation. The TENO5 stencil is able to achieve a result close to the one of the WENO9 stencil. Despite the smaller size and reduced computational cost of the TENO5 stencil as compared to the WENO9 stencil, the level of numerical dissipation is similar. Thus, it is more efficient to use the TENO5 stencil to achieve a desired level of numerical dissipation.

Again, the robustness of the implementation is tested by further increasing the resolution up to $36 \cdot 10^6$ cells. The resulting pressure and density distribution is shown in Fig. 11. Due to the absence of any physical viscosity, no convergence can be expected and the

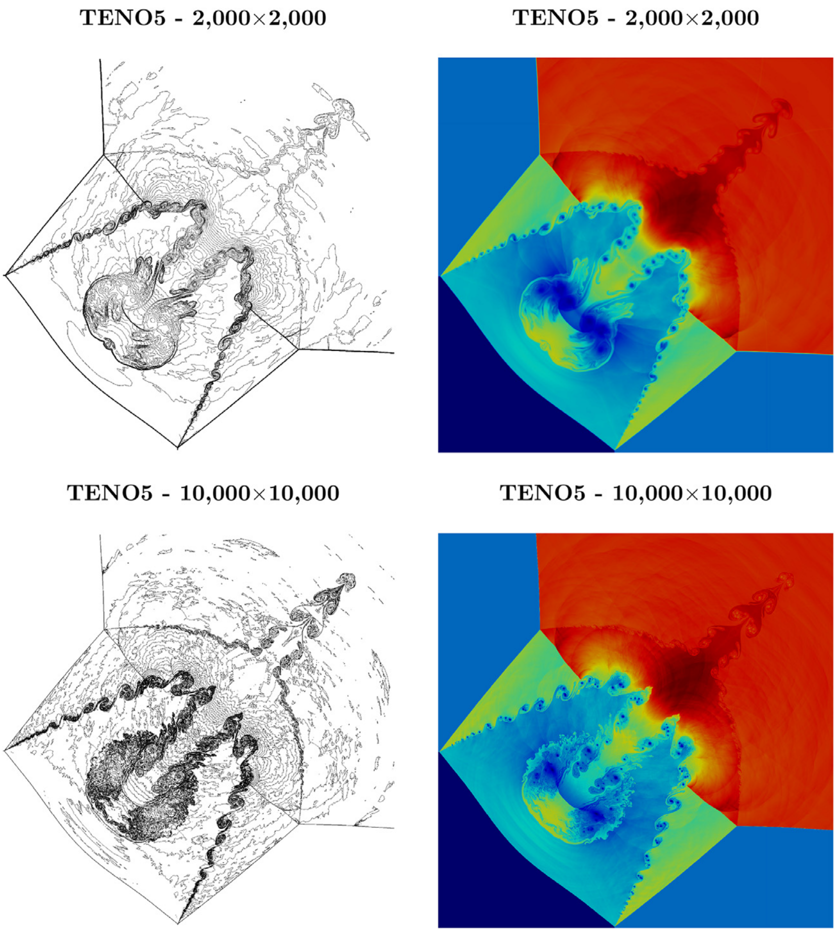

Fig. 12. 2D Riemann case at $t = 1.1$ in the region [0, 1.2] × [0, 1.2]: (left) 32 density contour levels from 0.15 to 1.7; (right) color density map (blue= 0.14 to red= 1.75). (For interpretation of the references to colour in this figure legend, the reader is referred to the web version of this article.)

reduction of the numerical dissipation with increasing resolution leads to finer and finer structures. All symmetries are quantitatively maintained to floating-point precision at the end of the simulation.

5.3. 2D Riemann case

Schulz-Rinne et al. [45] proposed a series of two-dimensional Riemann test cases with systematic permutations of shockwaves and expansion waves running in x- and y-direction, respectively. Here, we focus on the four-shock setup that was already studied by several groups [28,29,42]. However, similarly to Balsara et al. [28], we modify the domain size to [0, 2] × [0, 2] and simulate the problem until $t = 1.1$. This is advantageous since the relevant region now covers more than one quarter of the full domain at the end of the simulation. In literature, the initial quantities are rounded after five digits, resulting in measurable artifacts of the complex wave system. Here, we apply the exact Rankine-Hugoniot jump relations to obtain

$$\begin{array}{lllll}
\rho = 1.5, & u = 0, & v = 0, & P = 1.5, & \text{for } x > 1, \quad y > 1, \\
\rho = \frac{33}{62}, & u = \frac{4}{\sqrt{11}}, & v = 0, & P = .3, & \text{for } x < 1, \quad y > 1, \\
\rho = \frac{77}{558}, & u = \frac{4}{\sqrt{11}}, & v = \frac{4}{\sqrt{11}}, & P = \frac{9}{310}, & \text{for } x < 1, \quad y < 1, \\
\rho = \frac{33}{62}, & u = 0, & v = \frac{4}{\sqrt{11}}, & P = .3, & \text{for } x > 1, \quad y < 1.
\end{array} \tag{26}$$

For this test case, a cutoff value of $C_T = 10^{-4}$ was used for the TENO5 stencil.

The resulting density field (contours and color maps) is shown in Fig. 12 for a section of the computational domain. The two resolutions are chosen based on the reference configuration, see Fig. 11 of [28], and as example of an extreme resolution with $100 \cdot 10^6$ cells. Contrary to [28], here the diagonal symmetry of the guitar-like shape of the jet is completely maintained. The same is also shown for an extreme resolution together with the expected increased richness of the fine structures.

5.4. 3D implosion test case

Finally, we tested the symmetry preserving property of the framework in three dimensions. For this purpose, the two-dimensional test case of Liska and Wendroff [42] (Section 5.2) is extended to three dimensions in a straightforward way using an octahedral-shaped low-pressure area at the center of a cubical domain of size [0, 0.6] × [0, 0.6] × [0, 0.6]. The six corner points of the octahedron are placed at (0.3 ± 0.15, 0.3, 0.3), (0.3, 0.3 ± 0.15, 0.3) and (0.3, 0.3, 0.3 ± 0.15). With this setup, each of the eight octants of the coordinate system, which is centered in the middle of the octahedron, has identical flow conditions. Within each octant, the problem can be further split into six symmetric subdomains. Thus, the problem can be fully described by one-48th of the whole domain. In order to avoid an asymmetric initialization, the inner

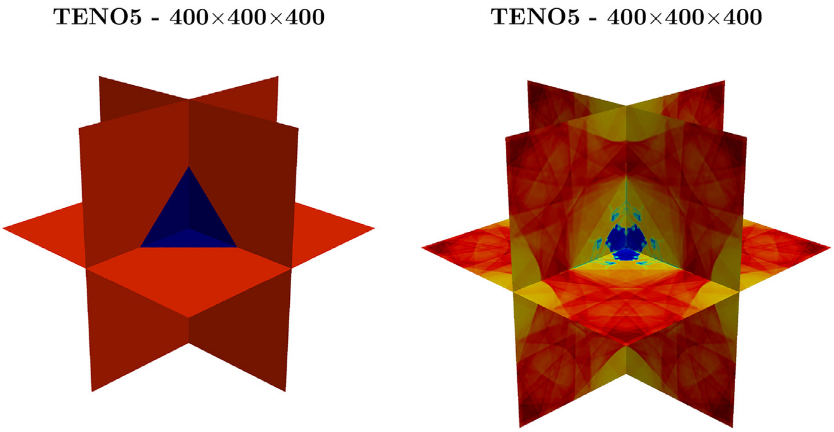

Fig. 13. 3D implosion: color density map (blue= 0.4 to red= 1.13) for $t = 0$ and $t = 2.5$. (For interpretation of the references to colour in this figure legend, the reader is referred to the web version of this article.)

low-pressure domain is given by

$$\begin{aligned}
(x-0.3)+(y-0.3)+(z-0.3) &< 0.15+10^{-10} \quad \cap \\
(x-0.3)+(y-0.3)-(z-0.3) &< 0.15+10^{-10} \quad \cap \\
(x-0.3)-(y-0.3)+(z-0.3) &< 0.15+10^{-10} \quad \cap \\
(x-0.3)-(y-0.3)-(z-0.3) &< 0.15+10^{-10} \quad \cap \\
-(x-0.3)+(y-0.3)+(z-0.3) &< 0.15+10^{-10} \quad \cap \\
-(x-0.3)+(y-0.3)-(z-0.3) &< 0.15+10^{-10} \quad \cap \\
-(x-0.3)-(y-0.3)+(z-0.3) &< 0.15+10^{-10} \quad \cap \\
-(x-0.3)-(y-0.3)-(z-0.3) &< 0.15+10^{-10}
\end{aligned} \tag{27}$$

with $(\rho, u, v, p)_{inner} = (0.125, 0, 0, 0.14)$, $(\rho, u, v, p)_{outer} = (1.0, 0, 0, 1.0)$ and $\gamma = 1.4$. Symmetry boundary conditions are applied at each side of the domain.

In Fig. 13, density contours are shown for both the initial time step $t = 0$ and the final time step $t = 2.5$ using a resolution of 400^3 cells. We monitored the floating-point representation of the state values in all 48 subdomains and found exact agreement for all simulation times. Furthermore, a jet along each diagonal similar to the one obtained in two dimensions can be detected using a density contour as shown in Fig. 14. Note, that each of the jets consists of six perfectly symmetric parts.

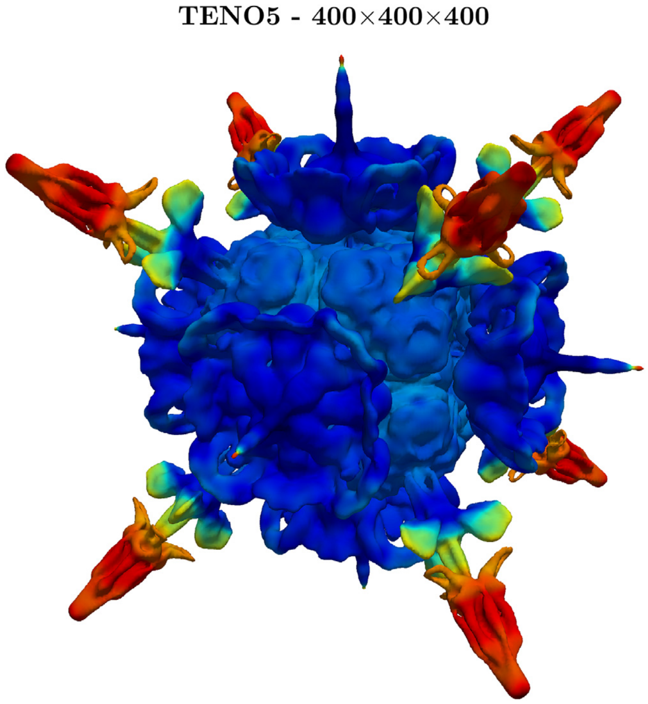

Fig. 14. 3D implosion $t = 2.5$: density contour line for the density value 0.86 colored according to pressure values (blue= 0.8 to red= 1.0). (For interpretation of the references to colour in this figure legend, the reader is referred to the web version of this article.)

6. Conclusion

Various examples of symmetry breaking using low-dissipative schemes are reported in literature. Often this effect is used to judge the quality, i.e. the effect of numerical dissipation, of a scheme. Clearly, high-order discretization schemes with highly resolved meshes allow to decrease numerical viscosity effects considerably. Thus, damping of the inherent physical instabilities in the inviscid Euler equations is now insufficient, and the onset of symmetry breaking with such low-dissipative schemes first is a manifestation of algorithmic imperfections rather than of the low dissipation of the numerical scheme.

We have identified floating-point truncation errors as the main source to trigger these instabilities. Due to their exponential growth the negligibly small initial disturbances grow rapidly during the simulation and may even dominate the final huge-scale topology of the simulation result. We show that such symmetry-breaking is not a physical result of highly accurate high-resolution schemes, but rather the result of algorithmic artifacts such as the lack of associativity, which no longer are hidden by numerical dissipation.

We present implementation strategies to evaluate consistently floating-point arithmetic within a finite volume solver as solution to the prescribed problem. A generalized procedure is provided to guarantee directional independence that allows for maintaining the inherent symmetries as shown for a broad range of test cases both in two and three dimensions. The symmetry of the state variables can now be maintained exactly up to floating-point precision independently of resolution.

The simulation of inviscid or very-large Reynolds number flows with extreme resolutions will become increasingly common with the evolution from peta- to exascaling computing power. In this paper we have addressed an important aspect of the increasing relevance of implementation verification that accompanies this evolution.

Declaration of competing interest

The authors declare that they do not have any conflict of interests.

Acknowledgments

This project has received funding from the European Research Council (ERC) under the European Union's Horizon 2020 research and innovation programme (grant agreement No. 667483). The authors gratefully acknowledge the Gauss Centre for Supercomputing e.V. for funding this project by providing computing time on the GCS Supercomputer SuperMUC at Leibniz Supercomputing Centre.

References

[1] Hadjadj A, Kudryavtsev A. Computation and flow visualization in high-speed aerodynamics. J Turbul 2005;6:N16.
[2] Bermejo-Moreno I, Campo L, Larsson J, Bodart J, Helmer D, Eaton JK. Confinement effects in shock wave/turbulent boundary layer interactions through wall-modelled large-eddy simulations. J Fluid Mech 2014;758:5–62.
[3] Kannan K, Kedelty D, Herrmann M. An in-cell reconstruction finite volume method for flows of compressible immiscible fluids. J Comput Phys 2018;373:784–810.
[4] Meng JC, Colonius T. Numerical simulation of the aerobreakup of a water droplet. J Fluid Mech 2018;835:1108–35.
[5] Shi J, Zhang Y-T, Shu C-W. Resolution of high order WENO schemes for complicated flow structures. J Comput Phys 2003;186(2):690–6.
[6] Cheng T, Lee K. Numerical simulations of underexpanded supersonic jet and free shear layer using WENO schemes. Int J Heat Fluid Flow 2005;26(5):755–70.
[7] Zhang Y-T, Shi J, Shu C-W, Zhou Y. Numerical viscosity and resolution of high-order weighted essentially nonoscillatory schemes for compressible flows with high reynolds numbers. Phys Rev E 2003;68(4):046709.
[8] Harten A, Engquist B, Osher S, Chakravarthy SR. Uniformly high order accurate essentially non-oscillatory schemes, III. J Comput Phys 1987;71(2):231–303.
[9] Liu X-D, Osher S, Chan T. Weighted essentially non-oscillatory schemes. J Comput Phys 1994;115(1):200–12.
[10] Jiang G-S, Shu C-W. Efficient implementation of weighted ENO schemes. J Comput Phys 1996;126(1):202–28.
[11] Zhang P, Wong SC, Shu C-W. A weighted essentially non-oscillatory numerical scheme for a multi-class traffic flow model on an inhomogeneous highway. J Comput Phys 2006;212(2):739–56.
[12] Carrillo JA, Gamba IM, Majorana A, Shu C-W. A WENO-solver for the transients of Boltzmann–poisson system for semiconductor devices: performance and comparisons with monte carlo methods. J Comput Phys 2003;184(2):498–525.
[13] Filbet F, Shu C-W. Approximation of hyperbolic models for chemosensitive movement. SIAM J Sci Comput 2005;27(3):850–72.
[14] Aràndiga F, Belda AM. Weighted ENO interpolation and applications. Commun Nonlinear Sci Numer Simulat 2004;9(2):187–95.
[15] Shu C-W. High order weighted essentially nonoscillatory schemes for convection dominated problems. SIAM Review 2009;51(1):82–126.
[16] Henrick AK, Aslam TD, Powers JM. Mapped weighted essentially non-oscillatory schemes: achieving optimal order near critical points. J Comput Phys 2005;207(2):542–67.
[17] Borges R, Carmona M, Costa B, Don WS. An improved weighted essentially non-oscillatory scheme for hyperbolic conservation laws. J Comput Phys 2008;227(6):3191–211.
[18] Balsara DS, Shu C-W. Monotonicity preserving weighted essentially non-oscillatory schemes with increasingly high order of accuracy. J Comput Phys 2000;160(2):405–52.
[19] Gerolymos G, Sénéchal D, Vallet I. Very-high-order WENO schemes. J Comput Phys 2009;228(23):8481–524.
[20] Balsara DS, Garain S, Shu C-W. An efficient class of WENO schemes with adaptive order. J Comput Phys 2016;326:780–804.
[21] Fu L, Hu XY, Adams NA. A family of high-order targeted ENO schemes for compressible-fluid simulations. J Comput Phys 2016;305:333–59.
[22] Fu L, Hu XY, Adams NA. Targeted ENO schemes with tailored resolution property for hyperbolic conservation laws. J Comput Phys 2017;349:97–121.
[23] Rossinelli D., Hejazialhosseini B., Hadjidoukas P., Bekas C., Curioni A., Bertsch A., et al. 11 PFLOP/S simulations of cloud cavitation collapse. Proceedings of the International Conference on High Performance Computing, Networking, Storage and Analysis2013;:1–13.
[24] Remacle J-F, Flaherty JE, Shephard MS. An adaptive discontinuous Galerkin technique with an orthogonal basis applied to compressible flow problems. SIAM Rev. 2003;45(1):53–72.
[25] Xu Z, Shu C-W. Anti-diffusive flux corrections for high order finite difference WENO schemes. J Comput Phys 2005;205(2):458–85.
[26] Sun Z-S, Luo L, Ren Y-X, Zhang S-Y. A sixth order hybrid finite difference scheme based on the minimized dispersion and controllable dissipation technique. J Comput Phys 2014;270:238–54.
[27] Delin C, Zhongguo S, Zhu H, Guang X. Improvement of the weighted essentially nonoscillatory scheme based on the interaction of smoothness indicators. Int J Numer Methods Fluids 2017;85(12):693–711.
[28] Balsara DS, Dumbser M, Abgrall R. Multidimensional HLLC Riemann solver for unstructured meshes–with application to euler and MHD flows. J Comput Phys 2014;261:172–208.
[29] Sutherland RS. A new computational fluid dynamics code i: Fyris alpha. Astrophys Space Sci 2010;327(2):173–206.
[30] Toro EF. Riemann solvers and numerical methods for fluid dynamics: a practical introduction. Springer Science & Business Media; 2013.
[31] LeVeque RJ. Finite volume methods for hyperbolic problems, 31. Cambridge University Press; 2002.
[32] Gottlieb S, Shu C-W, Tadmor E. Strong stability-preserving high-order time discretization methods. SIAM Rev 2001;43(1):89–112.
[33] Roe PL. Approximate riemann solvers, parameter vectors, and difference schemes. J Comput Phys 1981;43(2):357–72.
[34] Harten A, Lax PD, Leer Bv. On upstream differencing and godunov-type schemes for hyperbolic conservation laws. SIAM Rev 1983;25(1):35–61.
[35] Toro EF, Spruce M, Speares W. Restoration of the contact surface in the HLL-Riemann solver. Shock Waves 1994;4(1):25–34.
[36] Batten P, Clarke N, Lambert C, Causon DM. On the choice of wavespeeds for the HLLC riemann solver. SIAM J Sci Comput 1997;18(6):1553–70.
[37] Hu XY, Adams NA, Shu C-W. Positivity-preserving method for high-order conservative schemes solving compressible euler equations. J Comput Phys 2013;242:169–80.
[38] Johnsen E, Colonius T. Implementation of WENO schemes in compressible multicomponent flow problems. J Comput Phys 2006;219(2):715–32.
[39] Coralic V, Colonius T. Finite-volume WENO scheme for viscous compressible multicomponent flows. J Comput Phys 2014;274:95–121.
[40] Einfeldt B, Munz C-D, Roe PL, Sjögreen B. On godunov-type methods near low densities. J Comput Phys 1991;92(2):273–95.
[41] Qiu J, Shu C-W. On the construction, comparison, and local characteristic decomposition for high-order central WENO schemes. J Comput Phys 2002;183(1):187–209.
[42] Liska R, Wendroff B. Comparison of several difference schemes on 1D and 2D test problems for the euler equations. SIAM J Sci Comput 2003;25(3):995–1017.
[43] Hu X, Wang Q, Adams NA. An adaptive central-upwind weighted essentially non-oscillatory scheme. J Comput Phys 2010;229(23):8952–65.
[44] Schneider EE, Robertson BE. CHOLLA: A new massively parallel hydrodynamics code for astrophysical simulation. Astrophys J Supplement Ser 2015;217(2):24.
[45] Schulz-Rinne CW, Collins JP, Glaz HM. Numerical solution of the Riemann problem for two-dimensional gas dynamics. SIAM J Sci Comput 1993;14(6):1394–414.

A.2 A low dissipation method to cure the grid-aligned shock instability

RightsLink®

Home | Help | Live Chat | Sign in | Create Account

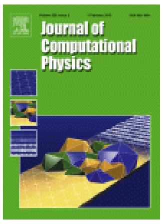

A low dissipation method to cure the grid-aligned shock instability

Author: Nico Fleischmann,Stefan Adami,Xiangyu Y. Hu,Nikolaus A. Adams

Publication: Journal of Computational Physics

Publisher: Elsevier

Date: 15 January 2020

Journal Author Rights

Please note that, as the author of this Elsevier article, you retain the right to include it in a thesis or dissertation, provided it is not published commercially. Permission is not required, but please ensure that you reference the journal as the original source. For more information on this and on your other retained rights, please visit: https://www.elsevier.com/about/our-business/policies/copyright#Author-rights

BACK CLOSE WINDOW

Journal of Computational Physics 401 (2020) 109004

Contents lists available at ScienceDirect

Journal of Computational Physics

www.elsevier.com/locate/jcp

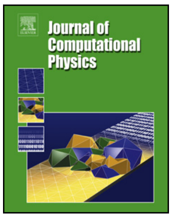

A low dissipation method to cure the grid-aligned shock instability

Nico Fleischmann *, Stefan Adami, Xiangyu Y. Hu, Nikolaus A. Adams

Technical University of Munich, Department of Mechanical Engineering, Chair of Aerodynamics and Fluid Mechanics, Boltzmannstraße 15, 85748 Garching, Germany

ARTICLE INFO

Article history:
Received 30 January 2019
Received in revised form 28 September 2019
Accepted 1 October 2019
Available online 4 October 2019

Keywords:
Shock instability
Carbuncle phenomenon
Low Mach number effect
Low-dissipation schemes
WENO
Shock-capturing

ABSTRACT

The grid-aligned shock instability prevents an accurate computation of high Mach number flows using low-dissipation shock-capturing methods. In particular one manifestation, the so-called carbuncle phenomenon, has been investigated by various different groups over the past decades. Nevertheless, the mechanism of this instability is still not fully understood and commonly is suppressed by the introduction of additional numerical dissipation. However, present approaches may either significantly deteriorate the resolution of complex flow evolutions or involve additional procedures to limit stabilization measures to the shock region.

Instead of increasing the numerical dissipation, in this paper, we present an alternative approach that relates the problem to the low Mach number in transverse direction of the shock front. We show that the inadequate scaling of the acoustic dissipation in the low Mach number limit is the prime reason for the instability. Our approach is to increase the "numerical" Mach number locally whenever the advection dissipation is small compared to the acoustic dissipation. A very simple modification of the eigenvalue calculation in the Roe approximation leads to a scheme with *less numerical dissipation than the original Roe flux* which prevents the grid-aligned shock instability. The simplicity of the modification allows for a detailed investigation of multidimensional effects. By showing that modifications in flow direction affect the shock stability in the transverse directions we confirm the multidimensional nature of the instability. The efficiency and robustness of the modified scheme is demonstrated for a wide range of test cases that are known to be particularly prone to the shock instability. Moreover, the modified flux also is successfully applied to multi-phase flows.

1. Introduction

Modern applications of computational fluid dynamics involve complex interactions across scales such as shock interactions with turbulent structures and multiphase interfaces [1,2]. In the last decades, a variety of different numerical approaches were developed aiming at schemes that combine high accuracy and high robustness [3]. Shock capturing methods based on Godunov's approach [4] nowadays are among the most successful methods for simulating compressible flows

---

* Corresponding author.
E-mail addresses: nico.fleischmann@tum.de (N. Fleischmann), stefan.adami@aer.mw.tum.de (S. Adami), xiangyu.hu@tum.de (X.Y. Hu), nikolaus.adams@tum.de (N.A. Adams).

https://doi.org/10.1016/j.jcp.2019.109004

involving shock waves and other discontinuities. Their versatility and ease of implementation make them advantageous over shock tracking methods, especially when new shock waves emerge during the simulation. Following Godunov's approach [4], cell-face fluxes are determined by Riemann problems, which can be solved locally. The popularity of the method is based on its straightforward extension to high-order reconstruction schemes, such as ENO [5] or WENO [6] schemes. Originally the exact Riemann solution was computed iteratively, which soon was replaced by more efficient approximate Riemann solvers.

Numerous approximate flux formulations have been developed in the past. They can be categorized roughly as complete and incomplete. Incomplete fluxes, such as e.g. HLL [7] or HLLE [8] solver, typically are more robust, at the expense of allowing only for a limited number of waves. Contact discontinuities usually are not captured explicitly, which often leads to unacceptable smearing of contact lines. Complete fluxes model explicitly each of the relevant waves of the underlying problem, e.g. for the three-dimensional Euler equations five waves are modeled including the contact discontinuity. Popular examples of complete Riemann approximations are HLLC [9], the Osher approximation [10] and the Roe approximation [11]. Upon combining complete Riemann solvers with high-order reconstruction schemes a minimum amount of numerical dissipation can be obtained. Such a low numerical dissipation is crucial for the accurate calculation of flow instabilities and wave transport. Despite the enormous effort spent on the development of approximate Riemann solvers, which enables the accurate simulation of various complex flow configurations, the design of an all-purpose low-dissipation high-resolution Riemann solver remains to be a challenge.

It turned out that a promising group of complete Riemann solvers fails spectacularly on certain flow configurations involving supersonic shock waves [12]. Since Peery and Imlay [13] first described their observation on the failure of the Roe flux approximation when applied to supersonic flows around a blunt body, intense research was devoted to discovering reasons and cures for this undesirable behavior. An instability, first reported in [13], leads to a characteristic deformation of the shock front which was called "carbuncle phenomenon" due to its excrescence-like appearance. The carbuncle phenomenon ruined many efforts to compute grid-aligned shock waves using low-dissipation upwind schemes. Quirk [12] presented a catalogue of cases where Godunov type schemes were known to fail. Three of the problems he reported, namely the carbuncle phenomenon, the kinked Mach stem of a double Mach reflection and a newly described odd-even decoupling problem have in common that they develop most prominently when a high Mach number shock wave propagates aligned with the computational grid. Quirk [12] noticed that some schemes possessing good shock capturing properties are more likely to be affected by such instabilities than more dissipative flux formulations, such as the HLLE Riemann solver. Quirk [12] concluded that insufficient dissipation at the contact line might be the reason for the instability. A large number of scientific publications since have addressed various aspects of the challenging problem. Although not being fully understood, it is generally believed that the prime reason for the shock instability is insufficient numerical dissipation in the region of the shock front.

The most popular approach to cure the instability is to increase locally the numerical dissipation of the underlying scheme. Peery and Imlay [13] achieved such a stabilization by smoothing the Roe eigenvalues, resulting in a bow shock smearing over several cells. Quirk [12] noted that the ad-hoc application of Harten's entropy fix to increase numerical dissipation of the contact and shear waves cures the problem, has, however, no physical justification. Sanders et al. [14] performed a linear analysis that revealed that the instability is caused by an insufficient cross-flow dissipation. They proposed a multi-dimensional modification to the Roe solver, where they apply an entropy fix that depends on neighboring interfaces. Due to the spatial arrangement of the incorporated interfaces the method is called H-correction. Later, Pandolfi and D'Ambrosio [15] modified the H-correction for the application to high-speed flow boundary layers. Both the analyses of Gressier and Moschetta [16] and Pandolfi and D'Ambrosio [15] investigated the behavior of different families of approximate Riemann solvers concerning the shock instability. They concluded that schemes that explicitly capture a contact discontinuity are always to some extent prone to the grid-aligned shock instability. Liou [17] found that the dissipative pressure term in the mass flux is responsible for the instability, which motivated him to design new schemes that are both stable and able to capture contact discontinuities. The conclusion of [17] that schemes with a mass flux that is independent of the pressure term are not affected by the carbuncle phenomenon (Liou's conjecture) was questioned by other authors [16,15,18]. They provided counterexamples including the AUSM$^+$ scheme [19]. Ren [20] developed a shock-stable scheme based on a rotated Roe flux formulation, which automatically introduces artificial dissipation in the relevant regions. Although his approach does not require an explicit detection procedure, there is a computational overhead since the Riemann problem has to be solved twice on every cell interface. Kim et al. [21] introduced an improved Roe scheme that is capable of accurately resolving contact discontinuities and is free of the shock instability. The authors of [21] introduced a Mach-number-based function that controls the feeding rate of pressure fluctuation into the numerical mass flux. More recently, Chen et al. [22] followed a similar approach to stabilize the Roe scheme by introducing shear viscosity into the momentum flux, controlled by a pressure-based sensing function to constrain the effect to the shock region. They noticed that the instability of the Roe scheme may not be caused by the pressure difference, but by inadequate shear viscosity. All procedures described so far have in common that they increase the dissipation of the Roe scheme in one way or another. Similar procedures have been developed for other types of Riemann solvers, e.g. for HLLC [23–25] or AUSM [26,27].

An alternative approach is using hybrid schemes where Riemann solvers of different families are combined. The appropriate scheme is chosen locally based on a control function that evaluates the local flow condition. Quirk [12] combined a Roe scheme with an HLL scheme and obtained good results. However, the control function involves problem-dependent parameter calibration and the overall scheme still is stabilized by local application of a more dissipative scheme. Rodionov [28] argued that the exact Riemann solver is physically the most consistent way to determine inviscid fluxes, however, the introduction of additional numerical dissipation moves the approximate solution further apart from the exact Riemann problem. Thus, he presented a new approach where the problem is not solved by corrections to the Riemann solver but by introducing an artificial viscosity similar to the molecular viscosity present in the Navier-Stokes equations. This approach is independent of the applied Riemann solver.

The present work relates the grid-aligned shock instability to another well-known difficulty of Godunov-type schemes in the low Mach number limit. Guillard et al. [29,30] performed an asymptotic analysis in terms of powers of the Mach number, which revealed an incorrect scaling behavior of pressure fluctuations when Godunov schemes are applied at vanishing Mach number. For a shock wave in the solution of a multi-dimensional high-Mach-number flow propagating in one direction of the underlying Cartesian grid, the disturbances parallel to the shock front travel at a low relative Mach number. For the Roe flux formulation the dissipative flux term in this case is dominated by the acoustic contribution, while the dissipation due to advection vanishes. We show two possible solution strategies to balance both contributions, and thus increase the Mach number for the calculation of the eigenvalues that determine the dissipative flux term. A locally decreased acoustic dissipation leads to an overall decrease of dissipation of the numerical scheme, while a locally increased advection dissipation leads to an overall increase of dissipation. The fundamental difference between our approach as opposed to previous attempts is that we cure the grid-aligned shock instability by a local *decrease of dissipation*. The implementation of our method into an existing Riemann solver is straightforward as it amounts to only few additional lines of code.

The remainder of the paper is organized as follows. In Section 2, the governing equations and the basic principles of Godunov-type methods are reviewed together with the flux formulations of the Roe approximation and a componentwise local Lax-Friedrichs approximation. The modifications made on the original schemes considering the low Mach number effect are presented in detail in Section 3. In Section 4, Quirk's odd-even decoupling case is investigated both qualitatively and quantitatively to demonstrate the robustness of the modified Roe flux. A demonstration of the multidimensional character of the carbuncle phenomenon is presented in Section 5. Finally in Section 6, the effectiveness of the low Mach number treatment is demonstrated for the full set of relevant test cases that are commonly referred to by literature addressing the grid-aligned shock instability. Conclusions are drawn in Section 7.

2. Governing equations and numerical approach

We consider an inviscid compressible flow that evolves according to the three-dimensional Euler equations

$$\mathbf{U}_t + \mathbf{F}(\mathbf{U})_x + \mathbf{G}(\mathbf{U})_y + \mathbf{H}(\mathbf{U})_z = 0, \tag{1}$$

where $\mathbf{U}$ is the density of the conserved quantities mass ρ, momentum $\rho\mathbf{v} \equiv (\rho u, \rho v, \rho w)$ and total energy $E = \rho e + \frac{1}{2}\rho\mathbf{v}^2$, with e being the internal energy per unit mass. The fluxes $\mathbf{F}$, $\mathbf{G}$ and $\mathbf{H}$ are defined as

$$\mathbf{F} = \begin{pmatrix} \rho u \\ \rho u^2 + p \\ \rho uv \\ \rho uw \\ u(E+p) \end{pmatrix}, \quad \mathbf{G} = \begin{pmatrix} \rho v \\ \rho uv \\ \rho v^2 + p \\ \rho vw \\ v(E+p) \end{pmatrix}, \quad \mathbf{H} = \begin{pmatrix} \rho w \\ \rho uw \\ \rho vw \\ \rho w^2 + p \\ w(E+p) \end{pmatrix}. \tag{2}$$

The set of equations is closed by the ideal-gas equation of state, where the pressure p is given by $p = (\gamma - 1)\rho e$ with a constant ratio of specific heats γ.

2.1. Finite volume approach

We apply Godunov's approach for finite volumes to solve this set of equations numerically. This procedure is widely used for hyperbolic equations. The time evolution of the vector of cell-averaged conservative states $\bar{\mathbf{U}}$ is given by

$$\frac{d}{dt}\bar{\mathbf{U}}_i = \frac{1}{\Delta x}(\mathbf{F}_{i-\frac{1}{2},j,k} - \mathbf{F}_{i+\frac{1}{2},j,k} + \mathbf{G}_{i,j-\frac{1}{2},k} - \mathbf{G}_{i,j+\frac{1}{2},k} + \mathbf{H}_{i,j,k-\frac{1}{2}} - \mathbf{H}_{i,j,k+\frac{1}{2}}), \tag{3}$$

where $\mathbf{F}$, $\mathbf{G}$ and $\mathbf{H}$ approximate the cell-face fluxes in x-, y- and z-direction, respectively. These fluxes are determined dimension-by-dimension from an approximate Riemann solver combined with a fifth-order WENO [6] spatial reconstruction scheme. Additional volume source terms, such as gravitational acceleration, are omitted here for simplicity. The resulting ODE (3) is integrated in time using a third-order strong stability-preserving (SSP) Runge-Kutta scheme [31].

2.2. Approximate Riemann solvers

The majority of state-of-the-art methods relies on approximate Riemann solvers since exact Riemann solvers are computationally expensive. Moreover, exact Riemann solvers are not helpful to suppress the carbuncle phenomenon since they are likewise affected by the shock instability [12]. Here, we focus on two approximate flux formulations, the classical Roe flux [11] and a componentwise local Lax-Friedrichs flux [6]. The Roe flux formulation is known to be particularly vulnerable to the carbuncle phenomenon. Its low numerical dissipation and its ability to capture contact waves accurately is generally believed to be the reason for this deficiency. The componentwise local Lax-Friedrichs flux is only slightly more dissipative and therefore similarly affected by the instability as the numerical examples in Sec. 4 and Sec. 6 demonstrate. Although both the Roe flux and the componentwise local Lax-Friedrichs flux are not positivity preserving in general, the latter one delivers numerically stable results in many flow conditions, where the Roe flux fails. In the following, only the x-direction is discussed. Due to the dimension-by-dimension approach, the other directions are handled the same way.

2.2.1. Roe Riemann flux

The classical Roe formulation gives the following numerical flux function

$$\mathbf{F}_{i+1/2}^{Roe} = \frac{1}{2}\left(\mathbf{F}_{i+1} + \mathbf{F}_i\right) - \frac{1}{2}\mathbf{R}_{i+1/2}\left|\mathbf{\Lambda}_{i+1/2}\right|\mathbf{R}_{i+1/2}^{-1}\left(\mathbf{U}_{i+1} - \mathbf{U}_i\right) \tag{4}$$

where $\mathbf{R}$ and $\mathbf{R}^{-1}$ are the right and the left eigenvector matrices of the Jacobian $\partial\mathbf{F}/\partial\mathbf{U}$, and $\mathbf{\Lambda}$ is the diagonal matrix formed with the eigenvalues

$$\lambda_1 = \hat{u} - \hat{c}, \qquad \lambda_{2,3,4} = \hat{u}, \qquad \lambda_5 = \hat{u} + \hat{c}. \tag{5}$$

Quantities with hat-notation "$\hat{.}$" denote density-based Roe averages

$$\hat{k} = \frac{\bar{k}_i \cdot \sqrt{\rho_i} + \bar{k}_{i+1} \cdot \sqrt{\rho_{i+1}}}{\sqrt{\rho_i} + \sqrt{\rho_{i+1}}} \tag{6}$$

where k has to be replaced by the quantity of interest, e.g. u. $\bar{k}_i$ and $\bar{k}_{i+1}$ are the cell-averaged variables of the cells adjacent to the cell face $i + 1/2$. No entropy-fix is applied for all computations in this paper.

The high-order spatial WENO reconstruction is performed in characteristic space using a finite difference formulation both on

$$\mathbf{F}_{i+1/2}^{+} = \mathbf{F}_i + \mathbf{R}_{i+1/2}\left|\mathbf{\Lambda}_{i+1/2}\right|\mathbf{R}_{i+1/2}^{-1}\mathbf{U}_i \tag{7}$$

and

$$\mathbf{F}_{i+1/2}^{-} = \mathbf{F}_{i+1} - \mathbf{R}_{i+1/2}\left|\mathbf{\Lambda}_{i+1/2}\right|\mathbf{R}_{i+1/2}^{-1}\mathbf{U}_{i+1}. \tag{8}$$

The final flux is obtained by

$$\mathbf{F}_{i+1/2}^{Roe} = \frac{1}{2}\left(\mathbf{F}_{i+1/2}^{+} + \mathbf{F}_{i+1/2}^{-}\right). \tag{9}$$

2.2.2. Componentwise local Lax-Friedrichs flux

The only difference between the Roe flux and the componentwise local Lax-Friedrichs flux (cLLF) is the choice of eigenvalues $\mathbf{\Lambda}$ in Eq. (4). While density-based Roe averages are applied for the Roe flux, the eigenvalues in the componentwise local Lax-Friedrichs flux are determined by

$$\begin{aligned}
|\lambda_1| &= \max\left(|u_i - c_i|, |u_{i+1} - c_{i+1}|\right), \\
\left|\lambda_{2,3,4}\right| &= \max\left(|u_i|, |u_{i+1}|\right), \\
|\lambda_5| &= \max\left(|u_i + c_i|, |u_{i+1} + c_{i+1}|\right).
\end{aligned} \tag{10}$$

Note that $\mathbf{R}$ and $\mathbf{R}^{-1}$ are identical for both flux formulations. Compared to the original local Lax-Friedrichs flux, often called Rusanov flux, this definition has different eigenvalues for each characteristic field. Thus, the cLLF flux is still close to the Roe flux with only slightly increased numerical dissipation.

2.2.3. Note on numerical dissipation

The flux formulation given in Eq. (4) has two parts. The first term on the right-hand-side is the central flux term, and the second term is the dissipative flux term. Since $\mathbf{R}$ and $\mathbf{R}^{-1}$ are only forward and backward coordinate transformations, the dissipative flux merely depends on $\mathbf{\Lambda}$. Again, two different contributions to the dissipative flux can be distinguished. The advection dissipation is proportional to $|u|$, while the acoustic dissipation is proportional to $|u \pm c|$. This distinction might be helpful to understand the proposed cure of the shock instability.

3. A modified flux formulation

We relate the grid-aligned shock instability to another well-known difficulty of Godunov schemes in the low Mach number limit. The connection can be deduced from the observation that the instability only occurs when the shock front moves aligned with the computational grid. For Cartesian grids, this situation involves vanishing but non-zero velocity components in spatial directions other than the shock propagation direction for cells covering the shock front. Note that a perfect alignment leads to a purely one dimensional situation and no instability occurs. A small deflection is always required to trigger the instability.

The asymptotic analysis on the Roe flux and general Godunov schemes by Guillard et al. [29,30] revealed that the centered terms of the flux formulations are of order $\mathcal{O}(1/M^2)$, while the dissipative terms are of order $\mathcal{O}(1/M)$ for low Mach numbers. Thus, even if the initial pressure contains fluctuations of order $\mathcal{O}(M^2)$, the dissipative flux term will lead to pressure fluctuations of order $\mathcal{O}(M)$ when $M \to 0$. These pressure fluctuations are mostly of acoustic origin due to the fact that, for vanishing Mach numbers, the acoustic contribution to the numerical dissipation is much larger than that of the advection.

The main goal of the proposed modifications therefore is to balance the advective and acoustic dissipation in the low Mach number limit.

3.1. A modified Roe-M flux

A straightforward way to decrease the imbalance of advective and acoustic dissipation and consequently to avoid the amplification of present pressure disturbances is to increase the Mach number value M in $\mathbf{\Lambda}$.

In case of the Roe flux, this can either be done by decreasing the acoustic dissipation

$$\lambda'_{1,5} = \hat{u} \pm \min\left(\phi \left|\hat{u}\right|, \hat{c}\right), \qquad \lambda'_{2,3,4} = \hat{u} \tag{11}$$

or by increasing the advection dissipation

$$\lambda''_{1,5} = u'' \pm \hat{c}, \qquad \lambda''_{2,3,4} = u'', \qquad u'' = \operatorname{sgn}(\hat{u}) \cdot \max\left(\frac{\hat{c}}{\phi}, \left|\hat{u}\right|\right) \tag{12}$$

where ϕ is a positive number of order $\mathcal{O}(1)$. Thus, the Mach number is limited to a value of $1/\phi$. It is important to notice that both formulations do not change the eigenvector matrix nor the central flux term, although both modifications lead to comparable acoustic and advection contributions to the numerical dissipation in the low Mach number direction of the flow. While the Roe flux with Eq. (12) increases the total local numerical dissipation, the Roe flux with Eq. (11) decreases it. In the context of globally low Mach number flows, Li and Gu [32] developed a similar procedure. They proposed an All-Speed-Roe scheme that involves a momentum interpolation in the central flux term and a more complex adjustment of the sound speed in the low Mach number limit with similar effect as Eq. (11). Here, a stabilizing momentum interpolation is not required since the purpose of our method is to cure grid-aligned shock instabilities which never occur in flows with globally low Mach number.

There are many different methods in literature that cure the shock instability by *increasing* the numerical dissipation. To the knowledge of the authors, however, there is no approach that achieves this goal by *further reducing the dissipation* of the already low-dissipation Roe flux. Thus, we will focus on the modification with eigenvalues determined by Eq. (11) throughout the paper, even though both formulations by Eq. (11) or Eq. (12) are effective to prevent the grid-aligned shock instability. The Roe flux with low Mach number treatment will be denoted Roe-M in the following.

3.2. A modified componentwise LLF-M flux

The same procedure of decreasing the acoustic dissipation applied to the componentwise local Lax-Friedrichs flux leads to eigenvalues

$$\begin{aligned}
\left|\lambda'_1\right| &= \max\left(\left|u_i - c'_i\right|, \left|u_{i+1} - c'_{i+1}\right|\right), \\
\left|\lambda'_{2,3,4}\right| &= \max\left(\left|u_i\right|, \left|u_{i+1}\right|\right), \\
\left|\lambda'_5\right| &= \max\left(\left|u_i + c'_i\right|, \left|u_{i+1} + c'_{i+1}\right|\right),
\end{aligned} \tag{13}$$

with

$$c'_{i,i+1} = \min\left(\phi \left|u_{i,i+1}\right|, c_{i,i+1}\right). \tag{14}$$

The componentwise local Lax-Friedrichs flux with low Mach number treatment will be denoted cLLF-M in the following.

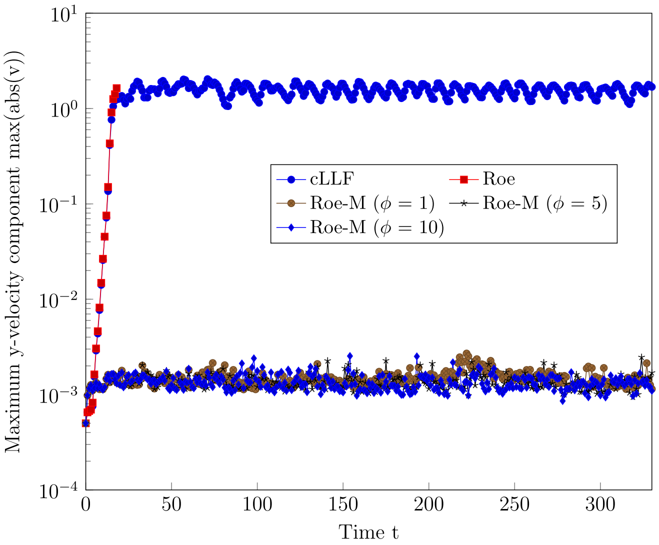

Fig. 1. Instability progress in Quirk's test case with $Ma = 6$.

4. Properties of the modified flux

In the following, a plane shock propagation along a rectangular duct with a defined disturbance level parallel to the shock propagation is considered to demonstrate the capabilities of the modified Roe flux, and to show the impact of the parameter ϕ on the shock stability property.

This test case was introduced by Quirk [12] as a minimal working example for the odd-even decoupling phenomenon. Despite its simplicity it is an efficient and reliable way to trigger the instability in combination with different numerical flux formulations. The rise of the instability can easily be investigated both qualitatively and quantitatively. The shock propagation is simulated on a domain of $[0, 2400] \times [0, 20]$ discretized with 2400×20 cells. Pre-shock density and pressure are set to unity, and all velocity components are set to zero. Originally, the disturbance was triggered by an odd-even offset of the center-line grid position, whereas we follow the approach of Kemm [33] and introduce artificial numerical noise to the primitive variables in the initial state since the computations are done with a Cartesian-coordinate formulation. Inflow and outflow conditions are applied at the left and at the right boundary, respectively. Symmetry boundary conditions, which are equivalent to reflecting wall conditions, are enforced both at the top and at the bottom boundary of the domain. We have performed simulations with the original $Ma = 6$ setup and with a more challenging $Ma = 20$ setup with initial conditions given by

$$(\rho, u, v, p) = \begin{cases} (1, 0, 0, 1) & \text{if } x > 5.0 \\ \left(\frac{216}{41}, 35\frac{\sqrt{35}}{36}, 0, \frac{251}{6}\right) & \text{else (for } Ma = 6 \text{ case)}, \\ \left(\frac{160}{27}, \frac{133}{8}\sqrt{1.4}, 0, 466.5\right) & \text{else (for } Ma = 20 \text{ case)}, \end{cases} \tag{15}$$

where the shock front is placed initially at $x = 5$. In order to monitor the growth rate of the disturbance quantitatively over time the maximum magnitude of the y-velocity component is evaluated in the whole domain as a measure of the deviation from the one-dimensional solution.

Fig. 1 shows the evolution of the velocity deviation for the $Ma = 6$ case when all initial primitive variables are superposed by uniform random perturbations ranging from $-0.5 \cdot 10^{-3}$ to $0.5 \cdot 10^{-3}$. Color maps of density and velocity for different flux formulations are presented in Fig. 2. Note that minimum and maximum color values are chosen with respect to extreme values within the carbuncle. As expected, the classical Roe flux shows an exponential instability that results in a carbuncle-like distortion of the shock front, see Fig. 2 left. The instability manifests itself most prominently by a significant rise of the velocity magnitude in the carbuncle region. The componentwise local Lax-Friedrichs flux behaves similarly as the Roe flux, with the difference that the simulation does not break due to a floating point exception. Instead the disturbance level remains bounded after amplification by three orders of magnitude until the end of the simulation, see Fig. 2 center. All Roe-type schemes with low Mach number treatment behave stable. Values of ϕ within a reasonable range between 1 and 10 show comparable results. Note that the simulation is performed up to a very late point in time, where the shock front, given in the right frame of Fig. 2, has already passed $x = 2300$ without showing any non-physical behavior.

The same procedure has also been applied for a stronger shock with $M = 20$. Fig. 3 shows the resulting velocity deviations. The error growth rate for the classical Roe and componentwise local Lax-Friedrichs scheme increases noticeably, whereas deviations for the modified Roe fluxes remain bounded. The classical Roe scheme breaks after very few time steps for the increased Mach number. The final density distribution of the componentwise local Lax-Friedrichs flux as shown in

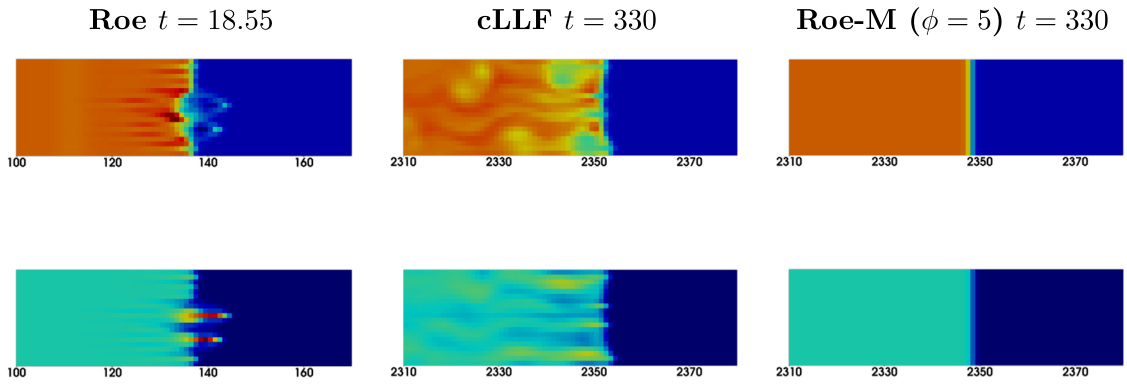

Fig. 2. Quirk's test case with $Ma = 6$, (top) color map of density from dark blue = 0.5 to red = 6.8, (bottom) color map of velocity magnitude from dark blue = 0 to red = 14.5. (For interpretation of the colors in the figure(s), the reader is referred to the web version of this article.)

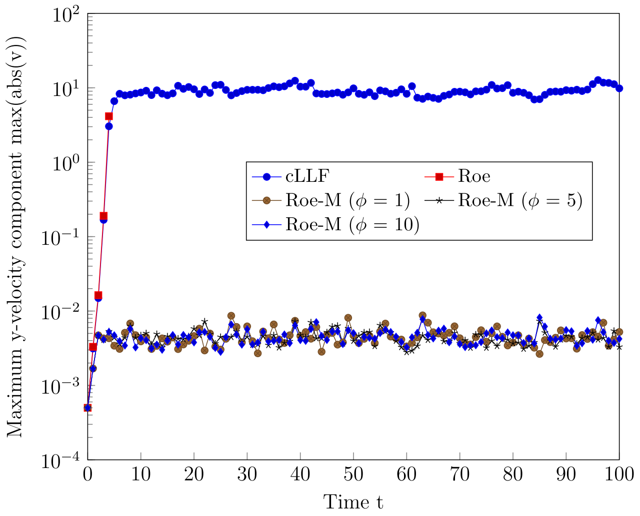

Fig. 3. Instability progress in Quirk's test case with $Ma = 20$.

Fig. 4 reveals that the shock wave is not only severely disturbed, but also moves with an incorrect wave speed. Instead, the analytically expected position of the shock front is recovered by the modified Roe flux. Again, the result obtained by the modified scheme shows no sign of an instability.

5. Note on the multidimensionality of the shock instability

It is known that purely one-dimensional cases are not affected by the grid-aligned shock instability unless they are formulated in two dimensions. Following the argumentation of Sec. 3, this behavior can now be explained as we have identified the pressure fluctuation induced by the low Mach number of the transverse direction to be the driving force of the instability. The Roe approximation relies upon a finite-difference approach that consists of a dimension-by-dimension evaluation of the numerical flux contributions. This allows for a selective application of the low Mach number modification to fluxes in specific coordinate directions. Thus, it should be possible to cure the instability only along pre-selected coordinate directions. We expect the stability to be cured for shocks moving aligned to the grid in y-direction when the modified flux is applied in x-direction and vice versa.

Due to its symmetry a Sedov blast wave problem is well-suited for demonstration. For this test case, a high pressure area with $P^{inner} = 3.5 \cdot 10^5$ is initiated at the center of the domain that covers exactly one cell in each of the four quadrants. The rest of the domain is set to a near vacuum state with $P^{outer} = 10^{-10}$. Density is set to unity and both velocity components are set to zero in the whole domain. Reflecting-wall conditions are applied at all boundaries. The domain is set to $[0, 2.4] \times [0, 2.4]$ with 480×480 cells.

Fig. 5 shows the pressure distribution at $t = 0.1$ for both the original and the modified Roe scheme. While for the original Roe flux four distinct carbuncles have established at each location where the shock front moves aligned to the grid, the Roe-M flux is able to prevent the occurrence of the carbuncles effectively and maintains a sharp shock front everywhere. Now, the low Mach number modification is only applied for fluxes in x-direction, respectively in y-direction. The results given in Fig. 6 confirm exactly our expectations.

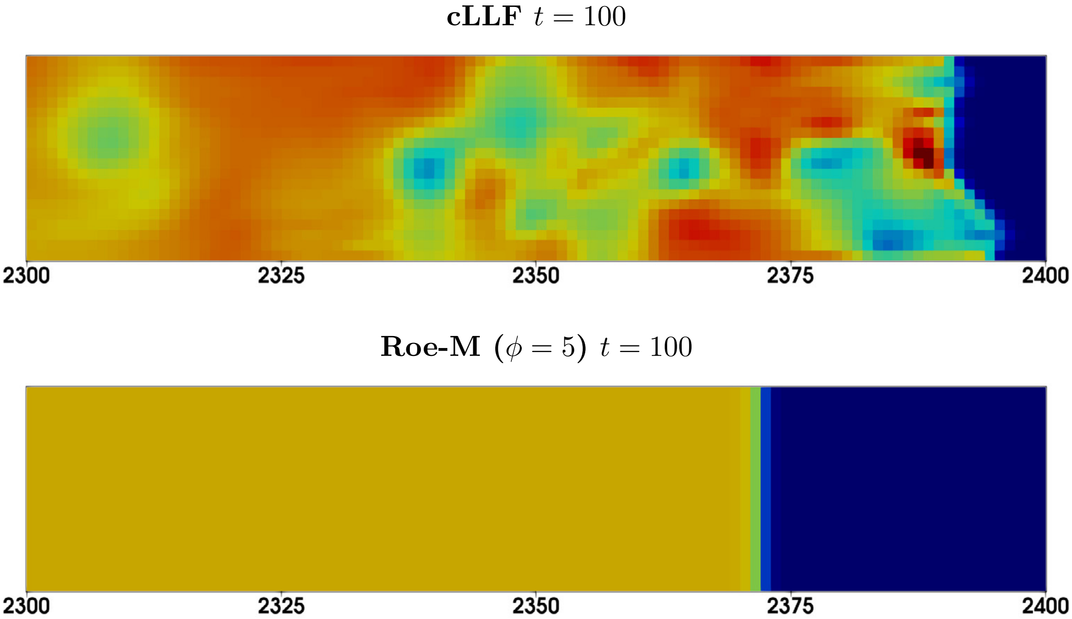

Fig. 4. Quirk's test case with $Ma = 20$, color map of density from dark blue = 1.0 to red = 8.0.

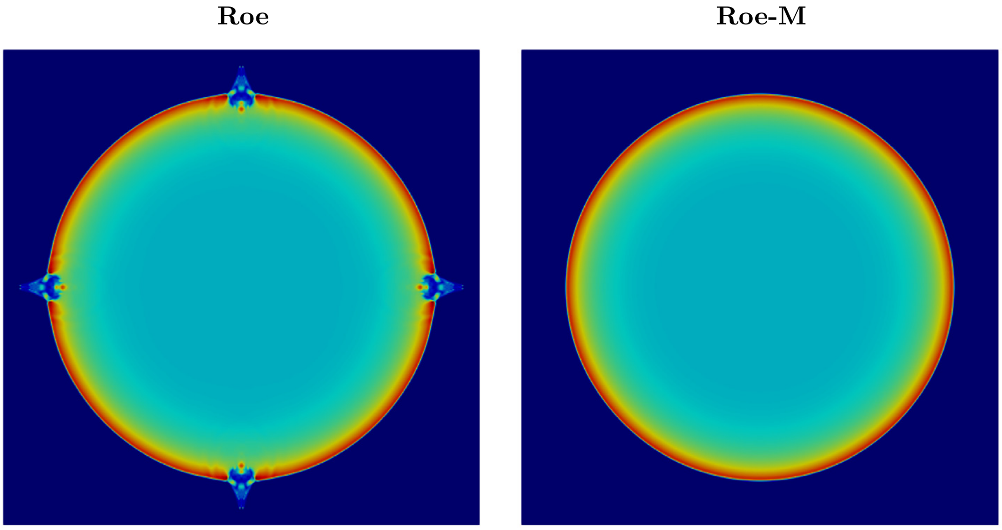

Fig. 5. Two dimensional Sedov blast wave at $t = 0.1$: color map of pressure from blue = 0 to red = 22.0.

The cure of the flux in one direction affects the stability of shocks moving in the other direction. Actually, the application of the modification in y-direction is sufficient to stabilize the odd-even decoupling case presented in Sec. 4 where the shock front moves in x-direction. Three-dimensional calculations of the Sedov blast wave show stable results only when the flux modification is applied at least to both other directions. Thus, the grid-aligned shock instability is a true multidimensional phenomenon.

6. Numerical results

In this section, we investigate a wide range of test problems that are known to suffer from the shock instability. Together with Quirk's odd-even decoupling and the Sedov blast wave, which were presented in the previous sections, the classical set of test cases consists of the double Mach reflection problem [34], the 90 degree corner flow problem [12], the flow around a blunt body [13] and the "physical" carbuncle set-up of Elling [35]. Additionally, we will consider two multi-phase cases, where we encountered carbuncle-like instabilities during a shock-interface interaction both with air/helium and water/air.

If not mentioned otherwise, calculations were performed using the classical fifth-order WENO scheme [6] combined with a third-order strong-stability-preserving Runge-Kutta time integration [31]. Whenever the problem does not rely on positivity preservation, we apply a Roe flux [11] and its low Mach number modification, otherwise the componentwise local Lax-Friedrichs [6] and the corresponding low Mach number modification are employed. The ϕ-value is always set to

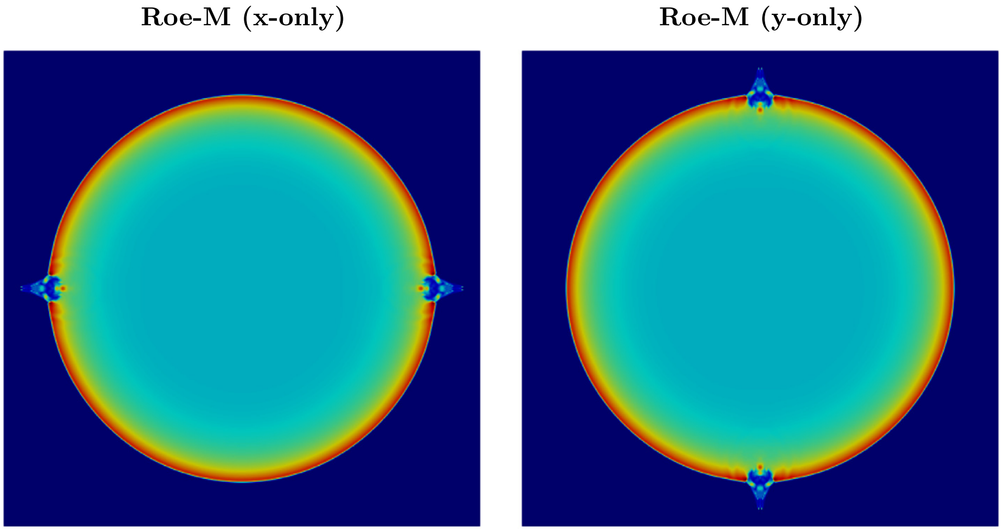

Roe-M (x-only) Roe-M (y-only)

Fig. 6. Two dimensional Sedov blast wave at $t = 0.1$: color map of pressure from blue = 0 to red = 22.0.

5. A level-set approach [36] is applied for multi-phase cases. The CFL number is set 0.6 for single-phase cases and 0.4 for cases that involve the level-set approach. The material is modeled as ideal gas with $\gamma = 1.4$.

6.1. Double Mach reflection problem

The problem of Woodward and Colella [34] on the double Mach reflection is a popular benchmark test for the quality of a Riemann solver. It consists of a shock front that hits a ramp that is inclined by 30 degrees. Shock unstable schemes such as e.g. the Roe approximation may produce an artificially kinked Mach stem as described by various authors [12,28,33].

The initial conditions for a Mach 10 shock wave are

$$(\rho, u, v, p) = \begin{cases} (1.4, 0, 0, 1) & \text{if } y < \sqrt{3}\,(x - 1/6) \\ \left(8, 33\frac{\sqrt{3}}{8}, -4.125, 116.5\right) & \text{else,} \end{cases} \tag{16}$$

and the final time is set to $t = 0.2$. While the computational domain typically is chosen as $[0, 4] \times [0, 1]$, here, we use an even larger domain of $[0, 4] \times [0, 7]$ to avoid any boundary effects of the shock wave moving along the upper boundary. The domain is discretized with 960×1680 cells. A Neumann boundary condition with zero gradients for all variables is applied at the left, right and upper boundary. Along the bottom boundary, at $y = 0$, the region from $x = 0$ to $x = 1/6$ is always assigned post-shock conditions, whereas reflecting-wall conditions are imposed from $x = 1/6$ to $x = 4$.

The problem of the kinked Mach stem is usually presented for low-order schemes. However, high-order schemes are likewise affected if the resolution is increased. The calculations are carried out with a fifth-order WENO-Z [37] scheme. Note, that the classical Roe flux is not able to deliver numerically stable results due to the instability at the leading Mach stem. Thus, the reference result is obtained using the componentwise local Lax-Friedrichs scheme. As shown in the top frame of Fig. 7, the componentwise local Lax-Friedrichs flux suffers from a kinked Mach stem, a typical configuration of the carbuncle phenomenon. The modified Roe flux with even less numerical dissipation than the original Roe flux is able to produce numerically stable and correct results, see bottom of Fig. 7.

6.2. Supersonic corner flow

Another well-known test case, which was already described by Quirk [12] in the context of shock instability, is the diffraction of a shock wave around a sharp corner. This problem yields complicated flow patterns and many schemes encounter the situation of odd-even decoupling in parts of the flow where the shock wave is aligned to the grid. The instability occurs in particular when the mesh is highly refined.

We use a domain of size $[0, 1] \times [0, 1]$, that is uniformly initialized with $(\rho, u, v, p) = (1, 0, 0, 1/1.4)$. Reflecting-wall boundary conditions are set everywhere, except of the upper left boundary at $x = 0$ from $y = 0.5$ to $y = 1$. Here, the post-shock condition of a Mach 5.09 shock wave is prescribed. The final time is set to $0.8/Ma$. The original Roe flux is known to produce both numerically unstable results due to the positivity violation at the cells near the corner and non-physical results due to a rarefaction shock wave that establishes in the flow behind the corner [12]. Thus, the reference solution is again obtained using the componentwise local Lax-Friedrichs flux combined with a third-order WENO scheme [6].

The left frame of Fig. 8 shows a schlieren image of density gradients at the end of the simulation. The non-physical odd-even decoupling along the upper part of the shock front is clearly visible. Since the modified Roe flux only affects

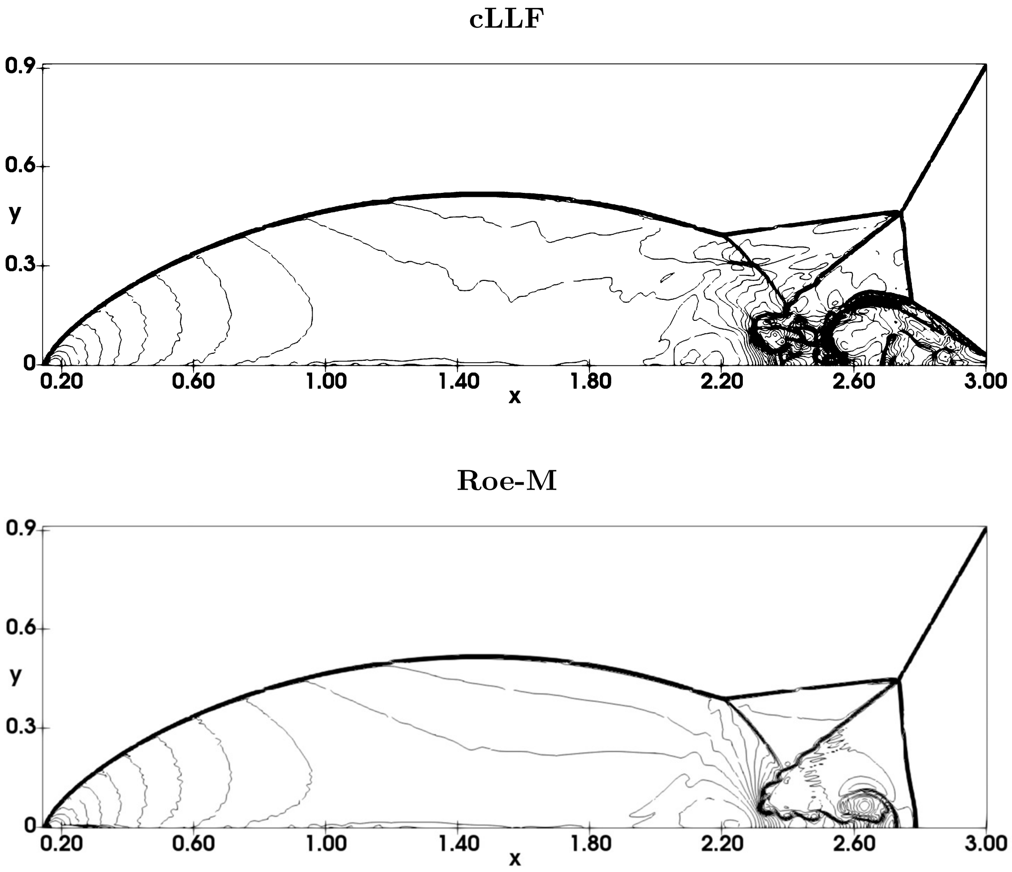

Fig. 7. Double Mach reflection of a Mach 10 shock wave: 40 density contours from 1.88783 to 20.9144 at $t = 2.0$.

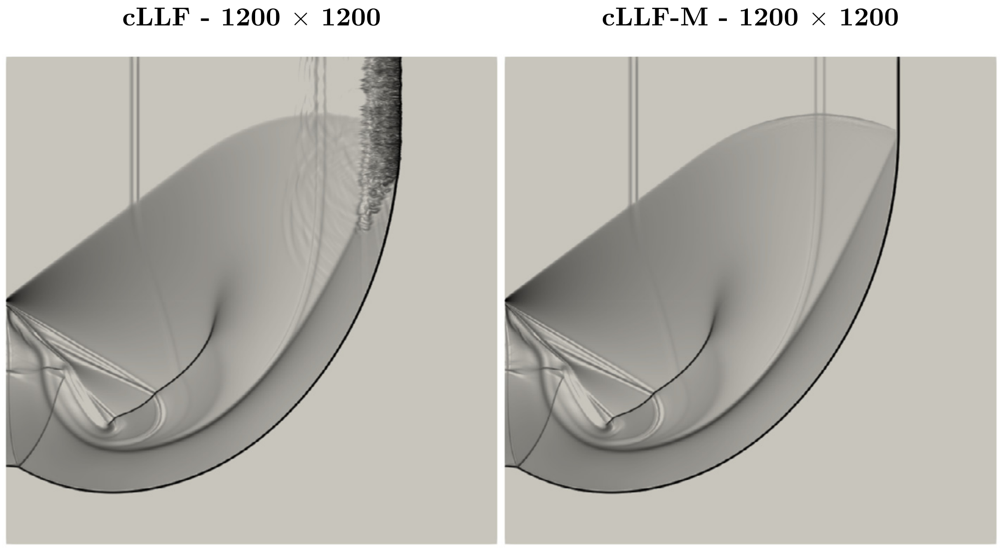

Fig. 8. Corner diffraction of a Mach 5.09 shock wave: logarithmic gradients of density from 2 to 1,000 at $t = 0.15717$.

the shock instability and does not improve the positivity of the scheme, numerically stable results cannot be expected. However, correct physical results are obtained for the shock front when the modified componentwise local Lax-Friedrichs flux is applied, see Fig. 8 right. Note that the flow structure in the rest of the domain is not affected. The stability of the modified componentwise local Lax-Friedrichs flux is demonstrated for a highly resolved grid with 4800 × 4800 cells. The flow field still does not encounter any non-physical behavior as shown in Fig. 9.

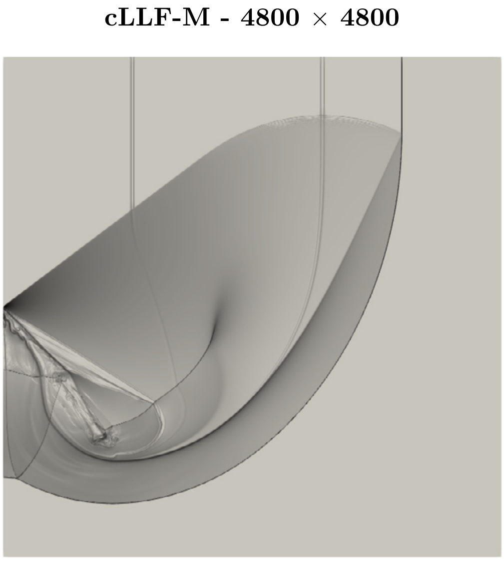

Fig. 9. Corner diffraction of a Mach 5.09 shock wave (high resolution): logarithmic gradients of density from 2 to 1,000 at $t = 0.15717$.

6.3. *Supersonic flow around cylinder*

The most widespread manifestation of the grid-aligned shock instability is the so-called carbuncle phenomenon. It was first described in [13] for a supersonic flow around a cylinder. This case is challenging for shock-capturing schemes not only due to the grid-alignment but also due to the steadiness of the shock. Godunov-type schemes are known to encounter difficulties for slowly moving and steady shocks [12,38]. The supersonic flow around a cylinder is often simulated using polar coordinates and implicit time integration up to a steady state [21,28]. However, in the context of this paper, we are mainly interested in the grid aligned shock instability, i.e. the carbuncle phenomenon, for Cartesian grids. Therefore, we apply the same Cartesian framework with explicit time integration as used for the other cases being aware of that the dissipation introduced by the time integration might not be enough to reach a fully converged steady state and a small resolved level of fluctuations around the steady shock may remain. The circular reflecting-wall condition representing the cylinder is approximated using a level-set approach [36]. The left and the remaining right boundary are set to inflow and outflow conditions, respectively. Top and bottom boundary conditions are set to Neumann boundary conditions with zero gradient for all variables. We investigated both a Mach 3 and a Mach 20 flow around the cylinder. The whole domain is initially set to $(\rho, u, v, p) = \left(1, \sqrt{1.4} \cdot Ma, 0, 1\right)$. The domain size is chosen to $[0, 0.3] \times [0, 0.8]$ for the Mach 3 case and $[0, 0.3] \times [0, 0.6]$ for the Mach 20 case, where the center of the cylinder ($D = 0.2$) is placed in the center of the right boundary. Simulations have been performed using a resolution of 80 cells per diameter, which is comparable to what is used in literature [28].

The resulting pressure distributions for the low Mach number case are shown in Fig. 10 together with Mach contour lines that are chosen identical to [28]. The final time $t = 1.5$ is large enough to ensure a fully developed bow shock. The application of the original componentwise local Lax-Friedrichs flux results in a noticeably disturbed flow field in the region of the stagnation point. The modified componentwise local Lax-Friedrichs formulation damps the fluctuations considerably. Minor residual oscillations can be noticed in the pressure and velocity distribution.

To investigate the situation further, a more challenging Mach 20 flow is considered. The resulting pressure distributions are shown together with Mach contour lines in Fig. 11. Now the original componentwise local Lax-Friedrichs flux suffers clearly form the classical shock instability resulting in the carbuncle phenomenon. The instability already occurs while the bow shock establishes. For the same point in time the modified componentwise local Lax-Friedrichs flux provides stable results. The simulation remains stable until the final time of 0.5 is reached. The level of residual perturbations is slightly higher than in the low Mach number case.

6.4. *Elling test*

The numerical experiment described by Elling [35] provides a flow configuration where a carbuncle-like flow evolution can be physically justified and thus, it should be correctly recovered by the numerical flow solver. The test case consists of an interaction of a steady shock front with a vortex filament. For this specific condition, a carbuncle-like flow pattern has been observed in experiments [39]. Some of the shock stable schemes that suppress the instability by additional numerical dissipation, such as the HLLE solver, are not able to recover this physically valid carbuncle-like structure [33].

The problem is set up with a steady shock that is placed at $x = 50$ in a domain of size $[0, 100] \times [0, 40]$, which is discretized by 1600×640 cells. The flow variables in the upstream region are set to $(\rho, u, v, p) = (1, 1, 0, 5/63)$ and the

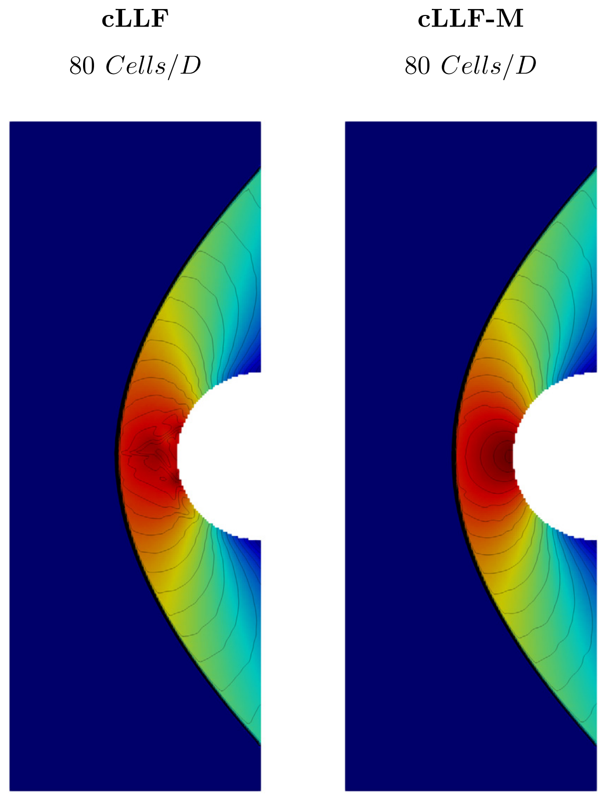
cLLF 80 $Cells/D$ **cLLF-M** 80 $Cells/D$

Fig. 10. Supersonic flow around cylinder $Ma = 6$ at $t = 1.5$: color pressure map (blue = 1.0 to red = 12.1) is overlaid by 25 Mach contours (0.1 to 2.5).

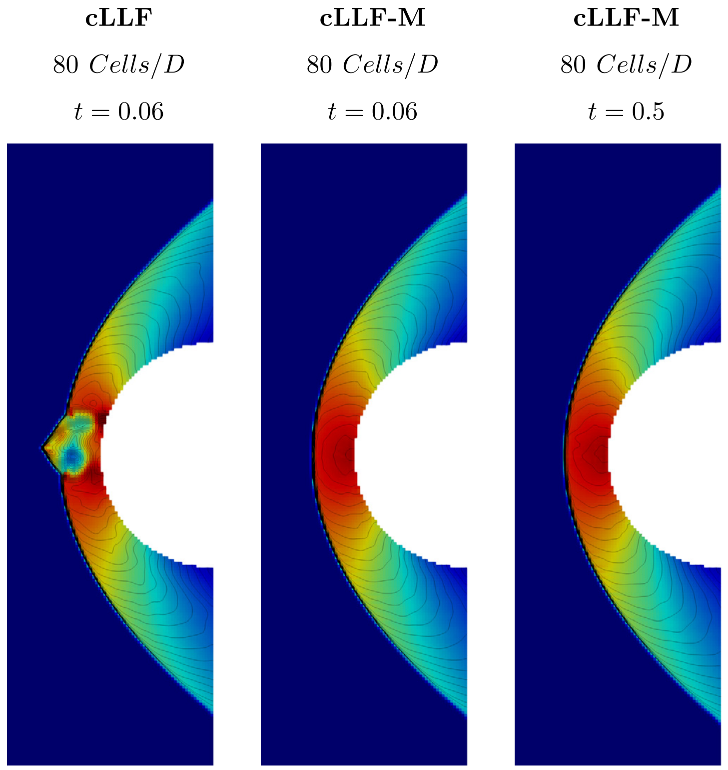
cLLF 80 $Cells/D$ $t = 0.06$ **cLLF-M** 80 $Cells/D$ $t = 0.06$ **cLLF-M** 80 $Cells/D$ $t = 0.5$

Fig. 11. Supersonic flow around cylinder $Ma = 20$: color pressure map (blue = 1.0 to red = 550) is overlaid by 25 Mach contours (0.1 to 2.5).

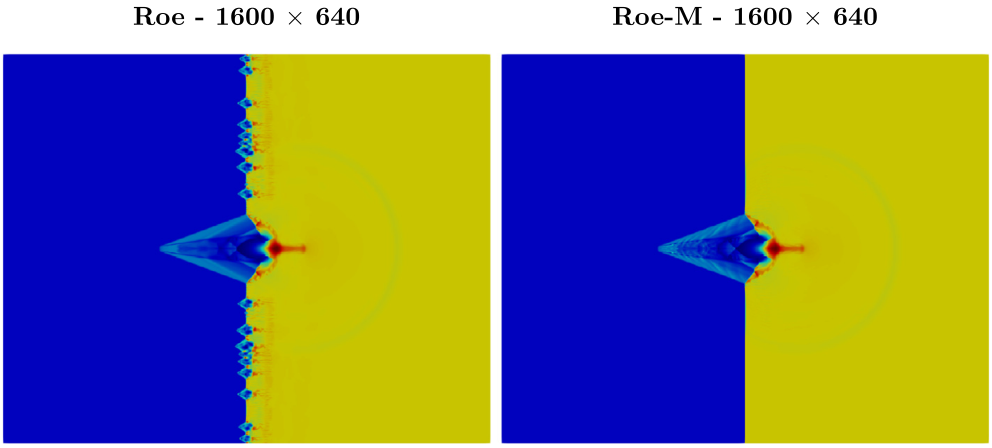

Fig. 12. Elling test case with a vortex filament interaction with a steady Mach 3 shock: density contours from dark blue = 0.35 to red = 6.0 at $t = 20$ for $x = [25, 75]$.

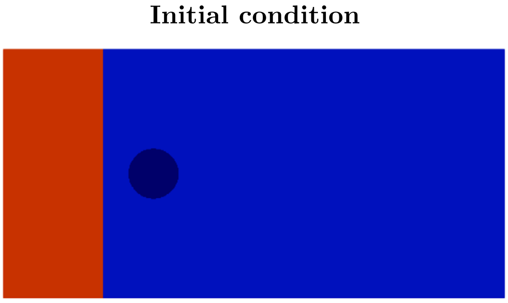

Fig. 13. Initialization of shock interface interaction of a helium bubble in air: density contours from dark blue = 0.138 to red = 6.5.

downstream variables are set to $(\rho, u, v, p) = (27/7, 7/27, 0, 155/189)$ corresponding to a steady Mach 3 shock. In the upstream flow the velocity is set to zero for $19.75 < x < 20.25$ imitating a vortex filament. Inflow and outflow conditions are applied at the left and right boundary, respectively. Reflecting-wall boundary conditions are set for the upper and lower boundary. The final time is set to 20.

Note, that the filament in our case consists of eight cells compared to one cell in the original case. This change is necessary to stabilize the simulation when the Roe approximation is applied. The left frame of Fig. 12 shows the final result for the density profile when the original Roe flux is applied. Besides the expected carbuncle-like structure smaller carbuncles develop along the shock front. However, the modified Roe scheme is able to produce a disturbance-free shock front, while it does not suppress the “physical” carbuncle that is triggered by the vortex, see Fig. 12 right. The reduced numerical dissipation is clearly visible in the fine structure of the “physical” carbuncle.

6.5. Shock interface interaction: helium bubble in air

The grid-aligned shock instability does not only affect single-phase cases, but it may also limit the numerical investigation of shock-interface interaction problems. The following case investigates the interaction of a Mach 6 shock wave in air ($\gamma = 1.4$) with a helium bubble ($\gamma = 1.66$) similar to the setup in [1]. The helium bubble is placed at $x = 0.15$, $y = 0.125$ within in a domain of size $[0, 0.5] \times [0, 0.25]$. The initial diameter of the bubble is set to $D = 0.05$. The shock front is initially placed at $x = 0.1$. The resolution is set to 512×256. The pre-shock domain is at rest with $\rho^{Air} = 1$, $\rho^{He} = 0.138$ and $p^{Air} = p^{He} = 1$. The post-shock values of air are identical to the Mach 6 case given by Eq. (15). Inflow and outflow conditions are applied at the left and right boundary, respectively. Neumann boundaries with zero gradient for all quantities are set at the remaining boundaries. The initial setup is given in Fig. 13.

When the original Roe approximation is applied, three distinct carbuncles occur which deteriorate the flow field behind the shock wave massively as depicted in the top frame of Fig. 14. The modified Roe approximation is able to prevent the occurrence of the carbuncles effectively. The resulting flow evolution with stable shock front is shown in the bottom frame of Fig. 14.

6.6. Shock interface interaction: air bubble in water

Finally, another two-phase setup is investigated featuring a water-air setup with a large density ratio as described in [2]. As the shock hits the air bubble, a strong transmitted shock wave starts to travel within the air bubble. When low

Roe

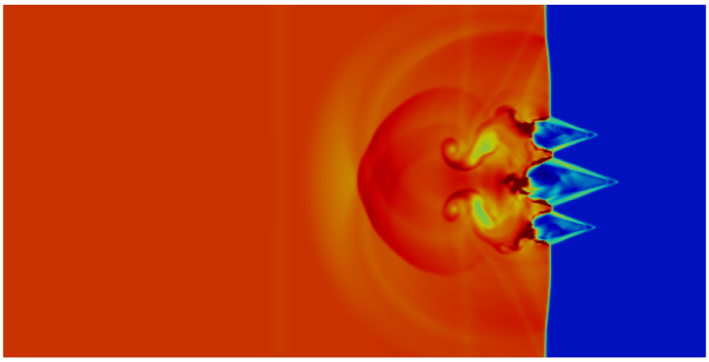

Roe-M

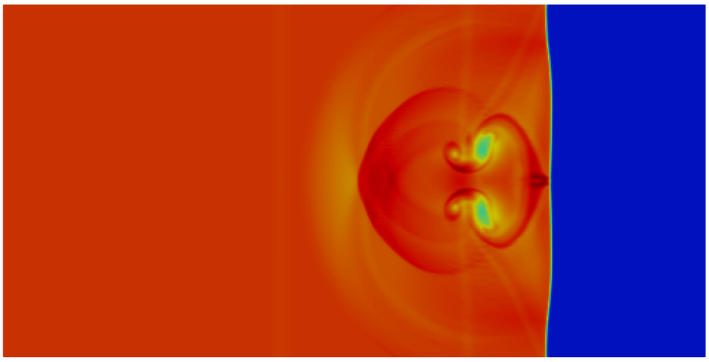

Fig. 14. Shock interface interaction of a helium bubble in air at $t = 0.04$: density contours from dark blue = 0.138 to red = 6.5.

dissipation schemes such as the Roe approximation are applied, the shock front in the air bubble may suffer from the grid aligned-shock instability.

We follow the setup of [2] with a domain size of $[0, 0.024] \times [0, 0.024]$, where the air bubble ($D = 0.006$) is placed in the middle of the domain. Inflow and outflow conditions are applied at the left and right boundary, respectively. Neumann boundaries with zero gradient for all quantities are set at the remaining boundaries. The shock front is initially placed at $x = 0.008$. The initial condition is given by

$$(\rho, u, v, p) = \begin{cases} \left(1323.65, 661.81, 0, 1.6 \cdot 10^9\right) & \text{water post-shock} \\ \left(1000, 0, 0, 10^5\right) & \text{water pre-shock,} \\ \left(1, 0, 0, 10^5\right) & \text{air,} \end{cases} \tag{17}$$

where water is modeled with a stiffened equation of state ($\gamma = 4.4$, $P_{\text{inf}} = 6 \cdot 10^8$) and air as ideal gas ($\gamma = 1.4$). The resolution is set to 640×640.

Fig. 15 shows the results for the density distribution for the whole domain, while Fig. 16 is focused on the velocity distribution in the air bubble at $t = 0.0029$. Again, the modified Roe flux is able to recover a sharp shock front without any instability effects.

7. Conclusion

In this paper, we have presented a procedure to obtain *low-dissipation* flux approximations that are stable against the grid-aligned shock instability and require only minor modifications to existing schemes. The procedure is motivated by connecting the grid-aligned shock instability to the well-known low Mach number effect of Godunov schemes. The typical setup for the instability consists of a shock front that propagates in one direction of the Cartesian grid, where the disturbances parallel to the front propagate in a low Mach number fashion. In this situation, the acoustic contribution to dissipation is dominant and leads to an amplification of pressure disturbances that causes the instability. The proposed procedure avoids the amplification and therefore cures the instability by limiting the ratio of the advection and the acoustic contribution to the dissipation term. Two possible implementations of the procedure were described in detail. Increasing the advection contribution to the dissipation term results in an increased overall dissipation, while reducing the acoustic dissipation leads to an decreased overall dissipation. A modified Roe approximation (Roe-M) and a modified componentwise local Lax-Friedrichs flux (cLLF-M) are given.

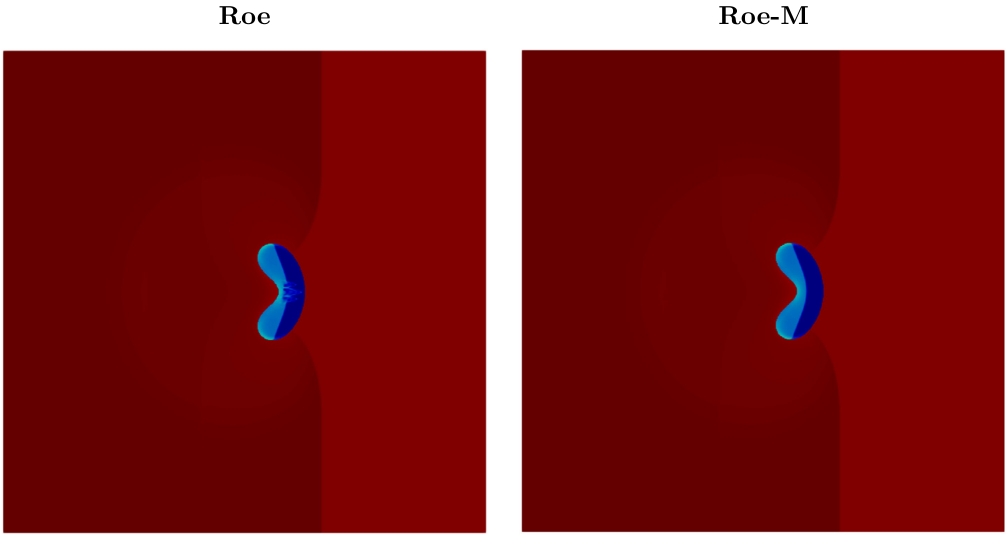

Fig. 15. Shock interface interaction of a air bubble in water at $t = 0.0029$: logarithmic color map of density from dark blue = 0.138 to red = 6.5.

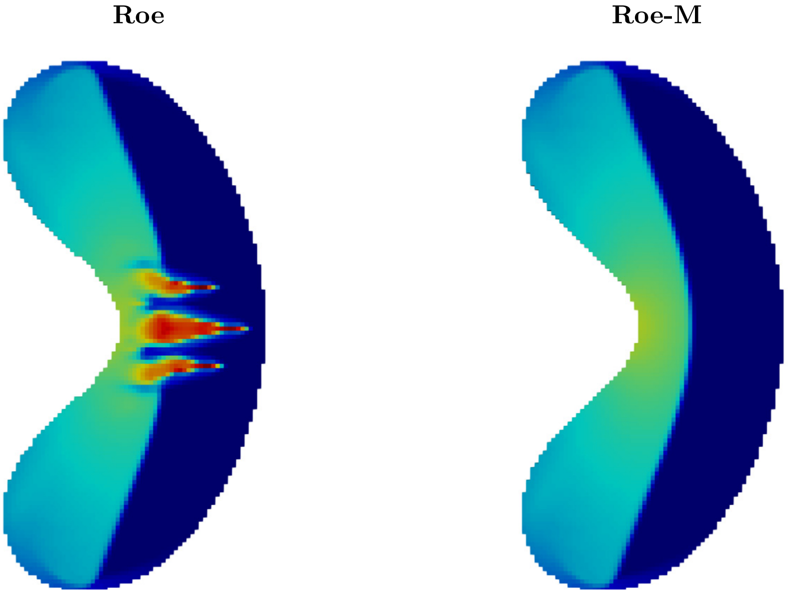

Fig. 16. Shock interface interaction of a air bubble in water at $t = 0.0029$: velocity magnitude within the air bubble from dark blue = 0 to red = 4400.

Results obtained with the low-Mach-number modified flux formulations for a comprehensive series of test cases confirm that the prime reason of the grid-aligned shock instability is not due to an insufficient amount of numerical dissipation, but due to the inadequate scaling of the dissipative flux contributions in the low Mach number limit. Moreover, we demonstrated that the shock instability can be cured by *reducing the overall dissipation* of the scheme. The preservation of high accuracy in all parts of the domain including the precise capturing of contact waves is therefore straightforward and does not require any further procedures. The Roe-M flux is stable against the grid-aligned shock instability, although it still exhibits other well-known deficiencies of the Roe flux such as lack of positivity and non-physical expansion shocks. The proposed method can be combined with entropy satisfying and positivity preserving techniques if required. The low Mach number treatment is most simple to apply to the Roe and componentwise local Lax-Friedrichs approximation, where only the calculation of the eigenvalues is affected. However, application to other flux formulations is also possible. Demonstrations of the Roe-M flux for two multi-phase applications including shock interactions with a helium bubble in air and an air bubble in water revealed excellent results and demonstrate that the proposed scheme is capable to simulate complex super- and hypersonic flow physics while maintaining high accuracy and robustness.

Declaration of competing interest

The authors declare that they have no known competing financial interests or personal relationships that could have appeared to influence the work reported in this paper.

Acknowledgements

This project has received funding from the European Research Council (ERC) under the European Union's Horizon 2020 research and innovation programme (grant agreement No. 667483).

References

[1] A. Bagabir, D. Drikakis, Mach number effects on shock-bubble interaction, Shock Waves 11 (3) (2001) 209–218.

[2] O. Haimovich, S.H. Frankel, Numerical simulations of compressible multicomponent and multiphase flow using a high-order targeted ENO (TENO) finite-volume method, Comput. Fluids 146 (2017) 105–116.

[3] E.F. Toro, Riemann Solvers and Numerical Methods for Fluid Dynamics: A Practical Introduction, Springer Science & Business Media, 2013.

[4] S.K. Godunov, A difference method for numerical calculation of discontinuous solutions of the equations of hydrodynamics, Mat. Sb. 89 (3) (1959) 271–306.

[5] A. Harten, B. Engquist, S. Osher, S.R. Chakravarthy, Uniformly high order accurate essentially non-oscillatory schemes, III, J. Comput. Phys. 71 (2) (1987) 231–303.

[6] G.-S. Jiang, C.-W. Shu, Efficient implementation of weighted ENO schemes, J. Comput. Phys. 126 (1) (1996) 202–228.

[7] A. Harten, P.D. Lax, B.v. Leer, On upstream differencing and Godunov-type schemes for hyperbolic conservation laws, SIAM Rev. 25 (1) (1983) 35–61.

[8] B. Einfeldt, On Godunov-type methods for gas dynamics, SIAM J. Numer. Anal. 25 (2) (1988) 294–318.

[9] E.F. Toro, M. Spruce, W. Speares, Restoration of the contact surface in the HLL-Riemann solver, Shock Waves 4 (1) (1994) 25–34.

[10] S. Osher, F. Solomon, Upwind difference schemes for hyperbolic systems of conservation laws, Math. Comput. 38 (158) (1982) 339–374.

[11] P.L. Roe, Approximate Riemann solvers, parameter vectors, and difference schemes, J. Comput. Phys. 43 (2) (1981) 357–372.

[12] J.J. Quirk, A contribution to the great Riemann solver debate, in: Upwind and High-Resolution Schemes, Springer, 1997, pp. 550–569.

[13] K. Peery, S. Imlay, Blunt-body flow simulations, in: 24th Joint Propulsion Conference, 1988, p. 2904.

[14] R. Sanders, E. Morano, M.-C. Druguet, Multidimensional dissipation for upwind schemes: stability and applications to gas dynamics, J. Comput. Phys. 145 (2) (1998) 511–537.

[15] M. Pandolfi, D. D'Ambrosio, Numerical instabilities in upwind methods: analysis and cures for the "carbuncle" phenomenon, J. Comput. Phys. 166 (2) (2001) 271–301.

[16] J. Gressier, J.-M. Moschetta, Robustness versus accuracy in shock-wave computations, Int. J. Numer. Methods Fluids 33 (3) (2000) 313–332.

[17] M.-S. Liou, Mass flux schemes and connection to shock instability, J. Comput. Phys. 160 (2) (2000) 623–648.

[18] M. Dumbser, J.-M. Moschetta, J. Gressier, A matrix stability analysis of the carbuncle phenomenon, J. Comput. Phys. 197 (2) (2004) 647–670.

[19] M.-S. Liou, A sequel to AUSM: AUSM$^+$, J. Comput. Phys. 129 (2) (1996) 364–382.

[20] Y.-X. Ren, A robust shock-capturing scheme based on rotated Riemann solvers, Comput. Fluids 32 (10) (2003) 1379–1403.

[21] S.-S. Kim, C. Kim, O.-H. Rho, S.K. Hong, Cures for the shock instability: development of a shock-stable Roe scheme, J. Comput. Phys. 185 (2) (2003) 342–374.

[22] S.-S. Chen, C. Yan, B.-X. Lin, Y.-S. Li, A new robust carbuncle-free roe scheme for strong shock, J. Sci. Comput. (2018) 1–28.

[23] S.D. Kim, B.J. Lee, H.J. Lee, I.-S. Jeung, Robust HLLC Riemann solver with weighted average flux scheme for strong shock, J. Comput. Phys. 228 (20) (2009) 7634–7642.

[24] Z. Shen, W. Yan, G. Yuan, A robust HLLC-type Riemann solver for strong shock, J. Comput. Phys. 309 (2016) 185–206.

[25] S. Simon, J. Mandal, A simple cure for numerical shock instability in the HLLC Riemann solver, J. Comput. Phys. 378 (2019) 477–496.

[26] K.H. Kim, C. Kim, O.-H. Rho, Methods for the accurate computations of hypersonic flows: I. AUSMPW+scheme, J. Comput. Phys. 174 (1) (2001) 38–80.

[27] K. Kitamura, E. Shima, Towards shock-stable and accurate hypersonic heating computations: a new pressure flux for AUSM-family schemes, J. Comput. Phys. 245 (2013) 62–83.

[28] A.V. Rodionov, Artificial viscosity in Godunov-type schemes to cure the carbuncle phenomenon, J. Comput. Phys. 345 (2017) 308–329.

[29] H. Guillard, C. Viozat, On the behaviour of upwind schemes in the low Mach number limit, Comput. Fluids 28 (1) (1999) 63–86.

[30] H. Guillard, A. Murrone, On the behavior of upwind schemes in the low Mach number limit: II. Godunov type schemes, Comput. Fluids 33 (4) (2004) 655–675.

[31] S. Gottlieb, C.-W. Shu, E. Tadmor, Strong stability-preserving high-order time discretization methods, SIAM Rev. 43 (1) (2001) 89–112.

[32] X.-s. Li, C.-w. Gu, An all-speed Roe-type scheme and its asymptotic analysis of low Mach number behaviour, J. Comput. Phys. 227 (10) (2008) 5144–5159.

[33] F. Kemm, Heuristical and numerical considerations for the carbuncle phenomenon, Appl. Math. Comput. 320 (2018) 596–613.

[34] P. Woodward, P. Colella, The numerical simulation of two-dimensional fluid flow with strong shocks, J. Comput. Phys. 54 (1) (1984) 115–173.

[35] V. Elling, The carbuncle phenomenon is incurable, Acta Math. Sci. 29 (6) (2009) 1647–1656.

[36] X.Y. Hu, B. Khoo, N.A. Adams, F. Huang, A conservative interface method for compressible flows, J. Comput. Phys. 219 (2) (2006) 553–578.

[37] R. Borges, M. Carmona, B. Costa, W.S. Don, An improved weighted essentially non-oscillatory scheme for hyperbolic conservation laws, J. Comput. Phys. 227 (6) (2008) 3191–3211.

[38] M. Bultelle, M. Grassin, D. Serre, Unstable Godunov discrete profiles for steady shock waves, SIAM J. Numer. Anal. 35 (6) (1998) 2272–2297.

[39] I.M. Kalkhoran, M.K. Smart, Aspects of shock wave-induced vortex breakdown, Prog. Aerosp. Sci. 36 (1) (2000) 63–95.

A.3 A shock-stable modification of the HLLC Riemann solver with reduced numerical dissipation

CCC RightsLink®

Home | Help | Live Chat | Sign in | Create Account

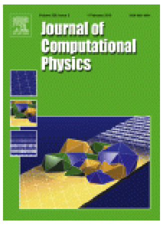

A shock-stable modification of the HLLC Riemann solver with reduced numerical dissipation

Author: Nico Fleischmann,Stefan Adami,Nikolaus A. Adams

Publication: Journal of Computational Physics

Publisher: Elsevier

Date: 15 December 2020

Journal Author Rights

Please note that, as the author of this Elsevier article, you retain the right to include it in a thesis or dissertation, provided it is not published commercially. Permission is not required, but please ensure that you reference the journal as the original source. For more information on this and on your other retained rights, please visit: https://www.elsevier.com/about/our-business/policies/copyright#Author-rights

BACK CLOSE WINDOW

Journal of Computational Physics 423 (2020) 109762

Contents lists available at ScienceDirect

Journal of Computational Physics

www.elsevier.com/locate/jcp

A shock-stable modification of the HLLC Riemann solver with reduced numerical dissipation

Nico Fleischmann [*], Stefan Adami, Nikolaus A. Adams

Technical University of Munich, Department of Mechanical Engineering, Chair of Aerodynamics and Fluid Mechanics, Boltzmannstraße 15, 85748 Garching, Germany

A R T I C L E   I N F O

Article history:
Received 1 February 2020
Received in revised form 31 July 2020
Accepted 4 August 2020
Available online 26 August 2020

Keywords:
Shock instability
Carbuncle phenomenon
HLLC
High-order schemes
WENO
Low-dissipation schemes

A B S T R A C T

The purpose of this paper is twofold. First, the application of high-order methods in combination with the popular HLLC Riemann solver demonstrates that the grid-aligned shock instability can strongly affect simulation results when the grid resolution is increased. Beyond the well-documented two-dimensional behavior, the problem is particularly troublesome with three-dimensional simulations. Hence, there is a need for shock-stable modifications of HLLC-type solvers for high-speed flow simulations.

Second, the paper provides a stabilization of the popular HLLC flux based on a recently proposed mechanism for grid aligned-shock instabilities Fleischmann et al. (2020) [8]. The instability was found to be triggered by an inappropriate scaling of acoustic and advection dissipation for local low Mach numbers. These low Mach numbers occur during the calculation of fluxes in transverse direction of the shock propagation, where the local velocity component vanishes. A centralized formulation of the HLLC flux is provided for this purpose, which allows for a simple reduction of nonlinear signal speeds. In contrast to other shock-stable versions of the HLLC flux, the resulting HLLC-LM flux *reduces the inherent numerical dissipation* of the scheme.

The robustness of the proposed scheme is tested for a comprehensive range of cases involving strong shock waves. Three-dimensional single- and multi-component simulations are performed with high-order methods to demonstrate that the HLLC-LM flux also copes with latest challenges of compressible high-speed computational fluid dynamics.

1. Introduction

Approximate Riemann solvers in combination with shock-capturing Godunov schemes [1] dominate modern computation of phenomena that involve complex flow interactions across scales such as shock interaction with multi-phase interfaces and turbulent scales. The application of high-order discretizations allows for an accurate prediction of many of such flows. However, over the last decades the grid-aligned shock instability has presented a barrier for robust computation of high Mach number flows using high-order discretizations with state-of-the-art low-dissipation Riemann solvers such as Roe [2] or HLLC [3,4]. Since the first description of the problem by Peery and Imlay [5] and Quirk [6] an extensive research on the topic resulted in a large number of scientific publications addressing various aspects. A summary of major developments to

---

[*] Corresponding author.
E-mail addresses: nico.fleischmann@tum.de (N. Fleischmann), stefan.adami@tum.de (S. Adami), nikolaus.adams@tum.de (N.A. Adams).

https://doi.org/10.1016/j.jcp.2020.109762

the present day can be found in [7,8]. Even though most of the research has focused on the Roe solver, also the HLLC solver is afflicted by the instability.

HLL-type solvers were originally developed by Harten, Lax and van Leer [3]. In combination with the nonlinear signal speed estimates of Einfeldt [9] and the restoration of the contact wave proposed by Toro et al. [4], the resulting HLLC Riemann approximation became one of the most successful and widespread Riemann solvers for hyperbolic systems [10,11]. An accurate estimation of the contact wave speed was communicated by Batten et al. [12]. Due to the explicit modeling of each wave of the governing Euler equations, HLLC is a complete Riemann solver with significantly reduced dissipation near contact discontinuities compared to the HLL scheme. The design of the HLLC flux allows for straightforward extensions to other types of hyperbolic equations, e.g. for magneto-hydrodynamics [13–15], by introduction of additional wave types. Moreover, the HLLC flux has been applied successfully to multi-component flows [16,17], and capillary forces have been introduced to simulate surface tension effects at liquid/gas interfaces [18]. Further recent applications are reviewed in [11].

While the HLLC flux is known to suffer from the shock instability, the stable behavior of the HLL flux was described already by Quirk [6]. He suggested to apply the HLL scheme near strong shocks in combination with lower-dissipation schemes, such as HLLC, in the remaining domain. These hybrid schemes lead to stable, but nevertheless contact preserving results. The switching procedure was improved by Kim et al. [19], where the dissipative HLL flux only is applied for the fluxes in transverse direction of the shock propagation. Another modification of the hybrid scheme was suggested in [20], where the dissipative HLL flux only is applied for two components of the flux. However, hybrid schemes may still significantly increase dissipation, and a switching procedure has to be provided. Additionally, the authors of [20] successfully tested the shock stability of the rotated Riemann solver method [21] applied to the HLLC flux, but they found that the latter approach is computationally rather expensive. The first pure HLLC-type flux with shock-stable properties, called HLLCM, was developed by Shen et al. [22] via smearing of the shear velocities on both sides of the contact line. This procedure introduces shear viscosity and stabilizes the calculation of strong shocks. However, the introduced amount of dissipation limits the accuracy of boundary layer calculations and therefore the authors again suggested to apply a hybrid HLLC-HLLCM version for complex flows. Recently, Xie et al. [23] proposed an HLLC-type Riemann solver with an additional pressure-dissipation term that is activated near shocks and damps spurious pressure perturbations. Simon and Mandal [24,25] proposed two different approaches to avoid the shock instability. They separated the HLLC flux into the inherent HLL part and an antidiffusive part. In their first approach [24], the activation of the antidiffusive term is controlled by a pressure-ratio-based multi-dimensional shock sensor. The resulting solver called HLLC-ADC restores the shock stability of the HLL flux. The second approach [25] is to apply a selective wave modification that increases the inherent dissipative HLL part in the vicinity of a shock wave. The antidiffusive term of the resulting HLLC-SWM flux remains identical to that of the original HLLC.

In comparison to the large number of proposed modifications of the Roe flux, the grid-aligned shock instability of the popular HLLC solver has found much less consideration in literature. The reason is probably, that the solution of most two-dimensional simulations remains bounded, and therefore the effect of the introduced disturbances is not as catastrophic as with the Roe flux. However, with increased resolution, high-order discretizations, and extension to three-dimensional simulations, the application of the HLLC flux is prone to develop severe carbuncles, similarly to that obtained with the Roe flux, as is shown in this paper.

In [8], the authors proposed a new possible mechanism of the grid-aligned shock instability. A wrong scaling behavior of numerical dissipation due to the local low Mach number in transverse direction of the shock front propagation was found to cause the numerical shock instability. A modification for the popular Roe flux and the local componentwise Lax-Friedrichs flux was proposed that proved to be shock stable. The present paper proposes a new shock-stable modification of the HLLC flux called HLLC-LM that is based on these findings. As a straightforward reduction of nonlinear wave speeds is not sensible for the classical HLLC formulation, a new centralized reformulation of the HLLC flux is derived. This alternative formulation allows for an analogous reduction of acoustic dissipation as with the modified Roe scheme without introducing additional difficulties. Most of the present shock-stabilizing variants of the HLLC flux restore the shock stability by adding additional dissipation in one way or the other, as motivated by the stability of the stable, but highly dissipative HLL scheme. In contrast, the proposed HLLC-LM flux with *less numerical dissipation* than the classical HLLC flux represents a fundamentally different approach in comparison to the earlier HLLC-HLL combination models. Moreover, in this paper the shock stability of both HLLC and HLLC-LM is studied using high-order methods in space and time, unlike the low-order examples presented in most of the aforementioned publications. We also investigate the grid-aligned shock instability for the HLLC solver in three dimensions and reveal that carbuncles are more likely to occur than in two dimensions.

The paper is organized as follows. In Section 2, the governing equations and the general framework of Godunov-type methods are reviewed together with the classical HLLC flux formulation. A centralized formulation of the HLLC flux is derived in the first part of Section 3, followed by the low Mach number adapted wave speed formulations resulting in the newly proposed HLLC-LM scheme. In Section 4, a comprehensive set of test cases is studied to verify the accuracy and shock stability of the new scheme. Results are also provided with high resolution including a study of three-dimensional effects. Finally in Section 5, calculations of complex flow phenomena that take advantage of the applied high-order schemes, such as a flow around a diamond and multi-component flows with nontrivial shock-interface interactions, are studied to further demonstrate both the stability and the reduced numerical dissipation of the HLLC-LM flux. Conclusions are drawn in Section 6.

2. Governing equations and numerical approach

We consider an inviscid compressible flow that evolves according to the three-dimensional Euler equations

$$\mathbf{U}_t + \mathcal{F}(\mathbf{U})_x + \mathcal{G}(\mathbf{U})_y + \mathcal{H}(\mathbf{U})_z = 0, \tag{1}$$

where $\mathbf{U}$ is the density of the conserved quantities mass ρ, momentum $\rho\mathbf{v} \equiv (\rho u, \rho v, \rho w)$ and total energy $E = \rho e + \frac{1}{2}\rho\mathbf{v}^2$, with e being the internal energy per unit mass. The fluxes $\mathcal{F}$, $\mathcal{G}$ and $\mathcal{H}$ are defined as

$$\mathcal{F} = \begin{pmatrix} \rho u \\ \rho u^2 + p \\ \rho u v \\ \rho u w \\ u(E+p) \end{pmatrix}, \quad \mathcal{G} = \begin{pmatrix} \rho v \\ \rho u v \\ \rho v^2 + p \\ \rho v w \\ v(E+p) \end{pmatrix}, \quad \mathcal{H} = \begin{pmatrix} \rho w \\ \rho u w \\ \rho v w \\ \rho w^2 + p \\ w(E+p) \end{pmatrix}. \tag{2}$$

The set of equations is closed by the ideal-gas equation of state, where the pressure p is given by $p = (\gamma - 1)\rho e$ with a constant ratio of specific heats γ.

2.1. Finite volume approach

Our numerical framework is identical to the one described in [8], where Godunov's approach [1] for finite volumes is applied to solve the given set of equations. The time evolution of the vector of cell-averaged conservative states $\bar{\mathbf{U}}$ is given by

$$\frac{d}{dt}\bar{\mathbf{U}}_i = \frac{1}{\Delta x}(\mathbf{F}_{i-\frac{1}{2},j,k} - \mathbf{F}_{i+\frac{1}{2},j,k} + \mathbf{G}_{i,j-\frac{1}{2},k} - \mathbf{G}_{i,j+\frac{1}{2},k} + \mathbf{H}_{i,j,k-\frac{1}{2}} - \mathbf{H}_{i,j,k+\frac{1}{2}}), \tag{3}$$

where Δx is the cell size of a uniform Cartesian grid and $\mathbf{F}$, $\mathbf{G}$ and $\mathbf{H}$ approximate the cell-face fluxes in x-, y- and z-direction, respectively. These fluxes are determined dimension-by-dimension from a Riemann solver combined with a high-order WENO spatial reconstruction scheme [26]. Additional volume source terms, such as gravitational acceleration, are omitted here for simplicity. The resulting system of ODE (3) is integrated in time using a high-order strong stability-preserving (SSP) Runge-Kutta scheme [27].

2.2. The HLLC Riemann solver

In order to avoid computationally expensive iterative solution of the Riemann problem, approximate Riemann solvers are commonly employed. In this paper, we focus on one specific approximation, the HLLC solver, which is one of the most popular and versatile Riemann solvers. It has been extended to a broad range of applications, also beyond classical computational fluid dynamics [11].

Toro et al. [4] define the HLLC flux as

$$\mathbf{F}^{HLLC} = \begin{cases} \mathbf{F}_L & \text{if } S_L \geq 0, \\ \mathbf{F}_{*L} = \mathbf{F}_L + S_L \cdot (\mathbf{U}_{*L} - \mathbf{U}_L) & \text{if } S_L < 0 \cap S_* \geq 0, \\ \mathbf{F}_{*R} = \mathbf{F}_R + S_R \cdot (\mathbf{U}_{*R} - \mathbf{U}_R) & \text{if } S_R > 0 \cap S_* \leq 0, \\ \mathbf{F}_R & \text{if } S_R \leq 0, \end{cases} \tag{4}$$

where two intermediate states, $\mathbf{U}_{*L}$ and $\mathbf{U}_{*R}$, are separated by the contact wave and are determined from

$$\boldsymbol{U}_{*K} = \frac{S_K - u_K}{S_K - S_*} \begin{pmatrix} \rho_K \\ \rho_K S_* \\ \rho_K v_K \\ \rho_K w_K \\ E_K + (S_* - u_K)\left(\rho_K S_* + \frac{p_K}{S_K - u_K}\right) \end{pmatrix} \tag{5}$$

with $K = L, R$, and $\mathbf{U}_L$, $\mathbf{U}_R$ being the reconstructed left and right face states, respectively.

Following Einfeldt [9], the maximum left and right nonlinear signal speed estimates are obtained from

$$S_L = \min(u_L - c_L, \hat{u} - \hat{c}), \qquad S_R = \max(u_R + c_R, \hat{u} + \hat{c}), \tag{6}$$

where $\hat{u}$ and $\hat{c}$ are determined from the Roe average

$$\hat{u} = \frac{u_L \cdot \sqrt{\rho_L} + u_R \cdot \sqrt{\rho_R}}{\sqrt{\rho_L} + \sqrt{\rho_R}} \tag{7}$$

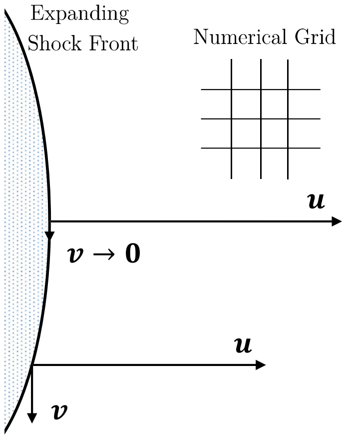

Fig. 1. Schematic illustration of the vanishing velocity component v in transverse direction of the shock front propagation.

and

$$\hat{c}^2 = \frac{{c_L}^2 \cdot \sqrt{\rho_L} + c_R^2 \cdot \sqrt{\rho_R}}{\sqrt{\rho_L} + \sqrt{\rho_R}} + \frac{1}{2} \frac{\sqrt{\rho_L}\sqrt{\rho_R}}{\left(\sqrt{\rho_L} + \sqrt{\rho_R}\right)^2} \left(u_R - u_L\right)^2 . \tag{8}$$

The contact wave speed is estimated according to Batten et al. [12] from

$$S_* = \frac{p_R - p_L + \rho_L u_L \left(S_L - u_L\right) - \rho_R u_R \left(S_R - u_R\right)}{\rho_L \left(S_L - u_L\right) - \rho_R \left(S_R - u_R\right)}. \tag{9}$$

High-order approximations for the left and right face states, $\mathbf{U}_L$ and $\mathbf{U}_R$, are obtained upon characteristic decomposition in combination with a high-order WENO scheme as described in detail in [28].

3. A shock-stable HLLC type solver with low Mach number modification

An inaccurate scaling behavior of the acoustic and advection contribution to the numerical dissipation in the low Mach number limit has been found to be the driving mechanism of the numerical grid-aligned shock instability [8]. The connection is motivated by the observation, that shock instabilities only occur when a high Mach number shock wave propagates almost perfectly aligned with the computational grid.

When the shock wave moves in x-direction as shown in Fig. 1, the velocity components of the local transverse direction v, respectively v and w for the three-dimensional case, have a vanishing magnitude. Consequently, the local directional Mach number will also vanish during the computation of the fluxes in transverse directions of the shock wave propagation. Note that a perfect alignment with zero Mach number in transverse directions leads to a one-dimensional situation where no instability occurs. A small deflection is always required to trigger the instability. There is a thorough documentation of the shortcomings of Riemann solvers in the low Mach regime [29–31] which dates back to the findings of Guillard et al. [32,33]. In [32], the authors showed that a wrong scaling behavior of the numerical dissipation leads to pressure fluctuations that may ruin the prediction of low Mach number flows using Godunov's approach. This flaw is now considered as the driving mechanism of the grid-aligned shock instability. In their recent publication, Chen et at. [34] performed a stability analysis to investigate the shock instability mechanism for simplified systems. Their results support the given argumentation as the authors also detect an inaccurate pressure dissipation of the Riemann solver at the vertical transverse face of the shock to be the driving mechanism for the instability. A minor modification that reduces the acoustic dissipation of the Roe Riemann solver in the low Mach number limit proved to be effective in suppressing the instability [8]. The reduction of acoustic dissipation can be achieved by reduction of the nonlinear eigenvalues of the Roe dissipation matrix for small Mach numbers. This procedure stabilizes simulations of supersonic flows. For dealing with global low Mach number flows near the incompressible limit, there are other methods available in literature [29–31].

A straightforward modification of the nonlinear signal speeds of the HLLC solver following [8] turns out to be ineffective in suppressing grid-aligned shock instabilities. The reason for the ineffectiveness can be found when the limit solution of the Roe-M flux and a modified HLLC flux with similarly reduced nonlinear signal speed are compared for vanishing Mach numbers. While the Roe-M approximation [8] reduces in the low Mach number limit to the central flux term

$$\mathbf{F}^{Roe-M} \xrightarrow{Ma\to 0} \frac{1}{2}\left(\mathbf{F_L} + \mathbf{F_R}\right), \tag{10}$$

a modified HLLC approximation with identical reduction of nonlinear signal speeds results in

$$\mathbf{F}^{HLLC-REDUCED} \xrightarrow{Ma\to 0} \begin{cases} \mathbf{F}_L & \text{if } S_* \geq 0, \\ \mathbf{F}_R & \text{if } S_* \leq 0. \end{cases} \tag{11}$$

Thus, differently from the limit solution of the Roe-M scheme, a straightforward modification of the HLLC flux leads to a pure classical upwind scheme. Upwinding is not required in the absence of shocks and, moreover, introduces an undesirable amount of numerical dissipation, which counteracts the objective of reducing dissipation. Thus, the goal is to find a formulation of the HLLC flux that continuously approaches the central flux term in the limit of low Mach numbers.

3.1. Central formulation of the HLLC flux

In a first step, the classical HLLC flux will be reformulated motivated by the derivation of the central Roe flux formulation. The intermediate flux F_{*L} can be determined using two alternative approaches

$$\mathbf{F}_{*L} = \mathbf{F}_L + S_L \left(\mathbf{U}_{*L} - \mathbf{U}_L\right) \tag{12}$$

and

$$\mathbf{F}_{*L} = \mathbf{F}_R + S_R \left(\mathbf{U}_{*R} - \mathbf{U}_R\right) + S_* \left(\mathbf{U}_{*L} - \mathbf{U}_{*R}\right). \tag{13}$$

While the traditional derivation of Eq. (12) applies the Rankine-Hugoniot condition only once starting from the left side, alternatively, the Rankine-Hugoniot condition can also be applied twice starting from the right side, Eq. (13). A central formulation of $\mathbf{F}_{*L}$ can be established by averaging both formulations and is given by

$$\mathbf{F}_{*L} = \frac{1}{2}\left(\mathbf{F}_L + \mathbf{F}_R\right) + \frac{1}{2}\left[S_L \left(\mathbf{U}_{*L} - \mathbf{U}_L\right) + S_* \left(\mathbf{U}_{*L} - \mathbf{U}_{*R}\right) + S_R \left(\mathbf{U}_{*R} - \mathbf{U}_R\right)\right]. \tag{14}$$

Analogously, the right intermediate flux can be determined by

$$\mathbf{F}_{*R} = \mathbf{F}_R + S_R \left(\mathbf{U}_{*R} - \mathbf{U}_R\right) \tag{15}$$

and

$$\mathbf{F}_{*R} = \mathbf{F}_L + S_L \left(\mathbf{U}_{*L} - \mathbf{U}_L\right) + S_* \left(\mathbf{U}_{*R} - \mathbf{U}_{*L}\right) \tag{16}$$

resulting in

$$\mathbf{F}_{*R} = \frac{1}{2}\left(\mathbf{F}_L + \mathbf{F}_R\right) + \frac{1}{2}\left[S_L \left(\mathbf{U}_{*L} - \mathbf{U}_L\right) - S_* \left(\mathbf{U}_{*L} - \mathbf{U}_{*R}\right) + S_R \left(\mathbf{U}_{*R} - \mathbf{U}_R\right)\right]. \tag{17}$$

By comparing Eq. (14) and Eq. (17) we note that only the sign of the third term, which is related to the contact wave, differs for both expressions. Finally, considering the requirement that $\mathbf{F}_{*L}$ is applied if $S_* \geq 0$ and $\mathbf{F}_{*R}$ is applied if $S_* \leq 0$, a central formulation of the HLLC flux is obtained by

$$\mathbf{F}^{HLLC} = \begin{cases} \mathbf{F}_L & \text{if } S_L \geq 0, \\ \mathbf{F}_R & \text{if } S_R \leq 0, \\ \mathbf{F}_* & \text{else} \end{cases} \tag{18}$$

with

$$\mathbf{F}_* = \frac{1}{2}\left(\mathbf{F}_L + \mathbf{F}_R\right) \frac{1}{2}\left[S_L \left(\mathbf{U}_{*L} - \mathbf{U}_L\right) + |S_*| \left(\mathbf{U}_{*L} - \mathbf{U}_{*R}\right) + S_R \left(\mathbf{U}_{*R} - \mathbf{U}_R\right)\right]. \tag{19}$$

3.2. On the numerical dissipation of HLL(C)-type solvers

Using the centralized formulation derived in Section 3.1 both the HLL and the HLLC flux in the subsonic regime can be written as

$$\begin{aligned} \mathbf{F}_{HLL} &= \frac{1}{2}\left(\mathbf{F}_L + \mathbf{F}_R\right) - \frac{1}{2}\left[|S_L| \left(\mathbf{U}_* - \mathbf{U}_L\right) + |S_R| \left(\mathbf{U}_R - \mathbf{U}_*\right)\right] \\ \mathbf{F}_{HLLC} &= \frac{1}{2}\left(\mathbf{F}_L + \mathbf{F}_R\right) - \frac{1}{2}\left[|S_L| \left(\mathbf{U}_{*L} - \mathbf{U}_L\right) + |S_*| \left(\mathbf{U}_{*R} - \mathbf{U}_{*L}\right) + |S_R| \left(\mathbf{U}_R - \mathbf{U}_{*R}\right)\right]. \end{aligned} \tag{20}$$

A connection to the Lax-Friedrichs flux can be established, when $|S_L| = |S_*| = |S_R| = |\lambda|$ is introduced into $\mathbf{F}_{HLL}$ or $\mathbf{F}_{HLLC}$ resulting in

$$\mathbf{F}^{\lambda}_{HLL(C)} = \frac{1}{2}\left(\mathbf{F}_L + \mathbf{F}_R\right) - \frac{1}{2}|\lambda| \left(\mathbf{U}_R - \mathbf{U}_L\right). \tag{21}$$

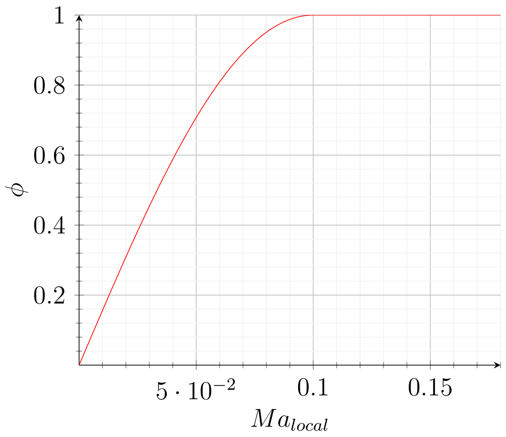

Fig. 2. Dependence of the activation function ϕ on the local Mach number Ma_{local} with $Ma_{limit} = 0.1$.

Now, the HLL(C) flux can be seen as a Lax-Friedrichs flux where the dissipation has been split into two (HLL), or three (HLLC) differently weighted contributions representing the general wave system of the underlying Riemann problem.

In the original formulation of the HLLC approximation (4), advection and acoustic contributions to the numerical dissipation are difficult to separate. However, the proposed central formulation of the HLLC solver allows for a separation of both contributions in analogy with the Roe flux, which is given by

$$\mathbf{F}_{Roe} = \frac{1}{2}\left(\mathbf{F}_L + \mathbf{F}_R\right) - \frac{1}{2}\mathbf{R}\left|\mathbf{\Lambda}\right|\mathbf{R}^{-1}\left(\mathbf{U}_R - \mathbf{U}_L\right). \tag{22}$$

The first part both in Eq. (19) and Eq. (22) is the central flux term, and the second term is the dissipation flux term, which is characteristic for each solver. The advection dissipation of the Roe flux is proportional to the eigenvalue $|u|$, and the acoustic dissipation of the Roe flux is proportional to the eigenvalues $|u \pm c|$. Analogously, the acoustic dissipation of the HLLC flux is related to the first and third term of the dissipation flux term as both terms are proportional to the acoustic signal speed S_L, respectively S_R. The advection dissipation is related to the center term, which is proportional to the contact signal speed S_*. Note that the situation for the HLLC flux is more complex than for the Roe flux since S_L and S_R also contribute to S_*, $\mathbf{U}_{*L}$ and $\mathbf{U}_{*R}$. However, the results of this paper indicate that the main contributions of advection and acoustic dissipation can be distinguished as discussed.

3.3. HLLC-LM flux with low Mach number correction

The main goal of the proposed modification is to balance the vanishing advective and dominant acoustic dissipation in the low Mach number limit by a reduction of overall dissipation. The central formulation of the HLLC flux given by Eq. (18) and Eq. (19) enables a straightforward application of the Mach number dependent reduction of nonlinear signal speeds according to

$$S_L^{HLLC-LM} = \phi \cdot S_L, \qquad S_R^{HLLC-LM} = \phi \cdot S_R \tag{23}$$

with

$$\phi = \sin\left(\min\left(1, \frac{Ma_{local}}{Ma_{limit}}\right) \cdot \frac{\pi}{2}\right) \tag{24}$$

and

$$Ma_{local} = \max\left(\left|\frac{u_L}{c_L}\right|, \left|\frac{u_R}{c_R}\right|\right). \tag{25}$$

u denotes the velocity component dependent on the direction of the cell-face Riemann problem. $S_L^{HLLC-LM}$ and $S_R^{HLLC-LM}$ are only applied for the final flux evaluation in Eq. (19). All previous procedures, especially the calculation of S_*, $\mathbf{U}_{*L}$ and $\mathbf{U}_{*R}$, are performed using the original values for S_L and S_R.

The application of the sine function in Eq. (24) causes a smooth decay of the acoustic dissipation as depicted in Fig. 2. The reference parameter Ma_{limit} is set to 0.1 for all calculations presented in this paper. This selection ensures that the modification will only be active if the local flow speed component is less than ten percent of the local sound speed. Otherwise, the classical HLLC formulation is fully recovered. The new scheme, denoted as HLLC-LM in the following, fully preserves the favorable low dissipation of HLLC at the contact line as the acoustic dissipation of HLLC-LM is reduced proportionally to the level of local velocities instead of the speed of sound for low Mach numbers while the advection dissipation remains unchanged.

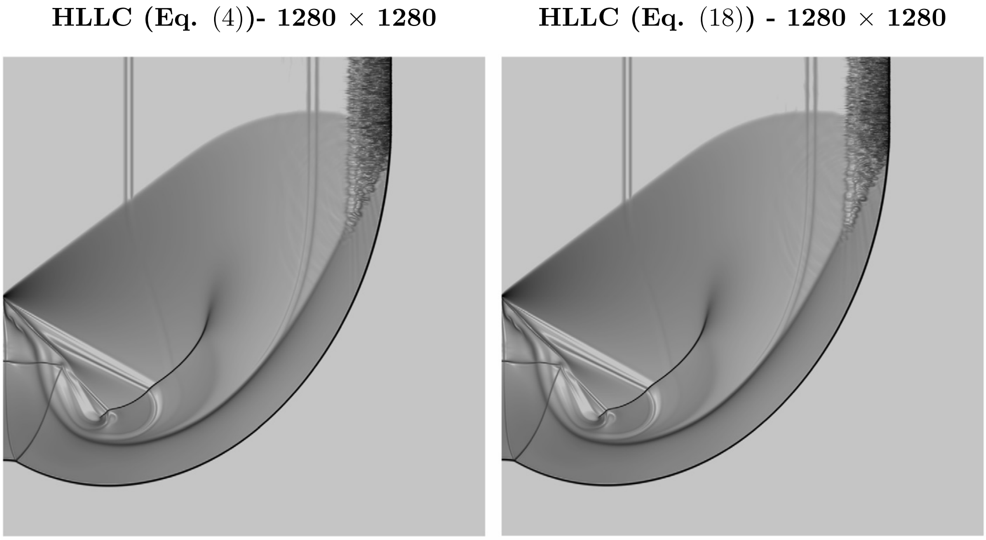

Fig. 3. Comparison of the classical HLLC formulation with the central HLLC formulation for the corner diffraction of a Mach 5.09 shock wave: logarithmic gradients of density from 1 to 1,000 at $t = 0.157$.

4. Central aspects of the grid-aligned shock instability with HLLC-type solvers demonstrated for classical test cases

The calculations in this section serve to study the evolution of the numerical shock instability when HLLC-type solvers are applied in combination with high-order schemes. Moreover, the stability of the HLLC-LM scheme with respect to the grid-aligned shock problem is demonstrated for a comprehensive set of cases with strong moving shocks that are prone to exhibiting this instability. If not mentioned otherwise, all calculations were performed using the classical fifth-order WENO scheme [26] for spatial discretization combined with a third-order strong-stability-preserving Runge-Kutta time integration [27] and the approximate Riemann solvers as described in the previous sections. The effective range of the shock-transverse Mach number modification in the HLLC-LM solver is always limited to local Mach numbers lower than 0.1. The fluid is modeled as ideal gas with $\gamma = 1.4$. The CFL number is set 0.6 for single-phase cases and 0.4 for cases with interfaces employing the level-set approach. The combination of a multiresolution procedure [35] and an adaptive local time stepping [36] enables efficient computation with high effective resolutions. In the following, the given resolution information defines the finest level. Shocks are discretized with the highest resolution in all presented cases due to the applied refinement criteria, whereas material interfaces are by definition on the highest level.

4.1. Corner flow problem I: verification of centralized HLLC formulation

As a first step, the proposed centralized HLLC formulation given in Eq. (18) and Eq. (19) is verified against the classical HLLC procedure for the diffraction of a shock wave around a sharp corner. This is a well-established test case, where the instability of the HLLC flux becomes apparent. This case was already selected by Quirk [6] to demonstrate the failure of low-dissipation Riemann approximations. Additionally, the problem yields complex flow patterns. Thus, it is well suited to compare results of different solvers and to verify our reformulations.

We use a domain of size $[0, 1] \times [0, 1]$, that is uniformly initialized with $(\rho, u, v, p) = (1, 0, 0, 1/1.4)$ and discretized by 1280×1280 cells. Reflecting-wall boundary conditions are set everywhere, except for the upper left boundary at $x = 0$ from $y = 0.5$ to $y = 1$. Here, the post-shock condition of a Mach 5.09 shock wave is prescribed. The final time is set to $0.8/Ma$. Even though the first-order HLLC approximation is known to be positivity preserving, this property is not guaranteed for high-order extensions [37]. We encountered instabilities in the vicinity of the corner point of the backward facing step at the inflow for all tested variants of the HLLC flux when combined with a fifth-order WENO scheme. Therefore, simulations were performed using a third-order WENO scheme [26].

Fig. 3 and Fig. 4 show schlieren images of the density gradients at the final time of the simulation. The results shown in the left frame of Fig. 3 are obtained applying the original HLLC formulation given in Eq. (4), whereas results shown in the right frame of Fig. 3 are obtained applying the centralized HLLC formulation given in Eq. (18) and Eq. (19). As expected, there are no distinguishable differences for both formulations. Moreover, all other test cases presented in this paper have been investigated without encountering any differences exceeding the floating-point roundoff error. We therefore conclude that Eq. (18) with Eq. (19) is a valid alternative representation of the HLLC flux.

4.2. Corner flow problem II: stability of HLLC-LM formulation

As a second step, the stability of the HLLC-LM scheme is demonstrated. The aforementioned corner flow simulations show severe disturbances in the backflow of the leading shock front similar to results obtained with the Roe Riemann

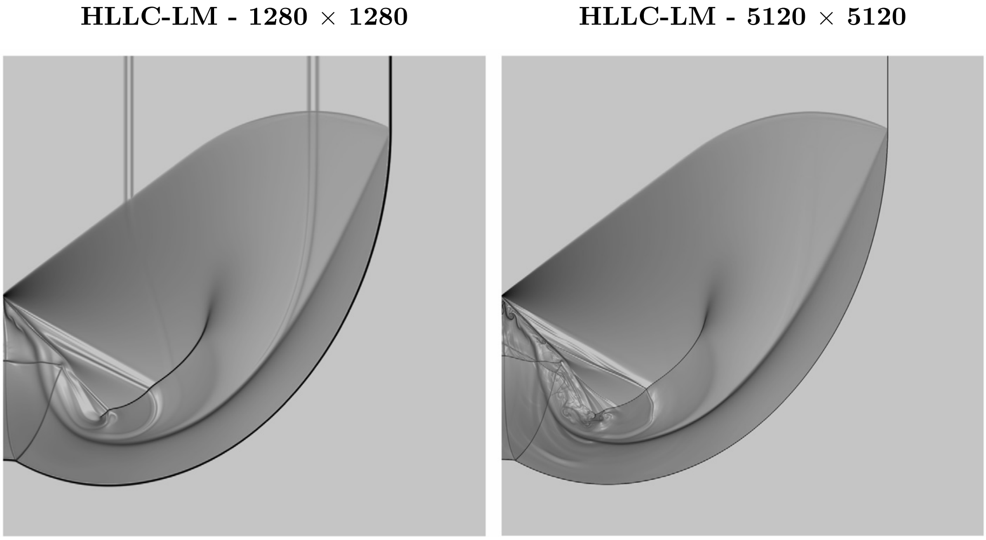

Fig. 4. Corner diffraction of a Mach 5.09 shock wave: logarithmic gradients of density from 1 to 1,000 at $t = 0.157$.

solver [6]. The left frame of Fig. 4 shows that the HLLC-LM is able to capture all details of the flow while preventing any disturbances of the shock wave. Additionally, a high-resolved simulation is performed using 16 times smaller cells. Typically, the instability is enhanced by higher resolutions, however, the results presented in the right frame of Fig. 4 are still free of any instability.

4.3. *Rayleigh Taylor instability: numerical dissipation at contact lines*

The inherent numerical dissipation of the original HLLC flux and HLLC-LM flux is compared by investigating a classical Rayleigh-Taylor instability. Two initial gas layers with different densities are exposed to gravity with unity magnitude, where the resulting acceleration is directed towards the lighter fluid. A small disturbance of the contact line triggers the instability. The computational domain is given by $[0, 0.25] \times [0, 1]$ and the interface initially is placed at $y = 0.5$. Initial states are given by $(\rho, u, v, p)_{y \leq 0.5} = (2, 0, -0.025c \cdot cos(8\pi x), 2y + 1)$ and $(\rho, u, v, p)_{y>0.5} = (1, 0, -0.025c \cdot cos(8\pi x), y + 1.5)$, where the speed of sound is $c = \sqrt{\frac{\gamma p}{\rho}}$ with $\gamma = \frac{5}{3}$. Top and bottom boundary states are fixed to $(1, 0, 0, 2.5)$ and $(2, 0, 0, 1)$, respectively. Symmetry boundary conditions are imposed at the left and right boundary.

The final density evolution for both solvers is shown in Fig. 5 for a resolution of 128 × 512. Results indicate a significant reduction of dissipation at the contact line when the HLLC-LM flux is applied instead of the original HLLC flux.

4.4. *Quirk's odd-even decoupling test: quantitative evaluation of the shock instability*

The results of the Section 4.2 indicate the effectiveness of the proposed method qualitatively, however, a detailed quantitative study is difficult to perform for the corner flow problem. For this purpose, the simple plane shock propagation along a rectangular duct with a defined disturbance level is studied. This test case was also proposed by Quirk [6] due to its simple setup. Nevertheless, it provides an effective and reliable way to trigger the odd-even decoupling near strong shocks, which is related to the grid-aligned shock instability. Moreover, it allows for a simple quantitative study of the rise of the instability.

The domain is set to $[0, 2400] \times [0, 20]$, and discretized with 2400 × 20 cells. Inflow and outflow conditions are applied at the left and at the right boundary, respectively. Reflecting wall conditions, which are equivalent to symmetry boundary conditions for inviscid flows, are enforced both at the top and at the bottom boundary of the domain. Pre-shock density and pressure are set to unity, and all velocity components are set to zero. Artificial numerical noise is introduced to all primitive variables in the initial state to trigger the instability [38,8]. We have performed simulations with the original Mach 6 setup and with a Mach 20 setup with initial conditions given by

$$(\rho, u, v, p) = \begin{cases} (1, 0, 0, 1) & \text{if } x > 5, \\ \left(\frac{216}{41}, 35\frac{\sqrt{35}}{36}, 0, \frac{251}{6}\right) & \text{else (for } Ma = 6 \text{ case)}, \\ \left(\frac{160}{27}, \frac{133}{8}\sqrt{1.4}, 0, 466.5\right) & \text{else (for } Ma = 20 \text{ case)}, \end{cases} \tag{26}$$

where the shock front is initially placed at $x = 5$. Both simulations are performed up to a late point in time till the shock front approaches the end of the domain. The final time is set to 330 for the low Mach number simulation and to 100 for the high Mach number simulation, respectively.

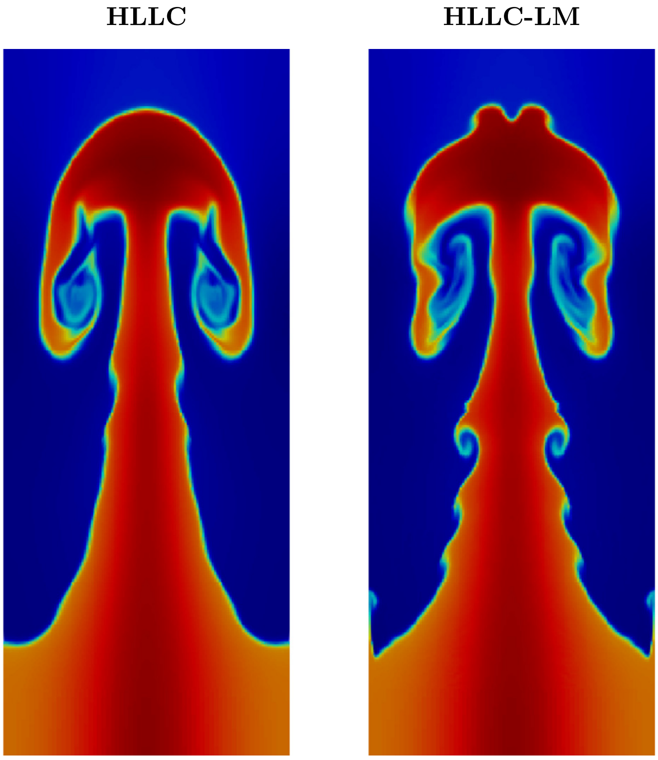

Fig. 5. Rayleigh-Taylor instability $t = 1.95$: density contours from 0.85 (blue) to 2.25 (red). (For interpretation of the colors in the figure(s), the reader is referred to the web version of this article.)

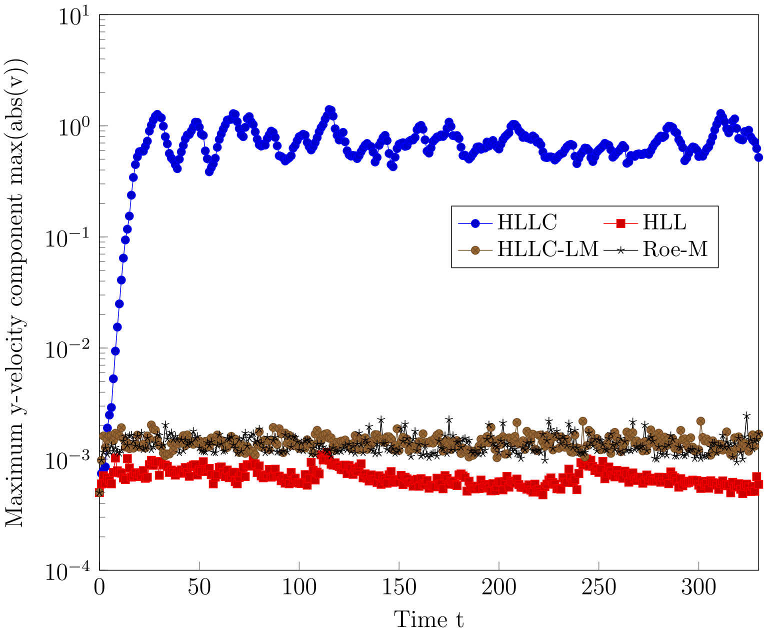

Fig. 6. Instability progress in Quirk's test case for Mach 6.

The maximum magnitude of the y-velocity component v in the domain provides a reasonable measure of the deviation from the one-dimensional solution, and therefore, it is well suited to monitor the growth rate of the disturbance quantitatively over time. Fig. 6 and Fig. 8 show the evolution of the velocity deviation for the Mach 6 and the Mach 20 case for different flux approximations when all initial primitive variables are superposed by uniform random perturbations ranging from $-0.5 \cdot 10^{-3}$ to $0.5 \cdot 10^{-3}$. In addition, the final density distributions are presented in Fig. 7 and Fig. 9. Besides the results for the discussed HLLC and HLLC-LM fluxes, the results for the more dissipative HLL flux [3] and the shock-stable Roe-M flux [8] are provided for comparison.

Simulations with the classical HLLC solver show an exponential instability where instabilities saturate at $\mathcal{O}(1)$ at around $t = 20$ for the low Mach number case and at around $t = 5$ for the high Mach number case. Unlike the Roe approximation,

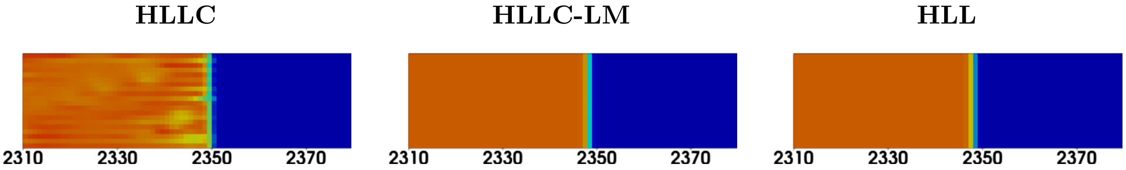

Fig. 7. Quirk's test case for Mach 6: color map of density from blue = 1.0 to red = 6.8 at $t = 330$.

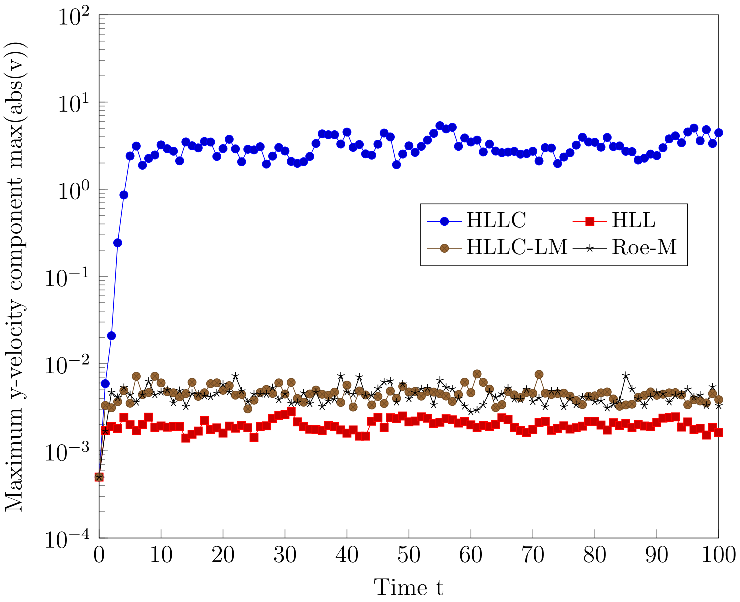

Fig. 8. Instability progress in Quirk's test case for Mach 20.

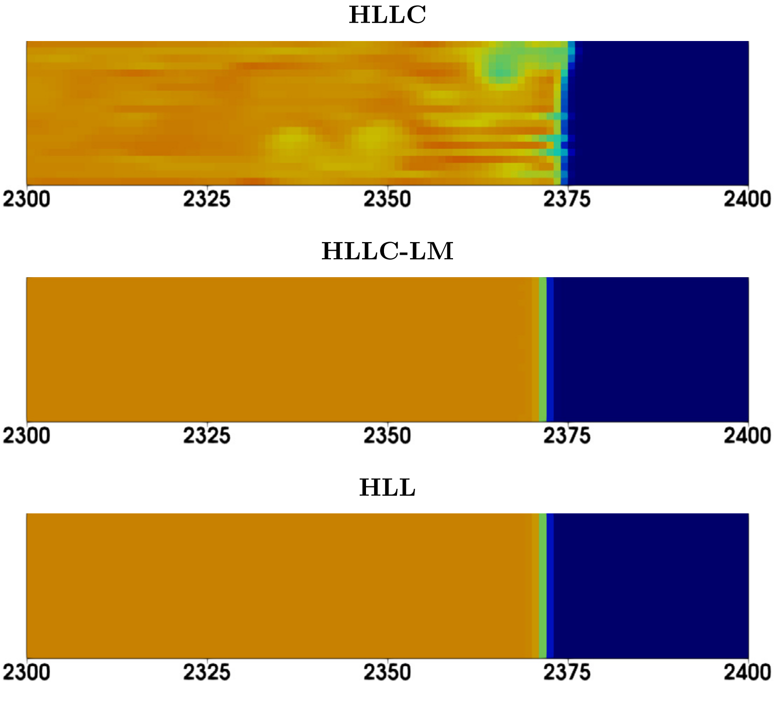

Fig. 9. Quirk's test case for Mach 20: color map of density from blue = 1.0 to red = 8.0 at $t = 100$.

the HLLC flux forms no distinct carbuncles, and density disturbances remain bounded. However, the instability disturbs the shock front significantly as shown in the left frame, respectively top frame, of Fig. 7 and Fig. 9. Moreover, when the final position of the shock front is compared to the analytically predicted position, an incorrect wave speed is obtained. This effect is even more dominant for the high Mach number case. With the modified HLLC-LM scheme, the stable and analytically predicted result is obtained as depicted in the middle frames of Fig. 7 and Fig. 9. The magnitude of disturbances

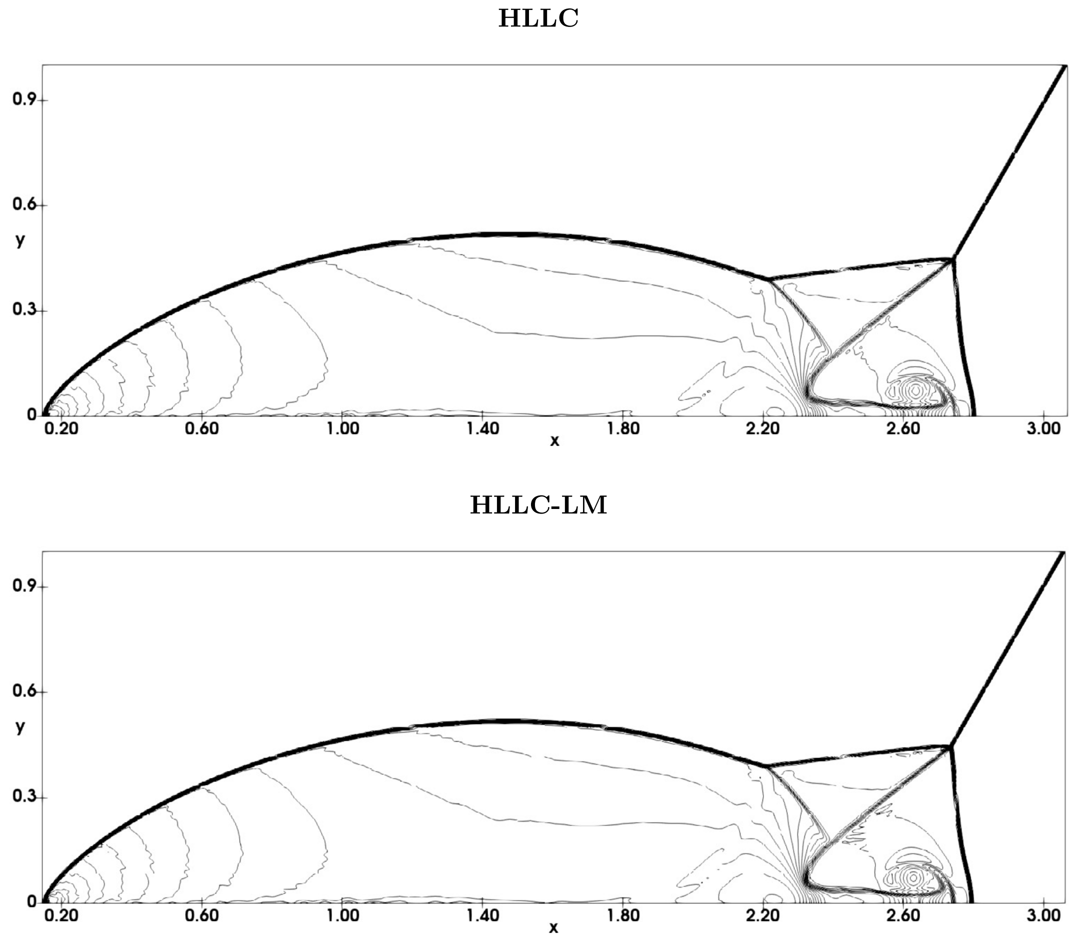

Fig. 10. Double Mach reflection of a Mach 10 shock wave: 40 density contours from 1.88783 to 20.9144 at $t = 0.2$.

is similar to the one obtained with the Roe-M formulation [8] and slightly higher than the one obtained with the HLL flux for both cases. The lower disturbances of the HLL flux can be explained by a significantly higher level of inherent dissipation of the scheme. However, no major differences can be observed in the qualitative density results for HLL and HLLC-LM, e.g. middle and bottom frame of Fig. 9.

4.5. Double Mach reflection problem: effect of resolution

Several numerical schemes encounter difficulties when simulating a double Mach reflection as proposed by Woodward and Colella [39]. The leading Mach stem may be kinked in consequence of the numerical shock instability [6,7]. The test case represents a Mach 10 shock wave hitting a solid ramp with an angle of 30 degrees. The initial shock wave is set up with

$$(\rho, u, v, p) = \begin{cases} (1.4, 0, 0, 1) & \text{if } y < \sqrt{3}\,(x - 1/6)\,, \\ \left(8, 33\frac{\sqrt{3}}{8}, -4.125, 116.5\right) & \text{else.} \end{cases} \tag{27}$$

A Neumann boundary condition with zero gradients for all variables is applied at the left, right and upper boundary. Along the bottom boundary, at $y = 0$, the region from $x = 0$ to $x = 1/6$ is always assigned post-shock conditions, whereas reflecting-wall conditions are imposed from $x = 1/6$ to $x = 4$. The domain size of $[0, 4] \times [0, 6.67]$ is chosen large enough to avoid any disturbances entering the domain at the upper boundary. The domain is discretized with 960×1600 cells and the final time is set to $t = 0.2$. Besides the large vertical domain size, this setup is commonly chosen in literature [40].

The final density contours for both HLLC and HLLC-LM are shown in Fig. 10. Both schemes deliver almost identical results with no visible deflection at the leading Mach stem. However, if the resolution is increased to 1920×3200 cells and the final time is set to $t = 0.28$ the results for both schemes differ significantly as shown in Fig. 11. A kinked Mach stem, together with a severe disturbance of the wall jet can be observed for the original HLLC scheme, whereas the HLLC-LM scheme is free of any instability.

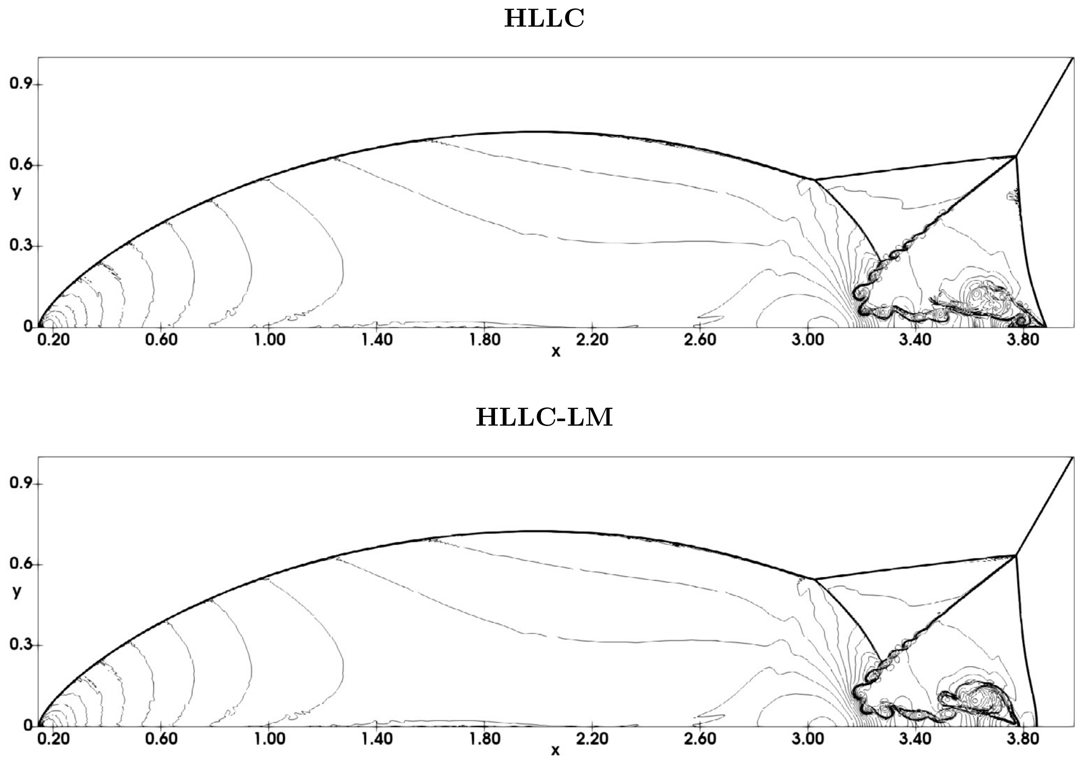

Fig. 11. Double Mach reflection of a Mach 10 shock wave: 40 density contours from 1.88783 to 20.9144 at $t = 0.28$.

4.6. Supersonic flow around cylinder: steady shock position

The next case predicts the bow shock resulting from a supersonic flow around a stationary cylinder. This case was first described by Peery and Imlay [5] to suffer from the carbuncle phenomenon. Unlike the other cases in this paper, the relevant shock wave is not moving, which renders the case particularly challenging for high-order shock-capturing schemes with explicit time integration. Following the argumentation in [8], we do not change the Cartesian grid nor the time integration, which likely results in a small resolved level of fluctuations around the steady shock due to the high order of the applied scheme. We include this case for the sake of completeness even though the application of high-order schemes here is not expected to reveal additional information for such configurations compared to low-order schemes.

The circular reflecting-wall condition representing the cylinder is approximated using a level-set approach [41]. At the left and the remaining right boundary inflow and outflow conditions are applied, respectively. Top and bottom boundary conditions are set to Neumann boundary conditions with zero gradient for all variables. Two different Mach numbers, $Ma = 3$ and $Ma = 20$, are studied with initial states $(\rho, u, v, p) = \left(1, \sqrt{1.4} \cdot Ma, 0, 1\right)$. The domain size is set to $[0, 0.3] \times [0, 0.8]$ for the lower Mach number, and $[0, 0.3] \times [0, 0.6]$ for the higher Mach number. Final times are chosen large enough to reach a fully developed bow shock. The cylinder with a diameter $D = 0.2$ is placed at the center of the right boundary and resolved by 160 cells per diameter.

Besides the HLLC and the HLLC-LM schemes, the more dissipative HLL scheme is also applied. Fig. 12 and Fig. 13 show the resulting pressure distributions and Mach contour lines that are chosen identical to [7] for both Mach number flows. All three schemes show comparable results for both Mach numbers. Note that also the HLL scheme reveals some disturbances in the backflow of the steady shock. These disturbances of the HLL scheme in combination with high-order methods have been reported in literature [42]. None of the schemes suffers from the carbuncle phenomenon with the described Cartesian setup. Moreover, the HLLC-LM scheme has been tested for a significantly increased resolution of 640 cells per diameter, where it still delivers stable results as shown in the right frames of Fig. 12 and Fig. 13.

4.7. The Sedov blast wave: comparison of shock instability in two and three dimensions

The next case of this section is the classical Sedov blast wave [43,37,7]. Due to its symmetry, the Sedov blast wave simulation is suitable to demonstrate the effect of the grid alignment on the numerical shock instability [8]. The test case consists of a high pressure area covering only few cells that is initiated at the center of the domain. The rest of the domain is set to a near vacuum state. The whole domain is initially at rest. The initial states are given by

$$(\rho, u, v, p) = \begin{cases} \left(1, 0, 0, 3.5 \cdot 10^5\right), & \text{if } \sqrt{x^2 + y^2} < 0.005, \\ \left(1, 0, 0, 10^{-10}\right), & \text{otherwise.} \end{cases} \tag{28}$$

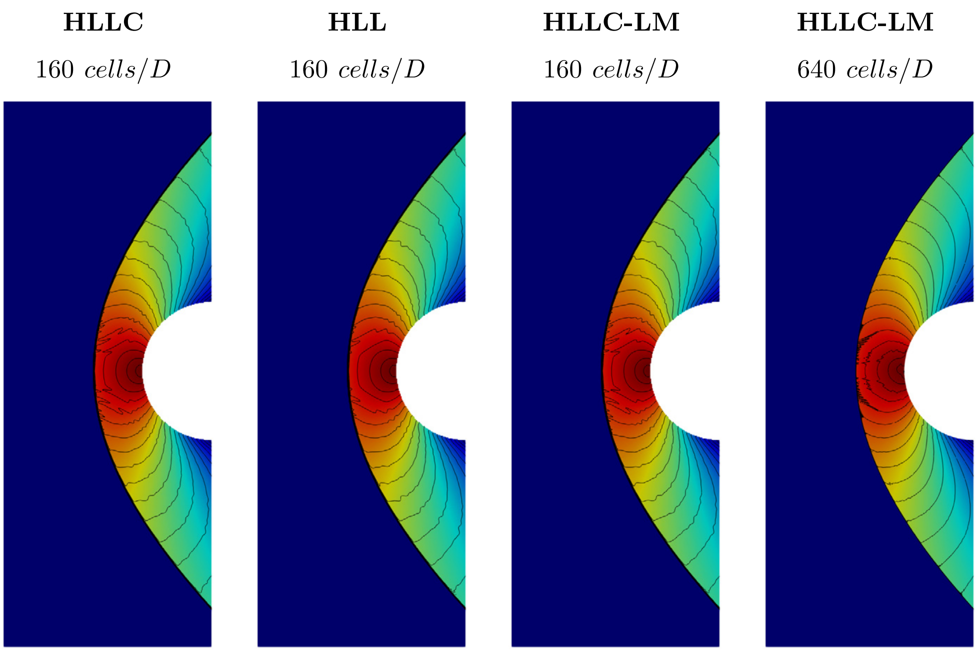

Fig. 12. Supersonic flow around cylinder $Ma = 3$ at $t = 1.5$: color pressure map (blue = 1.0 to red = 12.1) is overlaid by 25 Mach contours (0.1 to 2.5).

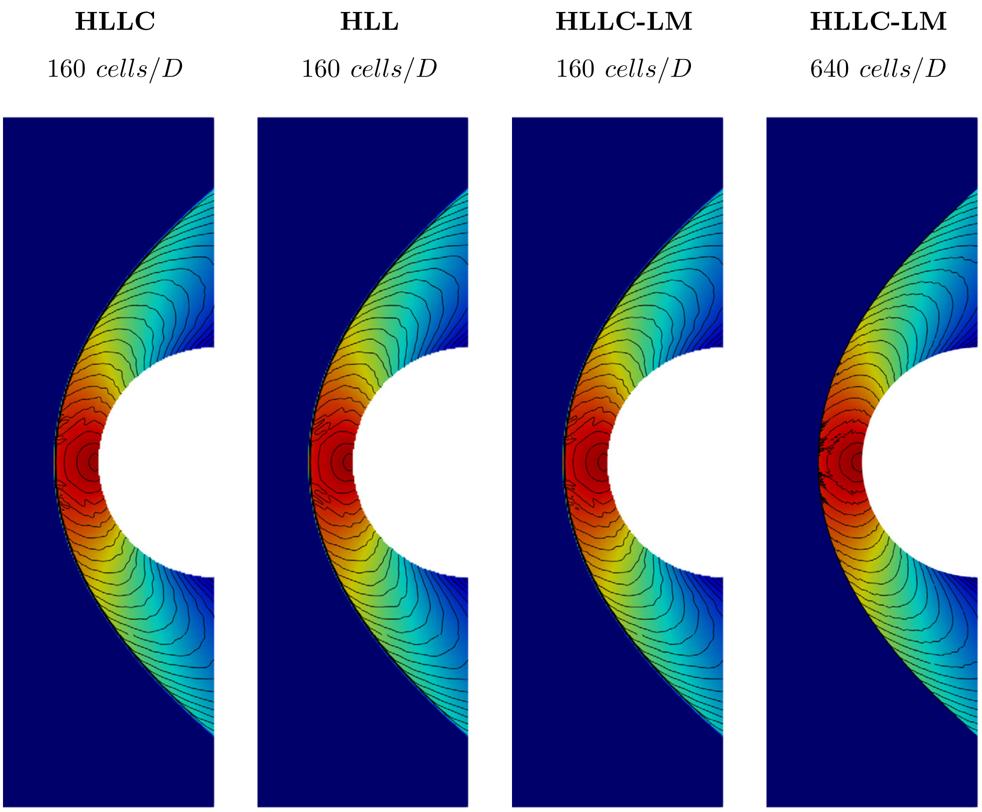

Fig. 13. Supersonic flow around cylinder $Ma = 20$ at $t = 0.5$: color pressure map (blue = 1.0 to red = 550) is overlaid by 25 Mach contours (0.1 to 2.5).

Reflecting-wall conditions are applied at all boundaries. The domain size is set to $[-1.2, 1.2] \times [-1.2, 1.2]$, and it is resolved by 960×960 cells. The final time is set to 0.1.

The schlieren image for logarithmic density gradients is given in Fig. 14 when using the HLLC flux and the HLLC-LM flux. At locations where the shock front propagates aligned with the computational grid, disturbances behind the shock wave can be observed. The magnitude of disturbances is smaller than for the Roe flux [8] and no carbuncles occur. The results obtained with the HLLC-LM flux are free of any disturbance.

Finally, we extend the problem to three dimensions in a straightforward way. The domain size is set to $[-2, 2] \times [-2, 2] \times [-2, 2]$ and is resolved by a resolution of $640 \times 640 \times 640$ cells. In order to save computational cost, only one-eighth of the

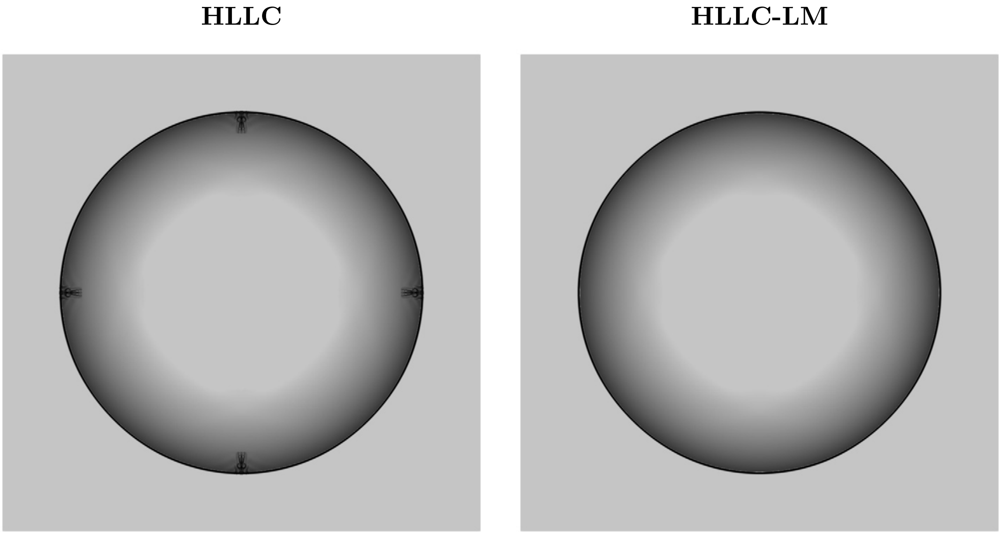

Fig. 14. Two-dimensional Sedov blast wave: logarithmic gradients of density from 1 to 500 at $t = 0.1$.

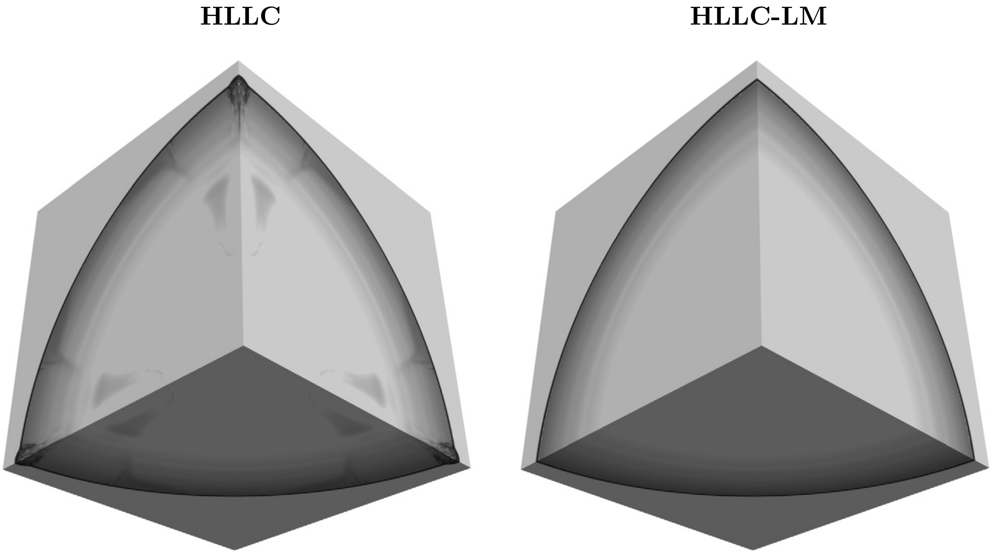

Fig. 15. Three-dimensional Sedov blast wave: logarithmic gradients of density from 1 to 500 at $t = 0.1$.

given domain is simulated and appropriate symmetry boundary conditions are applied. The setup is chosen according to Tasker et al. [43], where initial states are

$$(\rho, u, v, w, p) = \begin{cases} \left(1, 0, 0, 0, 23.757239 \cdot 10^{6}\right), & \text{if } \sqrt{x^2 + y^2 + z^2} < 0.0875, \\ \left(1, 0, 0, 0, 1 \cdot 10^{-10}\right), & \text{otherwise} \end{cases} \tag{29}$$

with $\gamma = \frac{5}{3}$. The final time again is set to 0.1.

Results for the three-dimensional Sedov blast wave are shown in Fig. 15 for both HLLC and HLLC-LM. Differently from the two dimensional case, the three-dimensional simulation reveals an increased level of disturbances and the occurrence of significant carbuncles for the HLLC flux. This indicates that the instability is enhanced for three-dimensional simulations. Following the argumentation of Section 3, this behavior can be explained as follows. A three-dimensional shock wave that propagates along one coordinate axis suffers from an excessive acoustic dissipation that is now introduced from two sides as the fluxes in both other directions have a vanishing Mach number. As expected, the reduction of acoustic dissipation in the HLLC-LM scheme also helps to prevent the grid-aligned shock instability in three-dimensional simulations.

4.8. Subsonic flow around cylinder: low Mach number flow

In addition to the shock-dominated flow problems presented before, the performance of the proposed HLLC-LM scheme also is tested in the global low Mach number regime using the well-known test case of a subsonic flow around a cylinder.

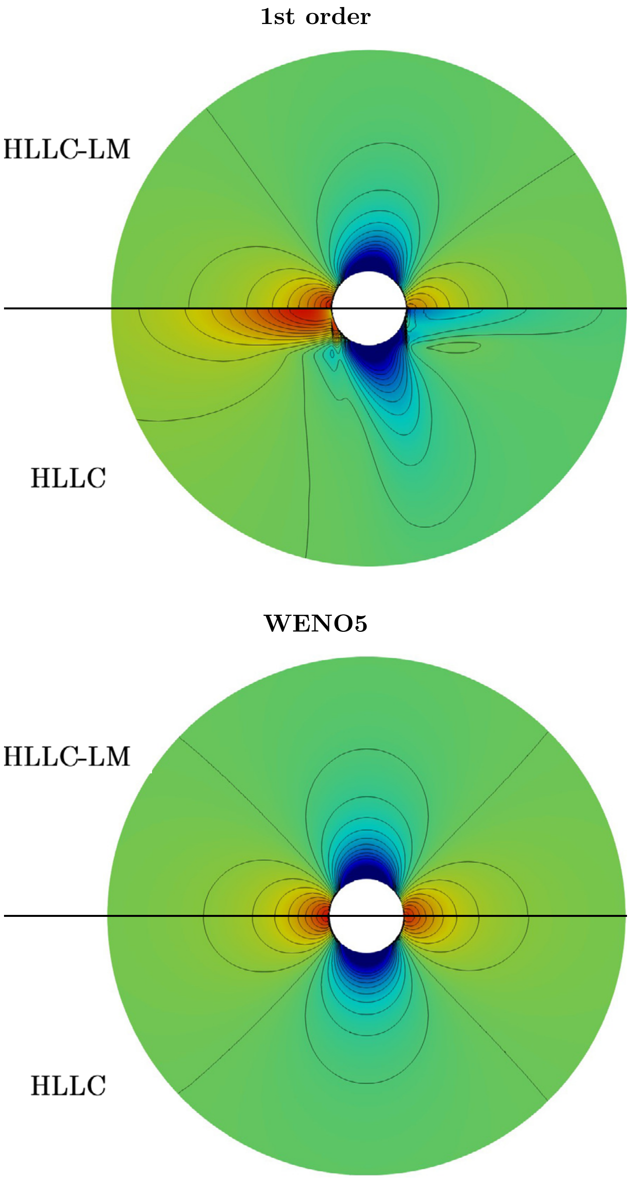

Fig. 16. Flow around a cylinder at $Ma = 0.01$ using first order (top) and WENO5 (bottom): color density map (blue = 0.99993 to red = 1.00007) is overlaid by 21 contour lines for normalized pressure fluctuations from $-7 \cdot 10^{-5}$ to $7 \cdot 10^{-5}$.

This flow configuration is troublesome for Godunov schemes in combination with Riemann solvers as comprehensively discussed in literature, e.g. [29]. Different modifications to Riemann solvers and preconditioning techniques have been proposed to increase the simulation accuracy of low Mach number flows [32,30,31].

The domain of size $[0, 80D] \times [0, 80D]$ is set large enough to avoid any interaction of reflected waves, which is crucial for the high-order simulation. The cylinder is placed in the center of the domain with a diameter $D = 1$. Initial density and pressure are set to unity in the entire domain. The initial velocity of $u = 0.01 \cdot \sqrt{1.4}$ results in a free-stream Mach number of 0.01. At all boundaries we apply Neumann boundary conditions with zero gradient for all variables. The effective resolution is set to 128 cells per diameter. The final time $t = 30$ is large enough to approach a steady state before disturbances due to reflections at the domain boundaries affect the region of interest around the cylinder. Note that the application of high-order schemes in combination with explicit time integration for the fully compressible evolution equations renders low Mach number simulations particularly expensive.

Fig. 16 shows the density distribution in the relevant region around the cylinder and 21 isocontours for pressure fluctuations $\delta p = p - p_0$ between $\pm\gamma Ma^2/2 = \pm 7 \cdot 10^{-5}$ similarly to [29] for HLLC and HLLC-LM using both a first-order and a WENO5-JS spatial discretization.

The fully symmetric flow field obtained with WENO5 shows excellent agreement with the expected result. In either case, the HLLC-LM solver shows similar or better performance than the original HLLC. Nevertheless, it should be pointed out that the HLLC-LM solver is primarily designed for applications in the high Mach number regime that suffer from shock instabilities. Due to the decreasing numerical dissipation in the low Mach number limit we expect the occurrence of pressure-velocity decoupling when the Mach number is further reduced.

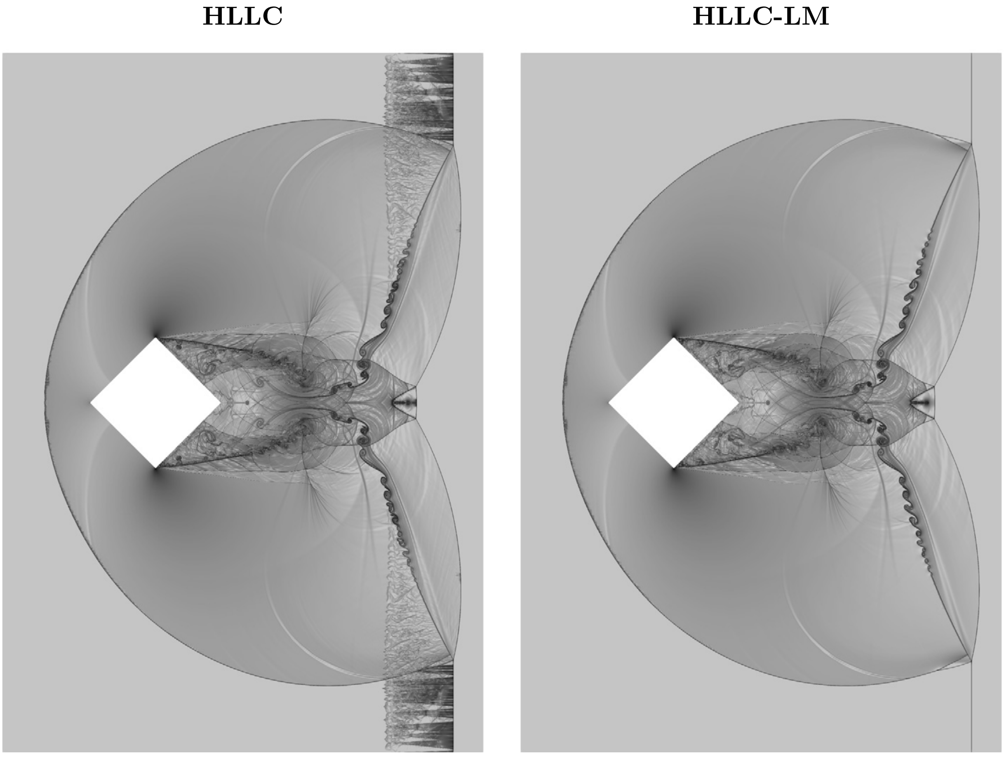

Fig. 17. Supersonic flow around a diamond-shaped obstacle with $Ma = 2.85$: logarithmic gradients of density from 1 to 1000 at $t = 0.5$.

5. Application to complex flow situations

The main motivation for the application of high-order low-dissipation schemes is an accurate prediction of highly complex flow situations. Therefore, we studied three additional types of test cases that involve interaction of shock waves with nontrivial structures and recent examples of multi-component flow simulations using the level-set approach [41].

5.1. Supersonic flow around diamond-shaped obstacle

The first example of a highly complex flow evolution is the supersonic flow around a diamond-shaped obstacle. The Mach number of 2.85 is chosen to be high enough to form a double Mach reflection during and after the shock wave propagates over the diamond [44]. The sharp geometry changes result in extremely complex flow patterns in the wake of the diamond. In addition to the double Mach reflection, this case also involves a bow shock in front of the obstacle and the classical odd-even decoupling situation near the leading shock wave. This makes the case particularly interesting to study in the context of this paper.

The shock wave is initialized with

$$(\rho, u, v, p) = \begin{cases} (3.714, 2.464, 0, 9.310) & \text{if } x < 0.375 \\ (1, 0, 0, 1) & \text{else,} \end{cases} \tag{30}$$

and the center of the diamond is placed at $x = 0.7$ and $y = 1.6$ with a distance $D = 0.6$ from corner to corner. The domain size is set to $[0, 2.2] \times [0, 3.2]$ and it is discretized with 7040×10240 cells. The final time is set to 0.5. Neumann boundary conditions with zero gradients for all variables are applied at the lower and upper boundary. Inflow and outflow conditions are imposed at the left and right boundary. The reflecting-wall condition representing the diamond is again approximated using a level-set approach [41].

Fig. 17 shows the final schlieren images of density gradients using both HLLC and HLLC-LM. An obvious disturbance behind the leading shock wave develops when the classical HLLC approximation is applied. This is caused by an odd-even decoupling effect, similarly to the corner flow presented in Section 4. Again, the HLLC-LM flux fully removes the disturbance. Note, that the complex flow evolution is not affected by the low Mach number correction. Further details can be observed within the double Mach reflection zone as shown in the zoomed region given in Fig. 18. The proposed HLLC-LM scheme results in a stable and disturbance-free flow field behind the leading Mach stem. Moreover, the decreased numerical dissipation of the HLLC-LM flux becomes apparent when the resolution of the wave patterns is compared.

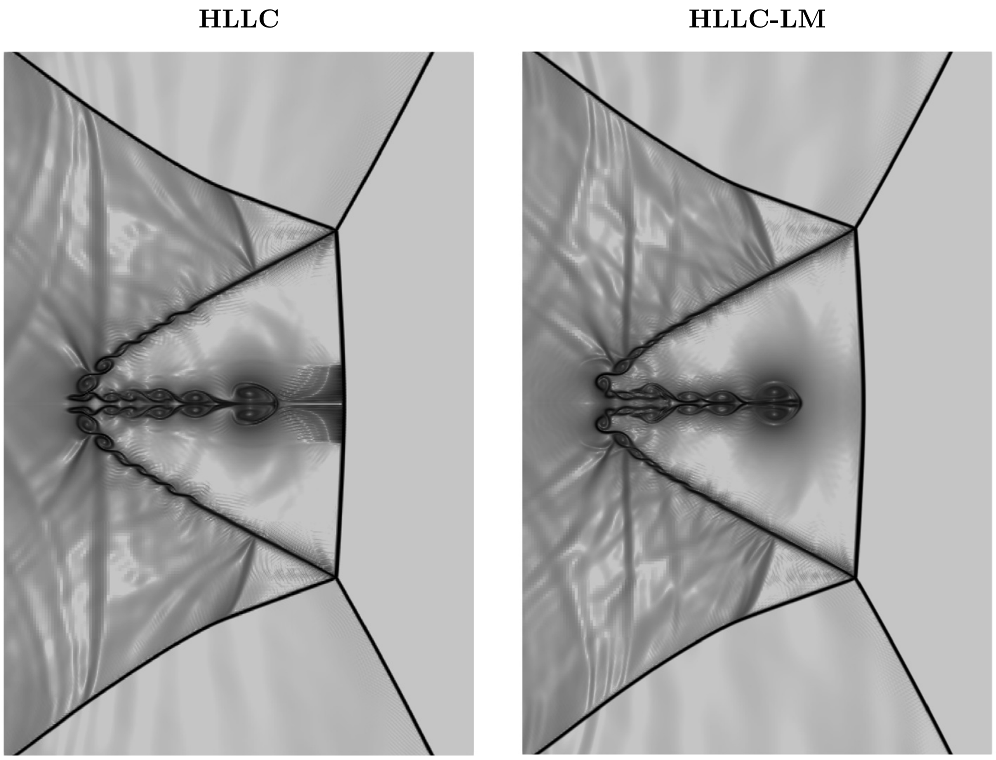

Fig. 18. Zoom on double Mach reflection in supersonic flow around a diamond-shaped obstacle with $Ma = 2.85$: logarithmic gradients of density from 1 to 1000 at $t = 0.5$.

5.2. Shock interface interaction: helium bubble in air

Another important application of high-order methods is the prediction of multi-component flows. In [8], it was shown that the grid-aligned shock instability limits the numerical investigation of shock-interface interaction problems. The same case of the interaction of a Mach 6 shock wave in air ($\gamma = 1.4$) with a helium bubble ($\gamma = 1.66$) is now studied with HLLC-type solvers.

Initial states are given by

$$(\rho, u, v, p) = \begin{cases} \left(\frac{216}{41}, 35\frac{\sqrt{35}}{36}, 0, \frac{251}{6}\right) & \text{air post-shock,} \\ (1, 0, 0, 1) & \text{air pre-shock,} \\ (0.138, 0, 0, 1) & \text{helium,} \end{cases} \tag{31}$$

where the shock is placed initially at $x = 0.05$. A helium bubble with initial diameter $D = 0.05$ is placed at $x = 0.1$, $y = 0.15$ within in a domain of size $[0, 0.4] \times [0, 0.3]$. Inflow and outflow conditions are applied at the left and right boundary, respectively. Neumann boundaries with zero gradient for all quantities are set at the remaining boundaries. The resolution is set to 1280×960, which resolves the helium bubble with 160 cells per diameter. The final time of the simulation is set to 0.035.

Fig. 19 shows the final density results for both HLLC and HLLC-LM. The numerical instabilities at the shock front induced by the HLLC approximation are not as dominant as for the Roe approximation [8]. Especially, no carbuncles can be observed. Instead, an odd-even decoupling develops in the backflow of the shock wave similar to the one observed for the previous example. As before, the HLLC-LM scheme produces a clean shock front without any disturbances. Moreover, the stability of the proposed scheme is tested for an extreme resolution of 1280 cells per diameter. The results shown in Fig. 20 still do not indicate any instability.

5.3. Shock interface interaction: air bubble in water in two and three dimensions

Finally, the challenging simulation of a strong 1.6 GPa shock wave in water interacting with an embedded air bubble was studied. The strong transmitted shock wave in air may suffer from the grid aligned-shock instability. First, the simulations in [8] were repeated in two dimensions with the HLLC-type solvers. Afterwards, a new fully three-dimensional simulation of the problem is presented.

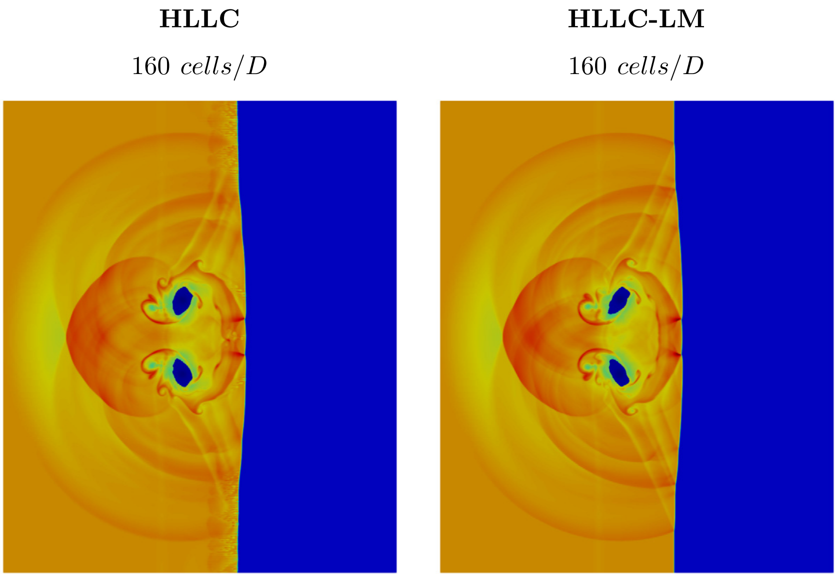

Fig. 19. Shock interface interaction of a helium bubble in air I: density contours from blue = 0.138 to red = 7.5 at $t = 0.035$.

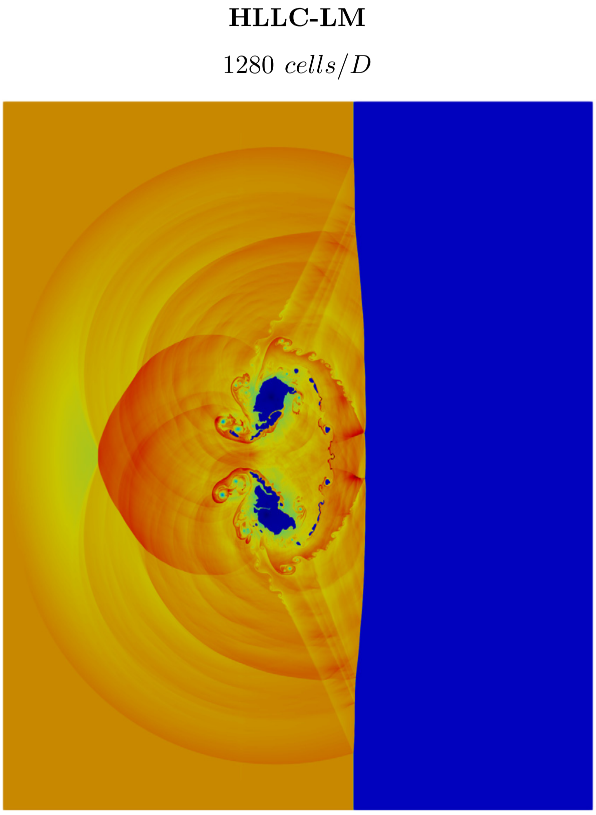

Fig. 20. Shock interface interaction of a helium bubble in air II: density contours from blue = 0.138 to red = 7.5 at $t = 0.035$.

The setup is chosen similar to [45] with initial states

$$(\rho, u, v, p) = \begin{cases} \left(1323.65, 661.81, 0, 1.6 \cdot 10^9\right) & \text{water post-shock} \\ \left(1000, 0, 0, 10^5\right) & \text{water pre-shock,} \\ \left(1, 0, 0, 10^5\right) & \text{air,} \end{cases} \tag{32}$$

where water is modeled with a stiffened equation of state ($\gamma = 4.4$, $P_{\text{inf}} = 6 \cdot 10^8$) and air as ideal gas ($\gamma = 1.4$). The domain size is set to $[0, 0.024] \times [0, 0.024]$, where an air bubble with diameter $D = 0.006$ is placed in the center. The shock front is initially placed at $x = 0.008$. Inflow and outflow conditions are applied at the left and right boundary, respectively.

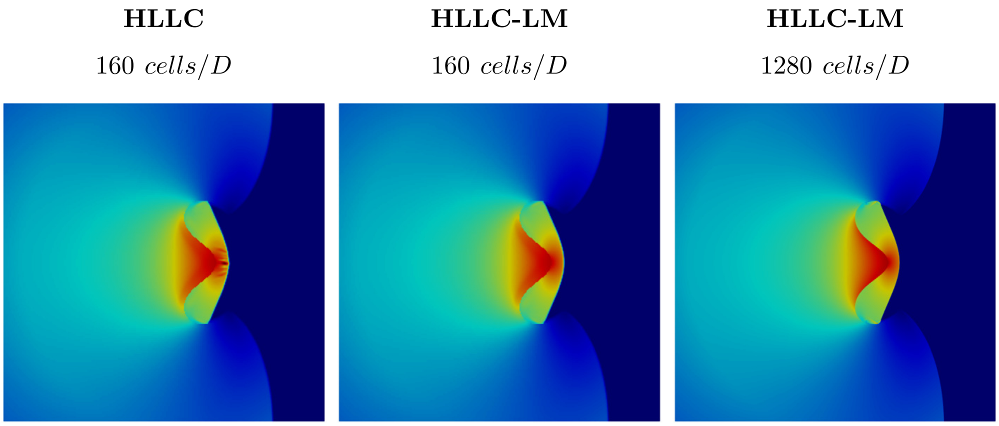

Fig. 21. Shock interface interaction of a air bubble in water at $t = 3 \cdot 10^{-6}$: velocity magnitude contours from blue = 0 to red = 2850.

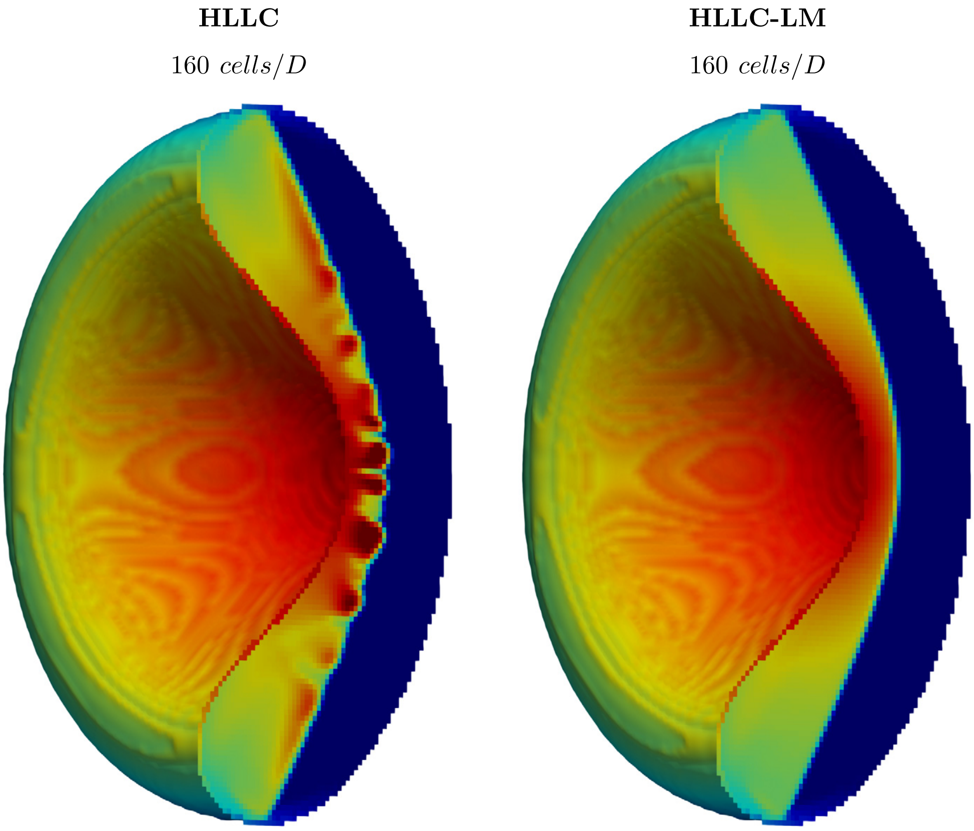

Fig. 22. 3D shock interface interaction of a air bubble in water: velocity magnitude within the air bubble from blue = 0 to red = 3500 at $t = 2.6 \cdot 10^{-6}$.

Neumann boundary condition with zero gradient for all quantities is set at the remaining boundaries. The bubble initially is resolved by 160 cells per diameter and the final time is set to $3 \cdot 10^{-6}$.

Velocity magnitude results for the HLLC and HLLC-LM solver are shown in Fig. 21. Similarly to the previous case with helium, the HLLC approximation does not create any carbuncles. However, the flow behind the shock wave in air is significantly disturbed. The HLLC-LM solver enables a stable prediction of the flow field. Again, the stability of HLLC-LM is further demonstrated by an extremely increased resolution of 1280 cells per diameter. The result of this simulation still is disturbance-free as shown in the right frame of Fig. 21.

We studied the same setup also in three dimensions with a straightforward extension of the domain in z-direction to $[0, 0.024] \times [0, 0.024] \times [0, 0.024]$. The resolution is chosen identically to the original two-dimensional case with 160 cells per diameter. Since the air bubble collapses faster in three dimensions, the final simulation time was reduced to $= 2.6 \cdot 10^{-6}$.

The results given in Fig. 22 demonstrate that the numerical instability is significantly stronger for three-dimensional simulations when the original HLLC solver is applied. Similar to the three-dimensional results for the Sedov blast wave in Section 4, now, small carbuncles can be observed, which never occurred in any of our two-dimensional simulations.

Nevertheless, the low Mach number modification in the HLLC-LM scheme leads to stable and carbuncle-free results as shown in the right frame of Fig. 22.

6. Conclusion

In this paper, the general idea that the low Mach number in transverse direction of the shock wave propagation is the reason for the grid-aligned shock instability has been exploited to design a shock-stable version of the popular HLLC approximate Riemann solver. A simple reduction of non-linear wave speeds as done for the Roe flux would lead to pure upwinding due to the one-sided definition of the HLLC flux. Therefore, a centralized formulation of the HLLC flux is proposed. Applying this centralized formulation does not only avoid the switching, but also allows for a straightforward reduction of nonlinear eigenvalues. A smooth reduction of acoustic dissipation is guaranteed using a sine function. The proposed version of the HLLC scheme with modified low Mach number behavior is denoted HLLC-LM. The modified flux *reduces the dissipation* during the flux calculation in case of low directional Mach number, and fully recovers the original HLLC flux otherwise. Thus, shock stability is retained by a *further reduction of the dissipation* of the HLLC approximation.

Results obtained with the centralized formulation have been thoroughly compared to the ones obtained with the classical formulation and found to be identical with respect to floating-point differences for all studied cases. The stability and accuracy of the HLLC-LM flux has been demonstrated for a comprehensive series of test cases commonly related to the grid-aligned shock instability. However, the prime goal of the high-order methods as applied throughout the paper is to simulate more complex flow situations than the classical carbuncle cases. The advantages of the HLLC-LM when applied to supersonic multi-component flows have been presented in detail. Stability can be maintained also for extremely high-resolved simulations. Although the HLLC flux might still be considered as suitable for most two-dimensional situations due to the fact that the occurring disturbances are commonly bounded and they rarely lead to large deviations unless resolution is drastically increased, this is not valid in three dimensions. The three-dimensional simulations presented in this paper demonstrate that the HLLC flux is likely to produce severe carbuncles similar to the Roe scheme. The HLLC-LM flux revealed excellent results also for three-dimensional simulations. Hence, the combination of HLLC-LM with state-of-the-art high-order methods allows for a robust and accurate simulation of current challenges in high-speed fluid dynamics.

CRediT authorship contribution statement

Nico Fleischmann: Conceptualization, Data curation, Investigation, Methodology, Software, Validation, Visualization, Writing - original draft. **Stefan Adami:** Project administration, Supervision, Writing - review & editing. **Nikolaus A. Adams:** Funding acquisition, Resources, Supervision, Writing - review & editing.

Declaration of competing interest

The authors declare that they have no known competing financial interests or personal relationships that could have appeared to influence the work reported in this paper.

Acknowledgements

This project has received funding from the European Research Council (ERC) under the European Union's Horizon 2020 research and innovation programme (grant agreement No. 667483).

The authors gratefully acknowledge the Gauss Centre for Supercomputing e.V. (www.gauss-centre.eu) for funding this project by providing computing time on the GCS Supercomputer SuperMUC at Leibniz Supercomputing Centre (www.lrz.de).

References

[1] S.K. Godunov, A difference method for numerical calculation of discontinuous solutions of the equations of hydrodynamics, Mat. Sb. 89 (3) (1959) 271–306.
[2] P.L. Roe, Approximate Riemann solvers, parameter vectors, and difference schemes, J. Comput. Phys. 43 (2) (1981) 357–372.
[3] A. Harten, P.D. Lax, B.v. Leer, On upstream differencing and Godunov-type schemes for hyperbolic conservation laws, SIAM Rev. 25 (1) (1983) 35–61.
[4] E.F. Toro, M. Spruce, W. Speares, Restoration of the contact surface in the HLL-Riemann solver, Shock Waves 4 (1) (1994) 25–34.
[5] K. Peery, S. Imlay, Blunt-body flow simulations, in: 24th Joint Propulsion Conference, 1988, p. 2904.
[6] J.J. Quirk, A contribution to the great Riemann solver debate, in: Upwind and High-Resolution Schemes, Springer, 1997, pp. 550–569.
[7] A.V. Rodionov, Artificial viscosity in Godunov-type schemes to cure the carbuncle phenomenon, J. Comput. Phys. 345 (2017) 308–329.
[8] N. Fleischmann, S. Adami, X.Y. Hu, N.A. Adams, A low dissipation method to cure the grid-aligned shock instability, J. Comput. Phys. 401 (2020) 109004.
[9] B. Einfeldt, On Godunov-type methods for gas dynamics, SIAM J. Numer. Anal. 25 (2) (1988) 294–318.
[10] E.F. Toro, Riemann Solvers and Numerical Methods for Fluid Dynamics: A Practical Introduction, Springer Science & Business Media, 2013.
[11] E.F. Toro, The HLLC Riemann solver, Shock Waves (2019) 1–18.
[12] P. Batten, N. Clarke, C. Lambert, D.M. Causon, On the choice of wavespeeds for the HLLC Riemann solver, SIAM J. Sci. Comput. 18 (6) (1997) 1553–1570.
[13] D.S. Balsara, M. Dumbser, R. Abgrall, Multidimensional HLLC Riemann solver for unstructured meshes – with application to Euler and MHD flows, J. Comput. Phys. 261 (2014) 172–208.
[14] S. Li, An HLLC Riemann solver for magneto-hydrodynamics, J. Comput. Phys. 203 (1) (2005) 344–357.
[15] K.F. Gurski, An HLLC-type approximate Riemann solver for ideal magnetohydrodynamics, SIAM J. Sci. Comput. 25 (6) (2004) 2165–2187.

[16] X. Hu, N.A. Adams, G. Iaccarino, On the HLLC Riemann solver for interface interaction in compressible multi-fluid flow, J. Comput. Phys. 228 (17) (2009) 6572–6589.
[17] E. Johnsen, T. Colonius, Implementation of WENO schemes in compressible multicomponent flow problems, J. Comput. Phys. 219 (2) (2006) 715–732.
[18] D.P. Garrick, M. Owkes, J.D. Regele, A finite-volume HLLC-based scheme for compressible interfacial flows with surface tension, J. Comput. Phys. 339 (2017) 46–67.
[19] S.D. Kim, B.J. Lee, H.J. Lee, I.-S. Jeung, Robust HLLC Riemann solver with weighted average flux scheme for strong shock, J. Comput. Phys. 228 (20) (2009) 7634–7642.
[20] K. Huang, H. Wu, H. Yu, D. Yan, Cures for numerical shock instability in HLLC solver, Int. J. Numer. Methods Fluids 65 (9) (2011) 1026–1038.
[21] Y.-X. Ren, A robust shock-capturing scheme based on rotated Riemann solvers, Comput. Fluids 32 (10) (2003) 1379–1403.
[22] Z. Shen, W. Yan, G. Yuan, A robust HLLC-type Riemann solver for strong shock, J. Comput. Phys. 309 (2016) 185–206.
[23] W. Xie, R. Zhang, J. Lai, H. Li, An accurate and robust HLLC-type Riemann solver for the compressible Euler system at various Mach numbers, Int. J. Numer. Methods Fluids 89 (10) (2019) 430–463.
[24] S. Simon, J. Mandal, A cure for numerical shock instability in HLLC Riemann solver using antidiffusion control, Comput. Fluids 174 (2018) 144–166.
[25] S. Simon, J. Mandal, A simple cure for numerical shock instability in the HLLC Riemann solver, J. Comput. Phys. 378 (2019) 477–496.
[26] G.-S. Jiang, C.-W. Shu, Efficient implementation of weighted ENO schemes, J. Comput. Phys. 126 (1) (1996) 202–228.
[27] S. Gottlieb, C.-W. Shu, E. Tadmor, Strong stability-preserving high-order time discretization methods, SIAM Rev. 43 (1) (2001) 89–112.
[28] N. Fleischmann, S. Adami, N.A. Adams, Numerical symmetry-preserving techniques for low-dissipation shock-capturing schemes, Comput. Fluids 189 (2019) 94–107.
[29] H. Guillard, B. Nkonga, On the behaviour of upwind schemes in the low Mach number limit: a review, in: Handbook of Numerical Analysis, vol. 18, Elsevier, 2017, pp. 203–231.
[30] F. Rieper, A low-Mach number fix for Roe's approximate Riemann solver, J. Comput. Phys. 230 (13) (2011) 5263–5287.
[31] X.-s. Li, C.-w. Gu, An all-speed Roe-type scheme and its asymptotic analysis of low Mach number behaviour, J. Comput. Phys. 227 (10) (2008) 5144–5159.
[32] H. Guillard, C. Viozat, On the behaviour of upwind schemes in the low Mach number limit, Comput. Fluids 28 (1) (1999) 63–86.
[33] H. Guillard, A. Murrone, On the behavior of upwind schemes in the low Mach number limit: II. Godunov type schemes, Comput. Fluids 33 (4) (2004) 655–675.
[34] Z. Chen, X. Huang, Y.-X. Ren, Z. Xie, M. Zhou, Mechanism study of shock instability in Riemann-solver-based shock-capturing scheme, AIAA J. 56 (9) (2018) 3636–3651.
[35] A. Harten, Adaptive multiresolution schemes for shock computations, J. Comput. Phys. 115 (2) (1994) 319–338.
[36] J.W. Kaiser, N. Hoppe, S. Adami, N.A. Adams, An adaptive local time-stepping scheme for multiresolution simulations of hyperbolic conservation laws, J. Comput. Phys. X 4 (2019) 100038.
[37] X.Y. Hu, N.A. Adams, C.-W. Shu, Positivity-preserving method for high-order conservative schemes solving compressible Euler equations, J. Comput. Phys. 242 (2013) 169–180.
[38] F. Kemm, Heuristical and numerical considerations for the carbuncle phenomenon, Appl. Math. Comput. 320 (2018) 596–613.
[39] P. Woodward, P. Colella, The numerical simulation of two-dimensional fluid flow with strong shocks, J. Comput. Phys. 54 (1) (1984) 115–173.
[40] F. Kemm, On the proper setup of the double Mach reflection as a test case for the resolution of gas dynamics codes, Comput. Fluids 132 (2016) 72–75.
[41] X.Y. Hu, B. Khoo, N.A. Adams, F. Huang, A conservative interface method for compressible flows, J. Comput. Phys. 219 (2) (2006) 553–578.
[42] L. Fu, A low-dissipation finite-volume method based on a new TENO shock-capturing scheme, Comput. Phys. Commun. 235 (2019) 25–39.
[43] E.J. Tasker, R. Brunino, N.L. Mitchell, D. Michielsen, S. Hopton, F.R. Pearce, G.L. Bryan, T. Theuns, A test suite for quantitative comparison of hydrodynamic codes in astrophysics, Mon. Not. R. Astron. Soc. 390 (3) (2008) 1267–1281.
[44] I. Glass, J. Kaca, D. Zhang, H. Glaz, J. Bell, J. Trangenstein, J. Collins, Diffraction of planar shock waves over half-diamond and semicircular cylinders: an experimental and numerical comparison, in: AIP Conference Proceedings, vol. 208, AIP, 1990, pp. 246–251.
[45] O. Haimovich, S.H. Frankel, Numerical simulations of compressible multicomponent and multiphase flow using a high-order targeted ENO (TENO) finite-volume method, Comput. Fluids 146 (2017) 105–116.

A.4 On an inconsistency of the arithmetic-average signal speed estimate for HLL-type Riemann solvers

CCC RightsLink®

Home | Help | Live Chat | Sign in | Create Account

On an inconsistency of the arithmetic-average signal speed estimate for HLL-type Riemann solvers

Author: Nico Fleischmann,Stefan Adami,Nikolaus A. Adams

Publication: Journal of Computational Physics: X

Publisher: Elsevier

Date: September 2020

Journal Author Rights

Please note that, as the author of this Elsevier article, you retain the right to include it in a thesis or dissertation, provided it is not published commercially. Permission is not required, but please ensure that you reference the journal as the original source. For more information on this and on your other retained rights, please visit: https://www.elsevier.com/about/our-business/policies/copyright#Author-rights

BACK CLOSE WINDOW

Journal of Computational Physics: X 8 (2020) 100077

Contents lists available at ScienceDirect

Journal of Computational Physics: X

www.elsevier.com/locate/jcpx

On an inconsistency of the arithmetic-average signal speed estimate for HLL-type Riemann solvers

Nico Fleischmann *, Stefan Adami, Nikolaus A. Adams

Technical University of Munich, Department of Mechanical Engineering, Chair of Aerodynamics and Fluid Mechanics, Boltzmannstraße 15, 85748 Garching, Germany

ARTICLE INFO

Article history:
Received 21 April 2020
Received in revised form 11 September 2020
Accepted 25 September 2020
Available online 30 September 2020

Keywords:
Approximate Riemann solver
HLL
HLLC
Signal speed estimates
Low-dissipation scheme

ABSTRACT

In this short note, we highlight the sensitivity of the HLL-type Riemann solver with respect to the choice of signal speed estimates and demonstrate a major deficiency of the arithmetic-average estimate. The investigation of two essential Riemann problems and a classical bow shock simulation reveals that inherent inconsistencies of the arithmetic-average estimate may lead to unexpected behavior and erroneous results.

1. Introduction

The development of computationally cheap but nevertheless stable and accurate approximations of the Riemann problem is crucial for the success of Godunov-type methods [1] in computational fluid dynamics. In combination with high-order discretizations, such as WENO schemes [2], these approximate-flux solvers have become popular nowadays for the simulation of complex multi-scale flow problems, e.g. shock interactions with phase interfaces or turbulent flows [3]. In particular, Roe and HLL-type Riemann solvers are applied in various state-of-the-art compressible flow solvers due to their favorable low numerical dissipation [4–6]. Common for such solvers is the need for proper estimations of the wave signal speeds. An overview of the topic can be found in [3]. In this short note, we highlight the sensitivity of the HLL-type Riemann solver with respect to the choice of signal speed estimates and demonstrate a major deficiency of the arithmetic-average estimate, which has become increasingly popular in recent publications [7–10].

In their fundamental work, Harten, Lax and van Leer [5] proposed design principles for simple but nevertheless robust approximate Riemann solvers where left and right states are linked through one or two intermediate states separated by waves. They did not propose actual estimates of the essential signal speeds for their approximations. They stated, however, that the estimates for the left- and right-going wave speed have to be lower, respectively upper bounds of the physical wave speeds. The popular HLL and HLLC Riemann approximations result from the combination of these design principles with suitable signal speed estimates as proposed by different authors [11,12,6,13,14].

Both Davis [11] and Einfeldt [12] simultaneously developed signal speed estimates for the HLL approximation. Besides the simple but rarely applied estimates $S_L = u_L - c_L$ and $S_R = u_R + c_R$, Davis also proposed

---

* Corresponding author.
E-mail addresses: nico.fleischmann@tum.de (N. Fleischmann), stefan.adami@tum.de (S. Adami), nikolaus.adams@tum.de (N.A. Adams).

https://doi.org/10.1016/j.jcpx.2020.100077

$$S_L^{Davis} = \min(u_L - c_L, u_R - c_R), \qquad S_R^{Davis} = \max(u_L + c_L, u_R + c_R) \tag{1}$$

for the minimum signal speed S_L and the maximum signal speed S_R with direct application of the left and right velocity u and speed of sound c. Instead, Einfeldt defines the generalized formulation

$$\hat{c}^2 = \frac{{c_L}^2 \cdot \sqrt{\rho_L} + c_R^2 \cdot \sqrt{\rho_R}}{\sqrt{\rho_L} + \sqrt{\rho_R}} + \frac{1}{2} \frac{\sqrt{\rho_L}\sqrt{\rho_R}}{\left(\sqrt{\rho_L} + \sqrt{\rho_R}\right)^2} \left(u_R - u_L\right)^2, \tag{2}$$

and the Roe average

$$\hat{u} = \frac{u_L \cdot \sqrt{\rho_L} + u_R \cdot \sqrt{\rho_R}}{\sqrt{\rho_L} + \sqrt{\rho_R}} \tag{3}$$

to determine the final signal speed estimates $S_L = \hat{u} - \hat{c}$ and $S_R = \hat{u} + \hat{c}$ as proposed in [12]. A blend of Davis' approach and Einfeldt estimates delivers slightly improved estimates given by

$$S_L^{Einfeldt} = \min(u_L - c_L, \hat{u} - \hat{c}), \qquad S_R^{Einfeldt} = \max(u_R + c_R, \hat{u} + \hat{c}) \tag{4}$$

which will be denoted 'Einfeldt estimates' for simplicity in the remainder of the paper. Batten et al. [13] proposed similar estimates to Eq. (4) with the only difference being that $\hat{c}$ is determined by the original Roe average instead of the generalized formulation of Einfeldt (2). The contact wave was reconstructed by Toro et al. [6] resulting in the HLLC approximate Riemann solver that covers all physical waves governed by the Euler equations. Moreover, the authors [6] suggested to determine the signal speeds from the constant intermediate pressure p^* instead of calculating them directly. p^* is approximated under the assumption that both nonlinear waves are rarefaction waves. Afterwards, the exact wave relations are applied to determine the signal speed estimates. Finally, Batten et al. [13] proposed an estimate for the velocity of the contact speed in the form of

$$S_* = \frac{p_R - p_L + \rho_L u_L \left(S_L - u_L\right) - \rho_R u_R \left(S_R - u_R\right)}{\rho_L \left(S_L - u_L\right) - \rho_R \left(S_R - u_R\right)}, \tag{5}$$

which follows directly from the acoustic wave speed estimates S_L and S_R, and left and right primitive states. Guermond and Popov [14] were the first to develop signal speed estimates that fulfill the essential boundedness criterion of Harten et al. [5]. They proposed both a direct and a more accurate iterative method to determine bounds for the physical wave speeds. Recently, Toro et al. [15] performed a detailed investigation on the boundedness of various signal speed estimates, where they showed that most established estimates do not bound the physical wave speeds in general. Furthermore, they provided new bound estimates for the fastest wave speeds. In recent publications [7–10], the accurate but computationally expensive Einfeldt signal speed estimate is more and more replaced by the simple arithmetic-average estimate with $\hat{u} = \frac{1}{2}\left(u_L + u_R\right)$ and $\hat{c} = \frac{1}{2}\left(c_L + c_R\right)$. This selection is reported to deliver results that are close to the ones obtained with the original Einfeldt estimate for a broad range of cases. However, the reasoning is highly empirical for strong shocks since a theoretical foundation is only given for sufficiently weak shocks, as remarked by Einfeldt [12]. Indeed, it can be easily shown that the arithmetic-average signal speed estimate contradicts to fundamental assumptions of the underlying Riemann approximation. In the following section, this will be demonstrated in detail for a simple moving shock wave and a steady shock wave. The application of the arithmetic average is particularly problematic for bow shock simulations as shown in detail in the third section. Additionally, a replacement of the original "if" statements by sign functions within the HLLC formulation is discussed. The latter implementation might (almost) completely hide the misbehavior of the arithmetic average.

2. Discussion of signal speed estimates for simple Rankine-Hugoniot shock conditions

First, the described signal speed estimates connected to the HLLC approximation are evaluated for a simple moving shock wave. This special case frequently appears in practical simulations, e.g. after initialization. In this example, we use a fixed pre-shock state with the primitive variables $\rho_R = 1.0$, $v_R = 0$ and $p_R = 1.0$. The left state of the shock is varied along the Hugoniot locus. In Fig. 1, the resulting left (dashed) and right (solid) nonlinear signal speed estimates, and the estimate for the contact velocity (dotted) using Eq. (5) are plotted together with the exact shock speed (bold) for moderate and high Mach numbers ranging from 1.01 to 4 and 1.01 to 20, respectively.

In the following, we analyze the resulting HLLC flux given by Toro et al. [6] in the form

$$\mathbf{F}^{HLLC} = \begin{cases} \mathbf{F}_L & \text{if } S_L \geq 0, \\ \mathbf{F}_{*L} = \mathbf{F}_L + S_L \cdot \left(\mathbf{U}_{*L} - \mathbf{U}_L\right) & \text{if } S_L < 0 \cap S_* \geq 0, \\ \mathbf{F}_{*R} = \mathbf{F}_R + S_R \cdot \left(\mathbf{U}_{*R} - \mathbf{U}_R\right) & \text{if } S_R > 0 \cap S_* \leq 0, \\ \mathbf{F}_R & \text{if } S_R \leq 0, \end{cases} \tag{6}$$

for the different signal speed estimates.

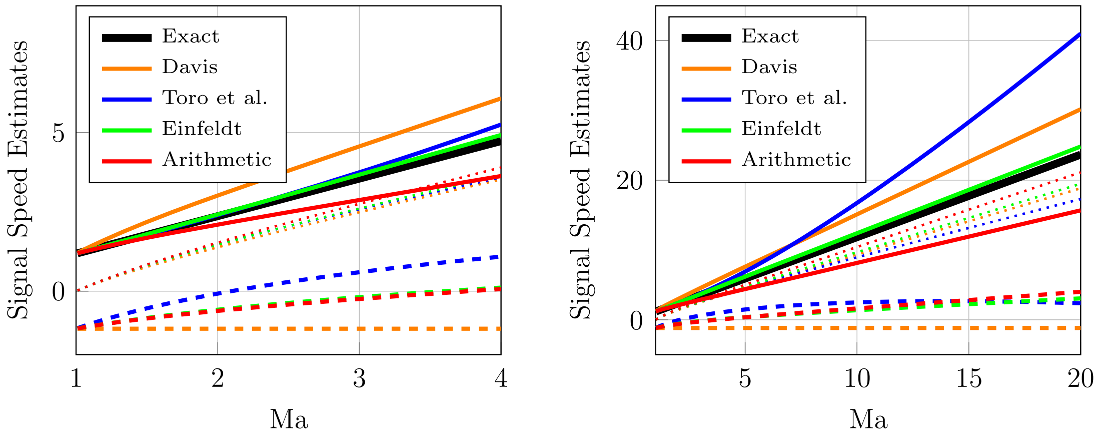

Fig. 1. Signal speed estimates for the HLL(C) approximation evaluated for a simple right-traveling shock wave for different Mach numbers (solid: right; dotted: contact; dashed: left).

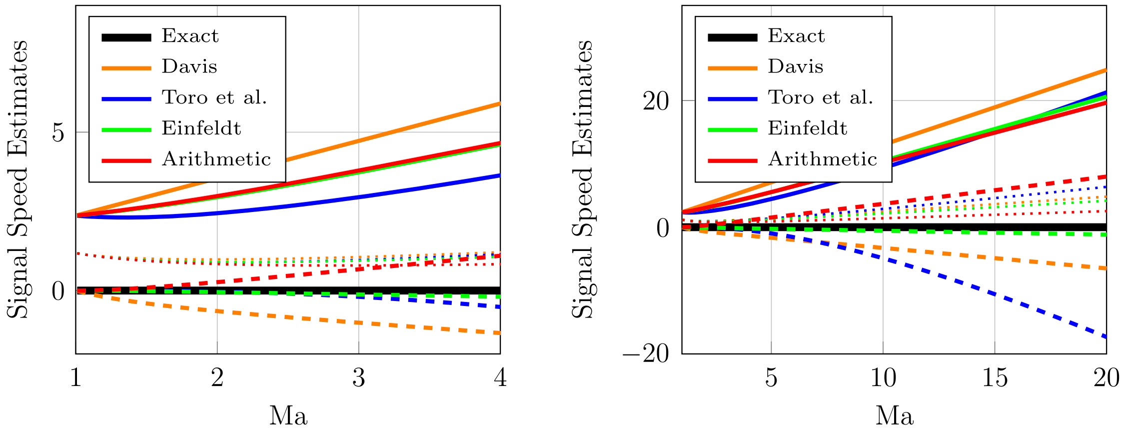

Fig. 2. Signal speed estimates for the HLL(C) approximation evaluated for a simple steady shock wave for different Mach numbers (solid: right; dotted: contact; dashed: left).

A supersonic condition with all signal speeds above zero is predicted for Mach numbers larger than ∼2.1 for the Toro estimate [6], ∼3.5 for the Einfeldt estimate (Eq. (4)-(2)), ∼3.6 for the arithmetic-average estimate and never for the Davis estimate (Eq. (1)). Below these values, the HLLC flux (6) is always given by $\mathbf{F}_{*L}$ since $S_* > 0$ holds true for all Mach numbers and all considered signal speed estimates. Note that $S_L^{Arithmetic}$ and $S_L^{Einfeldt}$ yield nearly identical results.

Although S_R does not directly affect the final flux estimation in this particular case, it is nevertheless interesting to study the differences among the described types of estimates. For moderate Mach numbers, the estimate of Davis considerably overestimates the physical wave speeds, whereas both the estimate of Einfeldt and Toro are only slightly larger. For $Ma > 6.7$, the estimate of Toro predicts the largest right-travelling wave speed, while the estimate of Einfeldt still is close to the physical value. In contrast, the arithmetic-average estimate for S_R systematically underestimates the physical wave speed, and therefore it violates the boundedness criterion of Harten et al. [5]. Moreover, the incorrect nonlinear signal speed estimates lead to an incorrect approximation of the contact velocity. In consequence, S_R even falls below the estimate for the contact velocity for $Ma > 3.3$, which is in contradiction to the fundamental assumption $S_L < S_* < S_R$ [11,12]. However, due to the construction of HLLC this flaw does not affect the resulting flux for simple moving waves. Note, that for $S_L < 0$ the left flux $\mathbf{F}_L$ is used, and for $S_L > 0$ the intermediate flux $\mathbf{F}_{*L}$ is used as $S_* > 0$ for any estimate. Since most practical scenarios consist of such simple moving waves, where the contact wave direction and the flow direction are identical, it can be explained why results obtained with the arithmetic average are often similar to ones obtained with the Einfeldt estimate despite the poor estimate $S_R^{Arithmetic}$. However, in the following we show that is cannot be relied upon.

The same procedure is applied to a steady shock problem with the fixed pre-shock conditions $\rho_L = 1.0$, $u_L = \sqrt{\gamma} \cdot Ma$ and $p_L = 1.0$. Post-shock states are obtained from the Rankine-Hugoniot jump condition for varying Mach numbers. The resulting signal speed estimates are shown in Fig. 2.

A similar qualitative behavior with switched left and right states as compared to the previous case can be observed. Arithmetic-average and Einfeldt estimates for S_R are almost identical. However, as S_* is still strictly positive, now the deviations in S_L directly affect the approximate flux. Again, the physical shock speed is not captured by the arithmetic-average estimate, and $S_L < S_* < S_R$ is violated. Moreover, this estimate leads to a pure supersonic flux selection independently of the Mach number, whereas all other estimates predict a subsonic case. The Einfeldt estimate again is close to the physical wave speed.

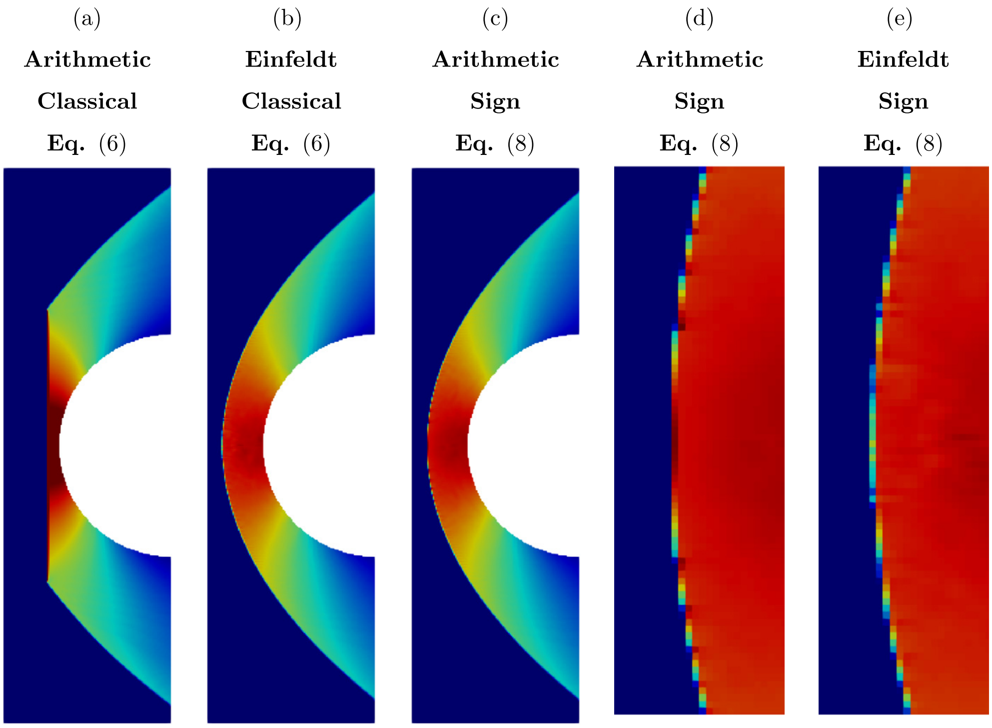

(a) **Arithmetic** **Classical** **Eq.** (6)

(b) **Einfeldt** **Classical** **Eq.** (6)

(c) **Arithmetic** **Sign** **Eq.** (8)

(d) **Arithmetic** **Sign** **Eq.** (8)

(e) **Einfeldt** **Sign** **Eq.** (8)

Fig. 3. Supersonic flow around cylinder for different HLLC flux formulations: color pressure map (blue= 1.0 to red= 550) at $t = 0.05$ resolved with 160 cells per diameter.

3. Effect on bow shock calculations

After the discussion of the specific Riemann problems, the adverse effect of the arithmetic-average estimate is now demonstrated for a classical test case, the supersonic flow around a cylinder. The setup and numerical scheme is chosen identical to [16] with a free-stream Mach number of 20. A classical fifth-order WENO scheme [2] has been applied combined with a third-order, explicit, strong stability-preserving time integration [17] using a CFL number of 0.4. The maximum time step is determined by

$$\Delta t = C_{CFL} \cdot \left[\max_{i,k} \left(\frac{|u_{i,k}| + c_{i,k}}{\Delta x} \right) + \max_{i,k} \left(\frac{|v_{i,k}| + c_{i,k}}{\Delta y} \right) \right]^{-1} \tag{7}$$

with u, v being the velocity components, c being the speed of sound and Δx, Δy being the cell dimensions. The simulation has been performed up to a final time of $t = 0.5$, where a fully developed bow shock is observed. The resulting pressure field is shown in Fig. 3(a) and Fig. 3(b) for the HLLC flux with both the arithmetic-average and the Einfeldt estimate. The application of the former leads to a blocking behavior during the built-up process of the bow shock combined with a massive overshoot in pressure and density in the cells along the shock. A similar behavior including the blocking at the bow shock front can be observed when the HLL flux is combined with arithmetic-average estimates (not shown here). The application of the Einfeldt estimate delivers results as described in literature with minor disturbances behind the shock front [16].

A compact formulation of the HLLC flux (6) using the sign function is given e.g. in [18] and reads

$$\begin{aligned} \mathbf{F}^{HLLC} =& \frac{1 + sign(S_*)}{2} \left[\mathbf{F}_L + S^- \left(\mathbf{U}_{*L} - \mathbf{U}_L \right) \right] + \\ & \frac{1 - sign(S_*)}{2} \left[\mathbf{F}_R + S^+ \left(\mathbf{U}_{*R} - \mathbf{U}_R \right) \right], \end{aligned} \tag{8}$$

with $S^- = \min(S_L, 0)$ and $S^+ = \max(S_R, 0)$.

Interestingly, the failure of the arithmetic-average estimate is almost completely hidden when the sign formulation is applied, see Fig. 3(c), where the arithmetic-average estimate was used in combination with the compact formulation (8). This can be explained by a subtle change in the sequence of algorithmic decisions. The classical formulation first evaluates $S_L > 0$ and immediately chooses the supersonic case if this holds true independently of S^*, whereas the sign formulation first evaluates S^*. If $S_L < S_* < S_R$ is valid, this change in the sequence of decisions will not lead to a different result. However, during the built-up process the contact-wave speed for the arithmetic-average estimate is negative, which is correct since the forming bow shock travels upstream towards the steady-state position, while the arithmetic-average estimate for

S_L is positive. In this case, the sign formulation nevertheless detects the correct right part, and happens to ignore the supersonic nonlinear arithmetic-average estimate. The classical formulation reproduces the incorrect supersonic case. A detailed investigation reveals that there are still minor overshoots in density and pressure at the tip of the bow shock also for the sign formulation as shown in Fig. 3(d). When the Einfeldt estimate is applied, the results for both flux formulations are always identical and no overshoot can be observed, see Fig. 3(e).

This example demonstrates that the described shortcomings of the arithmetic-average estimate can lead to unexpected consequences and wrong results that can be efficiently avoided by the application of mathematically consistent estimates.

4. Conclusion

We have shown in detail that the arithmetic-average estimate may deliver comparable results as the Einfeldt estimate for situations with simple moving shock waves that are dominant in most practical simulations, but may also lead to extremely poor prediction of nonlinear signal speeds for some specific cases, such as bow shocks. As a consequence of the erroneous nonlinear estimates evaluated in Eq. (5), principle assumptions of the underlying HLL-type solver, such as $S_L < S_* < S_R$ are violated by the arithmetic average. Moreover, this fundamental flaw may be hidden by an algorithmic reformulation of the original HLLC Riemann solver, which makes errors due to inaccurate signal speed estimates particularity hard to detect and may lead to unexpected behavior. In contrast to the Einfeldt estimate, both Davis and Toro estimates significantly overestimate signal speeds for strong shocks, which may lead to an increased numerical dissipation. Due to the mentioned facts, we recommend to avoid the arithmetic-average estimate wherever possible, and to apply classical, well-established estimates instead.

CRediT authorship contribution statement

Nico Fleischmann: Conceptualization, Data curation, Investigation, Methodology, Software, Validation, Visualization, Writing - original draft. **Stefan Adami:** Data curation, Project administration, Supervision, Writing - review & editing. **Nikolaus A. Adams:** Funding acquisition, Resources, Supervision, Writing - review & editing.

Declaration of competing interest

The authors declare that they have no known competing financial interests or personal relationships that could have appeared to influence the work reported in this paper.

Acknowledgements

This project has received funding from the European Research Council (ERC) under the European Union's Horizon 2020 research and innovation programme (grant agreement No. 667483).

The authors gratefully acknowledge the Gauss Centre for Supercomputing e.V. (www.gauss-centre.eu) for funding this project by providing computing time on the GCS Supercomputer SuperMUC at Leibniz Supercomputing Centre (www.lrz.de).

References

[1] S.K. Godunov, A difference method for numerical calculation of discontinuous solutions of the equations of hydrodynamics, Mat. Sb. 89 (3) (1959) 271–306.
[2] G.-S. Jiang, C.-W. Shu, Efficient implementation of weighted ENO schemes, J. Comput. Phys. 126 (1) (1996) 202–228.
[3] E.F. Toro, Riemann Solvers and Numerical Methods for Fluid Dynamics: A Practical Introduction, Springer Science & Business Media, 2013.
[4] P.L. Roe, Approximate Riemann solvers, parameter vectors, and difference schemes, J. Comput. Phys. 43 (2) (1981) 357–372.
[5] A. Harten, P.D. Lax, B.v. Leer, On upstream differencing and Godunov-type schemes for hyperbolic conservation laws, SIAM Rev. 25 (1) (1983) 35–61.
[6] E.F. Toro, M. Spruce, W. Speares, Restoration of the contact surface in the HLL-Riemann solver, Shock Waves 4 (1) (1994) 25–34.
[7] V. Coralic, T. Colonius, Finite-volume WENO scheme for viscous compressible multicomponent flows, J. Comput. Phys. 274 (2014) 95–121.
[8] M.L. Wong, S.K. Lele, High-order localized dissipation weighted compact nonlinear scheme for shock- and interface-capturing in compressible flows, J. Comput. Phys. 339 (2017) 179–209.
[9] D.P. Garrick, M. Owkes, J.D. Regele, A finite-volume hllc-based scheme for compressible interfacial flows with surface tension, J. Comput. Phys. 339 (2017) 46–67.
[10] N. Fleischmann, S. Adami, N.A. Adams, Numerical symmetry-preserving techniques for low-dissipation shock-capturing schemes, Comput. Fluids 189 (2019) 94–107.
[11] S. Davis, Simplified second-order Godunov-type methods, SIAM J. Sci. Stat. Comput. 9 (3) (1988) 445–473.
[12] B. Einfeldt, On Godunov-type methods for gas dynamics, SIAM J. Numer. Anal. 25 (2) (1988) 294–318.
[13] P. Batten, N. Clarke, C. Lambert, D.M. Causon, On the choice of wavespeeds for the HLLC Riemann solver, SIAM J. Sci. Comput. 18 (6) (1997) 1553–1570.
[14] J.-L. Guermond, B. Popov, Fast estimation from above of the maximum wave speed in the Riemann problem for the Euler equations, J. Comput. Phys. 321 (2016) 908–926.
[15] E. Toro, L. Müller, A. Siviglia, Bounds for wave speeds in the Riemann problem: direct theoretical estimates, Comput. Fluids 209 (2020) 104640.
[16] N. Fleischmann, S. Adami, X.Y. Hu, N.A. Adams, A low dissipation method to cure the grid-aligned shock instability, J. Comput. Phys. 401 (2020) 109004.
[17] S. Gottlieb, C.-W. Shu, E. Tadmor, Strong stability-preserving high-order time discretization methods, SIAM Rev. 43 (1) (2001) 89–112.
[18] E. Johnsen, T. Colonius, Implementation of WENO schemes in compressible multicomponent flow problems, J. Comput. Phys. 219 (2) (2006) 715–732.

Bibliography

[1] Abgrall, R. “How to prevent pressure oscillations in multicomponent flow calculations: a quasi conservative approach”. In: *Journal of Computational Physics* 125.1 (1996), pp. 150–160.

[2] Acker, F., Borges, R. d. R., and Costa, B. “An improved WENO-Z scheme”. In: *Journal of Computational Physics* 313 (2016), pp. 726–753.

[3] Allaire, G., Clerc, S., and Kokh, S. “A five-equation model for the simulation of interfaces between compressible fluids”. In: *Journal of Computational Physics* 181.2 (2002), pp. 577–616.

[4] Arora, M. and Roe, P. L. “On postshock oscillations due to shock capturing schemes in unsteady flows”. In: *Journal of Computational Physics* 130.1 (1997), pp. 25–40.

[5] Bader, G. and Kemm, F. “The carbuncle phenomenon in shallow water simulations”. In: *The second international conference on computational science and engineering (ICCSE-2014). Ho Chi Minh City, Vietnam*. 2014.

[6] Balsara, D. S., Dumbser, M., and Abgrall, R. “Multidimensional HLLC Riemann solver for unstructured meshes–with application to Euler and MHD flows”. In: *Journal of Computational Physics* 261 (2014), pp. 172–208.

[7] Balsara, D. S., Garain, S., Florinski, V., and Boscheri, W. “An efficient class of WENO schemes with adaptive order for unstructured meshes”. In: *Journal of Computational Physics* 404 (2020), p. 109062.

[8] Balsara, D. S., Garain, S., and Shu, C.-W. “An efficient class of WENO schemes with adaptive order”. In: *Journal of Computational Physics* 326 (2016), pp. 780–804.

[9] Balsara, D. S. and Shu, C.-W. “Monotonicity preserving weighted essentially non-oscillatory schemes with increasingly high order of accuracy”. In: *Journal of Computational Physics* 160.2 (2000), pp. 405–452.

[10] Batten, P., Clarke, N., Lambert, C., and Causon, D. M. “On the choice of wavespeeds for the HLLC Riemann solver”. In: *SIAM Journal on Scientific Computing* 18.6 (1997), pp. 1553–1570.

[11] Boniface, J.-C. “Rescaling of the Roe scheme in low Mach-number flow regions”. In: *Journal of Computational Physics* 328 (2017), pp. 177–199.

[12] Borges, R., Carmona, M., Costa, B., and Don, W. S. “An improved weighted essentially non-oscillatory scheme for hyperbolic conservation laws”. In: *Journal of Computational Physics* 227.6 (2008), pp. 3191–3211.

[13] Brio, M. and Wu, C. C. “An upwind differencing scheme for the equations of ideal magnetohydrodynamics”. In: *Journal of computational physics* 75.2 (1988), pp. 400–422.

[14] Bryngelson, S. H., Schmidmayer, K., Coralic, V., Meng, J. C., Maeda, K., and Colonius, T. “MFC: An open-source high-order multi-component, multi-phase, and multi-scale compressible flow solver”. In: *Computer Physics Communications* 266 (2021), p. 107396.

[15] Chauvat, Y., Moschetta, J.-M., and Gressier, J. “Shock wave numerical structure and the carbuncle phenomenon”. In: *International Journal for Numerical Methods in Fluids* 47.8-9 (2005), pp. 903–909.

[16] Chen, S.-s., Cai, F.-j., Xue, H.-c., Wang, N., and Yan, C. “An improved AUSM-family scheme with robustness and accuracy for all Mach number flows”. In: *Applied Mathematical Modelling* 77 (2020), pp. 1065–1081.

[17] Chen, S.-S., Yan, C., Lin, B.-X., and Li, Y.-S. “A New Robust Carbuncle-Free Roe Scheme for Strong Shock”. In: *Journal of Scientific Computing* (2018), pp. 1–28.

[18] Chen, Z., Huang, X., Ren, Y.-X., Xie, Z., and Zhou, M. “Mechanism study of shock instability in Riemann-solver-based shock-capturing scheme”. In: *AIAA Journal* 56.9 (2018), pp. 3636–3651.

[19] Chen, Z., Huang, X., Ren, Y.-X., Xie, Z., and Zhou, M. “Mechanism-Derived Shock Instability Elimination for Riemann-Solver-Based Shock-Capturing Scheme”. In: *AIAA Journal* 56.9 (2018), pp. 3652–3666.

[20] Chen, Z., Huang, X., Ren, Y.-X., and Zhou, M. “General procedure for Riemann solver to eliminate carbuncle and shock instability”. In: *AIAA Journal* 55.6 (2017), pp. 2002–2015.

[21] Coralic, V. and Colonius, T. “Finite-volume WENO scheme for viscous compressible multicomponent flows”. In: *Journal of Computational Physics* 274 (2014), pp. 95–121.

[22] Coralic, V. and Colonius, T. “Finite-volume WENO scheme for viscous compressible multicomponent flows”. In: *Journal of Computational Physics* 274 (2014), pp. 95–121.

[23] Coulombel, J.-f., Benzoni-Gavage, S., and Serre, D. “Note on a paper by Robinet, Gressier, Casalis & Moschetta”. In: *Journal of Fluid Mechanics* 469 (2002), p. 401.

[24] Davis, S. “Simplified second-order Godunov-type methods”. In: *SIAM Journal on Scientific and Statistical Computing* 9.3 (1988), pp. 445–473.

[25] Delin, C., Zhongguo, S., Zhu, H., and Guang, X. “Improvement of the weighted essentially nonoscillatory scheme based on the interaction of smoothness indicators”. In: *International Journal for Numerical Methods in Fluids* 85.12 (2017), pp. 693–711.

[26] Deng, X. “New high-order hybrid cell-edge and cell-node weighted compact nonlinear schemes”. In: *20th AIAA Computational Fluid Dynamics Conference*. 2011, p. 3857.

[27] Deng, X. and Zhang, H. “Developing high-order weighted compact nonlinear schemes”. In: *Journal of Computational Physics* 165.1 (2000), pp. 22–44.

[28] Don, W. S., Li, D.-M., Gao, Z., and Wang, B.-S. “A characteristic-wise alternative WENO-Z finite difference scheme for solving the compressible multicomponent non-reactive flows in the overestimated quasi-conservative form”. In: *Journal of Scientific Computing* 82.2 (2020), pp. 1–24.

[29] Don, W. S., Li, P., Wong, K. Y., and Gao, Z. “Improved symmetry property of high order weighted essentially non-oscillatory finite difference schemes for hyperbolic conservation laws”. In: *Adv. Appl. Math. Mech* 10.6 (2018), pp. 1418–1439.

[30] Dong, H., Fu, L., Zhang, F., Liu, Y., and Liu, J. “Detonation simulations with a fifth-order teno scheme”. In: *Communications in Computational Physics* 25.5 (2019), pp. 1357–1393.

[31] Dumbser, M., Moschetta, J.-M., and Gressier, J. “A matrix stability analysis of the carbuncle phenomenon”. In: *Journal of Computational Physics* 197.2 (2004), pp. 647–670.

[32] Einfeldt, B. “On Godunov-type methods for gas dynamics”. In: *SIAM Journal on Numerical Analysis* 25.2 (1988), pp. 294–318.

[33] Elling, V. “The carbuncle phenomenon is incurable”. In: *Acta Mathematica Scientia* 29.6 (2009), pp. 1647–1656.

[34] Engquist, B. and Osher, S. “One-sided difference approximations for nonlinear conservation laws”. In: *Mathematics of Computation* 36.154 (1981), pp. 321–351.

[35] Fedkiw, R. P., Aslam, T., Merriman, B., and Osher, S. “A non-oscillatory Eulerian approach to interfaces in multimaterial flows (the ghost fluid method)”. In: *Journal of computational physics* 152.2 (1999), pp. 457–492.

[36] Fleischmann, N., Adami, S., and Adams, N. A. “Numerical symmetry-preserving techniques for low-dissipation shock-capturing schemes”. In: *Computers & Fluids* 189 (2019), pp. 94–107.

[37] Fleischmann, N., Adami, S., and Adams, N. A. “A shock-stable modification of the HLLC Riemann solver with reduced numerical dissipation”. In: *Journal of Computational Physics* 423 (2020), p. 109762.

[38] Fleischmann, N., Adami, S., and Adams, N. A. “On an inconsistency of the arithmetic-average signal speed estimate for HLL-type Riemann solvers”. In: *Journal of Computational Physics: X* 8 (2020), p. 100077.

[39] Fleischmann, N., Adami, S., Hu, X. Y., and Adams, N. A. “A low dissipation method to cure the grid-aligned shock instability”. In: *Journal of Computational Physics* 401 (2020), p. 109004.

[40] Fu, L. “A very-high-order TENO scheme for all-speed gas dynamics and turbulence”. In: *Computer Physics Communications* 244 (2019), pp. 117–131.

[41] Fu, L., Hu, X. Y., and Adams, N. A. “A family of high-order targeted ENO schemes for compressible-fluid simulations”. In: *Journal of Computational Physics* 305 (2016), pp. 333–359.

[42] Fu, L., Hu, X. Y., and Adams, N. A. “Targeted ENO schemes with tailored resolution property for hyperbolic conservation laws”. In: *Journal of Computational Physics* 349 (2017), pp. 97–121.

[43] Gande, N. R. and Bhise, A. A. “Modified third and fifth order WENO schemes for inviscid compressible flows”. In: *Numerical Algorithms* (2020), pp. 1–31.

[44] Gande, N. R., Rathod, Y., and Rathan, S. “Third-order WENO scheme with a new smoothness indicator”. In: *International Journal for Numerical Methods in Fluids* 85.2 (2017), pp. 90–112.

[45] Garrick, D. P., Owkes, M., and Regele, J. D. “A finite-volume hllc-based scheme for compressible interfacial flows with surface tension”. In: *Journal of Computational Physics* 339 (2017), pp. 46–67.

[46] Gerolymos, G., Sénéchal, D., and Vallet, I. “Very-high-order WENO schemes”. In: *Journal of Computational Physics* 228.23 (2009), pp. 8481–8524.

[47] Glaister, P. “An approximate linearised Riemann solver for the Euler equations for real gases”. In: *Journal of Computational Physics* 74.2 (1988), pp. 382–408.

[48] Godunov, S. K. “A difference method for numerical calculation of discontinuous solutions of the equations of hydrodynamics”. In: *Matematicheskii Sbornik* 89.3 (1959), pp. 271–306.

[49] Goldberg, D. “What every computer scientist should know about floating-point arithmetic”. In: *ACM computing surveys (CSUR)* 23.1 (1991), pp. 5–48.

[50] Gottlieb, S., Shu, C.-W., and Tadmor, E. “Strong stability-preserving high-order time discretization methods”. In: *SIAM Review* 43.1 (2001), pp. 89–112.

[51] Gresho, P. M. and Chan, S. T. “On the theory of semi-implicit projection methods for viscous incompressible flow and its implementation via a finite element method that also introduces a nearly consistent mass matrix. Part 2: Implementation”. In: *International journal for numerical methods in fluids* 11.5 (1990), pp. 621–659.

[52] Gressier, J. and Moschetta, J.-M. “Robustness versus accuracy in shock-wave computations”. In: *International Journal for Numerical Methods in Fluids* 33.3 (2000), pp. 313–332.

[53] Guermond, J.-L. and Popov, B. “Fast estimation from above of the maximum wave speed in the Riemann problem for the Euler equations”. In: *Journal of Computational Physics* 321 (2016), pp. 908–926.

[54] Guermond, J.-L. and Popov, B. “Fast estimation from above of the maximum wave speed in the Riemann problem for the Euler equations”. In: *Journal of Computational Physics* 321 (2016), pp. 908–926.

[55] Guillard, H. and Murrone, A. “On the behavior of upwind schemes in the low Mach number limit: II. Godunov type schemes”. In: *Computers & Fluids* 33.4 (2004), pp. 655–675.

[56] Guillard, H. and Nkonga, B. “On the behaviour of upwind schemes in the low Mach number limit: A review”. In: *Handbook of Numerical Analysis*. Vol. 18. Elsevier, 2017, pp. 203–231.

[57] Guillard, H. and Viozat, C. “On the behaviour of upwind schemes in the low Mach number limit”. In: *Computers & Fluids* 28.1 (1999), pp. 63–86.

[58] Gurski, K. F. “An HLLC-type approximate Riemann solver for ideal magnetohydrodynamics”. In: *SIAM Journal on Scientific Computing* 25.6 (2004), pp. 2165–2187.

[59] Haimovich, O. and Frankel, S. H. “Numerical simulations of compressible multicomponent and multiphase flow using a high-order targeted ENO (TENO) finite-volume method”. In: *Computers & Fluids* 146 (2017), pp. 105–116.

[60] Hamzehloo, A., Lusher, D. J., Laizet, S., and Sandham, N. D. “On the performance of WENO/TENO schemes to resolve turbulence in DNS/LES of high-speed compressible flows”. In: *International Journal for Numerical Methods in Fluids* 93.1 (2021), pp. 176–196.

[61] Harlow, F. H. and Amsden, A. A. *FLUID DYNAMICS. A LASL Monograph.* Tech. rep. Los Alamos Scientific Lab., N. Mex., 1971.

[62] Harten, A. “High resolution schemes for hyperbolic conservation laws”. In: *Journal of Computational Physics* 49.3 (1983), pp. 357–393. ISSN: 0021-9991. DOI: https://doi.org/10.1016/0021-9991(83)90136-5. URL: https://www.sciencedirect.com/science/article/pii/0021999183901365.

[63] Harten, A. “ENO schemes with subcell resolution”. In: *Journal of Computational Physics* 83.1 (1989), pp. 148–184.

[64] Harten, A., Engquist, B., Osher, S., and Chakravarthy, S. R. “Uniformly high order accurate essentially non-oscillatory schemes, III”. In: *Upwind and high-resolution schemes*. Springer, 1987, pp. 218–290.

[65] Harten, A. and Hyman, J. M. “Self adjusting grid methods for one-dimensional hyperbolic conservation laws”. In: *Journal of computational physics* 50.2 (1983), pp. 235–269.

[66] Harten, A., Lax, P. D., and Leer, B. v. “On upstream differencing and Godunov-type schemes for hyperbolic conservation laws”. In: *SIAM Review* 25.1 (1983), pp. 35–61.

[67] Henderson, S. and Menart, J. “Grid study on blunt bodies with the carbuncle phenomenon”. In: *39th AIAA thermophysics conference*. 2007, p. 3904.

[68] Henrick, A. K., Aslam, T. D., and Powers, J. M. “Mapped weighted essentially non-oscillatory schemes: achieving optimal order near critical points”. In: *Journal of Computational Physics* 207.2 (2005), pp. 542–567.

[69] Hoppe, N., Adami, S., and Adams, N. A. “A modular massively parallel computing environment for three-dimensional multiresolution simulations of compressible flows”. In: *arXiv preprint arXiv:2012.04385* (2020).

[70] Hu, X. Y., Adams, N. A., and Shu, C.-W. “Positivity-preserving method for high-order conservative schemes solving compressible Euler equations”. In: *Journal of Computational Physics* 242 (2013), pp. 169–180.

[71] Hu, X. Y., Khoo, B., Adams, N. A., and Huang, F. “A conservative interface method for compressible flows”. In: *Journal of Computational Physics* 219.2 (2006), pp. 553–578.

[72] Hu, X. and Adams, N. A. “Scale separation for implicit large eddy simulation”. In: *Journal of Computational Physics* 230.19 (2011), pp. 7240–7249.

[73] Hu, X., Adams, N. A., and Iaccarino, G. “On the HLLC Riemann solver for interface interaction in compressible multi-fluid flow”. In: *Journal of Computational Physics* 228.17 (2009), pp. 6572–6589.

[74] Hu, X., Wang, Q., and Adams, N. A. “An adaptive central-upwind weighted essentially non-oscillatory scheme”. In: *Journal of Computational Physics* 229.23 (2010), pp. 8952–8965.

[75] Huang, K., Wu, H., Yu, H., and Yan, D. “Cures for numerical shock instability in HLLC solver”. In: *International Journal for Numerical Methods in Fluids* 65.9 (2011), pp. 1026–1038.

[76] Jiang, G.-S. and Shu, C.-W. “Efficient implementation of weighted ENO schemes”. In: *Journal of computational physics* 126.1 (1996), pp. 202–228.

[77] Johnsen, E. and Colonius, T. “Implementation of WENO schemes in compressible multicomponent flow problems”. In: *Journal of Computational Physics* 219.2 (2006), pp. 715–732.

[78] Johnsen, E. and Colonius, T. “Implementation of WENO schemes in compressible multicomponent flow problems”. In: *Journal of Computational Physics* 219.2 (2006), pp. 715–732.

[79] Kalkhoran, I. M. and Smart, M. K. “Aspects of shock wave-induced vortex breakdown”. In: *Progress in Aerospace Sciences* 36.1 (2000), pp. 63–95.

[80] Kemm, F. “A carbuncle free Roe-type solver for the Euler equations”. In: *Hyperbolic Problems: Theory, Numerics, Applications*. Springer, 2008, pp. 601–608.

[81] Kemm, F. “A note on the carbuncle phenomenon in shallow water simulations”. In: *ZAMM-Journal of Applied Mathematics and Mechanics/Zeitschrift für Angewandte Mathematik und Mechanik* 94.6 (2014), pp. 516–521.

[82] Kemm, F. “Heuristical and numerical considerations for the carbuncle phenomenon”. In: *Applied Mathematics and Computation* 320 (2018), pp. 596–613.

[83] Ketcheson, D. I. and Luna, M. Q. de. “Numerical simulation and entropy dissipative cure of the carbuncle instability for the shallow water circular hydraulic jump”. In: *arXiv preprint arXiv:2103.09664* (2021).

[84] Kikuchi, Y., Ohnishi, N., and Ohtani, K. “Experimental demonstration of bow-shock instability and its numerical analysis”. In: *Shock Waves* 27.3 (2017), pp. 423–430.

[85] Kim, K. H., Kim, C., and Rho, O.-H. “Methods for the accurate computations of hypersonic flows: I. AUSMPW+ scheme”. In: *Journal of Computational Physics* 174.1 (2001), pp. 38–80.

[86] Kim, S. D., Lee, B. J., Lee, H. J., and Jeung, I.-S. “Robust HLLC Riemann solver with weighted average flux scheme for strong shock”. In: *Journal of Computational Physics* 228.20 (2009), pp. 7634–7642.

[87] Kim, S.-S., Kim, C., Rho, O.-H., and Hong, S. K. “Cures for the shock instability: Development of a shock-stable Roe scheme”. In: *Journal of Computational Physics* 185.2 (2003), pp. 342–374.

[88] Kitamura, K. and Shima, E. “Towards shock-stable and accurate hypersonic heating computations: A new pressure flux for AUSM-family schemes”. In: *Journal of Computational Physics* 245 (2013), pp. 62–83.

[89] Klein, R. “Semi-implicit extension of a Godunov-type scheme based on low Mach number asymptotics I: One-dimensional flow”. In: *Journal of Computational Physics* 121.2 (1995), pp. 213–237.

[90] Kotov, D. V., Yee, H., and Sjögreen, B. “Comparative study of high-order positivity-preserving WENO schemes”. In: *positivity* 1 (2013), pp. 2–4.

[91] Leer, B. van. “The development of numerical fluid mechanics and aerodynamics since the 1960s: US and Canada”. In: *100 Volumes of ‘Notes on Numerical Fluid Mechanics’*. Springer, 2009, pp. 159–185.

[92] Leer, B. van and Nishikawa, H. “Towards the Ultimate Understanding of MUSCL: Pitfalls in Achieving Third-Order Accuracy”. In: ().

[93] LeVeque, R. J. *Finite volume methods for hyperbolic problems*. Vol. 31. Cambridge University Press, 2002.

[94] LeVeque, R. J. and Leveque, R. J. *Numerical methods for conservation laws*. Vol. 132. Springer, 1992.

[95] Li, S. “An HLLC Riemann solver for magneto-hydrodynamics”. In: *Journal of Computational Physics* 203.1 (2005), pp. 344–357.

[96] Li, X.-s. and Gu, C.-w. “An all-speed Roe-type scheme and its asymptotic analysis of low Mach number behaviour”. In: *Journal of Computational Physics* 227.10 (2008), pp. 5144–5159.

[97] Li, X.-s. and Gu, C.-w. “Mechanism of Roe-type schemes for all-speed flows and its application”. In: *Computers & Fluids* 86 (2013), pp. 56–70.

[98] Li, X.-s., Gu, C.-w., and Xu, J.-z. “Development of Roe-type scheme for all-speed flows based on preconditioning method”. In: *Computers & Fluids* 38.4 (2009), pp. 810–817.

[99] Liou, M.-S. “A sequel to AUSM: AUSM+”. In: *Journal of Computational Physics* 129.2 (1996), pp. 364–382.

[100] Liou, M.-S. “Mass flux schemes and connection to shock instability”. In: *Journal of Computational Physics* 160.2 (2000), pp. 623–648.

[101] Liska, R. and Wendroff, B. “Comparison of several difference schemes on 1D and 2D test problems for the Euler equations”. In: *SIAM Journal on Scientific Computing* 25.3 (2003), pp. 995–1017.

[102] Liu, X.-D., Osher, S., and Chan, T. “Weighted essentially non-oscillatory schemes”. In: *Journal of Computational Physics* 115.1 (1994), pp. 200–212.

[103] Mandal, J. and Panwar, V. “Robust HLL-type Riemann solver capable of resolving contact discontinuity”. In: *Computers & fluids* 63 (2012), pp. 148–164.

[104] Moschetta, J.-M., Gressier, J., Robinet, J.-C., and Casalis, G. “The carbuncle phenomenon: a genuine Euler instability?” In: *Godunov Methods*. Springer, 2001, pp. 639–645.

[105] Nonomura, T. and Fujii, K. “Robust explicit formulation of weighted compact nonlinear scheme”. In: *Computers & Fluids* 85 (2013), pp. 8–18.

[106] Osher, S. and Chakravarthy, S. “Upwind schemes and boundary conditions with applications to Euler equations in general geometries”. In: *Journal of Computational Physics* 50.3 (1983), pp. 447–481.

[107] Osher, S. and Solomon, F. “Upwind difference schemes for hyperbolic systems of conservation laws”. In: *Mathematics of Computation* 38.158 (1982), pp. 339–374.

[108] Paillere, H., Viozat, C., Kumbaro, A., and Toumi, I. “Comparison of low Mach number models for natural convection problems”. In: *Heat and mass transfer* 36.6 (2000), pp. 567–573.

[109] Pandolfi, M. and D’Ambrosio, D. “Numerical instabilities in upwind methods: analysis and cures for the “carbuncle” phenomenon”. In: *Journal of Computational Physics* 166.2 (2001), pp. 271–301.

[110] Park, S. H. and Kwon, J. H. “On the dissipation mechanism of Godunov-type schemes”. In: *Journal of Computational Physics* 188.2 (2003), pp. 524–542.

[111] Paula, T., Adami, S., and Adams, N. A. “Analysis of the early stages of liquid-water-drop explosion by numerical simulation”. In: *Physical Review Fluids* 4.4 (2019), p. 044003.

[112] Peery, K. and Imlay, S. “Blunt-body flow simulations”. In: *24th Joint Propulsion Conference*. 1988, p. 2904.

[113] Qiu, J. and Shu, C.-W. “On the construction, comparison, and local characteristic decomposition for high-order central WENO schemes”. In: *Journal of Computational Physics* 183.1 (2002), pp. 187–209.

[114] Quirk, J. J. “A contribution to the great Riemann solver debate”. In: *Upwind and High-Resolution Schemes*. Springer, 1997, pp. 550–569.

[115] Ramalho, M. and Azevedo, J. L. “A possible mechanism for the appearance of the carbuncle phenomenon in aerodynamic simulations”. In: *48th AIAA Aerospace Sciences Meeting Including the New Horizons Forum and Aerospace Exposition*. 2010, p. 872.

[116] Rasthofer, U., Wermelinger, F., Karnakov, P., Šukys, J., and Koumoutsakos, P. “Computational study of the collapse of a cloud with 12 500 gas bubbles in a liquid”. In: *Physical Review Fluids* 4.6 (2019), p. 063602.

[117] Remacle, J.-F., Flaherty, J. E., and Shephard, M. S. “An adaptive discontinuous Galerkin technique with an orthogonal basis applied to compressible flow problems”. In: *SIAM Review* 45.1 (2003), pp. 53–72.

[118] Ren, Y.-X. “A robust shock-capturing scheme based on rotated Riemann solvers”. In: *Computers & Fluids* 32.10 (2003), pp. 1379–1403.

[119] Rieper, F. “A low-Mach number fix for Roe’s approximate Riemann solver”. In: *Journal of Computational Physics* 230.13 (2011), pp. 5263–5287.

[120] Roberts, T. W. “The behavior of flux difference splitting schemes near slowly moving shock waves”. In: *Journal of Computational Physics* 90.1 (1990), pp. 141–160.

[121] Robinet, J.-C., Gressier, J., Casalis, G., and Moschetta, J.-M. “Shock wave instability and the carbuncle phenomenon: same intrinsic origin?” In: *Journal of Fluid Mechanics* 4 (2000), pp. 237–263.

[122] Rodionov, A. V. “Artificial viscosity in Godunov-type schemes to cure the carbuncle phenomenon”. In: *Journal of Computational Physics* 345 (2017), pp. 308–329.

[123] Rodionov, A. V. “Artificial viscosity to cure the carbuncle phenomenon: The three-dimensional case”. In: *Journal of Computational Physics* 361 (2018), pp. 50–55.

[124] Rodionov, A. V. “Artificial viscosity to cure the shock instability in high-order Godunov-type schemes”. In: *Computers & Fluids* 190 (2019), pp. 77–97.

[125] Rodionov, A. V. “Simplified artificial viscosity approach for curing the shock instability”. In: *Computers & Fluids* 219 (2021), p. 104873.

[126] Roe, P. L. “Approximate Riemann solvers, parameter vectors, and difference schemes”. In: *Journal of Computational Physics* 43.2 (1981), pp. 357–372.

[127] Roe, P. and Pike, J. “Efficient construction and utilisation of approximate Riemann solutions”. In: *Proc. of the sixth int’l. symposium on Computing methods in applied sciences and engineering, VI*. 1985, pp. 499–518.

[128] Rossinelli, D., Hejazialhosseini, B., Hadjidoukas, P., Bekas, C., Curioni, A., Bertsch, A., Futral, S., Schmidt, S. J., Adams, N. A., and Koumoutsakos, P. “11 PFLOP/s simulations of cloud cavitation collapse”. In: *SC’13: Proceedings of the International Conference on High Performance Computing, Networking, Storage and Analysis*. IEEE. 2013, pp. 1–13.

[129] Rusanov, V. V. *Calculation of interaction of non-steady shock waves with obstacles*. NRC, Division of Mechanical Engineering, 1962.

[130] Sanders, R., Morano, E., and Druguet, M.-C. “Multidimensional dissipation for upwind schemes: stability and applications to gas dynamics”. In: *Journal of Computational Physics* 145.2 (1998), pp. 511–537.

[131] Saurel, R. and Abgrall, R. “A simple method for compressible multifluid flows”. In: *SIAM Journal on Scientific Computing* 21.3 (1999), pp. 1115–1145.

[132] Saurel, R., Petitpas, F., and Berry, R. A. “Simple and efficient relaxation methods for interfaces separating compressible fluids, cavitating flows and shocks in multiphase mixtures”. In: *journal of Computational Physics* 228.5 (2009), pp. 1678–1712.

[133] Saurel, R., Petitpas, F., and Berry, R. A. “Simple and efficient relaxation methods for interfaces separating compressible fluids, cavitating flows and shocks in multiphase mixtures”. In: *journal of Computational Physics* 228.5 (2009), pp. 1678–1712.

[134] Schmidmayer, K., Bryngelson, S. H., and Colonius, T. “An assessment of multicomponent flow models and interface capturing schemes for spherical bubble dynamics”. In: *Journal of Computational Physics* 402 (2020), p. 109080.

[135] Schmidmayer, K., Petitpas, F., Le Martelot, S., and Daniel, É. “ECOGEN: An open-source tool for multiphase, compressible, multiphysics flows”. In: *Computer Physics Communications* 251 (2020), p. 107093.

[136] Shen, Z., Ren, J., and Cui, X. “On the carbuncle instability of the HLLE-type solvers”. In: *Journal of Physics: Conference Series*. Vol. 1290. 1. IOP Publishing. 2019, p. 012026.

[137] Shen, Z., Yan, W., and Yuan, G. “A stability analysis of hybrid schemes to cure shock instability”. In: *Communications in Computational Physics* 15.5 (2014), pp. 1320–1342.

[138] Shen, Z., Yan, W., and Yuan, G. “A robust HLLC-type Riemann solver for strong shock”. In: *Journal of Computational Physics* 309 (2016), pp. 185–206.

[139] Shi, J., Zhang, Y.-T., and Shu, C.-W. “Resolution of high order WENO schemes for complicated flow structures”. In: *Journal of Computational Physics* 186.2 (2003), pp. 690–696.

[140] Shu, C.-W. “High order weighted essentially nonoscillatory schemes for convection dominated problems”. In: *SIAM Review* 51.1 (2009), pp. 82–126.

[141] Shu, C.-W. and Osher, S. “Efficient implementation of essentially non-oscillatory shock-capturing schemes”. In: *Journal of computational physics* 77.2 (1988), pp. 439–471.

[142] Shyue, K.-M. “An efficient shock-capturing algorithm for compressible multicomponent problems”. In: *Journal of Computational Physics* 142.1 (1998), pp. 208–242.

[143] Simon, S. and Mandal, J. “A cure for numerical shock instability in HLLC Riemann solver using antidiffusion control”. In: *Computers & Fluids* 174 (2018), pp. 144–166.

[144] Simon, S. and Mandal, J. “A simple cure for numerical shock instability in the HLLC Riemann solver”. In: *Journal of Computational Physics* 378 (2019), pp. 477–496.

[145] Steger, J. L. and Warming, R. “Flux vector splitting of the inviscid gasdynamic equations with application to finite-difference methods”. In: *Journal of computational physics* 40.2 (1981), pp. 263–293.

[146] Sun, Z.-S., Luo, L., Ren, Y.-X., and Zhang, S.-Y. “A sixth order hybrid finite difference scheme based on the minimized dispersion and controllable dissipation technique”. In: *Journal of Computational Physics* 270 (2014), pp. 238–254.

[147] Sutherland, R. S. “A new computational fluid dynamics code I: Fyris Alpha”. In: *Astrophysics and Space Science* 327.2 (2010), pp. 173–206.

[148] Titarev, V. A. and Toro, E. F. “Finite-volume WENO schemes for three-dimensional conservation laws”. In: *Journal of Computational Physics* 201.1 (2004), pp. 238–260.

[149] Toro, E., Müller, L., and Siviglia, A. “Bounds for Wave Speeds in the Riemann Problem: Direct Theoretical Estimates”. In: *Computers & Fluids* 209 (2020), p. 104640.

[150] Toro, E. F. *Riemann solvers and numerical methods for fluid dynamics: a practical introduction*. Springer Science & Business Media, 2013.

[151] Toro, E. F., Müller, L. O., and Siviglia, A. “Bounds for wave speeds in the Riemann problem: Direct theoretical estimates”. In: *Computers & Fluids* 209 (2020), p. 104640.

[152] Toro, E. F., Spruce, M., and Speares, W. “Restoration of the contact surface in the HLL-Riemann solver”. In: *Shock Waves* 4.1 (1994), pp. 25–34.

[153] Tritschler, V., Hu, X., Hickel, S., and Adams, N. “Numerical simulation of a Richtmyer–Meshkov instability with an adaptive central-upwind sixth-order WENO scheme”. In: *Physica Scripta* 2013.T155 (2013), p. 014016.

[154] Tritschler, V., Zubel, M., Hickel, S., and Adams, N. “Evolution of length scales and statistics of Richtmyer-Meshkov instability from direct numerical simulations”. In: *Physical Review E* 90.6 (2014), p. 063001.

[155] Turkel, E. “Preconditioned methods for solving the incompressible and low speed compressible equations”. In: *Journal of computational physics* 72.2 (1987), pp. 277–298.

[156] Turkel, E. “Review of preconditioning methods for fluid dynamics”. In: *Applied Numerical Mathematics* 12.1-3 (1993), pp. 257–284.

[157] Van Leer, B. “Towards the ultimate conservative difference scheme. V. A second-order sequel to Godunov’s method”. In: *Journal of computational Physics* 32.1 (1979), pp. 101–136.

[158] Van Leer, B. “Flux-vector splitting for the Euler equation”. In: *Upwind and high-resolution schemes*. Springer, 1997, pp. 80–89.

[159] Van Leer, B., Thomas, J. L., Roe, P. L., and Newsome, R. W. “A comparison of numerical flux formulas for the Euler and Navier-Stokes equations”. In: (1987).

[160] Wang, B.-S., Don, W. S., Garg, N. K., and Kurganov, A. “Fifth-Order A-WENO Finite-Difference Schemes Based on a New Adaptive Diffusion Central Numerical Flux”. In: *SIAM Journal on Scientific Computing* 42.6 (2020), A3932–A3956.

[161] Wang, B., Xiang, G., and Hu, X. Y. “An incremental-stencil WENO reconstruction for simulation of compressible two-phase flows”. In: *International Journal of Multiphase Flow* 104 (2018), pp. 20–31.

[162] Wang, R. and Spiteri, R. J. “Linear instability of the fifth-order WENO method”. In: *SIAM Journal on Numerical Analysis* 45.5 (2007), pp. 1871–1901.

[163] Wermelinger, F., Rasthofer, U., Hadjidoukas, P. E., and Koumoutsakos, P. “Petascale simulations of compressible flows with interfaces”. In: *Journal of computational science* 26 (2018), pp. 217–225.

[164] Wong, M. L. and Lele, S. K. “High-order localized dissipation weighted compact nonlinear scheme for shock-and interface-capturing in compressible flows”. In: *Journal of Computational Physics* 339 (2017), pp. 179–209.

[165] Xie, W., Li, W., Li, H., Tian, Z., and Pan, S. “On numerical instabilities of Godunov-type schemes for strong shocks”. In: *Journal of Computational Physics* 350 (2017), pp. 607–637.

[166] Xie, W., Zhang, R., Lai, J., and Li, H. “An accurate and robust HLLC-type Riemann solver for the compressible Euler system at various Mach numbers”. In: *International Journal for Numerical Methods in Fluids* 89.10 (2019), pp. 430–463.

[167] Xu, K. and Li, Z. “Dissipative mechanism in Godunov-type schemes”. In: *International journal for numerical methods in fluids* 37.1 (2001), pp. 1–22.

[168] Xu, Z. and Shu, C.-W. “Anti-diffusive flux corrections for high order finite difference WENO schemes”. In: *Journal of Computational Physics* 205.2 (2005), pp. 458–485.

[169] Zeng, F., Shen, Y., Liu, S., and Liu, L. “A high performance fifth-order multistep WENO scheme”. In: *International Journal for Numerical Methods in Fluids* ().

[170] Zhang, H., Wang, G., and Zhang, F. “A multi-resolution weighted compact nonlinear scheme for hyperbolic conservation laws”. In: *International Journal of Computational Fluid Dynamics* 34.3 (2020), pp. 187–203.

[171] Zhang, R., Zhang, M., and Shu, C.-W. “On the order of accuracy and numerical performance of two classes of finite volume WENO schemes”. In: *Communications in Computational Physics* 9.3 (2011), pp. 807–827.

[172] Zhang, S., Jiang, S., and Shu, C.-W. “Development of nonlinear weighted compact schemes with increasingly higher order accuracy”. In: *Journal of Computational Physics* 227.15 (2008), pp. 7294–7321.

[173] Zhang, X. and Shu, C.-W. “Positivity-preserving high order finite difference WENO schemes for compressible Euler equations”. In: *Journal of Computational Physics* 231.5 (2012), pp. 2245–2258.

[174] Zhao, G., Sun, M., Xie, S., and Wang, H. “Numerical dissipation control in an adaptive WCNS with a new smoothness indicator”. In: *Applied Mathematics and Computation* 330 (2018), pp. 239–253.

[175] Zhu, J. and Shu, C.-W. “A new type of multi-resolution WENO schemes with increasingly higher order of accuracy”. In: *Journal of Computational Physics* 375 (2018), pp. 659–683.

[176] Zhu, J. and Shu, C.-W. “A new type of third-order finite volume multi-resolution WENO schemes on tetrahedral meshes”. In: *Journal of Computational Physics* 406 (2020), p. 109212.

[177] Zhu, Y. and Hu, X. “An L2-norm regularized incremental-stencil WENO scheme for compressible flows”. In: *Computers & Fluids* 213 (2020), p. 104721.